Hydrothermal Processes within the Active Layer above Alpine Permafrost in Steep Scree Slopes and their Influence on Slope Stability

Dissertation
zur
Erlangung der naturwissenschaftlichen Doktorwürde
(Dr. sc. nat.)
Vorgelegt der
Mathematisch-naturwissenschaftlichen Fakultät
der
Universität Zürich
von

Armin Rist
aus Deutschland

Promotionskomitee
Prof. Dr. Wilfried Haeberli (Vorsitz)
Dr. Marcia Phillips (Leitung der Dissertation)
Dr. Walter Ammann

Zürich 2007

Abstract

In alpine regions hydrothermal processes in the active layer are significant for the estimation of the consequences of climate change on the thermal state of alpine permafrost and on slope stability. As a consequence of global warming, the melting process of snow and ground ice may be accelerated and rainfall intensity in the Alps could increase. This could lead to increased water infiltration and percolation rates, to higher water contents in the active layer and to a thicker saturated zone above the impermeable permafrost table. These processes and the possibility of the permafrost surface acting as a potential shear plane moving into washed-out fine grained materials with a lower shearing resistance could also destabilize scree slopes, potentially resulting in hazardous slope failures.

In polar permafrost regions the hydrothermal regime of the active layer has already been studied in detail and for a long time. However, in alpine permafrost only little is known about the related processes. The objective of this study is therefore to investigate the interactions between the water and heat balance in the active layer underlain by permafrost and their influence on slope stability in steep alpine scree slopes. These questions have been studied under complex field conditions as well as under controlled laboratory experiments.

Field measurements were carried out at Muot da Barba Peider (2980 m a.s.l.) located in the Upper Engadin valley (Eastern Swiss Alps), above the village Pontresina on a NW oriented slope consisting of gneiss debris. In summer 2003 various sensors were buried in the active layer of this slope to measure thermal, hydrological and geotechnical parameters. Results based on three spring thawing periods showed that meteorological, hydrological and thermal ground as well as geotechnical parameters are closely correlated in time. The non-conductive heat transfer mechanisms of water convection and release of latent heat due to phase change of infiltrated snow meltwater caused instantaneous increases in ground temperature each year. The downslope displacement began simultaneously with the onset of continuous meltwater infiltration with the highest rates at the beginning and continuously decreasing during the course of the year.

To investigate the influence of the geotechnical factors *grain size*, *active layer water content* and *permafrost ice content* on the friction angle at the interface of these two layers, a series of systematic laboratory experiments were carried out in the climate chamber, for statistical analysis. A special inclinable shear box was developed, containing an artificial permafrost and active layer. The results showed a positive correlation between each single factor and the friction angle between the permafrost and the active layer. The stabilizing effect of a grain size increase was as expected. However, it is remarkable that the effects of the water and ice content on the friction angle were even higher.

In addition, creep and failure were simulated with an inclinable shear box (scale 1:2 relative to field) at conditions similar to those at the field study site concerning slope inclination and ground texture by water infiltration and successive deepening of the thawing front. These two factors could both be modified with climate change. The simulation showed that a slope failure is most likely in summer, if the thawing active layer deepens into finer grained materials and its water content is at field capacity or even higher due to a heavy rainfall. The situation during snowmelt is less critical, because a large amount of the infiltrated water freezes in the still cold active layer and the slope is therefore stabilized by the ice. However, the amount of ice formed during this period determines the water content during active layer thawing which is important for the disposition of slope failure in summer.

Whilst the hydrothermal conditions at slope failure could be determined in laboratory experiments, the field investigations showed when these conditions are most likely to occur throughout the year under the complex natural circumstances. Thus the study helps to improve the basis on which hydrothermal processes can be simulated numerically with a 3-dimensional mass and energy flux model and therefore potential slope instabilities related to global warming can be assessed.

Zusammenfassung

In alpinen Regionen sind hydrothermale Prozesse in der Auftauschicht von grosser Bedeutung für die Abschätzung der Folgen des Klimawandels auf den thermischen Zustand alpinen Permafrostes und die Hangstabilität. Aufgrund der globalen Erwärmung könnte der Schmelzprozess von Schnee und Untergrund-Eis beschleunigt und die Regenintensität in den Alpen zunehmen. Dies könnte zu erhöhten Infiltrations- und Perkolationsraten, zu höheren Wassergehalten in der Auftauschicht sowie zu einer mächtigeren gesättigten Zone oberhalb des wasserundurchlässigen Permafrostspiegels führen. Diese Prozesse und die Möglichkeit, dass sich der als potentielle Scherfläche fungierende Permafrostspiegel in ausgewaschenes Feinmaterial mit einer geringeren Scherfestigkeit verlagert, könnte zudem Schutthalden destabilisieren und möglicherweise zu gefährlichen Hangrutschungen führen.

In polaren Permafrost-Regionen ist das hydrothermale Regime der Auftauschicht bereits ausführlich und seit geraumer Zeit untersucht worden. Im alpinen Permafrost ist hingegen nur wenig über die damit einhergehenden Prozesse bekannt. Ziel der vorliegenden Arbeit ist es daher, die Interaktionen zwischen Wasser- und Wärmehaushalt in der Auftauschicht oberhalb des Permafrostes sowie deren Einfluss auf die Hangstabilität steiler alpiner Schutthalden zu erforschen. Die entsprechenden Fragen wurden einerseits unter komplexen Feldbedingungen und andererseits in kontrollierten Laborexperimenten untersucht.

Die Feldmessungen wurden am Muot da Barba Peider (2980 m ü. M.) im Oberengadin (östliche Schweizer Alpen) oberhalb des Dorfes Pontresina in einem NW exponierten Hang aus Gneiss-Schutt durchgeführt. Im Sommer 2003 wurden diverse Sensoren in der Auftauschicht des Hangs vergraben, um thermische, hydrologische und geotechnische Parameter zu messen. Resultate dreier Tauperioden im Frühjahr zeigten eine enge zeitliche Korrelation zwischen meteorologischen, hydrologischen, bodenthermischen, sowie geotechnischen Parametern. Die nicht-konduktiven Wärmetransportprozesse der Konvektion durch Wasser und das Freiwerden latenter Wärme infolge des Phasenübergangs des infiltrierten Schneeschmelzwassers löste jedes Jahr einen unmittelbaren Anstieg der Temperaturen im Untergrund aus. Die talwärts gerichtete Hangbewegung begann zeitgleich mit dem Einsetzen der kontinuierlichen Schmelzwasserinfiltration, wobei die höchsten Raten zu Beginn auftraten und im Verlauf des Jahres kontinuierlich abnahmen.

Zur Untersuchung des Einflusses der geotechnischen Faktoren *Korngrösse*, *Wassergehalt der Auftauschicht* und *Eisgehalt des Permafrostes* auf den Scherwinkel zwischen diesen beiden Schichten wurde eine Serie systematischer, statistisch ausgewerteter Laborexperimente durchgeführt. Eine neigbare Scherbox mit einer künstlichen Auftau- und Permafrostschicht wurde speziell hierfür entwickelt. Die Resultate zeigten eine positive Korrelation zwischen jedem einzelnen Faktor und dem Scherwinkel an der Grenzfläche Auftauschicht - Permafrost. Die stabilisierende Effekt aufgrund der Erhöhung der Korngrösse wurde erwartet. Es ist jedoch bemerkenswert, dass die Effekte des Wasser- und Eisgehaltes auf den Scherwinkel sogar noch höher waren.

Zusätzlich wurde das Kriechen und Abrutschen eines Hangs mit einer neigbaren Scherbox (Massstab 1:2 relativ zum Feld) unter ähnlichen Bedingungen wie auf der Untersuchungsfläche im Feld bezüglich Hangneigung und Textur simuliert, indem Wasser infiltriert und die Taufront sukzessive abgesenkt wurde. Diese beiden Faktoren könnten unter dem Einfluss des

Klimawandels beide modifiziert werden. Das Experiment zeigte, dass die Wahrscheinlichkeit einer Hangrutschung im Sommer am grössten ist, da die Auftauschicht zu dieser Zeit in feinere Sedimente hineinwachsen und ihr Wassergehalt aufgrund heftiger Regenfälle Feldkapazität erreichen oder sogar noch höher ansteigen kann. Die Situation während der Schneeschmelze ist weniger kritisch, da ein Grossteil des infiltrierten Wassers in der noch kalten Auftauschicht gefriert und das entstandene Eis den Hang stabilisiert. Die in dieser Periode gebildete Eismenge bestimmt jedoch den Wassergehalt während des Auftauens der Auftauschicht, und dieser ist wichtig für die Disposition einer Hangrutschung im Sommer.

Während die hydrothermalen Bedingungen, die möglicherweise eine Hangrutschung auslösen, in Laborexperimenten bestimmt werden konnten, zeigten die Felduntersuchungen, wann diese Bedingungen unter komplexen natürlichen Verhältnissen im Verlauf des Jahres am wahrscheinlichsten sind. Somit hilft die vorliegende Arbeit, die Grundlage zu verbessern, auf welcher hydrothermale Prozesse numerisch mit einem 3-dimensionalen Massen- und Energiebilanzmodell simuliert und damit potentielle Hanginstabilitäten aufgrund der globalen Erwärmung abgeschätzt werden können.

Acknowledgements

This study was funded by the Swiss National Science Foundation (project no. 200021-102002/1). I am also grateful to the Swiss Federal Institute for Snow and Avalanche Research SLF, Davos, for the scientific, financial and logistical support, without which this study would not have been possible.

I am deeply indebted to Marcia Phillips for her competent supervision of this work as well as her ongoing support. I would like to express my gratitude to Wilfried Haeberli for the sovereign direction of the work and his valuable scientific support. Walter Ammann and Sarah Springman are thanked for their valuable help with the geotechnical aspects.

Many thanks to Martin Kern, Joachim Heierli, Henning Loewe and Bernd Pinzer for their friendly help concerning physics, to Manfred Stähli for his competent and concrete support in hydrology, Oliver Korup who always helped me with questions concerning geomorphology, to Christian Rixen for his good advice concerning statistics, to Charles Fierz for his spontaneous help with radiation measurements, to Christoph Marty for enabling access to meteorological data, to Martin Schneebeli for the technical support concerning the TDR measurement setup, Mathieu Fauve and Anton Lüthi for their assistance with the laser measurements and to Peter Waldner for advice concerning electrical water conductivity measurements. For the fruitful and interesting discussions concerning permafrost and periglacial processes within and outside the framework of our ‘Frozen Coffees’ I want to say thank you to Marcia Phillips, Martina Luetschg, Valérie Herzig and Yannick Bischoff.

My special recognition goes to the electronics team with Martin Hiller, Reto Wetter, Pascal Winistörfer, Franz Herzog and Lloyd Beeler, to the mechanical workshop team with Christian Simeon, Andreas Tröger, Urs Sutter, Florian Michel, Bernhard Zingg and Franz Leuenberger, to Daniela Schmid who runs the cold chambers and to Léonie Fierz, Reto Kohlas and Arno Beeli from the IT team for their efficient and conscientious work in the construction, installation and maintenance of the field measurement equipment, laboratory devices and in the essential IT support.

I am grateful to the team of Stump ForaTec AG (Nänikon) for the delivery of reliable technical solutions to field measuring requirements and to Heli Bernina (Samedan) for the safe transport to the field study site by helicopter even in nasty weather conditions. I am deeply indebted to Ignacio from the building contractor Costa (Pontresina) without whose strong digging facilities, great experience and calmness the measuring equipment could never have been installed in the steep coarse debris slope at the field study site.

Thank you very much for your great assistance in the field and laboratory, for your commitment and the agreeable working atmosphere: Alejandro Casteller, Sandra Baumann, Christian Simeon, Reto Wetter, Martin Hiller, Pascal Winistörfer, Lloyd Beeler, Martina Luetschg, Christian Pfammatter, Adrian Räz, Julia Wessels, Yannick Bischoff, Valérie Herzig, Ariane Walz, Oliver Korup, Michaela Teich, Massimiliano Schwarz, Katharina Platzer, Daniela Schmid, Marc-André Baillifard, Corina Lardelli, Sabina Blum, Bianca Guggenheim, Martin Schärler, Daniel Ehrbar and Anja Schneiter.

Special thanks go to the Institute of Geotechniques (IGT) at the ETH Zurich for the expert testing of material excavated from the field (André Arnold, René Rohr, Andrea Thielen), the provision of laboratory facilities (Jan Laue) and the generous technical help (Juliane Buchheister) as well as the good collaboration and scientific support (Sarah Springman). I would like to express my recognition to Hannes Wydler and Hans Wunderli from the former Institute of Terrestrial Ecology (ITÖ) from the ETH Zurich for providing TDR probes and kindly giving technical support for their use. I am grateful to the Jürg Wolf and Walter Vetsch from the gravel plant Vetsch (Pragg-Jenaz) for the delivery of high quality materials, interest in my work and generous and competent consulting.

Indirect, but essential support to my study was given by the administration of SLF (especially Madeleine Oberhänsli) and the library (Cornelia Gansner) which I appreciate very much.

Many thanks to Marcia Phillips, Wilfried Haeberli, Walter Ammann and Antoni Lewkowicz for proof-reading my thesis and for their valuable advice and comments.

Last but not least I thank my colleagues Ariane Walz, Yannick Bischoff, Alejandro Casteller, Michaela Teich and Christian Bommer for the good climate in our office as well as my family and friends for their loyal moral support and enduring encouragement.

Contents

List of figures

List of tables

List of abbreviations

AL	Active Layer
AL_{post}	Active Layer position after main failure
AL_{pre}	Active Layer position before main failure
ASTM	American Society for Testing and Materials
AT	Air Temperature
BTS	Bottom Temperature of Snow cover
CALM	Circumpolar Active Layer Monitoring
CDD	Cumulated Downslope Displacement at the ground surface
CNRS	Centre National de la Recherche Scientifique
ETH	Eidgenössische Technische Hochschule Zürich (Swiss Federal Institute of Technology Zurich)
EWC	Electrical Water Conductivity
FS	Factor of Safety
GCL	Geosynthetic Clay Liner
GHF	Ground Heat Flux at the active layer base
GT	Ground Temperature
IGT	Institut für Geotechnik (Institute for Geotechnical Engineering)
ISO	International Standards Organization
IT	Information Technology
ITÖ	Institut für Terrestrische Ökologie (Institute for Terrestrial Ecology)
LISA	Level I Stability Analysis
MAAT	Mean Annual Air Temperature
MAGT	Mean Annual Ground Temperature
MDAT	Mean Daily Air Temperature
NHL	Net Heat Loss within a balance year (in this study starting at 1 May)
NW	Northwest
REA	Representative Elementary Area
REV	Representative Elementary Volume
RTC	Rate of Temperature Change
SFC	Soil Freezing Characteristic
SLF	Eidgenössisches Institut für Schnee- und Lawinenforschung (Swiss Federal Institute for Snow and Avalanche Research)
SMC	Soil Moisture Characteristic
TDR	Time Domaine Reflectometry
VIC	Volumetric Ice Content of the active layer
VWC	Volumetric Water Content of the active layer

List of symbols

Latin symbols

a	minimum distance from centre line of displacement marker column to front/ rear panel of active layer
A_{AL}	contact area between active layer and permafrost block
A_{AL_hz}	horizontal area of active layer surface or base
A_{box}	contact area between lower and upper shear frame
a_{max_I}	maximum slope of bearing ratio curve for an interval I
A_{tot}	sum of A_{AL} and A_{box}
A_w	free water surface
c	heat capacity
d_{AL}	grain size of active layer
d_{AL_col}	collective downslope displacement of active layer
$d_{AL\_col\_max}$	maximum shear distance of active layer
d_{AL_f}	active layer downslope displacement during main failure
$d_{AL\_grad\backslash roll}$	gradient of total deformation excluding influence of rolling in uppermost layer
$d_{AL\_grad\_shear}$	gradient of shear deformation
d_{AL_int}	internal downslope displacement of active layer
$d_{AL\_int\_max\backslash roll}$	maximum internal downslope displacement of active layer excluding influence of rolling
$d_{AL\_int\_min}$	minimum internal downslope displacement of active layer
d_{AL_per}	perpendicular displacement of active layer near surface
d_{PF}	grain size of permafrost layer
d_{th}	thaw depth
E	porosity
E_{AL}	porosity of active layer
E_{gravel}	porosity of gravel
E_{grit}	porosity of gravel
f	degree of freedom
f_{AL}	static friction coefficient between active layer and permafrost block
f_{box}	static friction coefficient between upper and lower shear frame
F_D	downslope force
F_{D_AL}	downslope force of active layer
F_{D_box}	downslope force of empty upper shear frame
F_R	friction force
F_{R_AL}	friction force between active layer and permafrost
F_{R_box}	friction force between empty upper and lower shear frame
g	earth’s gravitational constant
h_{AL_n}	normal height of active layer
h_{AL_v}	vertical height of active layer
h_{PF_n}	normal height of permafrost block
h_{sz}	water saturated zone above aquiclude

h_w	height of water saturated zone above permafrost surface
I	infiltration rate
I	interval of total profile length
I_D	relative dry apparent density
I_{D_AL}	relative dry apparent density of active layer
I_{D_PF}	relative dry apparent density of permafrost layer
J	radiation flux
$k_{a\_r1\_I}$	factor between maximum slopes of bearing ratio curves of aligned and roughness profile 1 for an interval I
$k_{a\_r2\_I}$	factor between maximum slopes of bearing ratio curves of aligned and roughness profile 2 for an interval I
k_f	hydraulic conductivity
$k_{r1\_r2\_I}$	factor between maximum slopes of bearing ratio curves of roughness profile 1 and 2 for an interval I
l	upslope length to end of catchment
L_0	actual profile length
l_{AL}	downslope length of active layer
l_{isa}	total length of stretches where intersection line cuts aligned profile
l_{isi}	total length of stretches where intersection line cuts roughness profile
l_m	horizontal measuring length of profile
l_{PF}	downslope length of permafrost block
l_r	profile length ratio
l_t	total analyzable horizontal profile distance of permafrost surface
l_{th}	maximum thaw length of permafrost surface at main failure
m	number of factor step combinations
m_1	arithmetic mean (first momentum) of amplitude distribution
m_2	variance (second momentum) of amplitude distribution
m_3	skewness (third momentum) of amplitude distribution
m_4	kurtosis (fourth momentum) of amplitude distribution
m_{AL}	mass of active layer
m_{AL_dry}	dry mass of active layer
m_{AL_w}	water mass of active layer
m_{box}	mass of empty upper shear frame
m_{s_dry}	dry soil mass
m_{s_wet}	wet soil mass
n	sample size
N	scaling factor for centrifuge modelling
N	experiment size (total number of single experiments)
n_{fme_1}	number of interacting factors of an arbitrary effect
n_{fme_2}	number of interacting factors of corresponding mixed effect
PF	permafrost (block/layer)
q	water discharge rate
Q	water discharge at front of permafrost surface
Q	heat energy
q_{AL}	relative internal downslope displacement
q_{AL_max}	maximum of relative internal downslope displacement

$q_{AL\_max\backslash roll}$	maximum of relative internal downslope displacement as it would be without rolling at surface of active layer
q_{AL_min}	minimum of relative internal downslope displacement
q_d	downslope discharge on the impermeable ice saturated layer
$q_{\Delta is}$	rate of change of ice storage in active layer
$q_{\Delta ws}$	rate of change of water storage in active layer
r	resolution
R	thaw-consolidation ratio
R_a	average roughness
R_{pm}	average peak roughness
R_q	root-mean-square roughness
$R_{z(DIN)}$	average total roughness
s^2	variance
s_d	standard deviation of effects
S_{i_PF}	degree of volumetric ice saturation of permafrost layer
S_{we_AL}	degree of water equivalent saturation of pore space of active layer
t	time
t	critical value of the student-distribution in statistics
T	temperature
T_0	initial temperature of permafrost block
$Tair$	ambient air temperature
T_{air_act}	actual ambient air temperature during experiment
$T_{air\_PF\_cool}$	ambient air temperature for cooling of permafrost block
T_{air_set}	set ambient air temperature during experiment
T_{AL}	temperature of active layer
t_{pa}	macro bearing ratio
T_{PF}	temperature of permafrost
T_{PF_s}	surface temperature of permafrost block
t_{pi}	micro bearing ratio
T_w	temperature of infiltration water
V	total volume
V_{AL}	volume of active layer
V_{AL_w}	water volume of active layer
V_{dis}	discharged water volume
V_{evap}	evaporated volume water
V_{inf}	infiltrated water volume
V_p	pore volume
V_{PF}	volume of permafrost block
V_s	volume of solid grains
V_w	volume of water
w	width of active layer and permafrost block
W	evaporation rate over free water surface
W_a	average waviness
W_g	evaporation rate over surface of active layer
W_q	root-mean-square waviness
W_t	total waviness height

W_z	average total waviness
x	horizontal distance
y	actual depth within surface profile
y_{lr}	vertical amplitude of linear regression line of measured surface profile section
y_{PF_a}	vertical amplitude of aligned surface profile
y_{PF_rough}	vertical amplitude of roughness profile
y_{PF_s}	vertical distance between laser gauge head and actually scanned point of permafrost surface
y_{PF_wavy}	vertical amplitude of waviness profile
$y_{PF\_wavy\_max}$	maximum vertical amplitude of roughness profile
$y_{PF\_wavy\_min}$	minimum vertical amplitude of waviness profile
z	depth below surface of respective layer (active layer or permafrost)
z_{AL_max}	thickness of active layer

Greek symbols

α	inclination angle
α	geometry parameter for TDR-measurements
α_0	inclination angle at which active layer would have undergone dAL_col without influence of upper shear frame
α_m	measurable inclination angle at which active layer has undergone d_{AL_col} influenced by upper shear frame
γ	mean
δ	confidence interval
Δ_a	average absolute slope of surface profile
Δd_{shear}	shear deformation
Δ_q	root-mean-square average slope of surface profile
Δq_{AL_roll}	relative displacement at surface of active layer due to rolling of grains
Δt	time interval
ΔT	temperature difference
ΔT_{PF}	temperature step of permafrost block when artificial active layer is deposited on it
ΔV_{dis}	discharged water volume
Δx	horizontal resolution of laser scanner
Δy	vertical resolution of laser scanner
Δz_{shear}	thickness of shear band
ε_{ra}	relative permittivity of air
ε_{rc}	relative permittivity of composed material
ε_{rs}	relative permittivity of soil
ε_{rw}	relative permittivity of water
ζ	angle of slope of surface profile
ζ_a	angle of average absolute slope of surface profile
ζ_{AL}	relative depth of active layer
ζ_q	angle of root-mean-square average slope of surface profile
θ_{AL}	volumetric water content of active layer
θ_{AL_0}	initial volumetric water content of active layer

θ_{AL_we}	volumetric content of water equivalent (water or ice) in active layer
θ_g	gravimetric water content
θ_{PF}	volumetric water content of permafrost
θ_v	volumetric water content
κ	thermal diffusivity of permafrost
λ	wavelength of surface profile
λ_a	average wavelength of surface profile
λ_c	cut-off wavelength of profile filter
λ_q	root-mean-square wavelength of surface profile
ρ	density
ρ_a	apparent density
ρ_{AL}	actual dry apparent density of active layer
ρ_{PF}	actual dry apparent density of permafrost layer
ρ_r	real density of the solid material
ρ_s	apparent density of dry soil
ρ_w	density of water
τ_f	shear strength against failure of active layer on permafrost
φ	inclination angle at which empty upper shear frame started to slide downslope on lower one
Φ	friction angle between acitve layer and permafrost (inclinination angle at maximum shear distance)
Ψ	angle of dilation

1 Introduction

Permafrost underlies a quarter of the earth's surface and affects a wide range of ecosystems (as was found by Humlum 1997) as well as human life (Haeberli 1992). The main part of this area belongs to the continuous permafrost zone in the polar regions (Péwé 1991). In these regions the main significance of the seasonally thawing active layer is the frost heave due to volume expansion by freezing of water. As great forces are engendered by this process, roads and buildings can be heavily damaged (Miller 1980). Phase changes within the active layer have to be taken in account, especially for the building of pipelines. The hydrothermal processes in the active layer above polar permafrost have already been studied in detail and for a long time (Schrott 1999), because settlements and infrastructure are built directly on the permafrost.

The research on alpine permafrost is relatively young compared to polar permafrost. Although permafrost in the European Alps is discontinuous and underlies only 5% of the area (Keller et al. 1998), it is highly relevant, because the bordering zones and the densely populated Alpine valleys are also affected by permafrost. There are two main reasons for research on alpine permafrost: (1) the effect of climate change on permafrost and (2) slope stability, which could decline, particularly at the surface with active layer deepening due to global warming. As these topics are closely linked to each other, the present study contributes to both of them in an integrative approach.

First a literature review of the present state of the research will be given. On the basis of this review the gap of knowledge and the resulting motivation for the present study will be derived. A hypothesis highlighting the anticipated processes occurring within the course of a year constitutes the starting point from which the objectives of the present study – given thereafter - can be approached.

1.1 State of research

According to the two topics the present study contributes to, the literature review is separated into (1) the hydrothermal regime and (2) the slope stability of the active layer in scree slopes.

1.1.1 Hydrothermal regime of the active layer in debris slopes

As permafrost is defined by means of thermal ground conditions (for example Muller 1945, Williams & Smith 1989, French 1996), it is a sensitive indicator of climatic variability (Lachenbruch & Marshall 1986). However, alterations in permafrost distribution and thickness may also reflect associated changes in geomorphological, hydrological, biogeochemical and ecological processes implying a wide range of research fields related to permafrost.

The first part of the present study is delimited by the following three conditions: (1) hydrothermal processes (2) in the active layer (3) on alpine scree slopes (with coarse blocky surface material). In the recent literature various investigations were found, in which each two of these conditions were fulfilled, i.e. $1 \cap 2$, $1 \cap 3$ and $2 \cap 3$, but only two which combined all three conditions, i.e. $1 \cap (2 \cap 3)$. The literature concerning the hydrothermal regime of the active layer in debris slopes will be reviewed according to this order.

Hydrothermal regime of the active layer in fine grained soils

Recent fundamental physical studies on water flow through porous media in general, which soils (in unfrozen and frozen state) also belong to, were performed for example by Friedman & Jones (2001), Veneziano & Essiam (2003) or Faybishenko (2004). In frozen soils the water dynamics are strongly influenced by phase change and the unfrozen water content strongly depends on the soil temperature; this relation is called soil freezing characteristic (SFC) and is related to the soil moisture characteristic (SMC; relation between water content and water potential). As measurement of the SMC is time-consuming, Flerchinger et al. (2006) investigated whether the deduction of the SMC from in situ determination of the SFC (by means of soil water content and temperature measurements) is applicable for model simulations of frozen and unfrozen soil water dynamics. This approach proved to work well. Stadler et al. (2000) developed a dye tracer technique under laboratory conditions for visualizing and quantifying water infiltration into frozen soils. These methods were transferred to the field by Stähli et al. (2004), where only the dye tracer technique proved to be applicable. The water in the active layer above polar permafrost is routed along preferential flowpaths rather than forming a saturated zone above the frost table because of local ground heterogeneity (Boike et al. 1996, Stadler et al. 1998). How the infiltration capacity of soils is reduced by frost (especially ice) and therefore the surface runoff is increased during snowmelt in spring, was studied by Bayard et al. (2005) in an area of seasonal frost. Burn (1990) found, that the coarser the soil is grained, the higher is the infiltration rate of snowmelt water.

Under conditions of perennially frozen ground the permafrost surface acts as an impermeable layer and therefore restricts the aquifer to the active layer which will be deepened by global warming (Humlum 1997, Haeberli & Beniston 1998). However, Kane et al. (1991) simulated numerically that a permafrost layer with a high ice content, which is therefore actually impermeable, will be replaced through climate warming induced phase change with a more permeable permafrost layer in future. Thus free water movement throughout the permafrost layer is possible. Ishikawa et al. (2005) found spatial variations of soil moisture conditions in the active layer to be caused by the permeability of permafrost at the southern boundary of its discontinuous occurrence in Mongolia; permafrost beneath north-facing forested slopes acts as an impermeable layer resulting in a wet active layer, while permafrost beneath flat pasture plains is permeable due to the ground temperature being only slightly below 0°C resulting in a dry active layer. In order to measure the saturated hydraulic conductivity above an impermeable permafrost layer in the field, Hayashi & Quinton (2004) developed a method using a Guelph permeameter. As the frozen part of the soil acts as an aquiclude in fine grained soils under a humid climate (at least in most cases), the actual thaw depth strongly influences the water storage capacity of the ground and therefore also the runoff. This relation was investigated on permafrost watersheds, in the alpine Yukon Territory (Canada) for the summer by Carey & Quinton (2005), in the southern mountainous taiga of eastern Siberia for the snowmelt period in spring by Suzuki et al. (2006) and in the same area for the whole year by Yamazaki et al. (2006).

Hinkel & Outcalt (1994) point out that water saturation of pore space inhibits vertical water and vapour transport, but in spring under unsaturated conditions melt water infiltrates and vapour migrates downward within the active layer. These processes cause a nearly instantaneous warming of the active layer due to snowmelt (Hinkel et al. 1997). This was confirmed for humid polar permafrost regions by Kane et al. (2001) and Hinkel et al. (2001) and for semiarid permafrost regions with a dry active layer by Ishikawa et al. (2006). During snowmelt Burn (1990) observed an increasing of ground temperatures down to 3m depth, which was due to conduction and sensible heat transferred downward by snowmelt water (or rainwater in summer as mentioned by Hinkel et al. (1997) rather than phase change. Boike et al. (1998) even suggested that purely conductive heat transfer occurs during active layer thawing, whereas during the active layer refreezing nonconductive heat transfer processes such as phase transformation, water advection and vapour diffusion were dominant (Hinkel et al. 1990, Boike et al. 1998). Nonconductive heat transfer is indicated by widely fluctuating positive and negative thermal diffusivity values in the active layer (Hinkel et al. 1990) and plays an important role for the zero-curtain effect (Outcalt et al. 1990). As the zone at the active layer base was found to be ice-enriched, it increases the latent heat required for thaw and thus acts as a thermal buffer (Shur et al. 2005); this ice-enriched zone is therefore called transition zone, the uppermost part of which merges with the active layer at sub-decadal to multi-centennial time scales and is referred to as the transient layer by the authors.

Hinkel et al. (1997) found evaporation and vertical vapour migration to be the fastest heat transfer mechanisms (15 cm/min) in fine grained soils before conductive propagation (8 cm/h on average), vertical water advection (1-5 cm/h) and vapour condensation, which are also nonconductive heat transfer processes and are in this combination referred to as internal distillation by Hinkel & Outcalt (1994). Latent heat turnover due to evaporation and condensation was found to be relevant to the total heat transfer of the soil also in semiarid permafrost regions with a dry active layer by Ishikawa et al. (2006). During the soil cooling in autumn internal distillation moderates the heat transformation in the active layer (Hinkel & Outcalt 1994). Romanovsky & Osterkamp (2000) point out that unfrozen water in the freezing and frozen active layer retards the cooling of the ground due to the latent heat introduced. In winter, when thermal gradients are very small due to the insulating snow cover, internal distillation is driven by osmotic gradients (Hinkel & Outcalt 1994). A correlation between delay of freezing of the pore water deeper than 50 cm below the surface and snow accumulation could be observed by Burn & Smith (1988) which can be attributed to the insulating effect of snow and will be further reviewed below.

Another effect of the active layer refreezing downwards from the surface as well as upwards from the permafrost table is the exclusion of ions in the water from ice, which leads to higher electrolyte concentrations in the intermediate unfrozen zone within the active layer (Hinkel et al. 1997) and to higher pore water pressures due to the volume expansion during freezing. This corresponds with the laboratory experiments carried out on silty soils during freezing and thawing by Harris & Davies (1998). A high pore water pressure was observed when the temperatures were negative. At the beginning of the zero curtain during thawing of the ground the pore water pressure falls rapidly, while it grows rapidly at the end of the thawing process. The increase in electrolyte concentration and pore water pressure are two reasons for freezing point depression besides the high load of the overlying material (Speck 1994). In spite of volumetric increase induced by phase transformation from water to ice, the frost heave effect is small in gravels, but strongly increases with decreasing particle size (Miller 1980).

The following scheme for the thermal and hydrological processes in the active layer above polar permafrost in the seasonal cycle was developed by Boike & Overduin (1999): winter quiescence, snowmelt, infiltration, evaporation and thawing in spring, precipitation, evaporation and maximum thawing depth in summer and finally, the refreezing of the active layer from the surface downwards and in cold permafrost also from the base upwards, as well as the first snowfall in autumn.

Hydrothermal processes in alpine permafrost on coarse debris slopes

Speck (1994) made valuable studies on the physical characteristics of ground materials in alpine permafrost areas which are referred to below. The ground is a polyphase system and therefore the freezing conditions are not isothermal. This means that there is not an exact zero-curtain but temperature declines with time between a liquidus-temperature, at the beginning of the freezing process, and a solidus-temperature, at the end of the freezing process. The unfrozen water content is only a function of the material (or a combination of several materials) and of the temperature and can be calculated by material-specific equations. The water permeability of the ground increases with grain size. Thus, blocky surface material, typical for the active layer above alpine permafrost, has a relatively high permeability of 10^{-4} to 10^{-5} m/s for 0°C at a porosity of 25%. Below 0°C the permeability will decline sharply and will reach a minimum of 10^{-14} m/s at –15°C, independently of material and initial water content. An equation to calculate the permeability at any temperature below 0°C is given by Makowski (1986). The heat capacity of liquid water, which is important for heat conduction as well as phase change, declines slightly with rising temperature but always is much higher (4216 J/(kg K) for 0°C) than that of ice (2500 J/(kg K)), gravel (1500 J/(kg K)) and air (1007 J/(kg K) for 27°C and 1 bar, Speck 1994). This implies that the higher the unfrozen water content, the higher the overall heat capacity will be. For the heat capacity under conditions of phase change the concept of the equivalent capacity as a temperature ground characteristic, which takes into account the latent heat, was developed by Makowski (1986). This approach is the most suitable for simulations of mass and heat flux processes with numerical models, because it fits best with field investigations. The different forms of heat transfer in the ground are conduction, free convection (mass transport in liquid phase caused by a density- and thus by a temperature-gradient), forced convection (mass transport in liquid or gas phase caused by a pressure-gradient), vapour migration and phase transformation.

Extensive field investigations on the hydrological processes in discontinuous mountain permafrost were carried out by Gardaz (1998). Alpine hydrological systems are influenced by mountain storage features such as the winter snow cover, perennial snow patches, glaciers and permafrost. Daily variations in the discharge of a rock glacier stream occurred in accordance with air temperature variations during snowmelt. At the beginning of this period (in June) the daily amplitude of the water discharge was observed to be higher than at the end (in September). The reason for this is the decline in flow volume during the process of snow melting. Whereas in June the time lag between daily air temperature development and the equivalent discharge was several hours, there was no time lag at the end of the melting period in September. This can be explained by the reduction of the snow depth during snow melt, because the percolation time of the melt water through the snow depends on its depth. When snow melt stops, runoff is mainly fed by groundwater in the subpermafrost layer. This implies that the influence of active layer melting and freezing on the discharge of alpine hydrological catchments towards the saturated water flow in the subpermafrost aquifer is negligible. During snowmelt the water infiltrated into the active layer from the snow cover above cannot percolate downward through the permafrost layer to the subpermafrost stratum, because the permafrost table is impermeable to water. However, this assumption made by Gardaz (1998) was previously disputed by Barsch (1993) for a special case: if there is a saturated zone of liquid water above the permafrost table or a zone of interflow on slopes, this border will be water permeable. On the other hand, a field study by Haeberli (1990b) on the rock glacier Murtèl I, Engadin, eastern Swiss Alps, the upper part of which consists of 90% ice by volume, showed that no ice from recent water exists below the permafrost table according to isotope studies. However, at least under water unsaturated conditions above the permafrost table the latter can be said to be water impermeable. Thus water from the active layer can only reach the subpermafrost if it infiltrates where permafrost is interrupted and then flows laterally beneath the permafrost layer (Gardaz 1998). The presence of an aquiclude (permafrost) at the bottom of the active layer and the high permeability of the active layer coarse grained material facilitates a rapid runoff of diluted surface melt water, which therefore has a low electrical conductivity. In contrast to this, solute-rich water with a high electrical conductivity slowly flows through the subpermafrost aquifer. During the refreezing period of the active layer the unfrozen water moves to the cooling front and in general in frozen ground to the cooling plane along the temperature gradient (Barsch 1993). The water which remains in the active layer at the end of autumn will freeze and be conserved over winter until active layer thawing occurs. Brenning (2005) estimated that a water equivalent of 0.3 km^3 per 1000 km^2 of mountain area (i.e. a water column of 30 cm) is stored in the Andes of Santiago de Chile, while this value is estimated to be one order of magnitude lower in the Swiss Alps.

Active layer thermal regime in slopes consisting of coarse blocky material

Geophysical methods have been applied successfully in alpine permafrost to determine the depth of the permafrost table, ice content and the internal structure (shape of permafrost table, its furrows and ridges) from the surface (Vonder Mühll et al. 2000). As a direct contact between the measurement equipment and the ground is needed for seismic and electrical surveys, these two methods have limited applicability in coarse materials. For this purpose gravimetry, ground-penetrating radar and electromagnetic induction are more suitable methods, because they do not require direct contact to the ground. An extensive and detailed investigation on geophysical methods for detecting permafrost in high mountains was effected by Hauck (2001).

The energy exchange processes at the boundary between the atmosphere and lithosphere over alpine permafrost with coarse textured ground as the active layer, investigated by Mittaz et al. (2000), are controlled by climatic factors such as solar radiation, cloudiness, etc. and by site-specific factors such as aspect, slope, surface roughness and snow cover thickness and duration. For the energy balance in case of an active layer consisting of coarse blocks, vertical as well as lateral advective energy fluxes are of great significance. These results agree with the studies on the thermal regime beneath coarse blocky materials at Plateau Mountain, South-Western Alberta, Canada carried out by Harris & Pedersen (1998). These authors also found the advective air movement through the voids between the coarse blocks to be very rapid compared to the slow heat conduction through the individual grains. The air advection thus provides a fast and deep-reaching adaptation of the ground temperatures to those in the atmosphere, i.e. the gradient of the ground temperature with depth is low. Also, the sensible heat transfer by penetration of rain and snow to greater depths is made easier in a coarse blocky active layer. However, air advection will only function if the snow cover is negligibly thin.

Humlum (1997) also investigated the thermal regime of coarse blocky active layers on three rock glaciers in Greenland. He found the surface layer to act as a thermal filter, either protecting the underlying permafrost when the snow cover is thin, or degrading it when the snow cover is thick. The exposure to strong winds is of great importance for the thermal regime of a coarse textured active layer, because forced summer ventilation of the active layer will effectively warm it (wind pumping effect). In conclusion, the thermal characteristics of the active layer are controlled by ground texture, topographic shading, aspect, exposure to wind and snow accumulation. A later study on the influence of the snow cover on interannual variations in ground thawing at two circumpolar-active-layer-monitoring (CALM) sites in Zackenberg (northeast Greenland) was performed by Christiansen (2004). The insulating effect of the snow cover on the ground thermal regime has a flattening deformation effect on interception ellipses generated by plotting annual cycles of air versus ground temperature (Beltrami 1996) and was studied in detail by Luetschg et al. (2004) and numerically modelled by Luetschg (2005). Besides the duration and depth of the snow cover Hanson & Hoelzle (2004) discovered the non-linear heating of the bouldery surface material of Murtèl rock glacier (eastern Swiss Alps) with increasing air temperatures and the micro-topography of rock glacier surfaces to have an important influence on the thermal regime of the active layer. They further point out that the ground thermal regime of the investigated rock glacier is much more influenced by vertical than by (lateral) advective air movement within the blocky deposit. In contrast, Delaloye et al. (2003) found the chimney effect (advection) within scree slopes, which they investigated in Creux du Van (Switzerland), to have a major influence on the ground thermal regime.

The dependence of the ground thermal regime on the grain size was also investigated in Asian mountainous permafrost regions. Gorbunov et al. (2004) reveal a significant difference between the thermal regime of coarse blocky materials and adjacent fine-grained soils in the northern Tien Shan. The mean annual ground temperature in the coarse deposits proved to be 2.5 to 4.0°C cooler than the mean annual air temperature. This allows permafrost to occur even under positive mean annual air temperatures. Within the framework of the construction of the railway across the Qinhai-Tibetan Plateau numerous investigations were conducted on the ground cooling effect of artificial coarse grained embankments due to air convection, for example by Sun et al. (2005) and Zhang et al. (2006).

Hydrothermal processes in the active layer on alpine debris slopes

Sawada et al. (2003) studied the thermal regime in a blocky slope underlain by sporadic permafrost on Mt. Nishi-Nupukaushinupuri (northern Japan). Besides the air circulation in winter they found the snowmelt infiltration in spring and the associated ice formation to be the major controls on the thermal regime of the active layer within the block slope. Their findings concerning the hydrothermal processes in spring could be confirmed for steep debris slopes in the discontinuous alpine permafrost zone by an investigation in the eastern Swiss Alps performed by Rist & Phillips (2005) which is part of the present study.

1.1.2 Slope stability of the active layer in debris slopes

Recent hazardous mass movements related to permafrost such as the Kolka-Karmadon rock/ice slide (see e.g. Haeberli et al. 2004) attract a lot of attention, both in the population and the media, and in the scientific community. However, slow mass movements in periglacial environments such as solifluction and permfrost creep are also highly significant through their influence on the long-term stability of infrastructure such as oil and gas pipelines (Bovis 1993), snow-supporting structures (Phillips 2006) and other Alpine infrastructure such as cable car and ski lift stations (Phillips et al. 2007). Both slow and rapid mass movements are likely to increase in sloping periglacial environments with further global warming due to intensified warming and thawing of ground ice, deepening of the active layer and increasingly extreme meteorological events such as intense rainfall or long periods of high air temperatures. Investigations on slope stability have therefore become increasingly important in the field of periglacial research over the past 20 years, especially in alpine regions. In the 1960s Haefeli (1967) emphasized the importance of the interactions between the main material components of the cryosphere for hillslope processes and made the link between creep and progressive failure for snow, rock and ice in general. A comprehensive review of slope movements in cold regions was conducted by Lewkowicz (1988), while Bovis (1993) in his review focused on Canadian contributions to this topic and emphasized the close relation between hillslope geomorphology and geotechnique.

Three sets of themes regarding slope stability are relevant for the present study: (1) the geomorphic aspects in alpine periglacial environments, (2) the geotechnical aspects of granular materials and (3) the theories on slope stability analysis.

Geomorphic aspect of periglacial mass movements

Mass movements in alpine periglacial environments can be classified by means of the geomorphic feature they originate from; these are (1) bedrock slopes, (2) rock glaciers and (3) soil- and debris-mantled slopes. As the mechanisms of the equivalent groups of mass movements differ considerably, they are usually investigated separately. The literature review of this study will mainly concentrate on the third category.

Bedrock slopes

For the stability of bedrock slopes in permafrost terrain, the filling and modification of discontinuities by water respectively ice is very important. Valuable studies related to this topic have been conducted e.g. by Tharp (1987), Davies et al. (2000), Davies et al. (2001), Gruber et al. (2004a), Gruber et al. (2004b) and Indraratna et al. (2005).

Rock glaciers

The dominant process of mass movement within rock glaciers is creep of the scree-ice mixture which rock glaciers consist of. This topic has already been studied for a long time and thus is well-documented by reviews e.g. by Barsch (1988) and Whalley & Martin (1992). As ice plays a dominant role for permafrost creep in rock glaciers, composite materials consisting of rock and ice were tested by means of geotechnical methods in various studies (Arenson et al. 2002, Arenson et al. 2004, Arenson & Springman 2005b, Arenson & Springman 2005a, Arenson & Palmer 2005). A synthesis of current publications on creep in permafrost and rock glaciers was recently published by Haeberli et al. (2006).

Soil- and debris-mantled slopes

Regarding soil- and debris-mantled slopes in periglacial environments, slow and rapid mass movements are distinguished, as their mechanisms differ considerably. However, rapid failures are often preceded by slow pre-failure movements. Slow mass movements in permafrost slopes consisting of coarse-textured material are referred to as permafrost creep. This process has mainly been investigated for rock glaciers (see above), but it is also relevant for debris-mantled slopes in permafrost terrain. However, the latter can be much steeper and contain less ice than rock glaciers. Thus, creep in steep debris-mantled permafrost slopes was investigated separately (for example by Phillips et al. 2003, Phillips et al. 2007).

Slow, downslope movements of saturated, non-frozen earth material behaving apparently as a viscous mass, over a surface of frozen material were defined as solifluction for example by Brown & Kupsch (1974). In a later review the term solifluction was redefined as slow mass wasting resulting from freeze-thaw action in fine-textured soils (Matsuoka 2001). Thus, the term solifluction developed a more general meaning within the last three decades. However, it can be argued that solifluction is a collective term including the two different processes gelifluction and frost creep (French 1976), which often operate in combination under natural conditions (Harris 1993). The difference between the angles of frost heave (perpendicular to ground surface) and thaw-induced resettlement (influenced by gravity, but also soil cohesion) results in a net downslope displacement, which is referred to as frost creep (Harris 1993). If the thaw consolidation ratio (Morgenstern & Nixon 1971) exceeds zero during thawing of ice-rich frozen ground, porewater pressures will rise and reduce the frictional strength of the thawed soil. Under these conditions, the downhill slope force is likely to cause a slow downslope movement in non-cohesive soils, which is referred to as gelifluction (Harris 1993). In case of one-sided freezing (from the ground surface downwards) which is the case for seasonal and permafrost at moderate mean annual ground temperatures (MAGT > -5°C), the gelifluction rate decreases with depth (Harris 1993) resulting in a concave deformation profile. In case of two-sided freezing (from the earth surface downwards and the active layer base upwards) which is true for cold permafrost (MAGT < -5°C), most ground ice is concentrated at the active layer base. When this ice melts during the thawing period, the entire active layer will move downslope in a plug-like manner (Egginton & French 1985). Lewkowicz & Clarke (1998) found the maximum active layer thaw depth to be correlated positively with its movement. As only the active layer moves, deformation takes place in a shear zone at its base. The increase of such mass wasting processes as well as change of water cycle and sediment flux is interpreted as a result of the global climate warming by Haeberli & Beniston (1998).

The field investigations on solifluction conducted globally until 2000 were reviewed by Matsuoka (2001) who distinguished three components of solifluction: (1) downslope movements originating from diurnal freeze-thaw action, (2) from annual freeze-thaw action (including plug-like displacements described above) and (3) retrograde movements caused by soil cohesion. The depth and thickness of ice lenses and freeze-thaw frequency were found to be the major controls on solifluction processes, but also soil moisture and slope angle proved to be important factors. It was surmised that both the surface velocity and the maximum depth of soil movement may be influenced by global warming via modified thermal and hydrological conditions. In recently performed studies on solifluction a trend towards automated measuring equipment emerged (e.g. Jaesche et al. 2003, Matsuoka 2005). Thus, data on soil movements and associated parameters could be recorded continuously and at a high temporal resolution, allowing to determine the seasonal variability of solifluction processes (Matsuoka 2005).

Whereas many factors potentially influencing solifluction interact in a complex manner under field conditions, the effect of each factor can be determined separately under controlled laboratory conditions. Probably the most comprehensive laboratory experiments simulating slope movements of periglacial environments were performed by Harris et al. within the last two decades. The first stage of their experiments comprised full-scale physical modeling of solifluction on an experimental slope for different fine-grained non-cohesive soils conducted in the cold laboratories of CNRS Centre de Géomorphologie, Caen, France (e.g. Harris 1993, Harris & Davies 1996, Harris et al. 1996). In contrast to field monitoring, their laboratory experiments did not depend on annual freeze-thaw cycles, but allowed the frequency of the freeze-thaw cycles to be increased and therefore to simulate solifluction much faster. In a subsequent stage of physical modeling of cryogenic slope processes a given solifluction displacement could be simulated even faster by using a centrifuge which allows to multiply earth's gravitational constant g by a factor N (Harris et al. 2001, Harris et al. 2003). According to geotechnical centrifuge scaling laws (Croce et al. 1985, Savidou 1988), linear dimensions (including the displacement due to solifluction) in the model should be scaled by a factor N to obtain corresponding field scale. For example, for soil testing in a centrifuge at 10 g, the downslope displacement due to solifluction is ten times larger within a given time than in the field.

Rapid mass movements in soil or debris-mantled periglacial slopes are due to weakening caused by excess water from thawing of snow and ground ice leading to high pore water pressures. The loss of strength depends on the rate of water liberation due to thawing of ice and the rate of water drainage determined by the rate of consolidation (e.g. Terzaghi & Peck 1967) and the hydraulic conductivity of the soil (Williams & Smith 1989). The relation between these effects was quantified by proposing the *thaw-consolidation ratio R* (Morgenstern & Nixon 1971). In fine grained thawing soils excess pore water pressures will arise if water is entrapped so that the weight of the overburden bears on the water, potentially triggering thaw slumps (Williams & Smith 1989). This kind of landslide is common and well-investigated in arctic permafrost regions (McRoberts & Morgenstern 1974, Burn 2000, Lewkowicz & Harris 2005b, Lewkowicz & Harris 2005a), but seldom occurs in alpine permafrost regions (e.g. Niu et al. 2005). In alpine regions planar slips or slides and debris flows are the most significant type of mass movements on soil- or debris-mantled slopes.

The consequences of a warming atmosphere on the hydro- and cryosphere in the European Alps and in particular on permafrost and related slope stability were evaluated in detail by Haeberli (1990a), and Zimmermann (1990), with regard to periglacial debris flows. In a further study on the relation between debris flows and climate change Zimmermann et al. (1997) found that about 75-80% of the debris flows observed in two periglacial catchments in the Western Swiss Alps (*Matter*- and *Saastal*) originated from permafrost terrain. Barsch (1993) pointed out that the risk of hazardous sheet slides and skin flows is highest under conditions of moisture oversaturation and high pore pressures in the active layer, which is in accordance with findings in polar permafrost regions. For the availability of sediments feeding debris flows the increase of temperature is crucial in alpine periglacial environments (Haeberli et al. 1993). Haeberli et al. (1999) assessed the consequences of loss of ice on natural hazards in alpine periglacial regions by means of temperature simulations with regard to stability of steep slopes and case studies. In addition, hydrological conditions have major controls on periglacial landslides. The principal triggering mechanisms for debris flows in high mountain areas such as in the *Ritigraben* torrent (Western Swiss Alps) are abundant rain and snowmelt with subsequent runoff (Rebetez et al. 1997). Analysis of climatological data for the last three decades in the region of *Ritigraben* revealed that the frequency of extreme rainfall events in

August and September has increased. According to Rebetez et al. (1997), similar trends were observed for the 20th century in Switzerland in general. Gardaz (1998) stated that a main problem in the identification of slope instabilities in alpine periglacial areas is the lack of knowledge of the lateral water input from adjacent hydrological sub-systems, which could lead for example to the breaching of moraines. The contribution of apparent cohesion to the stability of moraine slopes was studied by Springman et al. (2003) by means of field and laboratory investigations. The suction within scree due to capillary forces prevailing under partially saturated conditions was shown to increase the shear strength. However, artificial rainfall experiments in the field carried out in the same study showed that due to water suction, this cohesion gradually decreases during infiltration, leading to potential instabilities with progressive saturation.

Geotechnical aspect of granular materials

Irrespective of the slope geometry, the granular material on the slope has certain geotechnical properties; the most important one concerning slope stability is the shear strength, defined as the ability of soil to sustain load without undue distortion or failure in the soil mass, where the peak difference between the initial and the actual stress is normally taken as failure (Al-Khafaji & Andersland 1992). The shear strength of a soil sample can be measured by a number of laboratory tests, the two most common ones being the direct shear and triaxial tests. While the shear plane is predetermined in a shear test by the interface between the upper and lower frame of the shear box, it can develop freely in a triaxial test. Both tests, their range of application and their advantages and disadvantages were described in Al-Khafaji & Andersland (1992). A comparison of different interface testing apparatuses (including the direct shear box) was conducted by Kishida & Uesugi (1987).

In geotechnique, cohesive soils (e.g. clays) are distinguished from cohesionless soils regarding the cohesion due to the minerals themselves (without water and ice). For the present study only cohesionless soils respectively granular materials are relevant. The reviewed literature of these materials is subdivided into studies on (1) frictional behaviour of dry granular materials, (2) cohesive behaviour of granular materials due to water suction and (3) due to ice.

Frictional behaviour

Theoretical studies on the continuum mechanics of porous materials (including granular materials) were edited for example by Ehlers (2001) and Ehlers & Bluhm (2002). The approach of conducting experiments with idealized granular materials and subsequently simulating them numerically, was found to yield significant insight into the mechanisms of failure. Onda & Matsukura (1997) even reduced the three-dimensionality of granular materials to a two-dimensional problem by using an assembly of aluminium rods to perform tilting box experiments as well as direct shear tests. The experiments and the simulation using a simple physical model led them to conclude that instabilities of slopes composed of dry granular assemblies are mainly triggered by rolling on the slope surface rather than frictional sliding. In another study the influence of the packing of granular materials on the shear strength was investigated by triaxial and plain strain compression testing of face-centered-cubic and rhombic packing configurations of steel spheres (O'Sullivan et al. 2004).

A frequently cited paper of fundamental relevance for geotechnique was published by Bolton (1986) on the strength and dilatancy (volume expansion during shearing) of sands. The critical state angle of shearing resistance of soil which can be revealed by shearing at constant volume was stated to be mainly a function of mineralogy. The difference between the critical state angle and the angle of internal friction of compacted sand (proportional to angle of dilatancy) correlated to the rate of dilation which depends on its relative density and the mean effective stress. On the basis of this correlation a new relative dilatancy index was defined which allows the angle of dilatancy to be calculated depending on the relative density and the mean effective stress. Shibuya et al. (1997) developed a new sophisticated direct shear box for measuring the strength and dilatancy of soils in direct simple shear. Using this apparatus they found an optimum configuration of boundary conditions (wall friction, opening between the two shear frames, constraint by loading platen) allowing the shearing in the box to approach the ideal simple shear mode of deformation as closely as possible.

As the shear plane is placed through the granular material in a direct shear box test, the angle of internal friction can be derived from this test. In order to measure the frictional behavior between two different materials the shear plane has to be placed at the interface between these two materials which reveals the interface friction angle. This was done by Kishida & Uesugi (1987) who used a simple shear apparatus to perform tests on sand-steel interfaces. They introduced the normalized roughness (roughness of steel surface relative to 50% diameter of sand) which proved to be well correlated to the coefficient of friction between the two materials. The influence of the roughness of steel and the crushability of the granular material (amongst other factors) on the frictional behavior between the steel surface and the granular material was investigated by Yasufuku (2002). The grain crushing process was found to be associated with a gradual increase of the interface friction angle. In addition, the latter increases with roughness of the steel surface, but decreases with mean grain size. For the use of geotextiles, especially geosynthetic clay liners (GCLs), their frictional behavior underneath a soil layer is of particular interest. Von Maubeuge & Eberle (1998) therefore conducted shear tests on gravel-covered hydrated GCLs in tilted shear boxes to measure the long-term interface friction angle between the soil and the geotextile under realistic conditions. As has been shown above, geotechnical testing of the shear behavior of granular materials is usually performed with complex measuring devices which are often suitable for use in the laboratory only. In contrast, Blijenberg (1995) developed a simple and cheap in-situ method to determine the angle of internal friction of coarse, cohesionless debris by performing a cut (by digging away scree) on a slope until it fails. However, this method only worked for the determination of the kinetic angle of internal friction, but not for the static one, which is higher.

Cohesive behavior due to water suction

In order to describe the effect of water in granular materials on its stability various terms are used in the related literature such as (apparent) cohesion, (water or matrix) suction, capillary, (negative) pore-water pressure and surface tension. It has to be considered that the meaning of these terms partly differ, however they all refer to the same phenomenon.

Prior to about 2000 the research problems were mainly studied on a macroscopic scale (using conventional geotechnical test apparatus) and models were mainly empirical. An important step was the development of the shear strength theory for unsaturated soils proposed by Fredlund et al. (1978). This theory was applied in multistage direct shear testing on glacial till by Gan & Fredlund (1988). The results of this study showed that the relation between suction and shear strength is nonlinear; the angle of internal friction with respect to the difference between air and pore water pressure approaches the effective angle of internal friction (without the effect of suction) at low suctions and reduces substantially with the suction increasing. In a combined study comprising laboratory saturated and unsaturated strength tests and field suction measurements Krahn et al. (1989) showed that the loss of cohesive strength of a soil is caused by the dissipation of negative pore water pressures and can lead to slope failure, especially near the surface. They stated that the optimal water content for slope stability prevails at a suction of 50 kPa. This indicated that the shear strength of a soil is neither highest under completely saturated nor under completely dry conditions, but somewhere in between. Babu et al. (2005) developed a simple method for the evaluation of shear strength from suction or vice versa using a fitting parameter for the measured data.

Recent studies have focused on the cohesive behavior due to water by investigating the interparticle processes at a microscopic scale (at low stress levels) and simulating them with physical rather than empirical models. These models are based on the physical analysis of the well-defined interactions of particles connected by liquid bridges (e.g. Pierrat & Caram 1997). Nase et al. (2001) investigated the liquid-induced cohesion at a particle-level and from this they derived two characterization criteria (granular bond number and collisional number), which proved to work well to simulate the transition from free-flowing to cohesive behavior. Nowak et al. (2005) used a frictionless liquid-bridge model to simulate the stability within a pile of moist granular material. The experimentally determined angle of repose depending on system size, grain size and surface tension could be reproduced by their model. Herminghaus (2005) presented recent advances in modeling of wet granular materials with an emphasis on statistical models accounting for dynamics and phase transitions.

The authors of a third group of studies tried to take the advantages of both empirical models based on conventional geotechnical tests (at a macroscopic scale) and physically based models (at a microscopic scale). On the basis of direct shear tests van Mechelen (2004) found the apparent cohesion to be controlled by the surface tension between 0.5 and 3 kPa. In addition, the author combined the equation for the shear strength of unsaturated soils proposed by Fredlund et al. (1978) with the equation by Rowlinson & Widom (1982) relating the pressure difference across the air-liquid interface of a liquid bridge between two particles to the surface tension. The experimental results fitted well to the combined model. Kim & Sture (2004) carried out direct tension and shear tests to assess the tensile strength and the apparent cohesion in sand depending on water and fines content. The results were in accordance with the water bridge model (explaining apparent cohesion) and revealed that the tensile strength, the apparent cohesion and the angle of internal friction of sand increases with a volumetric water content between 0.5 and 4.0%.

Cohesive behavior due to ice

The books by Phukan (1985) and Andersland & Ladanyi (2004), both entitled ‘Frozen Ground Engineering’, provide extensive and detailed information on the mechanical properties of frozen soils. In addition, a comparison of these books reveals the progress of research in this field over the last two decades. The cohesive role of ice in frozen ground with regard to slope stability has a major influence on the two soil properties (1) creep strength and (2) shear strength.

To investigate the influence of ice on the creep behavior of frozen soils first the behavior of pure ice had to be understood. Temperature-controlled laboratory creep tests on randomly oriented polycrystalline ice (dominating ice type in pore space according to Andersland & Ladanyi 2004) subjected to uniaxial compression were conducted by Glen (1952, 1955, 1974) and revealed a rheological response of ice with time comprising the following periods: (1) small instantaneous deformation (elastic strain), (2) deformation at a gradually decreasing creep rate (transient or primary creep), (3) deformation at a steady rate (constant or secondary creep) and (4) deformation at an accelerated rate (tertiary creep) finally leading to (5) failure. The three creep periods are typical for the deformation of a viscoplastic crystalline material (Phukan 1985). The main factors controlling the establishment of a particular creep mode are the magnitude and duration of the applied load and the ice temperature (Phukan 1985). After a detailed review of the mechanics of ice creep an Arrhenius type of equation was developed including the effect of temperature (Phukan 1985). Morgenstern et al. (1980) found the shear strain rate of ice to decrease with decreasing temperatures at a given shear stress. At warmer temperatures, Glen (1974) found the creep process to accelerate as a result of pressure at intergranular contacts combined with intergranular sliding. The phenomenon of pressure melting is defined by the Clausius-Clapeyron equation (Hillel 1980).

For the creep behavior of multiphase frozen soils the content of ice in relation to soil particles is crucial (Phukan 1985). At very low contents of soil particles (i.e. bulk densities less than 950 kg/m^3) the creep rate may be enhanced in comparison with pure ice, as the soil particles reduce the grain size of the ice crystals. However, at higher contents of soil particles the creep rate is reduced, as the soil particles impede the dislocations within the ice, thereby suppressing ice creep.

The shear strength of frozen soils can be estimated by the uniaxial strength depending on time (due to ice) plus the time-independent strength due to the frictional response of the soil particles for a given stress level (Roggensack 1977). According to Vyalov (1962) the Mohr-Coulomb failure criterion may be used to calculate the shear strength of frozen soils. There, the component of cohesion due to ice depends on the ice content, strength and area in contact with the soil particles (Phukan 1985). The frictional component (represented by the angle of internal friction) depends on the ice content, the packing of the soil grains and the size, shape, distribution and number of grain-to-grain contacts, where the ice content depends on temperature (Phukan 1985).

For frozen sand Goughnour & Andersland (1968) and Kaplar (1971) found that grain-to-grain contact is established at a volumetric particle content of about 40%, resulting in rapid increase in strength with increasing sand density. However, the strength only increases as long as the sand remains ice saturated; below saturation the strength of frozen sand rapidly decreases with decreasing ice content (Kaplar 1971, Baker 1979). Equivalent results were found by Nickling & Bennett (1984) who conducted shear tests on coarse-grained frozen debris. Their tests showed a marked increase in shear strength when the ice content was increased from ice free to ice saturated conditions (25%), but a reduction in shear strength when the ice content was further increased to supersaturated conditions. These changes in shear strength with ice content could be directly attributed to the changes in internal friction and the cohesive effects of the pore ice. Two decades later Arenson et al. (2004) performed triaxial tests on similar materials (artificially frozen coarse-grained debris from two rock glaciers in the Upper Engadine, Swiss Alps). In contrast to Nickling & Bennett (1984) they generally found the peak shear strength to be increased with decreasing volumetric ice content. However, as they chose volumetric ice contents only higher than 29%, all samples were probably at least ice saturated, and therefore these results are in good accordance with the earlier findings. In addition, Arenson et al. (2004) demonstrated that large strains have a significant influence on the strength of frozen granular materials.

Besides the dominant effect of the temperature on the soil strength at the 0°C-transition due to phase change (see above), it is also relevant below 0°C for the strength of frozen soils. As was shown for example by Haynes & Karalius (1977) a decrease in temperature (below 0°C) causes an increase in strength of a frozen soil, but also an increase in brittleness, which is manifested by a more significant drop of strength after the peak.

Theory on slope stability analysis

With regard to this study the research on slope stability analysis can be structured as follows: (1) the concept of disposition to assess the spatial and temporal risk of slope instabilities, (2) the slope types and equivalent failure theories, (3) the infinite slope model as most important case for natural slopes, (4) the relevance of the infinite slope model for slopes in periglacial environments.

Concept of disposition

The concept of disposition was developed by Kienholz (1995) for the assessment of the spatial and temporal probability of natural processes in general. The term disposition means the susceptibility of an area to the development and triggering of a natural process, in this case of slope instability. The concept of disposition distinguishes three criteria relevant for the probability of a natural process to occur: (1) the basic or constant disposition with only a long-term variability (decades to centuries) governing the spatial occurrence of slope instabilities, (2) the variable disposition with a medium-term variability (days to decades) governing the temporal occurrence of slope instabilities as well as their frequency and magnitude, and (3) the triggering events with a short-term variability (minutes to days).

Slope types and failure theories

An important base for the quantification of the stability of natural slopes are the principles studied in engineering soil and rock mechanics e.g. by Taylor (1948) and Lambe & Whitman (1969). These studies helped to develop the limit equilibrium theory (Morgenstern & Sangrey 1978) which aims to compute an average factor of safety, defined as the ratio of stresses resisting failure to the stresses required to bring a slope into a state of limiting equilibrium along a potential failure interface. Concerning the shape of this failure interface and the subsequent failure mechanism, three main types of slopes are distinguished (combining Sidle et al. 1985, Al-Khafaji & Andersland 1992): (1) infinite slopes, where the cross section of the surface is straight and the thickness of the potentially failing soil mantle constant and very small compared with the downslope length, resulting in a planar slip surface parallel to the slope surface; (2) finite slopes where the thickness of the potentially failing soil mass has at least the same order of magnitude as the length of the slope from the top to toe and the slip surface is circular; (3) complex slopes with non planar and noncircular slip surfaces. For each of these slope types different stability analysis models accounting for the respective slip surfaces were developed. For infinite slopes Skempton & DeLory (1957) provided the basic and widely applied infinite slope model which is described in detail below. For finite slopes with a circular slip surface the method of slices stability analysis was formulated by Bishop (1955), splitting the potential failing mass into vertical slices with a small width compared to the slope length and calculating the balance of forces for each slice assuming the resultant forces on the sides of the slices being only horizontal. A general slope stability analysis considering all boundary and equilibrium conditions which is applicable to slopes with planar, circular or noncircular potential slip surfaces was developed by Morgenstern & Price (1965). In order to evaluate slope stability additionally under general, rapid (undrained) conditions, Baker et al. (1993) proposed an approach integrating laboratory testing, boundary value analysis, undrained stress paths and the identification of the slip surface by minimization techniques.

Infinite slope stability model

To conduct a stability analysis using the infinite slope (stability) model a vertical, partially submerged slice within the potential failing layer (parallelogram in cross section) is considered (Al-Khafaji & Andersland 1992). The balance of forces acting on this soil slice at the state of limit equilibrium has to be established, including the driving and resisting forces (see above). The driving forces are represented by the downslope force caused by the weight of the slice and any additional static (e.g. vegetation) or dynamic loading (e.g. rockfall). The resisting forces comprise the friction or shear force tangential to the base of the slice (governed by its normal force and the angle of internal friction) and cohesive forces due to the soil particles (e.g. for clay) or water or ice in the pore space (see above). However, the normal force and thus the friction are reduced by the uplift force caused by water saturation (submerged part of slice), leading to the effective normal force. Relating the forces to the area of the base of the slice results in the equivalent stresses. The factor of safety can then be calculated by means of these forces respectively stresses. Iverson & Major (1986) improved this basic type of infinite slope model by a normalization of the limit equilibrium solution providing three dimensionless parameters governing the potential of infinite slope failure.

According to Sidle et al. (1985) factors affecting the stability of an infinite slope comprise geomorphic ones (e.g. geologic and tectonic setting, slope shape), soil properties (e.g. grain size distribution, hydraulic conductivity, mineralogy), hydrology (e.g. infiltration by rainfall or snowmelt, groundwater flow, evaporation), vegetation (e.g. reinforcement by plant roots, transpiration), seismicity and land use management (e.g. timber harvesting, burning, road construction). Amongst these factors the groundwater seepage is one of the most relevant ones in triggering failure (e.g. Iverson & Major 1986). The calculation of the factor of safety with a single value for each parameter is called deterministic analysis (Hammond et al. 1992). However, many field conditions being relevant for the slope stability analysis are highly variable in space and time; e.g. the soil properties (e.g. texture, moisture content, hydraulic conductivity, shear strength) and the increase in pore water pressure after heavy rainfall, which is the over-riding factor in triggering landslides in many cases (Sidle et al. 1985). To account for these uncertainties probabilistic approaches were performed, i.e. to estimate the probability of slope failure rather than a single factor of safety (Sidle et al. 1985, Hammond et al. 1992). A powerful probabilistic method is the Monte Carlo simulation which is used in the slope stability software LISA (Hammond et al. 1992); for this a large number of factors of safety are calculated by using a randomly selected set of input values each time. The probability of failure can then be determined by relating the number of parameter sets revealing a factor of safety less than or equal to one to the total number of calculated parameter sets. In addition, a sensitivity analysis is helpful in assessing the relative influence of the various parameters influencing slope stability (Sidle et al. 1985) and is illustrated by Gray & Megahan (1981) for the infinite slope model. According to Sidle et al. (1985) a sensitivity analysis consists of four steps: (1) selection of a realistic range of values for each input parameter, (2) calculation of a base factor of safety using the median for each parameter, (3) varying each input parameter across its range of values while holding all other parameters constant and calculating the factor of safety for each altered data set, (4) plotting the results as influence of the change of factors (relative to median) on the change of the factor of safety (relative to median).

Application of the infinite slope model in periglacial regions

In periglacial infinite slopes the potential shear plane is usually defined by the surface of the frozen ground (respectively the active layer at the time of maximum thaw depth) which is roughly parallel to the slope surface and therefore generally allows to apply the infinite slope model (Phukan 1985, Williams & Smith 1989, Andersland & Ladanyi 2004). However, McRoberts & Morgenstern (1973) observed skin flows on thawing slopes with a very low inclination (2-3°) which could not be explained by a conventional slope analysis and were ascribed to excess pore water pressures (which arise when water released by melting of excess ice is entrapped in the pore space; see above). Thus, a modified stability analysis for ice oversaturated thawing slopes was developed by McRoberts & Nixon (1977), where the excess pore water pressure is accounted for by the thaw consolidation ratio (see above).

1.2 Motivation

The investigations reviewed in the state of the research above build an important base for the present study. However, the literature review also shows that to date no field investigations have been carried out in mountain permafrost regions on hydrothermal processes within a coarse-grained active layer on steep scree slopes and the influence on their stability. In previous laboratory studies, the geotechnical behaviour of homogeneous granular materials of which scree slopes consist, was tested with elaborate technical equipment. However, for plug-like movements of the active layer it is important to distinguish between an immobile frozen layer (permafrost) and a sheared off unfrozen layer (active layer) which was not considered in laboratory experiments until now. There is evidently a gap of knowledge here.

The role of the active layer as a thermal buffer between the atmosphere and the underlying permafrost in alpine areas, which is particularly important in the light of climate change, and the influence of the water in this context, are especially poorly understood at present. Which hydrothermal processes in the active layer are important for this buffering effect, and how fast are the diurnal and seasonal atmospheric fluctuations transmitted to the permafrost by the active layer? Does the active layer act as a thermal filter not only in rock glaciers (as was found by Humlum 1997), but also in steep scree slopes, or is the thermal regime of the active layer in steep topographic situations not comparable to that of rock glaciers due to the presence of additional lateral water fluxes?

This last question leads to the problem of slope stability. Until now, the influence of snowmelt or rainwater infiltration and that of the ice and unfrozen water content on the near surface creep of debris slopes in permafrost terrain has not been known. Such slow creep displacements are relevant for constructions in alpine permafrost. In addition, steep scree slopes could be destabilized in the next few decades with active layer deepening due to global warming, potentially triggering mass movements. In this context important issues are the time of the year during which the active layer is not completely frozen and particularly when the greatest thaw depth is reached, when the ice or liquid water content is highest, how the ice content influences the water permeability through the ground, what ground temperatures are and how these parameters are correlated to the slope movement and stability. These questions show that slope stability of the active layer above alpine permafrost in steep coarse blocky slopes is closely related to the hydrothermal processes in this environment.

The reasons for the lack of research addressing the questions shown above are probably the combination of extremely difficult conditions such as high slope inclination (up to 40°), coarse textured ground and fast percolation of water due to large pore sizes and high porosities. In spite of all these difficulties it is an important challenge to investigate the hydrothermal regime of the active layer in steep blocky alpine permafrost terrain, because this type of ground surface covers an area much bigger than that covered by rock glaciers, which have nevertheless been studied much more intensively.

1.3 Hypothesis

As the seasonal scheme of the hydrological processes in the active layer developed by Boike & Overduin (1999) (see 1.1.1) is only applicable in arctic permafrost areas with fine grained soils, it has to be modified for the conditions reigning in alpine permafrost. In permafrost zones hydrological processes are closely connected with thermal ones. Thus in the following text they will be referred to as hydrothermal processes. The boundary conditions of the alpine environment imply more intense solar radiation, higher mean annual air temperatures and greater seasonal and diurnal temperature fluctuations, deeper snow cover, lower ice content in the ground, coarser ground texture (especially at and near the surface and with much larger pore sizes and porosities), and rougher topography with much higher slope inclinations (Hoelzle 1994). In addition, more pronounced downslope water fluxes - especially in the ground rather than at the surface - have to be considered. This modified scheme for the assumed hydrothermal processes (Figure 1.1) is described below and serves as a hypothesis for the present study.

The annual cycle of the seasonally changing hydrothermal processes in the active layer above permafrost in steep alpine terrain can be divided into four clearly defined temporal phases. The winter-phase starts when the active layer is completely frozen, i.e. the maximum temperature is 0°C in all depths of the stratum. During this time a deep snow cover is present, which insulates the underlying ground and almost completely prevents air exchange between atmosphere and ground. A notable exception to this occurs in the presence of funnels in the snow cover, which occur in early winter and facilitate the movement of air from the ground into the atmosphere (Bernhard et al. 1998) along the thermal gradient. The funnels also serve as pathways for vapour migration from the interstices between the blocks to the snow cover surface, where the vapour conversely sublimates, forming hoar frost crystals (Bernhard et al. 1998). As the vapour pressure in the ground pore spaces filled with air is therefore reduced, a small part of the pore ice will sublimate to vapour. Thus by this process latent heat is transferred from the ground (sublimation) to the snow cover surface (converse sublimation). As soon as snow melt begins, the winter-phase ends. The same process occurs to a lesser extent with the formation of depth hoar within the snowpack.

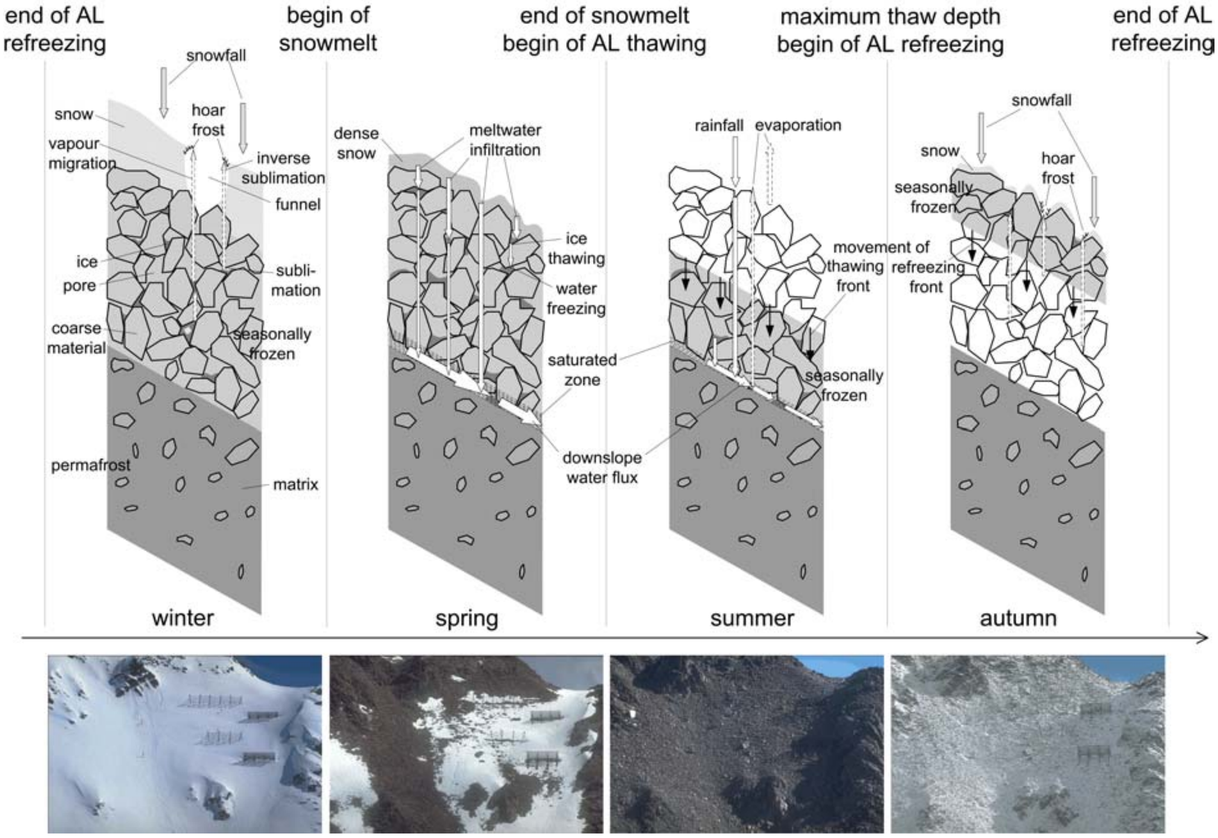

Figure 1.1: *Hypothetical temporal distribution of hydrothermal processes in the active layer (AL) above alpine permafrost on steep scree slopes. The photos were taken by an automatic camera looking at the study site (section 2.1) above Pontresina.*

In the period from the beginning to the end of snow melt, which depends on the air temperature and the amount of snow, the spring-phase takes place. The snow becomes wetter and therefore denser and funnels disappear, so air and vapour exchange between ground and atmosphere is reduced to a minimum. Meltwater infiltrates into the ground and percolates downwards quite rapidly, due to the high permeability of the ground. As the ground temperature is still below 0°C, a part of the infiltrated water will freeze on the blocks and a large amount of latent heat is released. This process therefore results in a rapid ground temperature increase. During snowmelt the highest ice content of the year is therefore reached. Although large quantities of ice form in the interstices, the hydraulic conductivity will remain high enough for the unfrozen water to percolate through the ground down to the permafrost table. This surface is impermeable to water (Gardaz 1998) as the permafrost layer consisting of few larger blocks but mainly of fine grained material and ice is permanently frozen. Due to this and because of the high slope inclination, the liquid water having percolated downward through the active layer will partly freeze at the permafrost table but mainly run off laterally and form a saturated zone. The freezing implies release of latent heat and therefore an increase in temperature. According to the diurnal fluctuations in air temperature and therefore in snowmelt intensity, there will also be a diurnal periodicity in the regime of the lateral water flux at the bottom of the active layer but with a time-lag of several hours, as has been observed for rock glaciers by Gardaz (1998) and for torrents originating from rock glaciers by Bajewsky & Gardner (1989), Johnson (1981) and Tenthorey (1993). The amplitude of the lateral water discharge as well as its time-lag will decline towards the end of the melting period of spring similar to the regime of rock glaciers (Gardaz 1998).

When the entire snowpack has melted, the active layer below begins to thaw as suggested by Vonder Mühll et al. (2001). During the following summer-phase the thawing front moves downwards until the maximum thaw depth is reached. As the rainfall occurring in this time is partially compensated by evaporation driven by the stronger radiation, the lateral water flux and the saturated zone at the bottom of the active layer will be smaller than during the period of snowmelt. The absence of the snow cover now facilitates warming by solar radiation as well as an air exchange from the warm atmosphere to the cold ground, where the ice in the pore spaces will melt and contribute a part of the lateral water flow. Thus the ice content in the active layer is reduced during this time of the year.

After the maximum thaw depth has been reached and air temperature starts to decrease again, active layer cooling and later refreezing occurs from the surface downwards (Vonder Mühll et al. 2001), which is characteristic for the autumn-phase. The snow cover during this season is generally still thin and therefore the insulating effect much lower than in winter. In addition the emissivity and albedo of the snow cover are much higher than the values for the uncovered ground surface independent of its thickness. The ground can therefore lose large amounts of heat and cools down effectively (this is the autumn snow cover effect as described by Keller (1994). As a consequence of this cooling phenomenon, the vapour in the pore spaces will resublimate and the ice content will increase. The latent heat released by this process will be transferred from ground to atmosphere by air convection because of the steep thermal gradient. A part of the vapour also migrates along this temperature gradient up to the snow cover surface, where it transforms to hoar frost or depth hoar in the deeper layers of the snowpack (Phillips & Schweizer 2007). Once the active layer is completely frozen, the annual cycle of hydrothermal processes will start again.

1.4 Objectives

In order to test the hypothesis and to contribute to fill the gap of knowledge shown above, the following objectives were set:

1. Development of suitable methods to measure key parameters of hydrothermal processes in a high alpine environment (harsh climatic conditions, high slope inclination, coarse-grained debris) and the installation of the equivalent equipment which automatically and reliably delivers data.
2. Determination of the correlations between hydrological and thermal processes in the active layer above alpine permafrost in steep coarse-grained debris slopes under the complex combination of interacting field conditions with a special focus on the snowmelt period.
3. Measuring the influence of these hydrothermal processes in the active layer on the thermal state of the underlying permafrost.
4. Development of a device to quantify slope stability of the active layer above permafrost under realistic but controlled laboratory conditions.
5. Quantifying the effect of hydrothermal and granulometric factors on slope stability by means of the friction angle between an artificial active layer and permafrost block.

6. Estimation of the hydrothermal conditions required for an active layer failure by means of a physical simulation in the laboratory under boundary conditions similar to those at the field study site concerning slope inclination and grain size distribution.

2 Field investigations

In laboratory experiments the selected factors can be controlled and the resulting variables measured with high accuracy. This allows the effect of each factor on a resulting variable to be determined separately. However, the transfer of laboratory results to the field is critical, because field conditions are much more irregular and complex than the simplified and idealized laboratory conditions, due to the various interacting factors being involved in nature. In order to gain a realistic picture of the hydrothermal processes occurring within the active layer in alpine scree slopes, field investigations were carried out at a representative study site. Representative parameters functioning as indicators for the water and heat balance of the active layer were focused on for this. In contrast to laboratory experiments the influencing factors could not be set, but only measured as the resulting variables. The hydrothermal processes could be interpreted by temporal correlations between the measured parameters. Spatial and temporal fluctuations of the observed processes were accounted for by effecting measurements at two locations within the study site over a period of nearly three years.

2.1 Study site

The study site is located above Pontresina on Muot da Barba Peider (46°29’56’’ N, 9°55’50’’ E), in the Upper Engadin, Eastern Swiss Alps (Figure 2.1). The inner-alpine moderately continental climate is favourable for the presence of permafrost. The study site is situated at 2950 m a.s.l. on a NW oriented, 37° slope. The slope consists of scree originating from a gneiss rock wall above. In a vertical soil profile the uppermost half metre mainly consists of coarse gravel with grain sizes up to 50 cm. The portion of fine material (sand and silt) increases with depth and at the bottom of the active layer nearly the whole pore space of the gravel is filled with matrix material. The mean annual air temperature in the period from 1997 to 2001 was –3.2°C (Phillips et al. 2003) and the presence of permafrost was verified using BTS (bottom temperature of snow cover) and borehole data to a depth of 18 m by Phillips (2000).

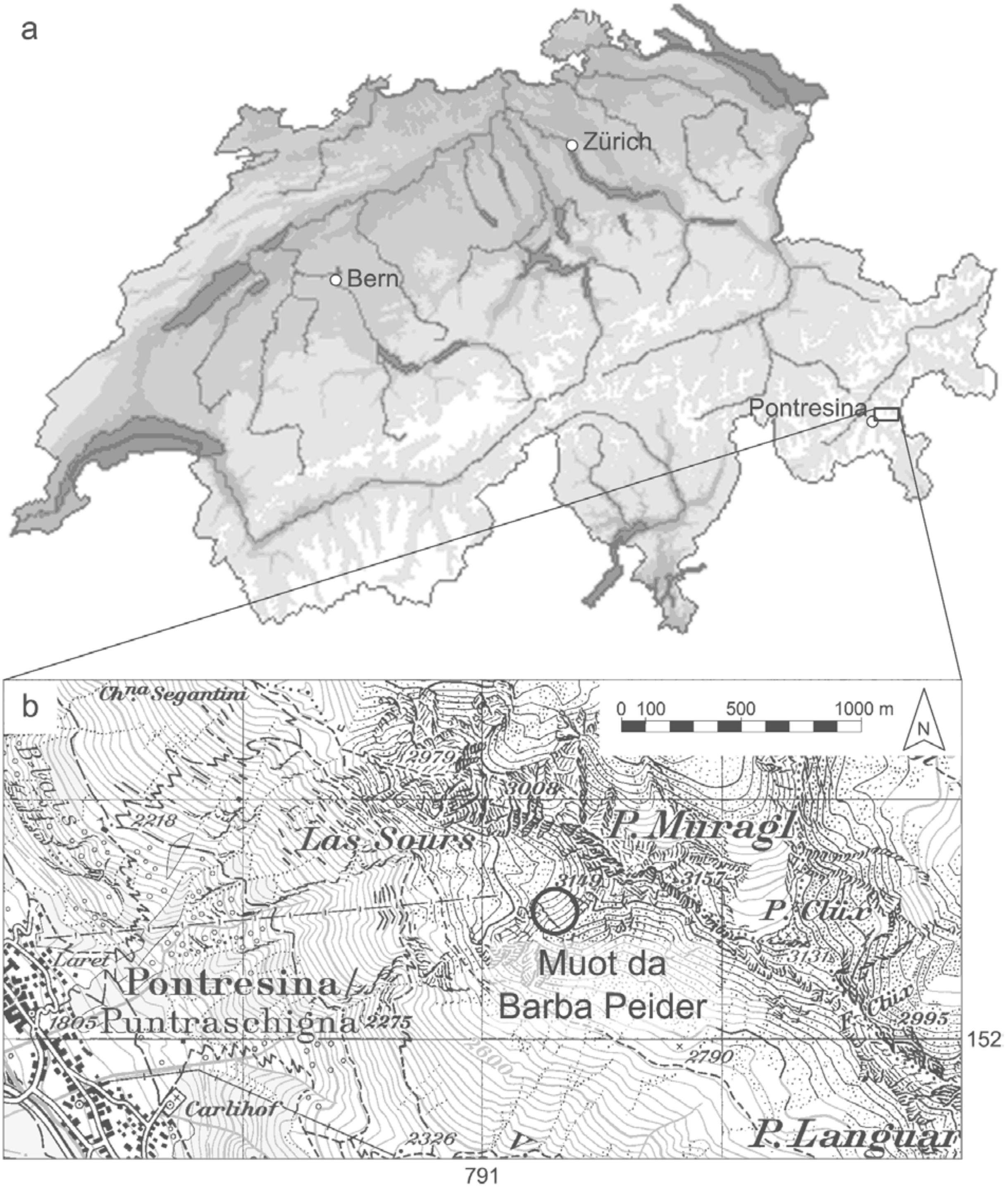

Figure 2.1: *Geographical location of the study site: a) in Switzerland (black rectangle; map source: http://www.meteonews.ch/pix/rest/schweiz_ort.gif (2005)); b) on the slope above Pontresina (black circle; map source: extract from the* Julierpass *topographical map No. 268, 1:50 000 reproduced by permission of swisstopo (BA056857)).*

2.2 Field methods

2.2.1 Field research infrastructure

The interactions between snow-supporting structures and alpine permafrost have been investigated on this study site since 1996 by Phillips et al. (2003). Field research infrastructure therefore already existed and served as a valuable base for this project: on the opposite slope an automatic camera takes pictures of the site three times weekly. Snow gauges (Figure 2.3, Table 2.1) allow determination of the temporal evolution of snow depth. In addition, an ultrasonic probe was installed 3.5 m above the ground in autumn 2004 to measure the snow depth more precisely and with a higher temporal resolution (Figure 2.3, Table 2.1). A 4 m^2 lysimeter measures the infiltration rate of snow melt or rain water into the ground (Figure 2.3, Table 2.1). The water collected by the 20 cm deep lysimeter bath is conducted via an outlet tube into a small container with a known volume which tilts automatically when it is full. The number of tilts is counted electronically within a time step and thus the infiltration rate can be calculated. The downslope displacement of the slope has been measured by an inclinometer in a 6 m deep borehole once a year from 1996 to 2004 (Phillips et al. 2003). Using the vibrating wire technique the inclinometer measures the angle of the borehole against the vertical axis at a given depth which allows to calculate the downslope displacement depending on depth. Air temperature is measured at 3.5 m height. An empty 8 m deep test borehole was free to be equipped for further investigations.

2.2.2 Field measuring array

For the presented project, additional measuring equipment was installed at the study site in August 2003: in addition to the existing equipment, two horizontal measuring lines were installed (Figure 2.3a). In order to determine the spatial variability of the measured parameters the measuring lines were set above each other in the slope and both equipped with the same instruments (Figure 2.3b). As the active layer is confined to the scree (Phillips 2000), it was possible to bury the equipment for the underground measurements within it. Trenches were dug by hand down to the permafrost table where ground ice occurred which limited further digging (Figure 2.2).

***Figure 2.2**: Digging of trenches at field study site to install the measuring equipment within the active layer (large picture). When the permafrost table was reached, ground ice occurred (picture in upper right corner) and thus limited further digging.*

However, because of the steep slope and the loose surface material the trenches were so unstable that they collapsed spontaneously. Temporary slope stabilization precautions therefore had to be installed, using wooden planks and iron rods. An overview of all parameters and instruments (existing and newly installed) is shown in Table 2.1. Electronically collected data were registered with a 1 MB data logger (Campbell Scientific CR10X). The data were downloaded on a portable memory at regular intervals. The energy for the measurements was supplied by storage batteries which were charged with a solar panel (Figure 2.3b).

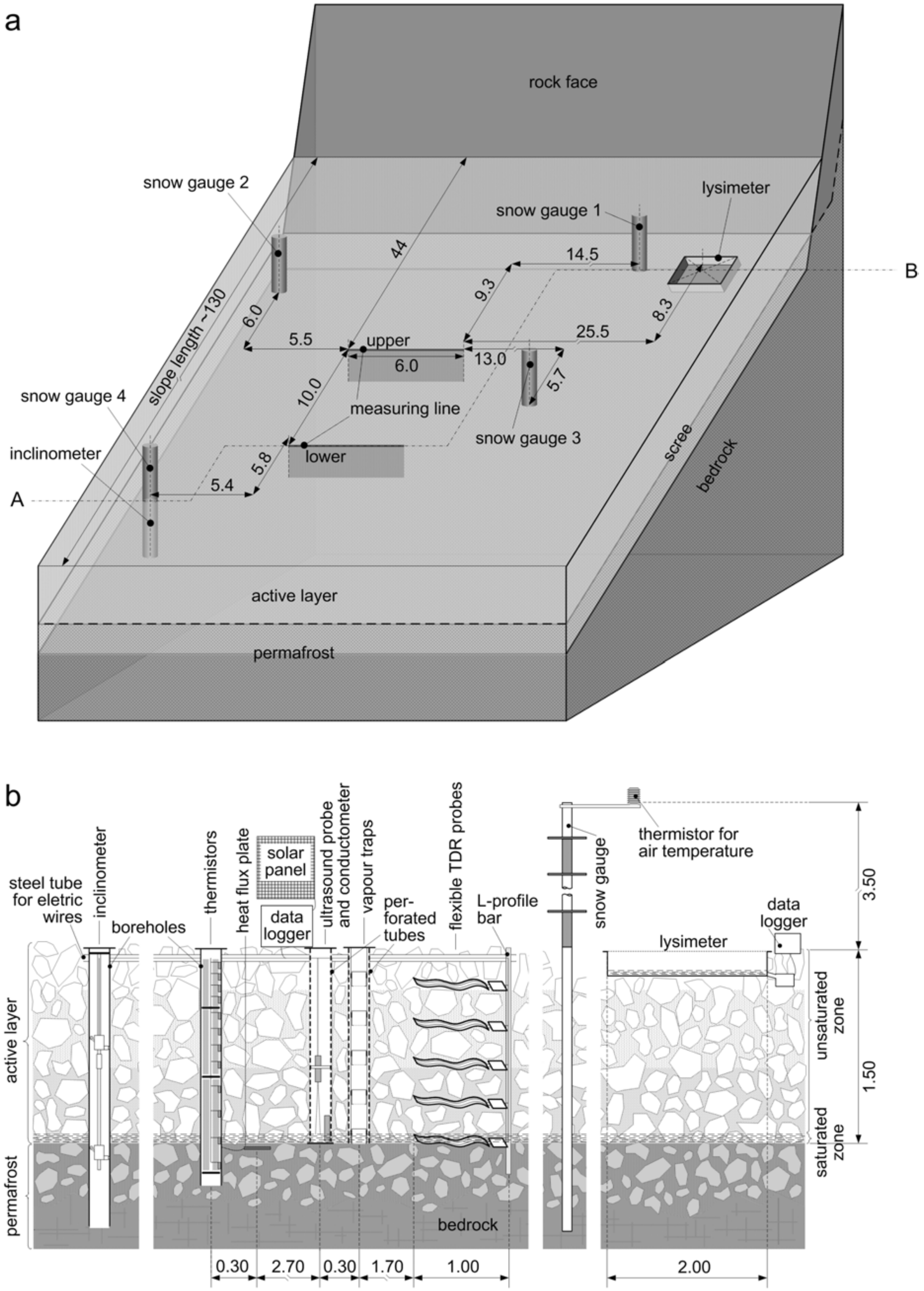

***Figure 2.3**: Measuring array in the scree slope of the study site: a) overview; b) details in the cross section A – B (Figure 2.3a). Figure is not to scale. Distances are given in metres.*

***Table 2.1**: Overview of measured parameters and used measuring methods. In the case of air temperature, height above ground surface is given; for all other parameters, the distance is depth below ground surface. [1]Time Domain Reflectometry, [2]for calibration in sand, [3]since 11 November 2004.*

parameter	unit	measuring line	vertical position towards ground surface [m]	measuring interval [h]	measuring instrument	measuring precision
air temperature	°C	-	3.5	2	temperature logger (UTL-1)	±0.25 °C
ground temperature	°C	upper	0.1, 0.2, 0.3, 0.4, 0.6, 0.8, 1.0, 1.3, 1.6, 1.9, 2.3, 2.7	2	thermistor chain (Stump, YSI 44008)	±0.1 °C
		lower	0.1, 0.2, 0.3, 0.4, 0.6, 0.75, 0.8, 1.0, 1.15, 1.3, 1.54, 1.6			
heat flux at interface permafrost-active layer	W/m^2	upper	1.5	2	self calibrating heat flux plate (Hukseflux, HFP01SC)	±3 %
		lower	1.6			
surface level of ice saturated zone	mm	upper	1.5	2	ultrasound probe (UNAM 30I6103/S14)	±1 mm
		lower	1.6			
electrical water conductivity	µS/cm	upper	1.5	2	electrical water conductivity measure (ISO-measuring cell)	±7 µS/cm
		lower	1.6			
vertical vapour flux in ground	mm/d	upper and lower	0.3, 0.6, 0.9, 1.2, 1.5	2	vapour traps (SLF; GORE TEX)	-
volumetric water content	-	upper and lower	0.3, 0.6, 0.9, 1.2, 1.5	2	TDR[1]-probes (CS616-L, modified by SLF)	±2 %[2]
water infiltration rate	mm/h	-	0.0	2	lysimeter (box: Omlin, logger: Messmatik, Tynitag-Plus Re-ed)	±2 %
downslope displacement	mm	-	0.0	2	vibrating wire in-place inclinometer (Geokon, Typ 6300-1)	±0.02 %
snow depth	cm	-	0.0	48-72	snow gauges/automatic camera	±10 cm
				0.5	ultrasound probe[3] (Campbell SR50)	±1 mm

2.2.3 Measurements in detail

The parameters measured and the equivalent instrumentation of the study site are described in detail below unless they have already been dealt with in the chapter ‘Field research infrastructure’ including the meteorological parameters air temperature and snow depth and the hydrological parameter infiltration.

Hydrological ground parameters

To measure the surface level of the ice saturated zone above the permafrost table, an ultrasound probe was placed in a perforated steel tube allowing the ice to attain the same level in the tube as in the surrounding ground (Figure 2.3b, Table 2.1). The probe was calibrated in the laboratory by measuring the current reflection time for preset distances to a reflecting surface. In the same perforated tube the electrical water conductivity was measured with a conductometer (Figure 2.3b, Table 2.1). Electrical conductivity allows estimation of how long the infiltrated water has been in contact with the ground (Waldner 2002). As a reference for the conductivity value of water which has not yet come in contact with the ground and has originated from snowmelt, snow was taken from the field, melted and its electrical conductivity measured in the laboratory on 26 April 2006 (shortly before snowmelt period). For this, 30 snow samples were collected in the field, at two locations, in snow pits. 15 samples were collected at each location, equally distributed over the depth of the snow pits.

Five vapour traps consisting of tin cans with a GoreTex barrier at one end, as described in Smith & Burn (1987) were located in another perforated tube in which the vapour pressure was expected to attain a comparable value as in the surrounding ground. (Figure 2.3b, Table 2.1). The vapour traps were weighed before being installed and after a known period of time during which the temperature gradient in the ground was favourable to an upward vapour flux. TDR (time domain reflectometry) probes were used to measure water content in the soil. As the electrical power supply was very limited at the study site, a traditional TDR system could not be used to measure soil water content. Therefore the dielectric permittivity could not be calculated as recommended in Menzel (1995), and consequently the three-phase mixing model of Roth et al. (1990) including the temperature compensation was also not applicable to determine the volumetric water content. Therefore the values measured in the inhomogeneous material of the field cannot be seen as correct absolute water contents. However, they reflect the temporal and spatial variability of water contents in the ground. A relative volumetric water content is therefore introduced, defined as the actually measured volumetric water content divided by the maximum value during the measuring period. CS616-reflectometer probes were used instead of a traditional TDR system. To obtain an average value for the volumetric water content in the coarse-grained material the original 30 cm long steel rods were replaced by a flexible 100 cm long polyethylene flat band-cable with embedded copper conductors, as described in Waldner (2002). Five of these modified probes were buried horizontally, one below the other, in the active layer (Figure 2.3b, Table 2.1). To avoid a disturbance of the water percolation within the ground due to the measuring bands, 1 cm holes were punched into the polyethylene insulation. The modified probes were calibrated in the laboratory by measuring the running time of the signal at preset water contents in a sand/water mixture. To achieve reproducibility of the measurements, the calibration was carried out in homogeneous sand and not in the inhomogeneous, blocky field material.

Thermal ground parameters

Twelve thermistors were installed in a vertical tube in each measuring line. In the upper line an existing empty borehole could be used, which allowed the three deepest thermistors to be placed in the permafrost (Figure 2.3, Table 2.1). In the lower measuring line a vertically buried polyethylene tube was used instead of a borehole. The thermistors were calibrated in the laboratory at 0°C using a snow-water mixture. A heat flux plate was placed at the interface between the active layer and the permafrost to determine the heat flux between these two layers (Figure 2.3, Table 2.1). As the sensor requires good physical contact with the surrounding material, the round plate – 80 mm in diameter and 5 mm thick – was embedded in fine-grained soil.

Geotechnical parameters

An in-place inclinometer was installed in an existing borehole equipped with an inclinometer tube and previously used for discontinuous inclinometer measurements (Figure 2.3a and b). This allowed the downslope displacement at the slope surface to be recorded continuously.

2.3 Field results and interpretation

The parameters measured were sorted in their order of cause and effect. Meteorological parameters are presented and analyzed first, then the ground parameters and within the latter, first the hydrological parameters and then the thermal and geotechnical ones. This allowed the dependent parameters to be interpreted on the basis of the independent ones analyzed before.

2.3.1 Meteorological conditions

The mean daily air temperature (MDAT) measured from 2004 to 2006 varied between minimum values in the range of –21°C to –23°C and maximum values in the range of 10°C to 13°C (Figure 2.4). However, as there are longer gaps in the measurements due to technical problems with the data logger, the extreme values may slightly differ from the recorded ones in reality. The slope of the seasonal increasing trend of MDAT in spring steepened each year by 0.3°C within the measuring period, being 3.6°C per month in 2004, 3.9°C per month in 2005 and 4.2°C in 2006. Accordingly, also the date when the increasing trend of MDAT changed from negative to positive temperatures in spring became earlier each year, developing from 7 June 2004, to 20 May 2005 and to 15 May 2006. The equivalent date in autumn when the decreasing trend of MDAT drops below 0°C could not be determined due to lack of data. Independently from the seasonally determined trend of MDAT, the short term air temperature fluctuations were very high with up to 24°C in 10 days.

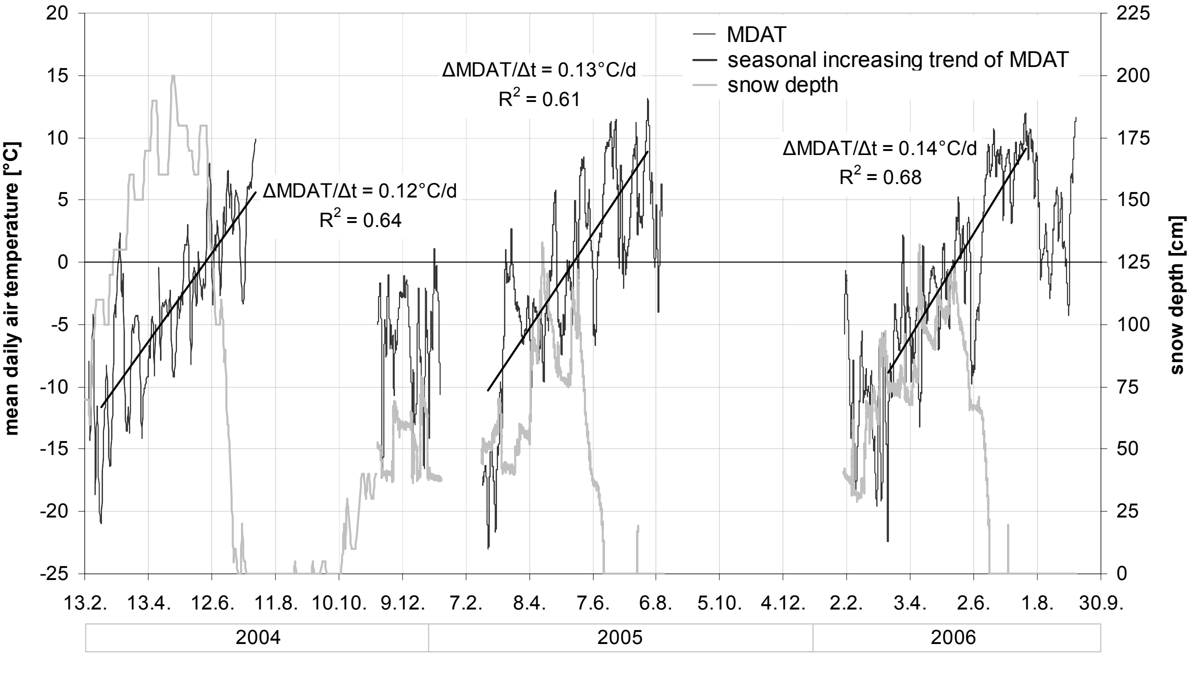

Figure 2.4: Meteorological conditions within the measuring period 2004 to 2006 at the study site. MDAT = mean daily air temperature, d = day. Note that the snow depth was measured by a different method and at different time intervals before and after 11 November 2004 (see Table 2.1). Additionally, note the lack of data for the snow depth from 14 January to 22 February 2005 and from 12 August 2005 to 30 January 2006.

In 2005 and 2006 the maximum snow depth only reached about two thirds of the value attained in 2004. It was reached at an earlier date each year within the measuring period (6 May 2004, 20 April 2005, 11 April 2006). The period with a snow cover of at least 100 cm depth (the depth required to insulate the ground from external influences, according to Stoop 1989, Vonder Mühll & Haeberli 1990) lasted four months in 2004, but only about a sixth of this (19 days) in 2005 and a fifth of this (26 days) in 2006. It is even more important for the ground thermal conditions that the end of this period occurred about one month earlier in 2005 and 2006 than in 2004. According to these results the date when the study site became free of snow was about three weeks earlier in 2005 (17 June) and 2006 (16 June) than in 2004 (7 July). This tendency may also be caused by the increasing trend of MDAT in spring, steepening from year to year. However, three years are too short for the indication of a long term trend of both air temperature and snow depth.

In summary spring air temperature and snow depth conditions in 2004 were more favorable for permafrost maintenance, i.e. ground cooling, than in 2005 and 2006.

2.3.2 Hydrological ground parameters

Infiltration

The average of the mean daily infiltration rate during continuous snowmelt (daily infiltration) in spring slightly decreased over the period of observation from 18 mm/d in 2004, to 17 mm/d in 2005 and 16 mm/d in 2006 (Figure 2.5).

The maximum daily infiltration rates ranging from about 70 mm/d (2006) to 100 mm/d (2005) were more than twice as high as the equivalent values at the meteorological station at Piz Corvatsch (height: 3315 m a.s.l.; coordinates: 783160/143525; source of data: MeteoSchweiz, www.meteoschweiz.ch) and were reached at an earlier date each subsequent year within the measuring period (29 June 2004, 19 June 2005 and 14 June 2006). The high maximum hourly infiltration rates (which were still in the range of normal values for infiltration due to snowmelt in high Alpine regions) may be due to the measurement in the slope causing not only vertical but also lateral water fluxes. In addition, they were equivalent to extreme rainfall such as the events during the catastrophic flooding at end of August 2005 in the European Alps when a peak value of 16mm/h was measured for example in the region of Gasen/Haslau, Styria, Austria (Lang et al. 2006, by unpublished data from the Hydrographic Service of Styria, www.wasserwirtschaft.steiermark.at). However, as the snowmelt water infiltration measured by the lysimeter may be additionally influenced by lateral fluxes (especially in a slope), it is difficult to compare with values for rainwater infiltration. The date of the maximum hourly infiltration rate due to snowmelt also became earlier each year within the measuring period (30 June 2004, 18 June 2005 and 13 June 2006).

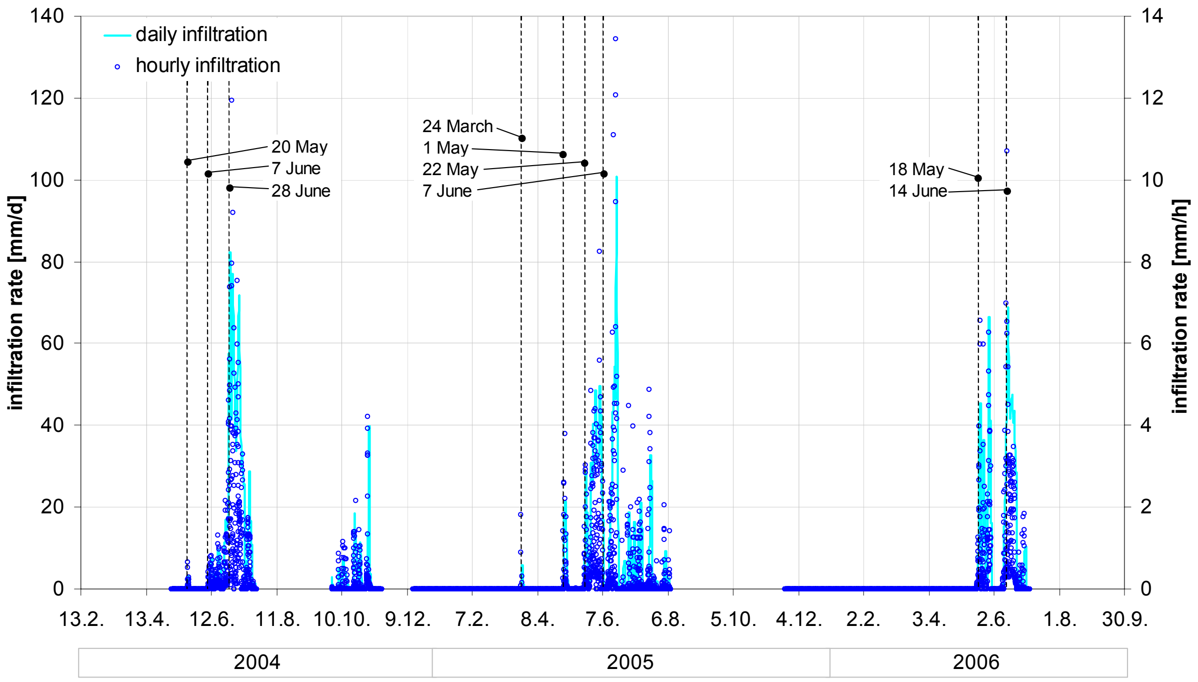

***Figure 2.5**: Daily and hourly infiltration rates measured with a lysimeter, denoting the cumulated infiltration height during a day and an hour. Note that the infiltration rate may not be zero during periods of missing data. However, the data series are complete during the snowmelt periods each year. The vertical black dashed lines indicate dates of changes in the infiltration rate which are important for the volumetric water contents and the temperatures in the active layer and will be referred to when they are analyzed later.*

Level of ice saturated zone

Until the begin of snowmelt in spring 2005 at the 21 May no reliable data could be gained on the level of the ice saturated zone above the permafrost surface due to technical problems with the measuring equipment (Figure 2.6).

In winter 2003/04 the measurements were strongly disturbed by snow drift through the coarse surface material and the holes in the wall of the piezometer tube. Thus, the uppermost half meter of the perforated piezometer tube was covered with a foil to prevent snow from being blown in. As the sensor head of the ultrasound probes proved to be susceptible to ice formation due to converse sublimation of vapour, the sensor head was protected by a thin waterproof adhesive foil new probes which did not influence the measurement. With these improvements at least the probe in the lower measuring line provided reliable data (Figure 2.6). However, as the signal was still very noisy, it was smoothed by means of a simple manual approximation following the highest concentration of measured values (approx. lower m.l. rel. to piezometer base, Figure 2.6). The roughly stable level of the measured values after 30 August 2005 (to 19 May 2006) and 29 July 2006 indicates that fine material was washed into the piezometer tube and deposited at its base up to a height of about 160 mm to 170 mm in 2005 and 175 mm in 2006. As this only allowed the level of the ice saturated zone to be observed above the level of the deposited material, the ice level was set to zero when the maximum thaw depth was reached (12 September 2005 and 3 August 2006, compare Figure 2.11a) and linearly interpolated in between. The increase within the deposited material (until 19 May 2006) remained unknown. The distance from the base of the piezometer tube to the maximum thaw depth was added to gain the approximated ice level relative to the permafrost surface (Figure 2.6). Relating the ice in the saturated zone (assuming a porosity of 40%) to the total height of the active layer leads to an approximation for the minimum ice content of the active layer (the ice in the unsaturated zone could not be determined). It is presupposed that segregation ice and therefore oversaturated conditions can be excluded.

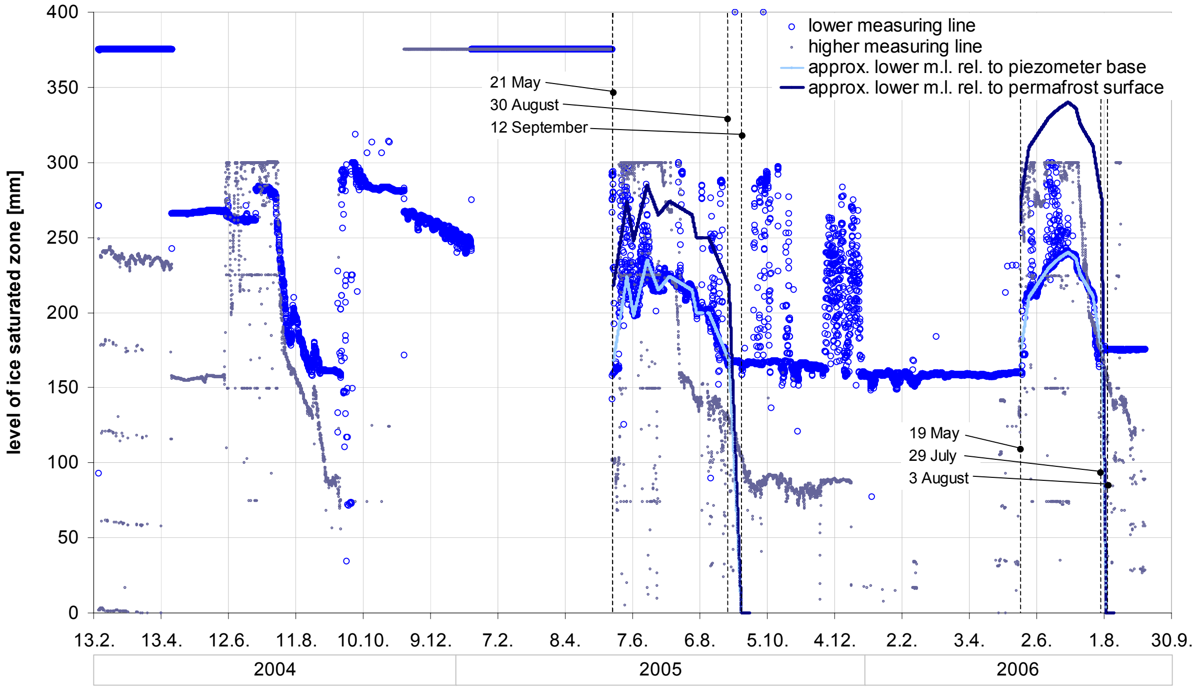

***Figure 2.6**: Derivation of level of ice saturated zone above permafrost surface from ultrasound measurements in the piezometer. The vertical black dashed lines indicate crucial dates and are described in the text.*

The measurements show that significant ground ice formation took place during the infiltration of snowmelt water (compare Figure 2.5). The ice saturated zone at the active layer base measured here could also be observed in similar coarse grained periglacial slopes by other researchers (for example Sawada et al. 2003) as well as in the laboratory simulation of meltwater infiltration (see 3.4) and is referred to as the transition zone by Shur et al. (2005).

Water and ice content

During winter the volumetric water contents (VWC) were roughly stable and at a low level ranging from 4% to 9% (Figure 2.7).

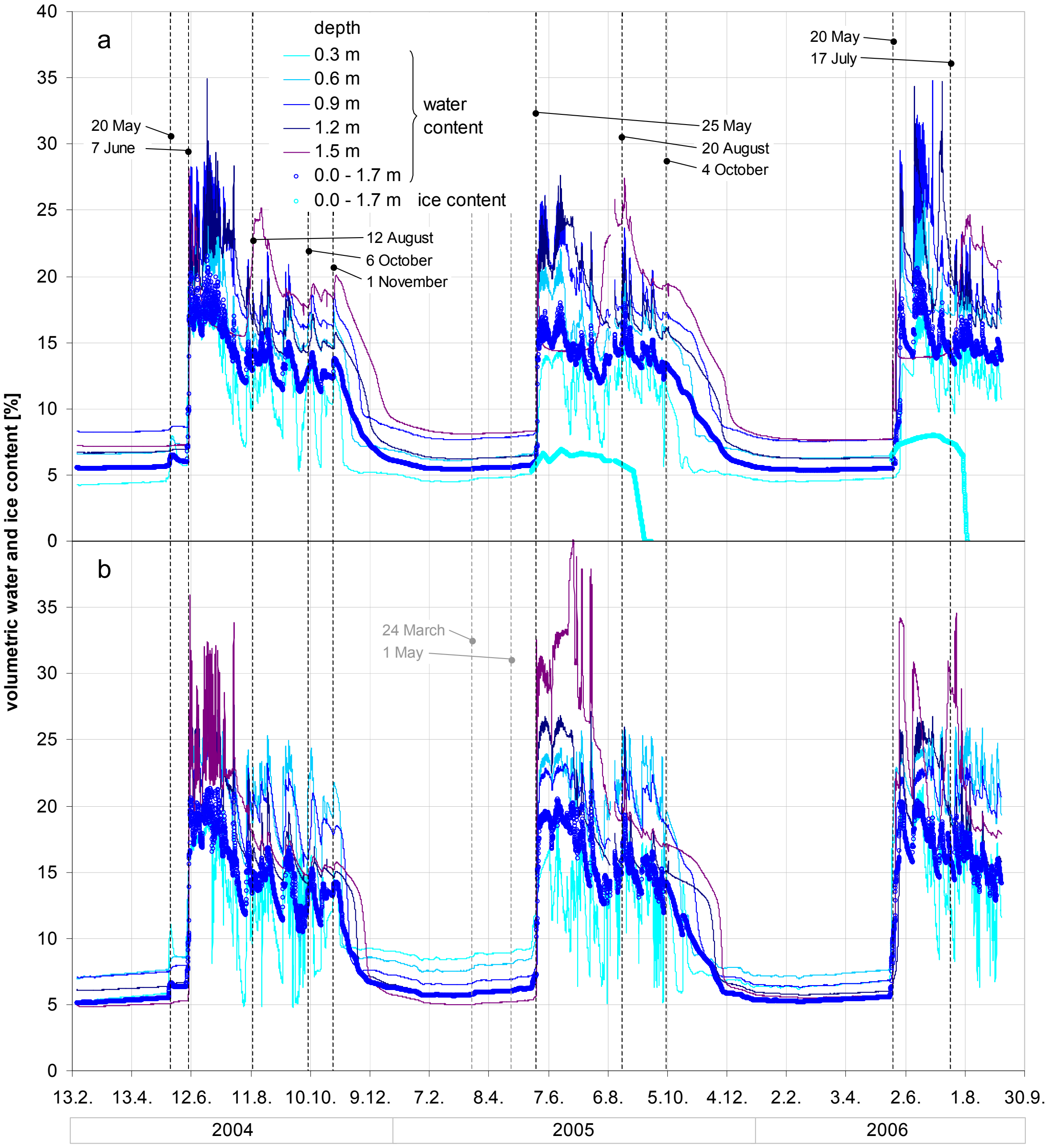

***Figure 2.7**: Volumetric water and ice contents of the active layer, determined with TDR probes: a) lower measuring line, b) upper measuring line. Note that the ice content may not be zero out of the range of available data and that no data at all could be determined for the upper measuring line due to technical problems. As the determination of the ice contents are based on ice in the saturated zone only, they have to be regarded as minimum values. The vertical black dashed lines indicate dates of crucial changes and are described in the text, the vertical grey dashed lines indicate important dates for the ground temperatures and will be discussed in chapter 2.3.3.*

The most pronounced and instantaneous increase of the year occurred in spring followed by the highest values of the year ranging between 28% and 40% (the latter value means saturation of the pore space). As this increase coincided with the begin of the continuous (i.e. daily) infiltration period in spring each year (7 June 2004, 25 May 2005, 20 May 2006), it can be attributed to snowmelt. In accordance with the MDAT-trend in spring changing from negative to positive temperatures earlier each year, also the starting date of snowmelt water infiltration and the equivalent increase in VWC of the ground occurred earlier each following year within the measuring period. The VWC even responded to the short early infiltration pulse on 21 May 2004. This response was most pronounced close to the surface of the active layer, but was strongly dampened with increasing depth. The same effect could be observed on 1 May 2005, but only in the upper measuring line and was less pronounced. The marked instantaneous increase of the VWC in 2004 first occurred near the surface (in 0.3 m depth at 20h on 7 June); the VWCs in deeper layers followed this response, with the delay increasing with depth. At 1.5 m below the surface the response occurred at 20h on 9 June, so the percolation front moved 1.2 m downwards in 48 hours, i.e. the mean percolation rate was 25 mm/h. Thus, the hydraulic conductivity of the active layer is about twice as high as the maximum infiltration rate measured within the period of observation (compare Figure 2.5) indicating well draining conditions. However, in 2005 the equivalent increase occurred at the same time throughout the active layer and in 2006 the VWC even responds first at the active layer base (1.5 m depth), but last close to the surface (0.3 m depth). This can only be explained by preferential flow through the ground and ponding on the impermeable permafrost surface.

After this increase in VWC due to snowmelt, strong diurnal fluctuations occurred, which can be attributed to diurnal frost changes. Fluctuations at a scale of days to weeks showed a very steep linear increase and an exponential decrease indicating the hydrological dampening effect of the active layer. As long as snow is present, the diurnal and longer-term fluctuations of VWC are controlled by radiation and air temperature. After the snowmelt period the diurnal fluctuations therefore disappeared. However, the longer-term fluctuations remained during summer, caused by the alternation of rain and dry periods. Independent of these fluctuations the VWC showed a declining trend by about 5% to 10% from spring to the end of summer. After 1 November 2004 and 4 October 2005 the VWC continuously declined due to an absence of infiltration events and to freezing of ground water (in addition to runoff and evaporation). The decline occurred in an exponential manner and without further fluctuations. This characteristic allows the autumn to be defined in terms of hydrology. Accordingly, the hydrological winter starts when roughly stable VWCs are reached, and then the annual cycle starts again.

As long as the ground remained below 0°C in spring, the minimum volumetric ice content of the active layer (VIC) increased when water was infiltrated and therefore it was positively correlated to the average water content of the active layer (Figure 2.6). However, when the thawing front penetrating downwards reached the ice saturated zone, the VIC rapidly decreased and the infiltration of warm rainwater even accelerated this process.

Electrical water conductivity

Distinct increases in electrical water conductivity (EWC) were often closely correlated to increases in volumetric water content, especially close to the permafrost surface (for example at dates indicated by black vertical dashed lines in Figure 2.8).

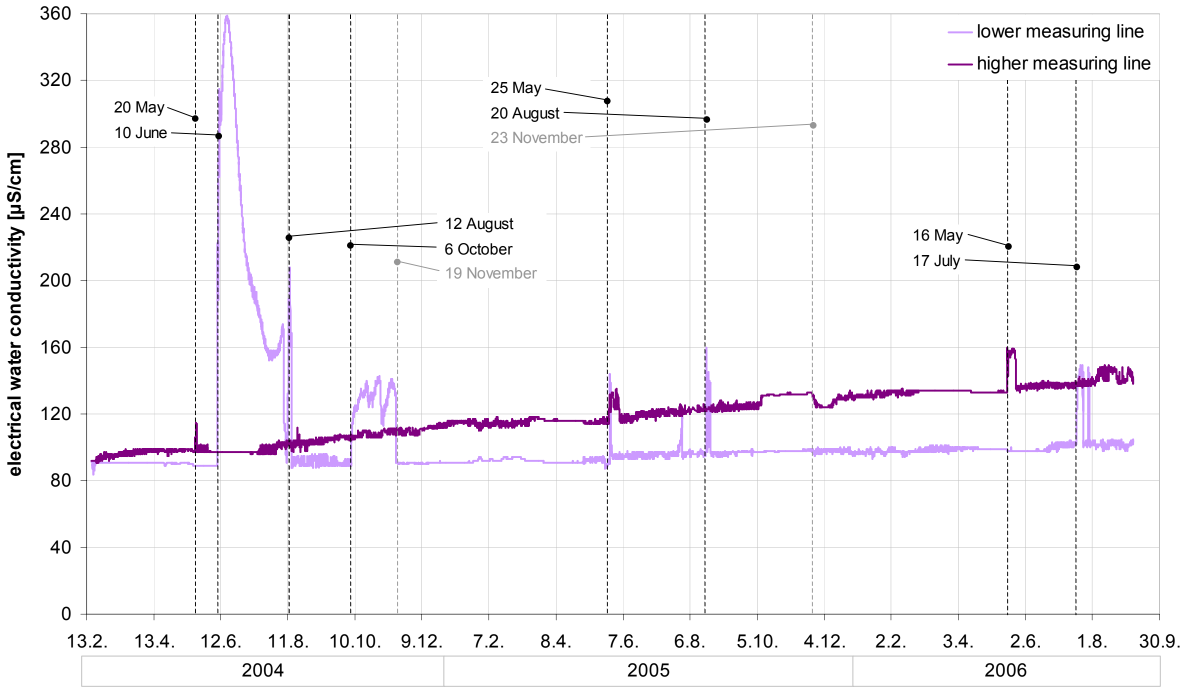

***Figure 2.8**: Electrical water conductivity at the active layer base, measured with a conductivity probe in the piezometer tube. The vertical dashed lines indicate dates of crucial changes and are described in the text.*

The increases can be attributed to the infiltration of snowmelt water in spring and rainwater in summer and autumn. As the ground water is diluted by the infiltrated water, the EWC could be expected to decrease rather than increase. However, as there was no saturated zone between the infiltration phases, the EWC was higher, when water was present (instead of air). In comparison with the EWC of snowmelt water before infiltration into the ground (mean = 4.8 µS/cm, standard deviation = 2.2, n = 30), the measured values at the active layer base were one to two orders of magnitude higher. This indicates that the infiltrated meltwater had intensive contact with the mineral ground.

The peak due to meltwater infiltration in the lower measuring line was much higher in 2004 (17 June) than in the following years. As the infiltration in 2004 was the first one after the installation of the measuring equipment, mineral particles were washed into the tube and round the probe, increasing the EWC. This effect was diminished in the following years.

It is remarkable that distinct increases of the EWC did not occur at the same time in the lower and upper measuring lines, except for 25 May 2005. This can be explained by the paths of the groundwater flow strongly varying in space, thus the conductivity probes may not be immersed simultaneously in both measuring lines.

In most cases, increases in EWC were followed by decreases after only a few days. This was different before 19 November 2004 in the lower measuring line and before 23 November 2005 in the upper measuring line (grey dashed lines in Figure 2.8), when increased values lasted for five to six weeks. As the end of these periods coincided with the zero-curtain in autumn (Figure 2.9), the decrease in EWC was likely caused by freezing of water and the electrical conductivity of ice is much lower than that of water.

Vapour flux

The highest vapour flux was measured close to the ground surface (0.3 m depth) with 10^{-3} mm/d. The second highest value occurring at the interface between the active layer and the permafrost (1.5 m depth) was more than one order of magnitude smaller.

2.3.3 Thermal ground parameters

Ground temperatures

Temperature-time series

In the lower measuring line the active layer (1.7 m deep) had a mean annual temperature of –1.7°C during two complete years within the measuring period. In comparison, the upper measuring line proved to be slightly warmer, indicated by the mean annual temperature of the uppermost 1.7 m of –1.5°C.

The development of ground temperatures (GT) in the active layer and in the upper zone of the permafrost can be divided into the following six periods each year (Figure 2.9, Table 2.2). (1) GTs were negative throughout the active layer and increased with depth, i.e. the temperature gradient was negative, declining with depth. The delay and damping of surface temperature fluctuations also typically increased with depth. (2) GTs remained negative, but the temperature gradient became positive when the temperatures close to the surface increased more rapidly than those at lower depths. This change could occur very rapidly (2004 and 2005) or gradually (2006). The period is finished by a marked temperature increase at all depths. (3) This period was characterized by the GTs remaining stable with isothermal conditions at 0°C ('zero-curtain') nearly throughout the active layer. (4) GTs became positive, first at the surface and subsequently downwards, but the temperature remained close to 0°C in the permafrost. Strong diurnal temperature variations occurred, decreasing with depth. The period ended when the downward penetrating thawing front reached the active layer depth, i.e. the maximum thaw depth. (5) The active layer cooled back, but yet without significant freezing. During this period the near surface GTs still showed diurnal fluctuations. At the end of the period the GT at the ground surface passes below the 0°C-limit for the last time within the annual cycle. (6) GTs were at or below 0°C throughout the active layer. Thus, an autumn zero-curtain appeared. As the freezing front penetrated downward from the surface, the separation of the GTs from the autumn zero-curtain first took place at the surface and subsequently downwards. The period was completed when the GT at the active layer base just became negative, indicating the end of phase change from water to ice. Thereafter the cycle started again.

Meteorological, thermal and hydrological parameters demonstrated close correlations in time. Under conditions of a negative GT gradient, ice sublimates in the relatively warm depths of the active layer or unfrozen water evaporates. The vapour then flows upwards along the temperature gradient and refreezes or condenses, when it is cold enough (Smith & Burn 1987). As the temperature gradient was mostly negative close to the surface, the highest vapour flux was measured here.

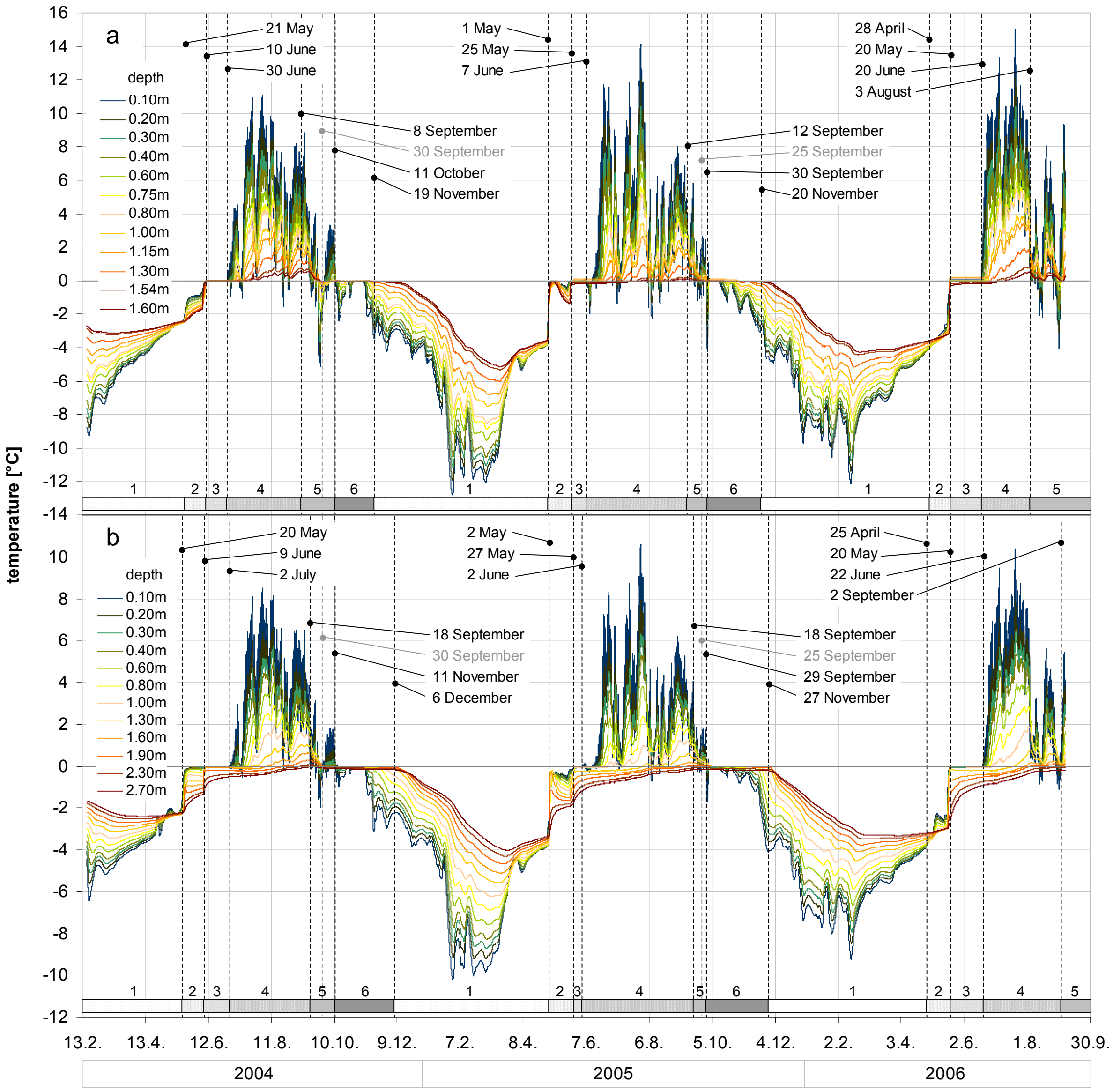

***Figure 2.9**: Ground temperatures: a) lower measuring line, b) upper measuring line. The vertical black dashed lines indicate dates of crucial changes. The annual cycle of the ground temperatures was divided into characteristic periods by means of these dates indicated by the grey shaded horizontal bars. The numbers above the bars refer to the overview in Table 2.2 and the description in the text. Note that the periods 1 and 5 at the begin and end of the data series are not complete. The vertical grey dashed lines indicate the onset of the autumn zero-curtain at the active layer base and will be referred to in Figure 2.13.*

It is remarkable that distinct GTs changes in spring from period 1 to 2, 2 to 3 and 3 to 4 coincided or were shortly preceded by marked changes in the infiltration rate, the VWC or both (compare Figure 2.5, Figure 2.7 and Figure 2.9). As the GT increase before period 2 was quite slow, it can likely be ascribed to purely conductive heat transfer. When the seasonal trend of the MDAT exceeded 0°C, the onset of snowmelt was caused, which is indicated by a sharp decrease in the snow depth (Figure 2.4). The resulting infiltration of meltwater could be delayed by some days, because the snow cover can store some water in its pore space (Jordan

1995). At least when the infiltration continued daily, it caused marked increases in VWC and according to the convective heat transfer also marked increases in GT throughout the active layer (transition from period 2 to 3). However, the thermal regime in period 2 differed considerably between the observed years and can be understood by the thermal conditions before and the different hydrological processes.

***Table 2.2**: Overview of periods within the annual hydrothermal cycle of the active layer (AL) divided up by means of ground temperatures (GT). The periods are shown in Figure 2.9 and described in the text below.*

period	hydrothermal conditions and processes in AL	thermal events in AL
1	GTs negative throughout AL temperature gradient negative constant low water content	
		change of temperature gradient
2	GTs negative throughout AL temperature gradient positive ground ice warms	
		initiation of ice melting throughout AL
3	GTs isothermal at 0 °C throughout AL spring zero-curtain ground ice melts throughout AL	
		ice in uppermost AL-layer completely thawed
4	thawing front moves from surface downwards separation from zero-curtain progresses downwards response of near surface GTs to diurnal air temperature fluctuations	
		maximum thaw depth
5	cooling of AL, but mainly above freezing response of near surface GTs to dirunal air temperature fluctuations	
		GT at ground surface passing 0 °C for last time in annual cycle
6	GTs 0 °C at least at AL-base, otherwise negative temperature gradient 0 or negative autumn zero-curtain freezing front moves from surface downwards	
		end of AL-refreezing
1	annual cycle starts again (see above)	

In spring 2004 the water resulting from the small preceding infiltration event on 20 May was mainly absorbed by the near-surface ground layer. Therefore the increase of VWC was highest close to the surface and declined with depth (Figure 2.7). The infiltration of meltwater into frozen ground implies that heat was transferred to the ground by convection, resulting in a GT increase. As it was highest at the top of the active layer and lowest at its base, the temperature gradient changed its direction. With convection being a rapid heat transfer mechanism, this change occurred suddenly. The second thawing event on 7 June 2004 caused rapid snowmelt and thus resulted in a much higher infiltration than the first event (Figure 2.5). There was then enough water for a strong increase of VWC at all depths in the active layer. Although the water infiltration front reached the base of the active layer as late as June 9 2004, an instantaneous GT increase at this depth already occurred two days before (and three days before the onset of the zero curtain), when the water content was still low. This phenomenon is probably due to large pores in the ground which acted as preferential flow paths and therefore enabled the water to flow downwards rapidly. As the permafrost table is impermeable (Gardaz 1998) – at least in the short term, the water partly refroze there and partly ran downslope. The latent heat released by the refreezing process probably explains the instantaneous temperature increase at the depth of the permafrost table (Hinkel & Outcalt 1994, Kane et al. 2001).

In spring 2005 the isolated infiltration events on 24 March and 1 May were reflected very slightly in the VWC and only in the upper measuring line, but not at all in the lower one, although the infiltration rates were higher than for the event on 20 May 2004 (Figure 2.7). In contrast, the GTs throughout the active layer clearly responded at least to the infiltration event on 1 May 2005 by increasing rapidly, in the lower measuring line even to 0°C. This indicates that the infiltrated water used preferential flow paths through the large pores in the coarse talus to penetrate downwards and froze before the VWC could increase. The latent heat released by freezing then caused the sharp increase in GTs. The fact that they did not remain at 0°C forming a zero-curtain, but rapidly declined again thereafter, is an additional indication for fast and complete freezing of the infiltrated water. In contrast to the infiltration event on 20 May 2004, the mean GT of the active layer was about 1.5°C lower on 1 May 2005 (Figure 2.9), causing faster freezing and therefore preventing a clear change in VWC.

In spring 2006 no isolated preceding infiltration event occurred and accordingly no increase in VWC. In contrast to the years before, when the onset of period 2 was caused by fast convective heat transfer, the inversion of the temperature gradient only took place gradually, as it was driven by heat conduction.

After period 2 the course of the temperatures between the years was similar. As soon as enough thermal energy had been transferred to the active layer by water and thus preventing it from being completely frozen, water coexisted in the solid and liquid phase. Under these conditions the GTs remained exactly at 0°C (zero-curtain) nearly in the entire active layer until all the ice had melted. The GT first separated from the zero-curtain near the surface (transition period 3 to 4, Figure 2.9). This date was shortly preceded by the disappearance of the snow cover only in 2006, while the snow depth was still about 40 cm in 2004 and 2005 at this time (Figure 2.4). Nevertheless, the shielding and insulating effect of the snow cover against solar radiation and warm air temperatures were no longer efficient enough to prevent the thermal conditions of the atmosphere from penetrating through the snow cover and influencing the GTs, either positively as in 2004 or negatively as in 2005 (compare Figure 2.4 and Figure 2.9). These thermal data were in accordance with the hydrological ones; the positive air temperatures shortly before the end of the zero-curtain (2004 and 2006) caused high infiltration rates enforcing the warming of the ground, while the negative air temperatures at 7 June 2005 corresponded to an infiltration pause (compare Figure 2.4 and Figure 2.5). As the duration of the zero curtain increased with depth, the process of ice melting within the active layer lasted longest at its base, i.e. at the permafrost table. However, at this depth the GT does not become positive, because before all ice can melt, refreezing of the active layer starts (transition period 4 to 5), when the air temperature decreases and the winter season begins. Due to atmospheric cooling the GT first dropped below 0°C at the surface (transition period 5 to 6) and remained longest at isothermal conditions with increasing depth (transition period 6 to 1). The GTs in the permafrost (upper measuring line) remained at the zero-curtain after the maximum thaw depth had been reached, indicating melting processes. This suggests the presence of a transition zone below the active layer as proposed by Shur et al. (2005) where seasonal phase changes (modifications of ice and water content) occur, but where the temperature never exceeds 0°C. The data from the upper measuring line demonstrated that the hydrological processes within the active layer not only influence its thermal regime, but also the upper permafrost, at least in the transition zone.

Rate of temperature change

From the temperature-time series the rates of temperature change (RTC, temperature difference per time at a given depth) were calculated (Figure 2.10), as had been done by Kane et al. (2001) at a tundra site in the northern foothills of the Brooks Range (Alaska). The RTC indicates the dominant type of heat transfer as is illustrated below.

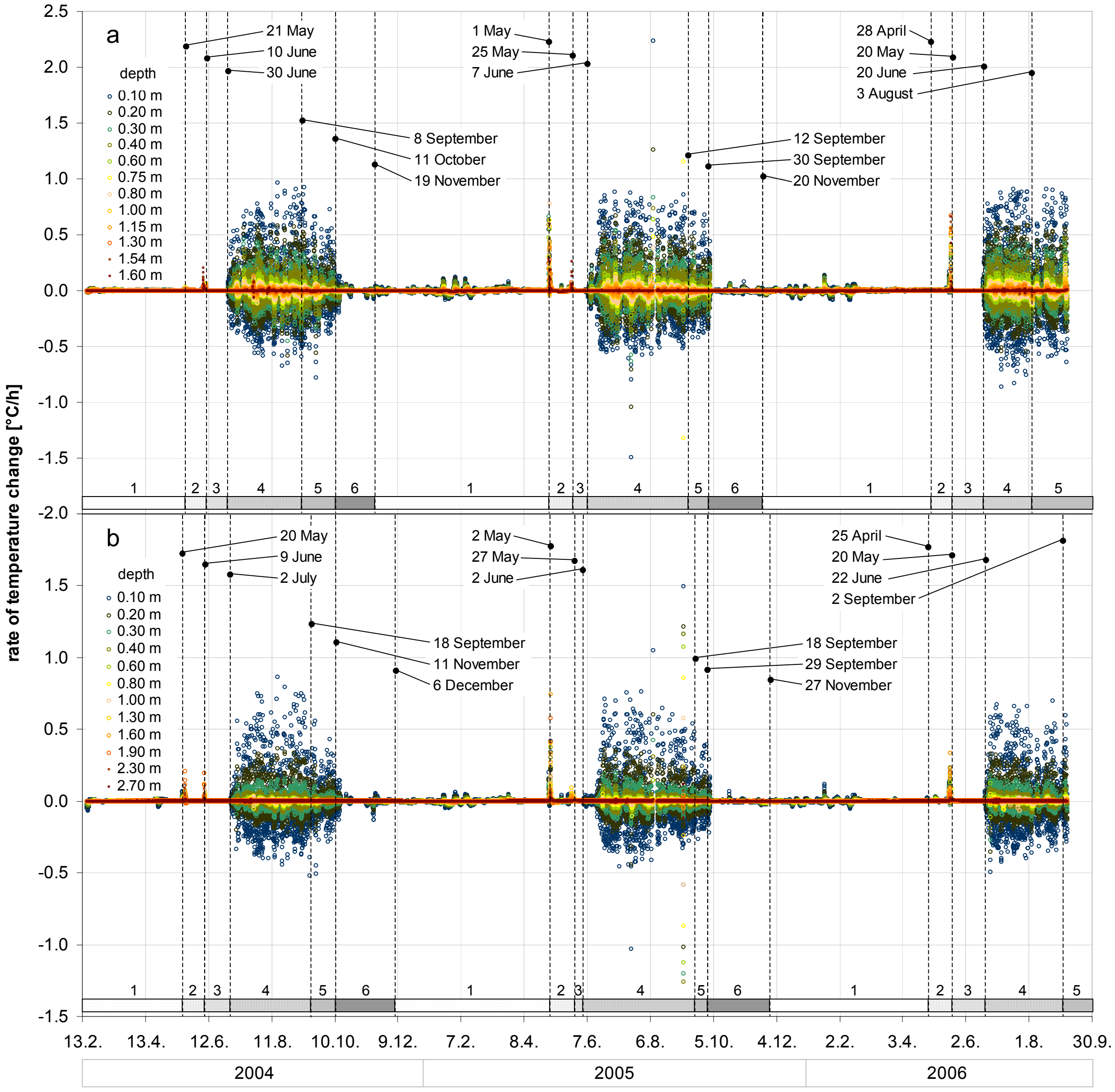

Figure 2.10: *Rates of temperature change: a) lower measuring line, b) upper measuring line. The division of the annual thermal cycle indicated by the vertical black dashed lines and the grey shaded horizontal bars is equivalent to the divisions in Figure 2.9.*

In winter (period 1) the RTCs were relatively low. Alternations between positive and negative values occurred, mainly at intervals of several days, and daily alternations were rare. During the last few weeks of winter (before the onset of snow melt water infiltration), the RTCs reflecting the thermal activity, were nearly 0°C/h. This can be explained by the atmospheric temperature fluctuations being strongly dampened by the snow cover, which is greatest towards the end of the winter. The onset of meltwater infiltration events in spring (transition period 1 to 2 and 2 to 3) was closely correlated to sharp peaks of the RTC with mainly positive values which were independent of the depth, i.e. occurred throughout the active layer. This response reflects the rapid heat transfer by convection due to meltwater infiltration. During the zero-curtain in spring (period 3) the RTCs remain at exactly 0°C/h throughout the AL, i.e. thermal quiescence. This indicates the coexistence of water and ice and phase change, which postulates isothermal conditions at 0°C for thermodynamic reasons. In summer (periods 4 and 5) the RTC revealed the most extreme values of the year (maximum 2.2°C/h; minimum -1.5°C/h), fluctuated daily and the absolute values clearly declined with depth. Without the insulating effect of the snow cover the atmospheric temperature fluctuations (daily warming and nocturnal cooling) directly penetrated into the ground, but the response was dampened with increasing depth due to the overburden ground layers. During the autumnal freezing period (period 6) the temperature changes became much lower than in summer and even came to a standstill during the autumn zero-curtain, which was shorter than the spring one. The thermal decoupling between the atmospheric and ground thermal regime can be attributed to the appearance of a snow cover and additionally to the coexistence of water and ice during the zero-curtain. In contrast to the spring zero-curtain with a clear onset due to rapid convective heat transfer, the onset of the autumn zero-curtain occurred gradually with depth, as it is driven mainly by heat conduction, while latent heat was involved in both seasons. In addition, more ice had to melt in spring than water had to freeze in autumn (difference is infiltrated meltwater). Dividing the annual thermal cycle by means of RTCs would roughly result in the same periods established by means of GTs, at least in winter and spring. However, the point of maximum thaw depth (transition period 4 to 5) and the end of the autumn zero-curtain at all depths (transition period 6 to 1) cannot be detected by means of RTCs. It can be concluded that sharp positive peaks of the RTC during a prevailing snow cover are due to thermal convection by snowmelt water infiltration, while the low base values indicate conduction which is strongly dampened by the insulating snow cover. Constant RTC-values of exactly 0°C/h indicate the release or absorption of latent caused by phase change during the spring and autumn zero-curtain. This is in good accordance with the findings of Kane et al. (2001).

Temperature-depth profiles

Temperature-depth profiles were generated by means of the temperature-time series for characteristic situations within the thermal cycle to be analyzed (Figure 2.11). The date when the lowest near-surface temperature was reached in winter only ranged within about 2.5 weeks. At this time the ground surface temperature (which is well approximated by the temperature at a depth of 10 cm) is equal to the bottom temperature of the winter snow cover (BTS, Haeberli 1985). The BTS was colder in the lower than in the upper measuring line by about 3°C each year and colder in 2005 and 2006 than in 2004 by the same temperature difference. The high BTS in 2004 reflects the thermal disturbance due to the installation of the measuring equipment as well as the effect of the exceptionally high temperatures in summer 2003. The nearly equal BTS values of 2005 and 2006 demonstrates that this disturbance was compensated in 2005.

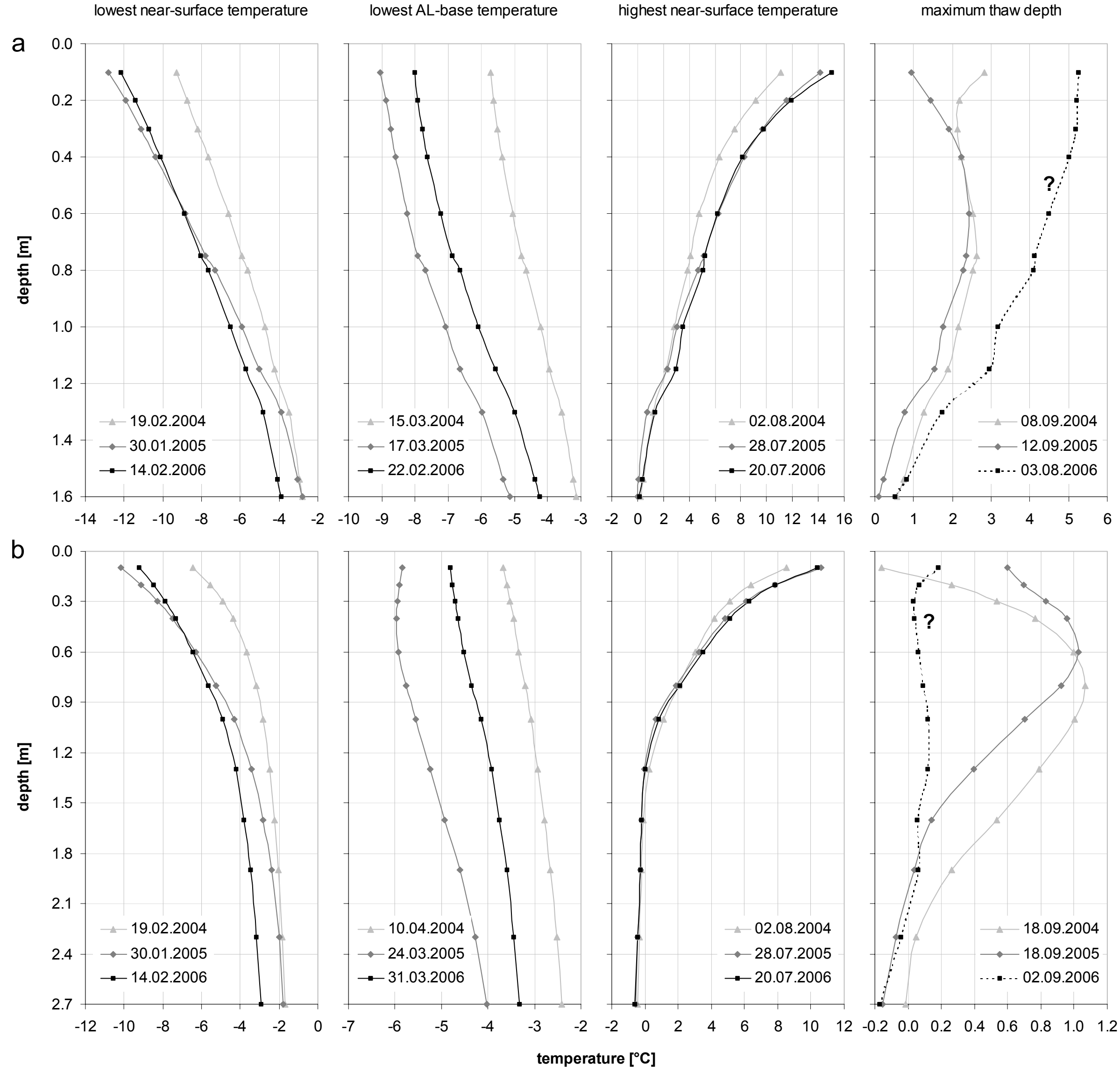

***Figure 2.11**: Temperature-depth profiles for four characteristic situations (headings): a) lower measuring line, b) upper measuring line. AL = active layer. Note that the scale of the x-axis is specifically adapted to the range of each plot and that the scale of the y-axis (vertical depth below the ground surface) differs between a) and b). As the data acquisition for this study ended on 6 September 2006, the maximum thaw depth was likely not yet reached in the last year.*

The date of the lowest temperature at the active layer base was delayed in the upper measuring line compared to the lower by 1 week (2005) to more than 5 weeks (2006). This delay was caused by the active layer being deeper in the upper measuring line than in the lower (see maximum thaw depth in Figure 2.11), thus the cold atmospheric temperature signal needed more time to propagate down to the active layer base. This propagation time is equivalent to the period between the lowest near-surface temperature and the lowest temperature at the active layer base. It ranged between about one week (lower measuring line, 2006) and nearly eight weeks (upper measuring line, 2005). This wide range was caused by differences in the gradient between the temperatures of the atmosphere and at the AL-base, by the depth of the

AL (which could vary between the years) and the conditions of heat transfer in the ground with the main varying factors being the water and ice content. In comparison with 2004 the lowest temperatures at the active layer base were 1 to 2°C colder in 2006 and 2005. Thus, the thermal disturbance due to the installation of the measuring equipment was smaller at the active layer base than near the surface.

The date of the highest near-surface temperature in summer differed only by about a week between the years, however, it arrived earlier in each successive year. On this date, the uppermost 80 cm of the active layer was warmer in 2005 and 2006 than in 2004 (by 2-4°C at 10 cm depth). Regarding this result in context with the values of the lowest near-surface temperature being higher in 2004 (see above), the response of the ground temperatures to the atmospheric seem to be more inert in 2004 than in 2005 and 2006. Maybe this was caused by a higher air content of the ground in 2004 due to reallocation by the installation of the measuring equipment a few month before, while the ground could settle until 2005.

The maximum thaw depth appeared to be more than a month earlier in 2006 compared to the years before. This is most likely due to the fact that the actual maximum thaw depth within 2006 was not yet reached when the data acquisition was finished at 6 September. In the lower measuring line the temperature at 1.6 m depth was higher than 0°C each year. Obviously the trench which was dug to install the measuring equipment did not extend to the permafrost table. As the digging was done in August 2003, the maximum thaw depth was not yet reached and therefore the lowermost thermistor could only be located at the actual thaw depth at this time. However, extrapolating the temperature-depth profiles of the lower measuring line reveals the maximum thaw depth and therefore the active layer depth to be about 1.7 m in 2004, 1.65 m in 2005 and more than 1.7 m in 2006. As the thermistors in the upper measuring line extended into the permafrost (because they could be installed in a borehole), the maximum thaw depth could directly be determined and was 2.6 m in 2004, 2.0 m in 2005 and more than 2.1 m in 2006. The deeper thaw depth in 2004 can be attributed again to the thermal disturbance by the installation of the measuring equipment in the summer before. However, it remains unclear why this disturbance had a much higher effect in the upper measuring line, although the borehole already existed and therefore the disturbance should have been less than in the lower measuring line.

Air-ground temperature relations

In order to analyze the heat transfer from the (atmospheric) air to the ground, interception figures (phase-space plots) for air temperatures (AT) and ground temperatures (GT, according to Beltrami 1996) were generated at several depths (Figure 2.12).

Plotting AT versus GT under idealized conditions (annual sinusoidal AT oscillation, pure heat conduction, constant heat conductivity of ground, no snow cover, no rain) results in elliptic interception figures, whose long principal axis flattens with increasing depth (Beltrami 1996). However, according to the latter also under realistic meteorological conditions, but without a snow cover and phase changes of water, the cloud of data points is captured by an ellipse. If a snow cover in winter occurs, the long principal axis of the winter part of the ellipse will be flatter than in summer, which arises from the insulating effect of the snow cover. Further deviations of AT-GT interception figures from the shapes described above indicate that non-conductive heat transfer mechanisms are involved including phase change and convection of water.

According to this theory the interception figures of the present study clearly show a declining slope of the long principal axis with increasing depth (Figure 2.12). This can be explained by the fluctuations of the atmospheric AT being delayed and dampened with depth, i.e. the deeper the observed point below the ground surface the more independent the GT becomes of the AT. Near the ground surface (0.1 m depth) the long principal axis of the cloud of data points for GTs at or below 0°C (winter conditions) was flatter than for positive GTs (summer conditions). This can be attributed to the influence of the snow cover (insulation and high albedo). However, the variation of AT over a wide range at nearly isothermal ground conditions at exactly 0°C, indicates a distinct thermal decoupling between AT and GT due to non-conductive heat transfer. This decoupling is interpreted as phase change with the associated transfer of latent heat, i.e. the presence of a zero-curtain. However, there are preferential GT-levels also below 0°C depending on depth. On the one hand these levels are interpreted as initial GTs at the begin of a well insulating snow cover, because they are conserved thereafter.

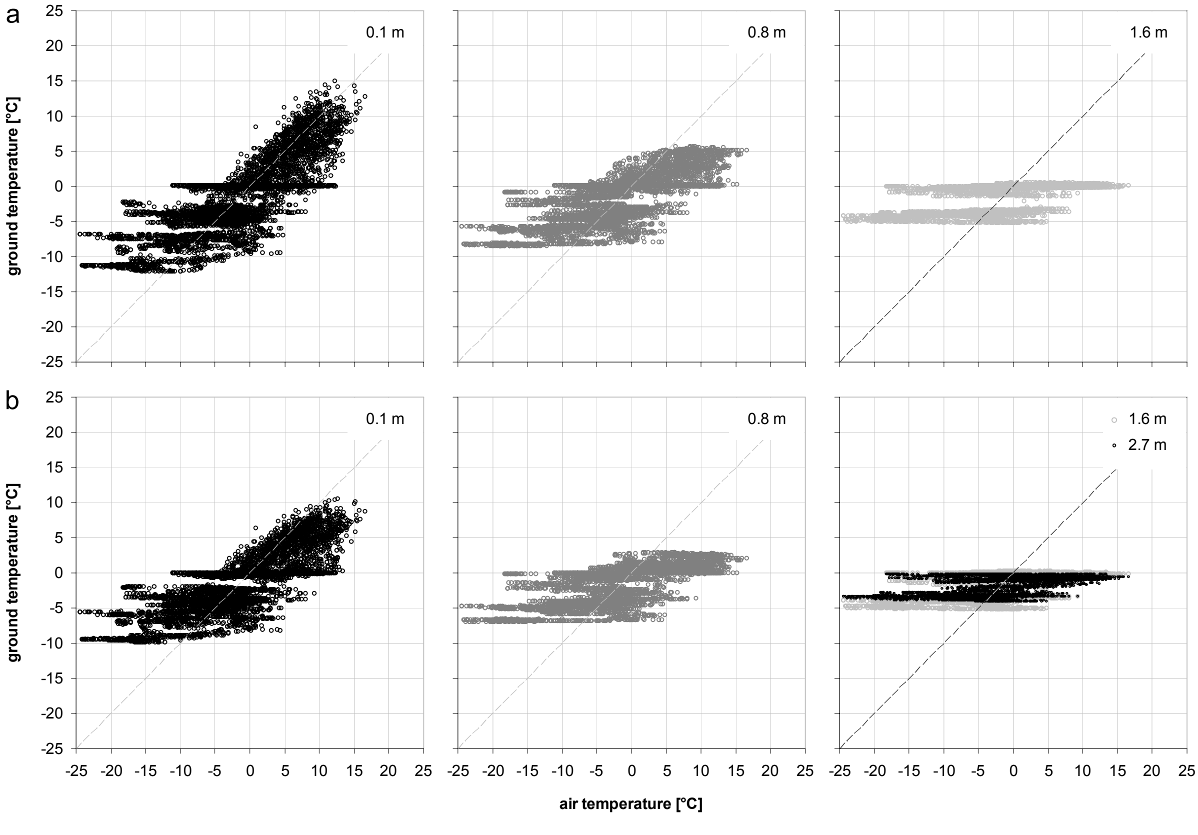

Figure 2.12: *Ground temperature versus air temperature: a) lower measuring line, b) upper measuring line. The depth below ground surface is given in the upper right corner. The diagonal dashed lines denote the cases for which air and ground temperatures would be exactly identical. Note that there are longer periods of missing data due to the lack of air temperatures (see Figure 2.4) which are not visible in these plots.*

These initial GTs can vary from year to year depending on the meteorological conditions. On the other hand these levels can be raised when heat is transferred to the ground by water convection due meltwater infiltration which will also change the ground thermal conductivity by means of modified water and ice contents. After such an infiltration event the supplied heat will be distributed in the ground and a new isothermal GT-level will be established under the thermal protection of the snow cover.

Ground heat flux

The ground heat flux at or rather near the active layer base (GHF) was negative throughout period 1 in winter (Figure 2.13), i.e. heat was transferred from the permafrost to the active layer and from there to the atmosphere.

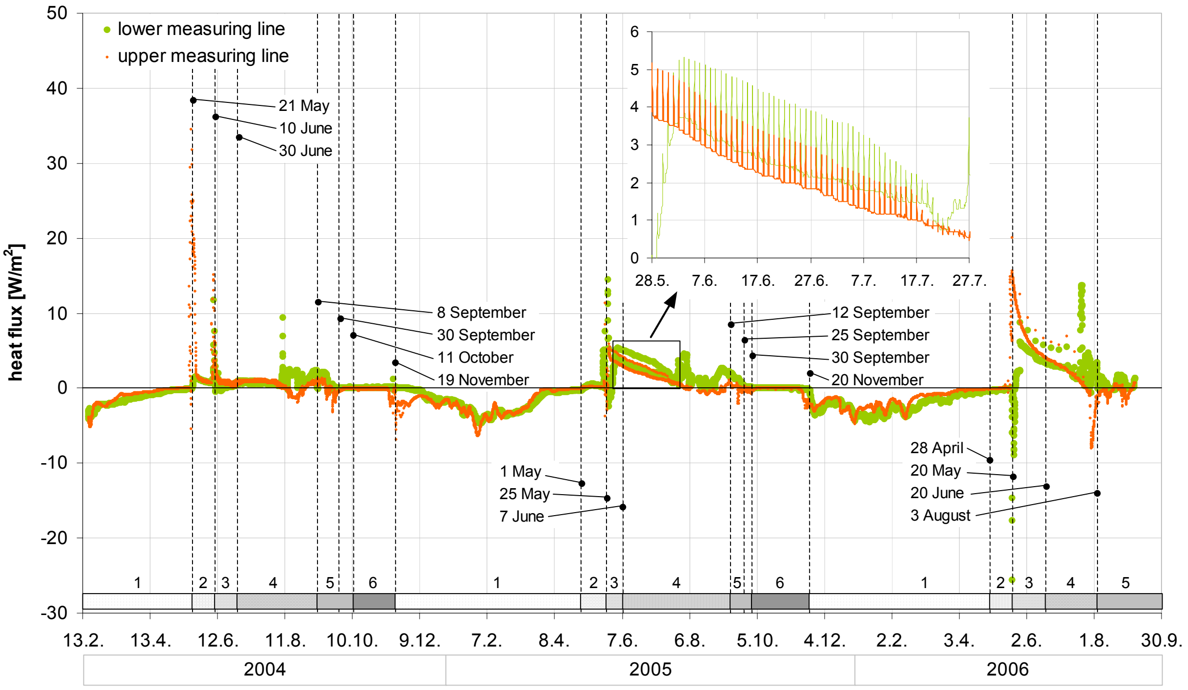

__Figure 2.13__: Heat flux at or rather near the active layer base. The division of the annual thermal cycle indicated by the vertical black dashed lines and the grey shaded horizontal bars is equivalent to the division in Figure 2.9a and refers to the lower measuring line. Two additional dashed lines were inserted at the onset of the heat flux remaining at zero in autumn (30 September 2004 and 25 September 2005).

During winter the negative GHF roughly reflected the GTs (compare Figure 2.9 and Figure 2.13) whose gradient was accordingly negative (i.e. GT increased with depth). When the ground temperature gradient changed its direction (transition period 1 to 2), the GHF became positive. The instantaneous and most extreme GHF fluctuations of the year occurred at the transition from period 1 to 2 and/or 2 to 3, thus they corresponded with the onset of snowmelt water infiltration events and the equivalent strong increases in the VWC at the active layer base (compare Figure 2.5 and Figure 2.7). The infiltration of snowmelt water implies a convective heat transfer to the ground. In addition, the infiltrated snowmelt water with a temperature of 0°C partly froze in the cold ground and latent heat was released as a result. However, latent heat cannot be detected by the heat flux plate. The strong increase in GHF reflects the efficiency of heat transfer by the infiltration of snowmelt water into frozen ground. As the heat flux plate was placed at a depth of 1.6 m, but the actual permafrost surface acting as a ponding layer was slightly deeper (Figure 2.11), the infiltrated water partly froze underneath the heat flux plate and thus heat was conducted upwards resulting in negative GHF-values (for example on 20 May 2006). However, with the infiltration going on the values gradually declined from the peak and therefore the net effect of the meltwater infiltration on the GHF was clearly positive.

This decline occurred in a sigmoid manner with the slope being lowest at the point of inflection (Figure 2.13). Note that the spring zero-curtain (period 3) was not reflected in the declining course of the GHF. This indicates that heat was transferred to the ground, although the temperature-depth gradient was zero, which can only be explained by thermal convection. The daily fluctuations of the GHF during the sigmoid decline (most pronounced in 2005, see detail which is zoomed in on in Figure 2.13) show that the heat gain was higher by day than by night, because the infiltration stopped then due to colder temperatures. The fluctuations in the GHF due to the temperature difference between day and night proved to be much smaller (see end of period which is zoomed in on in Figure 2.13). The fact that the values during the sigmoid decline were much lower in 2004 than in the following years may be caused by the disturbance due to the installation of the measuring equipment few months before which perhaps resulted in a poor contact between the heat flux plate and the ground. This contact likely improved with time due to natural settling of the disturbed ground.

GHF-peaks in the second half of period 4 and the first half of period 5 can be attributed to the infiltration of rainwater (as no infiltration data are available for this periods, compare with the increases of VWC during summer instead (Figure 2.7), which reflect the infiltration events due to rainfall). However, in the upper measuring line the GHF partly even decreased to negative values shortly after rainfall. As the permafrost surface is deeper in the upper measuring line, the negative GHFs may be caused by the warm rainwater ponding and freezing underneath the heat flux plate resulting in the release of latent heat and thus a negative temperature gradient.

The onset of the autumn zero-curtain at the active layer base on 30 September 2004 and 25 September 2005 as well as its end coincided with the periods in which the measured GHF exactly remained zero (compare Figure 2.9 and Figure 2.13). This shows that the uptake of latent heat was the only heat transfer mechanism during the autumn zero-curtain, because the heat flux plate used cannot detect latent heat (but only temperature differences). The contrast of this coincidence to the spring zero-curtain (see above) is thus attributed to the missing component of convective heat transfer. As the latent heat released by freezing could neither be vertically transferred by conduction due to a missing temperature gradient, nor by convection, the measured GHF remained zero.

2.3.4 Geotechnical parameters

The course of the cumulative downslope displacement at the ground surface (CDD) was similar each year (Figure 2.14).

In winter when the ground was frozen the slope was at a standstill which can be attributed to the stabilization due to the cohesion of ice. Towards the end of this roughly stable period the CDD showed a slight retrograde tendency (less than 1 mm) which means an upslope displacement. This may be caused by the overall contraction of the ground due to cooling in winter.

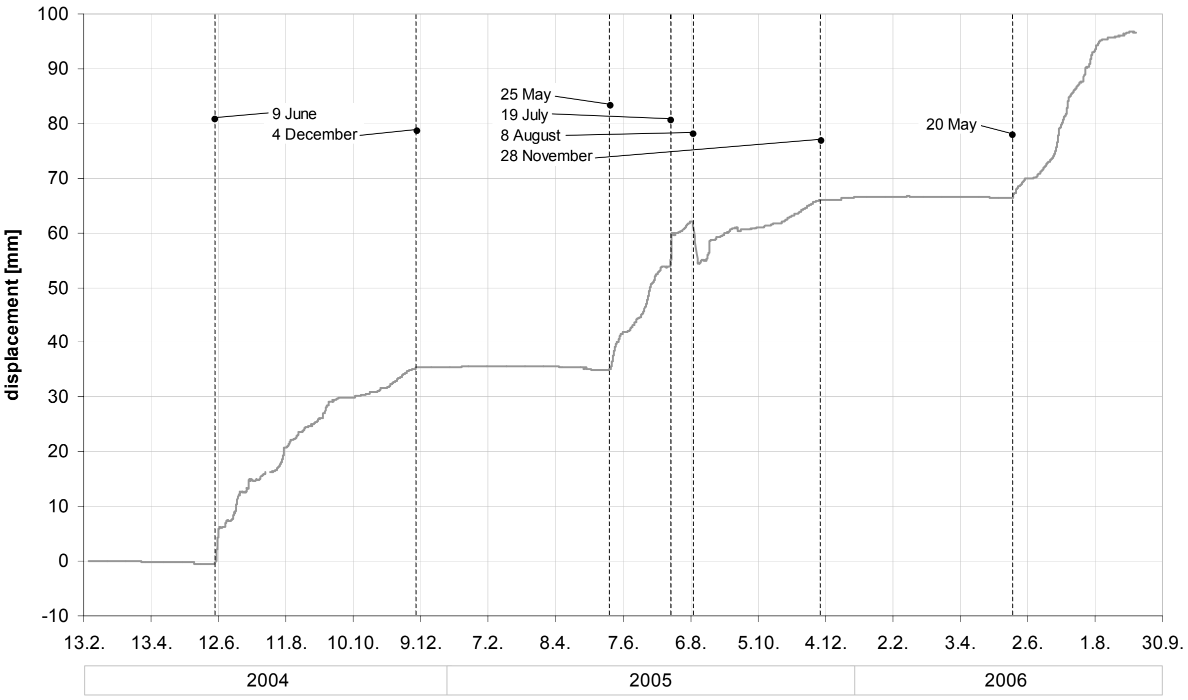

***Figure 2.14**: Cumulative downslope displacement at the ground surface. The vertical dashed lines indicate dates of crucial changes and are described in the text.*

Only two to three days after the onset of the continuous meltwater infiltration the slope suddenly started to creep on 9 June 2004, 25 May 2005 and 20 May 2006 (compare Figure 2.5 and Figure 2.14). Although the infiltration increased thereafter, the displacement rate (slope of CDD-curve) declined. It is therefore suggested, that the dominant mechanism controlling CDD is not liquefaction, but rather melting of ice bonds between the mineral grains. During the quiescent period at the slope scale (see above) the grains may have slightly moved against each other at microscopic scale due to the expansion of ice which is referred to as cryoturbation. When the ice bonds melted in spring by infiltration the grains rearranged themselves under the influence of gravity, the capillary forces and the current of the water and therefore the whole ground resettled leading to an instantaneous increase of the CDD.

Ground settlement and the associated CDD continued throughout spring and summer, but the displacement rate gradually declined over this period. This response may have been caused by increasing interlocking of the grains resulting in a gradually increasing slope stability. On 4 December 2004 and 28 November 2005 the quiescent winter period with a roughly stable CDD started. These dates roughly correlated to the end of the autumn zero-curtain at the active layer base (compare Figure 2.9 and Figure 2.14). This supports the supposition made above that the slope is stabilized by the cohesion due to ground ice.

In summer 2005 marked irregularities occurred. The instantaneous increase in CDD on 19 July coincided with a heavy infiltration event due to rainfall (compare Figure 2.5) and thus may have been caused by the pressure due to the water current, by lubrication due moistening of the grain surfaces or even liquefaction due to increased pore water pressures. The upslope movement at the 8 August 2005 was induced when the inclinometer was removed for the annual measurement and subsequently reinstalled.

2.4 Discussion of field investigations

2.4.1 Water balance

To establish a water balance for the active layer the elements infiltration, sublimation, evaporation, water and ice storage and discharge must be considered. As the sublimation was only marginal in comparison with the other elements (see page 35), it could be neglected. Evaporation was not measured, but is anticipated to be very low due to the coarse grained material at the active layer surface. If lateral water fluxes are excluded and the downslope discharge q_d on the impermeable ice saturated layer (which is mostly the upper part of the permafrost) is assumed to increase proportionally to the area, its flux per area can be calculated as

$$q_d = I - \left(q_{\Delta ws} + q_{\Delta is}\right) \tag{2.1}$$

where I is the infiltration rate, $q_{\Delta ws}$ the rate of change of the water storage and $q_{\Delta is}$ the rate of change of the ice storage in the active layer; the latter fluxes could be calculated by means of the water and ice contents (see Figure 2.7) and the depth of the active layer. All the water (equivalent) fluxes involved can be shown on one diagram (Figure 2.15).

First it has to be mentioned that theoretically only the change of the water and ice storage can either be positive or negative, while the infiltration and discharge are restricted to positive values. However, in fact there are negative values for the discharge, especially at the begin of snowmelt (transition period 2 to 3, Figure 2.15). On the basis of the figures this happened when the sum of water and ice storage change exceeded the infiltration rate. As the first negative discharge peaks in 2005 and 2006 (shortly before the transition from period 2 to 3) had exactly the same absolute values as the peaks of the ice storage change at this time, they solely can be attributed to superelevated ice storage change. In reality this change was likely to be much slower, but the lack of data for the ice content before (see Figure 2.7) revealed such artificially high values. The remaining apparently negative discharge values are due to the spatial variability of the water balance between (1) the places where the infiltration and the water/ice contents (measuring lines) were measured, (2) the measuring lines and the horizontally adjacent places to the left and right and (3) the measuring lines and upslope of them. Concerning the variability type (1) the infiltration must have been higher at the place of the measuring lines than at the lysimeter in case of negative discharge values. According to the variability types (2) and (3) the assumption that the discharge increased proportionally to the area proved not to be true. Regarding type (2) a negative discharge means that lateral water fluxes occurred from places adjacent to the measuring lines. As regards type (3) a negative discharge means that the downslope discharge entering the soil column at the measuring line from above was higher than the downslope discharge leaving it below. In fact all three variability types are likely to have contributed to the appearance of negative discharge values besides the ones explained by the artificial peaks in ice storage change.

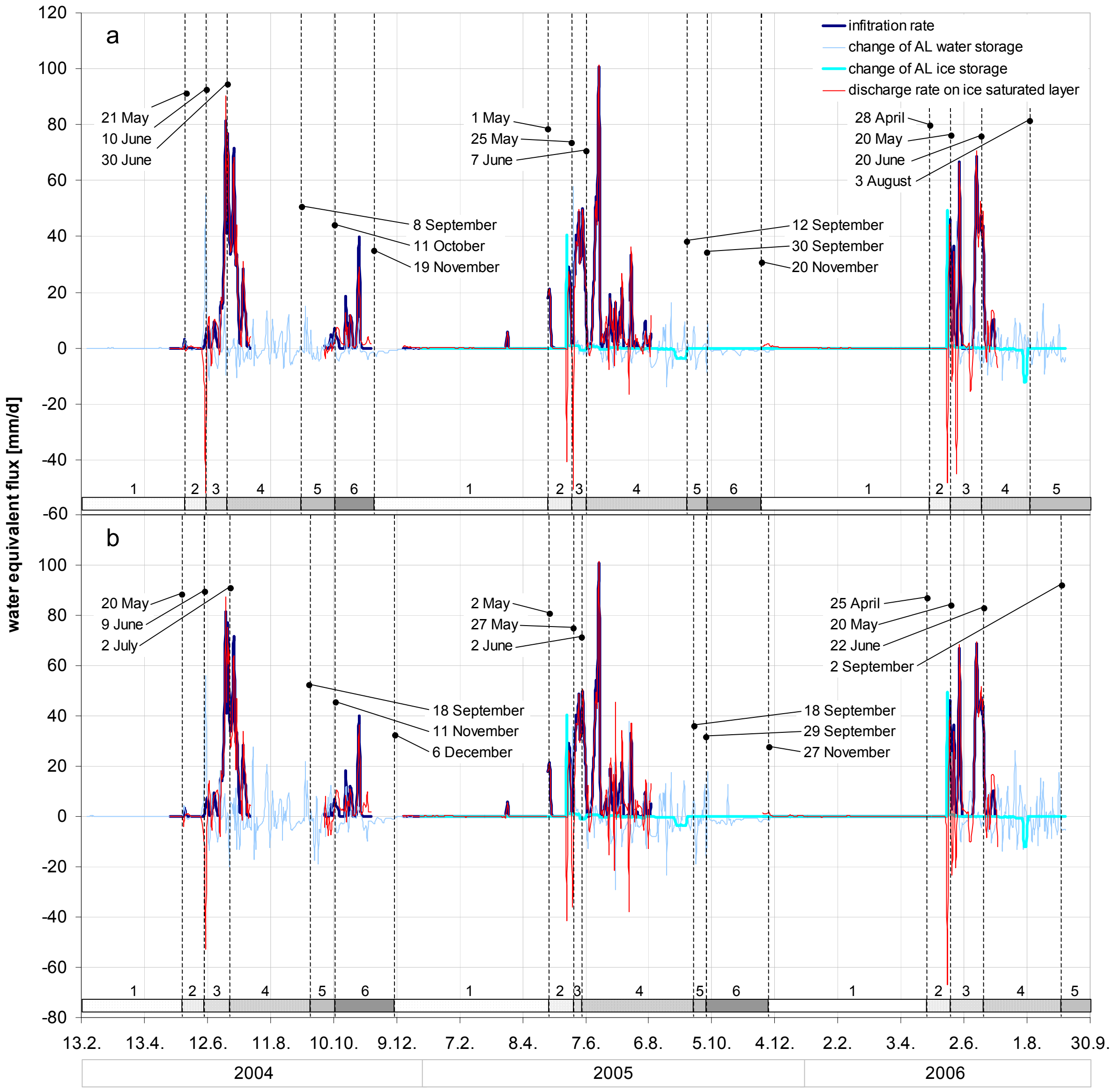

Figure 2.15: *The four most important water (equivalent) fluxes for the water balance of the active layer: a) lower measuring line, b) upper measuring line. As no data were available for the change of the ice storage in 2004, the discharge rate was calculated without considering this element of the water balance. Note that the discharge was only determined in the period of time for which infiltration data were available (see Figure 2.5). The division of the annual thermal cycle indicated by the vertical black dashed lines and the grey shaded horizontal bars refer to Figure 2.9. AL = active layer.*

The highest changes in water storage by a wide margin did not occur at the same time as the highest infiltration rates, but shortly after the onset of continuous (daily) snowmelt. Thereafter the water storage change fluctuated within a range of absolute values up to a third of the peak value in spring. In autumn the fluctuations became less and storage changes converged to zero until about end of December. Note that the slightly increasing trend in autumn towards zero does not mean an increase of the water storage, but only that the declining rate increased, i.e.

its absolute values became less. During winter the water storage remained constant (i.e. change was zero) until the meltwater infiltration started again the following spring.

As the infiltration rate was clearly higher than the change of the water and ice storage for the most time (besides the begin of continuous snowmelt), the discharge values were mainly close to the infiltration values. This response can be attributed to the low field capacity of the active layer; in spring the active layer storage first was filled resulting in high water storage changes. As the discharge was only slightly influenced by its fluctuations thereafter, this means that nearly all the infiltrated water percolated through the active layer and ran off on the impermeable permafrost surface as discharge.

The yearly integration of the daily water (equivalent) fluxes results in the cumulated heights of the water columns for each analyzed element of the water balance (Figure 2.16). In order to guarantee comparability between the years of the water and heat balance (see 2.4.2) each balance year starts on the first in the month of the earliest date over the measuring period at which a snowmelt infiltration pulse affected the whole active layer regarding either the hydrological or the thermal regime. This date proved to be 1 May.

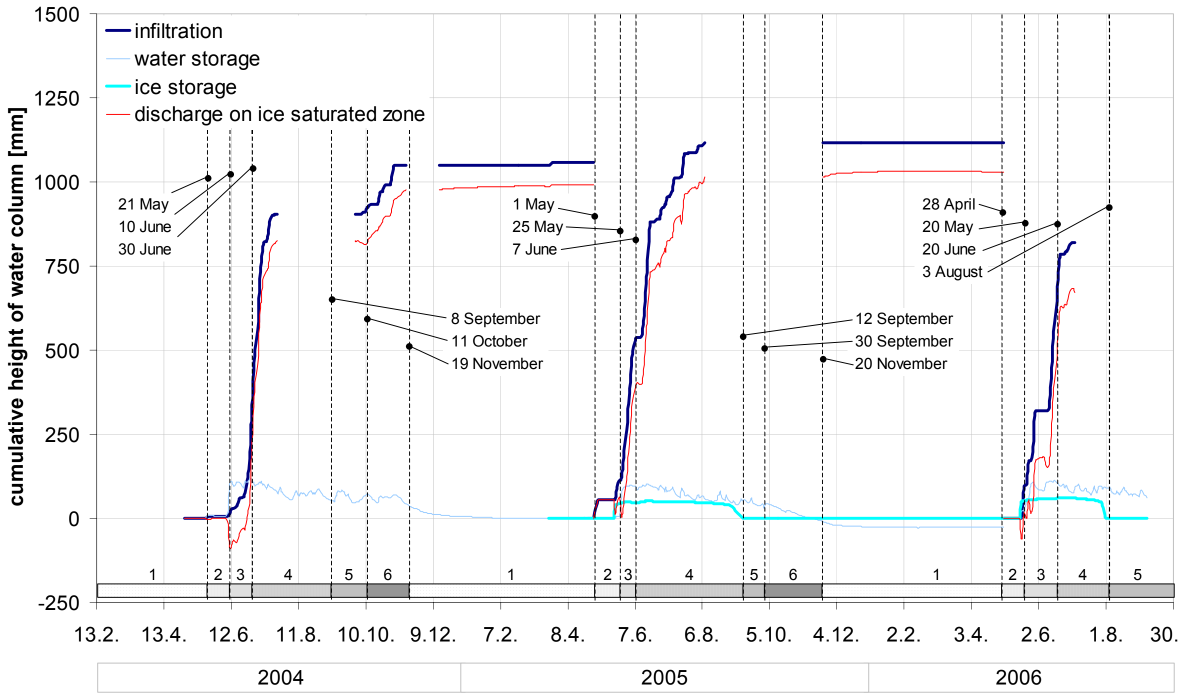

***Figure 2.16**: Yearly cumulative height of water column for the four most important elements of the water balance of the active layer. Each balance year begins on 1 May (see text). As the results for the lower and upper measuring line are very similar, the average of both is displayed only. The division of the annual thermal cycle indicated by the vertical black dashed lines and the grey shaded horizontal bars equals the division in Figure 2.9a and refer to the lower measuring line.*

Note that the water storage reached a constant value close to zero at the end of each water balance year. This constant value indicates the net difference of the water storage in comparison with the year before.

2.4.2 Heat balance

The yearly integration of the ground heat flux (Figure 2.13) results in the cumulative heat gain of the permafrost per area and thus a heat balance at the interface between the active layer and the permafrost (Figure 2.17).

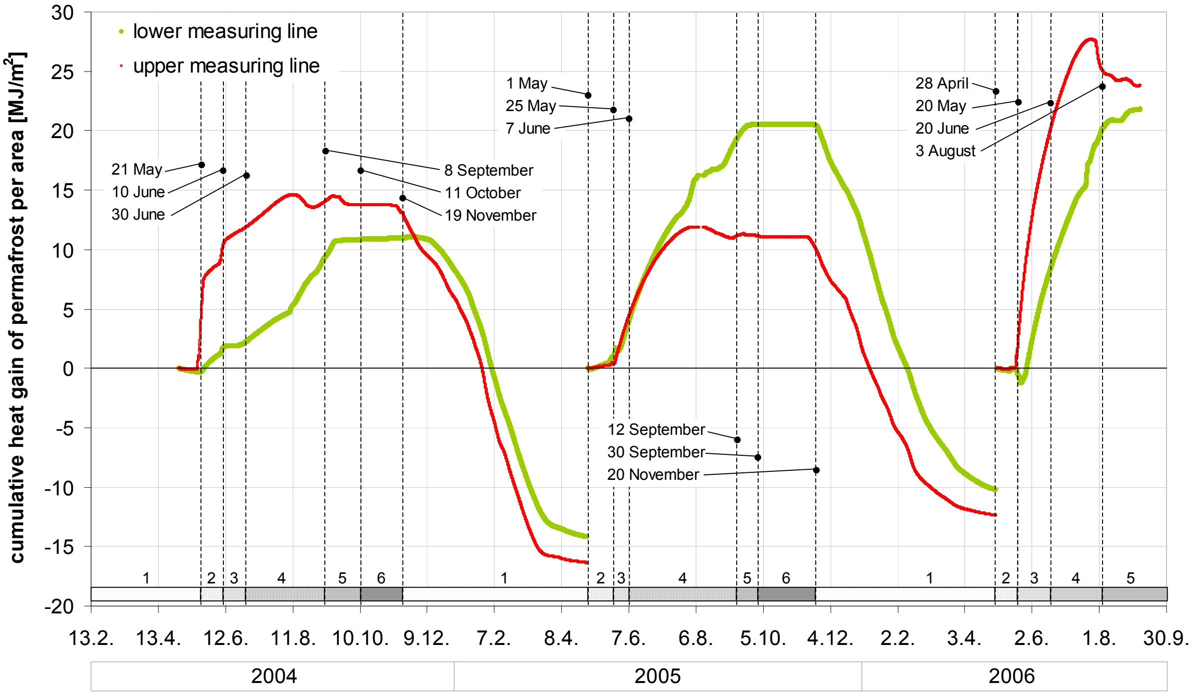

Figure 2.17: Heat balance at the interface between the active layer and the permafrost by means of the yearly cumulative heat gain per area. Each balance year begins on 1 May (reason see Figure 2.16). The division of the annual thermal cycle indicated by the vertical black dashed lines and the grey shaded horizontal bars is equivalent to the division in Figure 2.9a and refers to the lower measuring line.

Regarding the heat balance each balance year can be distinguished into three sections; (1) heat supply to the ground lasting until about end of September, (2) more or less stable section without major heat exchange between the atmosphere and the ground until about mid-November to the beginning of December and (3) heat loss from the ground to the atmosphere which declined towards the end of the balance year. The first marked increase of the heat supply (section 1) roughly coincided either with the transition from period 1 to 2 or 2 to 3 (relative to the division of the annual thermal cycle of Figure 2.9). Deviations were due to the spatial variability of the ground temperatures and the heat fluxes between the places where they were measured. As the transition from periods 1 to 2 or 2 to 3 (see Figure 2.5 and Figure 2.9) were caused by snowmelt infiltration, their major influence on the ground heat balance is therefore indicated. After snowmelt had finished, the further heat supply to the ground was due to warming by air temperature and radiation as well as rainwater infiltration. Towards the end of this section the heat supply showed higher fluctuations in the upper measuring line than in the lower. This can be explained by the fact that the heat flux plate in the upper measuring line was positioned at a shallower depth relative to the permafrost surface than in the lower measuring line. The stable section (2) can be attributed to refreezing of the active layer, as it coincided with the autumn zero-curtain (see Figure 2.9 and Figure 2.13). During winter the ground lost heat due to atmospheric cooling. The negative value for the heat energy at the end of this section denotes the net heat loss within a balance year (NHL). From the balance year 2004/05 to 2005/06 the NHL increased by 4 MJ/m^2 for each measuring line which is about a fourth of the total NHL in 2004/05. According to the last heat energy values in 2006 (6 September) being higher than the values at the equivalent dates the years before, the increasing trend of the NHL seems to continue in the balance year 2006/2007.

2.4.3 Relation between water and heat balance

During the period of marked increase in cumulative heat supply close to the beginning of each balance year the ground was still insulated and shielded from radiation by a deep snow cover. The strong heat supply can thus only be caused by infiltration of snow meltwater. In spring 2005 and 2006 the heat increase correlated with the amount of infiltrated snowmelt water (at 0°C each time), however, it did not correlate in spring 2004. For example the small amount of infiltrated water at the transition from period 1 to 2 caused a large heat increase (especially in the upper measuring line), while the much larger infiltration amounts at the transition from period 2 to 3 and 3 to 4 yielded much lower heat increases (compare Figure 2.16 and Figure 2.10). The 250 mm of water infiltrating within period 3 in 2004 resulted even in a standstill of the heat supply in the lower measuring line. The strong initial response of heat supply in 2004 was probably due to the very first infiltration after ground disturbance by installation of measuring equipment. As the ground was more loosely packed after this disturbance, the infiltrated water could percolate rapidly through the active layer to its base and directly influence the heat flux there. According to the explanation for the effect of the first infiltration on the cumulated downslope displacement (2.3.4), the ground thereafter settled by cryoturbation, capillary and current of the water, especially as it was the very first time after the disturbance.

While the cumulative infiltration showed distinct steps in spring and summer, especially in 2005 and 2006, they were not reflected in the course of the cumulative heat energy (compare periods 2 to 4 in Figure 2.16 and Figure 2.17). This indicates the hydrothermal dampening effect of the active layer to atmospheric changes. Longer data series and a continuous measurement of the infiltration throughout the year would allow to analyze whether the increasing trend of the heat balance will increase and whether it is associated with higher cumulated infiltration. In addition, detailed measurements (rather than a calculation) of the discharge on the ice saturated layer would be helpful for a better understanding of the hydrothermal balance of the active layer in talus slopes. However, for physical modeling of the active layer hydrothermal regime the inner structure (not only texture) of the ground is the limiting information, as it governs its hydraulic and thermal properties - for example by means of pore connectivity and tortuosity. As long as this information cannot be determined realistically in the field by effective methods, simulations of the active layer hydrothermal regime are likely to be more realistic by empirical-probabilistic rather than physical models.

The study shows that hydrological processes play a key role in the thermal regime of an active layer consisting of coarse blocky material, especially during the thawing period. When a snow cover is absent, conductive heat transfer and air circulation through the big voids of the blocky material are additionally relevant for the energy balance. However, the dampening of the thermal effect of air with depth is assumed to be higher than for water.

2.4.4 Suitability of measuring equipment and reliability of data

Most of the measuring equipment functioned properly and delivered reliable data for at least three thawing periods, but with the increasing monitoring time the data delivery is likely to be disrupted due to the destruction of the equipment by processes such as surface erosion and creep. The technical problems with the ultrasound probes were due to freezing of moisture which was absorbed by the porous sensor material. This was solved by protecting the sensor with a vapour-impermeable adhesive tape.

The measurement of the electrical water conductivity proved to be unsuitable for determining whether the water running over the permafrost surface originated from the snow cover or from pore ice in the ground, which was expected to reflect the contact time of the water with the mineral ground. As a further approach to detect the origin of the meltwater running over the permafrost surface depending on time, the conductivity probe could be positioned in a buried bath allowing the electrical water conductivity always to be measured under saturated conditions. In order to prevent freezing, the bath should be emptied in autumn. The vapour flux could not be measured accurately by vapour traps. However, they gave a rough estimation of relative rather than absolute values.

The measurement of the infiltration throughout the year and the water discharge on the ice saturated zone analogous to the measurement in the laboratory (see chapter 3.4) would result in a more reliable water balance. In addition, they would allow the ice content of the active layer (below saturation) to be determined. However, there are considerable technical problems in realizing this approach. To guarantee a defined catchment area for an exact water balance it should be bordered by vertical impermeable barriers extending into the permafrost (to prevent water loss underneath the barriers when the permafrost surface lowers). In addition, the infiltrated and discharged water can only be measured when it remains in the liquid phase and does not refreeze. Large amounts of heating energy for the lysimeters would therefore be required which is difficult to be supplied to a remote location such as the study site, even by solar panels as the slope is oriented NW. The ice content of the ground could be estimated alternatively by the indirect method of dielectric spectroscopy which was presented by Bittelli et al. (2004).

The reliability of the data is mainly limited by their spatial variability between the places where the single parameters were measured. However, placing the sensors more closely together would result in mutual disturbance of the measurements. The problem of incomparability of the parameters due to their spatial variability especially appeared when they were used to calculate another parameter such as the discharge for which the calculation yielded negative and thus impossible values. The inaccuracy of the discharge as well as the lack of suitable models (other than Darcy’s Equation) and information on the inner structure of the ground controlling its hydrological properties (especially the conductivity depending on pore connectivity and tortuosity) made it impossible to calculate the correct height of the water saturated zone above the impermeable layer realistically.

2.4.5 Relevance of results in context of climate change

The active layer is very likely to deepen with future climate change. This will be caused not only by warmer air temperatures but also by higher infiltration due to faster snowmelt and more extreme rainfall events in summer. Whether the storage of water and ice in the active layer will increase or decrease is difficult to predict. On the one hand, more water will be infiltrated due to increased precipitation, but on the other hand more water will evaporate due to higher air temperatures. Under the assumption of a later snow cover at the beginning of winter and for a given infiltration, the increase of the water and ice storage would delay the deepening of the active layer and permafrost degradation; the higher the ice storage, the more effectively the ground will be protected from warming in spring due to the large latent heat of fusion of ice and the large heat capacity of water. However, this mechanism requires effective freezing before the onset of an insulating snow cover, otherwise the reduced heat supply in spring will just be compensated by the reduced heat loss in autumn due to phase change.

The creep rates of debris slopes situated in alpine permafrost regions are projected to increase with climate change, in particular due to higher precipitation, but especially due to higher infiltration rates in spring when the main downslope displacement occurs. This alteration will be most relevant for infrastructure located in alpine permafrost regions.

2.5 Summary of field investigations

The aim of the field investigations in this study was to obtain a better understanding of the interactions of hydrological and thermal processes in the active layer of alpine permafrost in steep terrain with coarse-grained blocky surface material. Specially developed measuring equipment was installed in the active layer of a steep debris slope above Pontresina on Muot da Barba Peider, in the Upper Engadin, Switzerland, to determine ground temperatures, heat flux, water infiltration rate, soil water contents, surface level of the ice saturated zone, electrical water conductivity, vapour flux and downslope displacement. In addition, meteorological parameters such as air temperature and snow depth were measured. Results based on three spring thawing periods showed that meteorological, hydrological and thermal ground as well as geotechnical parameters are closely correlated in time. The non-conductive heat transfer mechanisms of water convection and release of latent heat due to phase change of infiltrated snow meltwater caused instantaneous increases in ground temperature each year. The downslope displacement began simultaneously with the onset of continuous meltwater infiltration with the highest rates at the beginning and continuously decreasing during the course of the year. This can be explained by resettlement of the ground due to melting of the ice bonds between the mineral grains and the forces due to the presence of flowing water in the ground. The data gained from the two equally equipped measuring lines proved to have similar ranges and temporal courses. However, the differences between the two lines reflect the spatial variability of soil structure and hence of the hydrothermal parameters in the scree slope within a distance of only 10 m. These are the first detailed hydrothermal investigations that have been effected in a steep, coarse-grained active layer above alpine permafrost.

3 Laboratory experiments

In the field various factors such as ground temperatures, water contents or slope movements interacting in a complex manner influenced the measured resulting variables. Therefore all these factors have to be considered in the interpretation of the data. However, under the complex field conditions the separate determination of the effect of each potentially influencing factor on a resulting variable remains uncertain. In contrast, laboratory experiments allow exclusion and control of each factor and therefore to determine its equivalent contribution to the total effect on the resulting variable separately. Additionally, controlled and safe slope failures can be performed in the laboratory. Laboratory experiments were therefore conducted within this study to improve the understanding of the factors and processes which govern the water and heat balance and its influence on slope stability in an active layer consisting of scree. Two kinds of experiments were effected in the laboratory: (1) systematic 4-factorial shear test series and (2) a physical simulation of a thaw-induced failure of the active layer. In the systematic 4-factorial shear test series the effects of grain size, water content of the active layer and ice content of the permafrost were determined statistically. In the physical simulation of a thaw-induced failure of the active layer thermal, hydrological and geotechnical processes occurring during meltwater infiltration and active layer thawing were studied. The experiments were carried out in the climate chamber at SLF where the air temperature can be set between -5°C and 35°C.

3.1 Analysis of granular materials

The granular material used for the laboratory experiments originates from the gravel plant Vetsch in *Pragg-Jenaz* (*Grisons*, Switzerland). The raw material is recent bed load of the third order river *Furnabach* flowing into the river *Landquart*, a tributary of the river *Rhine*. The *Furnabach* has an alpine hydrologic regime. Geologically, its drainage basin lies in the penninic flysch and Grison schist series (Baugeologie und Geo-Bau-Labor Chur, 2005). Lithologically the granular material contains 90% sedimentary rocks (limestone, sandstone, odd clay schists) and 10% vein minerals (quartz, partly grown into calcite) according to Baugeologie und Geo-Bau-Labor Chur, (2005). To attain an angularity of the mineral grains similar to that one of the grains in a high alpine scree slope, crushed and not rounded material was used for the experiments.

Four different grain types were used in the experiments: silty sand, sand, gravel and grit. Their relevant geotechnical properties are given in Table 3.1 and Figure 3.1.

***Table 3.1**: Characterization of the used grain types by selected geotechnical properties 1)data by Baugeologie und Geo-Bau-Labor Chur, 2005. 2)data by Kieswerk Vetsch, 2006, 3)determination according to ASTM (2000b), 4)determination according to ASTM (2000a), 5)determination of the angle of repose of the material dried at 105°C; sample size = 30.*

granules	**silty sand**	**sand**	**gravel**	**grit**
grain size [mm]	0-0.5	0-2	0-22	16-22
specific density [10^3 kg/m^3] 1)	2.7	2.7	2.7	2.7
pouring apparent density [10^3 kg/m^3]	1.4	1.6 2)	1.7 2)	1.4 2)
min. apparent density [10^3 kg/m^3] 3)	1.3	1.6	1.7	1.3
max. apparent density [10^3 kg/m^3] 4)	1.8	2.1	2.1	1.5
relative pouring density	0.2	0.0	0.0	0.5
pouring porosity	0.5	0.4	0.4	0.5
min. porosity	0.3	0.2	0.2	0.4
max. porosity	0.5	0.4	0.4	0.5
angle of repose [°] 5)	39.9	40.2	44.2	43.0

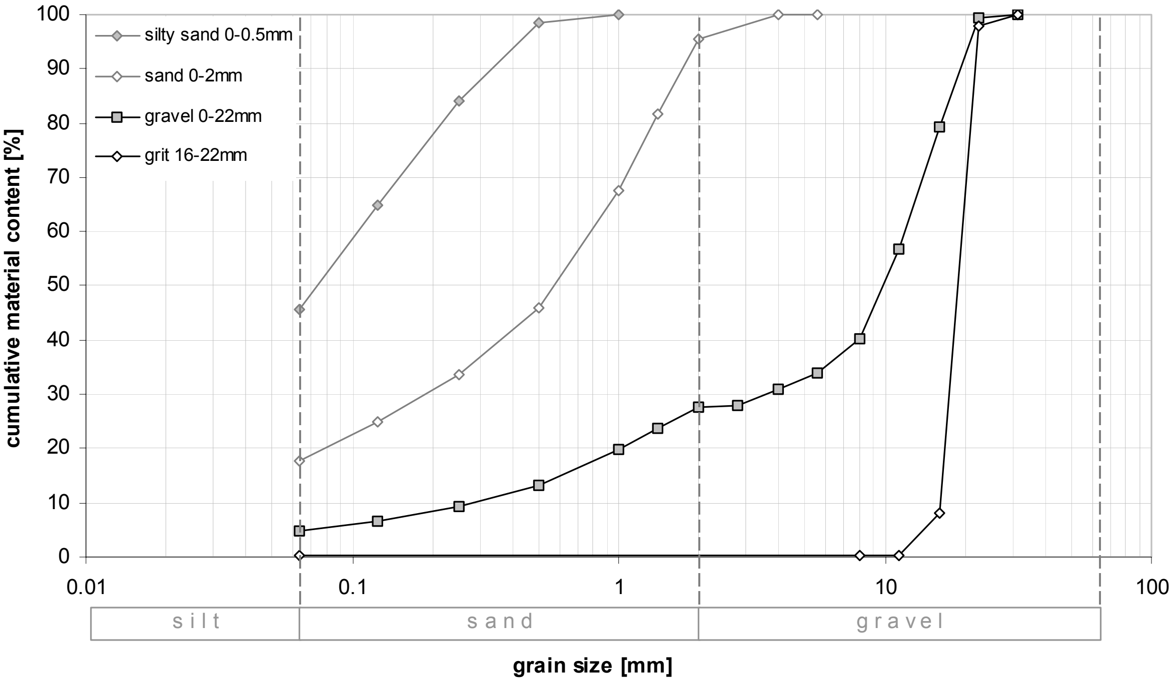

***Figure 3.1**: Grain size distribution curves of the used grain types. The data for silty sand 0-1 mm, sand 0-2 mm and grit 16-22 mm were measured by Baugeologie und Geo-Bau-Labor Chur, 2005. Gravel 0-22 mm is a composition of different granules produced by the gravel plant. The grain size distribution was calculated with the fraction of composites and their grain size distributions.*

3.2 Development of inclinable shear apparatus

3.2.1 Requirements

The investigation of the processes of rapid failure of the active layer on permafrost under realistic, but controlled conditions requires a special measuring device. As the infinite slope model is anticipated for the rapid failure of the active layer representing the mobile layer on the permafrost representing the immobile layer, the measuring device has to be based on this model. According to the infinite slope model it should allow plug-like movements of the active layer to be investigated. Slow plug-like movements are described as typical style of periglacial solifluction for high ice contents at the permafrost surface (Harris & Davies 1996). As solifluction is regarded as pre-failure strain by Harris et al. (1995) and therefore is important for the final rapid failure of the active layer, the required measuring device should also allow the investigation of these slow pre-failure processes. As the surface irregularities of the shear plane (i.e. the permafrost) are crucial for the frictional behavior and thus for shearing between the immobile and mobile layer, the device should allow the surface characteristics of the shear plane to be quantified. Furthermore it should allow the influence of water on slope stability to be studied, which requires inclined conditions (e.g. to induce water runoff). In addition, the inclination is necessary for a realistic simulation of slope failure in the laboratory, also taking into account surficial rolling (compare Onda & Matsukura 1997). Finally the measuring device should be suitable for testing not only fine material, but also gravel (which is typical for alpine scree slopes), although coarse material is not limiting slope stability under dry conditions. However, the grain size also influences the water balance, the effect of which on slope stability still is not sufficiently understood and was therefore investigated in this study.

3.2.2 Solution

To fulfill the requirements described above an inclinable shear box was developed (Figure 3.2). The upper frame (orange) of the shear box contains the simulated active layer, the lower frame (green) the simulated permafrost surface layer. The shear box itself is anchored onto a fixed array for the slope adjustment. The shear box can be inclined by lifting the rear end of the lower shear frame via a cable winch mounted on the fixed array. The upper shear frame is guided on the lower shear frame by rollers and therefore allows the simulated active layer to freely slide downslope on the simulated permafrost. As in the field, the shear stress is therefore induced by the weight of the active layer itself, in contrast to a horizontal shear box where shearing is induced by an external force applied to one of the shear frames (Kishida & Uesugi 1987). In a horizontal shear box the layer sheared off is pushed by the rear panel of the moving shear frame and therefore compressed in front of the rear panel. In contrast, the layer sheared off in an inclinable shear box is pulled downslope by its own weight and therefore compressed at the front panel of the moving shear frame. Whereas in conventional shear boxes homogenous material is tested, materials with different properties for the mobile and immobile layer kept by the shear frames were tested with the shear box used in this study. Instead of the term ‘internal friction angle‘ implying a homogenous material, the term ‘friction angle’ (between the active layer and the permafrost) is used in this study. By making the permafrost layer longer than the active layer by more than the maximum shear distance, the shear area between the two layers was kept constant during the whole experiment, which is not the case for a conventional shear box.

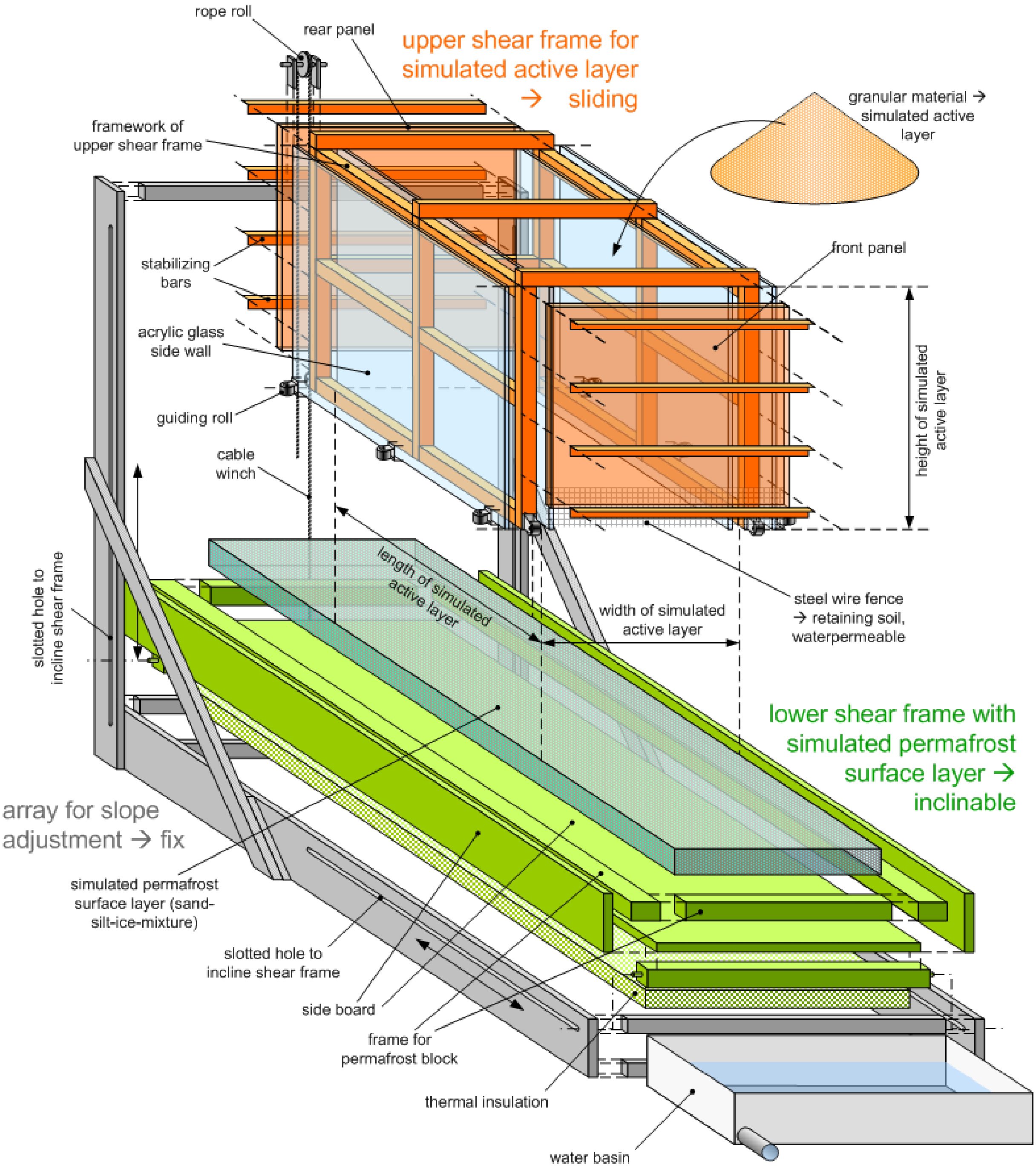

Figure 3.2: *Exploded sketch of the developed inclinable shear box.*

3.2.3 Construction

First the inclinable shear box was realized in the scale 1:5 relative to the active layer depth at the field study site (see chapter 2). On the basis of test experiments with this small shear box it was optimized and thereafter a big shear box on the scale of 1:2 could be built. The small shear box was used for the systematic 4-factorial screening shear test series in order to reduce the effort for the many single experiments (see below). For the physical simulation of a thaw-induced failure of the active layer the big shear box was used in order to operate under conditions as close to reality as possible and to reduce the impact of the measuring probes on the investigated processes.

3.3 Systematic 4-factorial screening shear test series

3.3.1 Methods of systematic shear test series

Experimental setup

The experiments were conducted in the climate chamber at SLF with the air temperature set at 1°C. The permafrost blocks used were produced in a cold chamber at an air temperature of -10°C. For the systematic 4-factorial screening shear test series the 1:5-shear box was used (Figure 3.3).

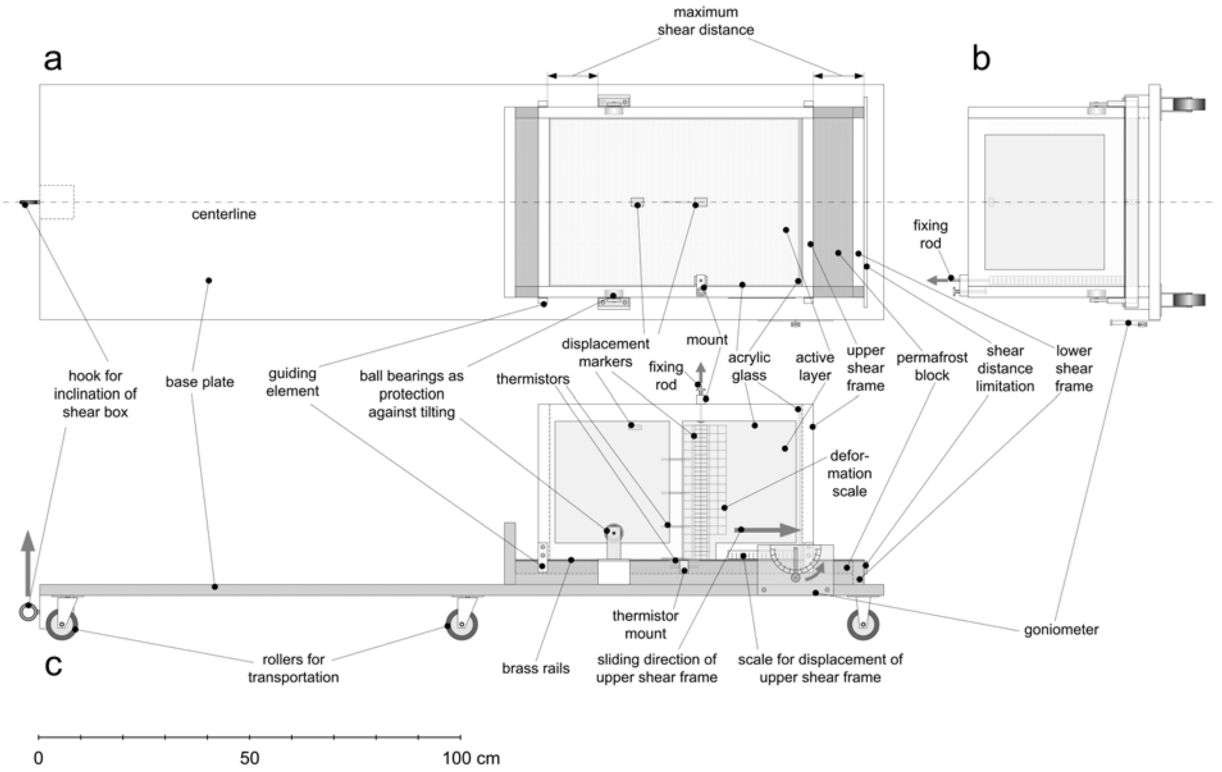

Figure 3.3: *1:5-shear box: a) plan view, b) front view, c) side view, base plate and lower shear frame as longitudinal section.*

The shear box itself is mounted on a wooden base plate with rollers underneath to enable easy transportation of the whole device. The lower immobile shear frame containing the artificial permafrost layer is 800 mm long, 400 mm wide and 33 mm deep (inner dimensions). The treated wooden boards are water resistant. The upper moveable shear frame is 585 mm long, 392 mm wide (inner dimensions) and filled with the granular material to be tested up to a height of 320 mm above the permafrost surface to simulate the active layer. Its framework is made of water resistant wooden beams and its walls consist of acrylic glass (4 mm thick) which allows the processes within the artificial active layer to be observed. The acrylic glass is 4 mm thick for the side and back walls, but 10 mm thick for the front wall, where the highest pressures develop. The joints in the inner edges of the upper frame are sealed with silicon. The upper shear frame is guided on the lower one by four plastic guiding elements attached onto the lower edges of the framework. The wooden beams of the upper shear frame can slide on brass rails mounted on top of the side walls of the lower shear frame to keep the sliding friction of the shear box itself low. Ball bearings fixed at the base plate allow a transversal sliding movement of the upper shear frame relative to the lower one, but prevent tilting between the two frames. The sliding movement of the upper shear frame is limited by the attachment of the ball bearings and a wooden cross beam mounted at the front of the lower shear frame.

Experimental parameters

The experimental parameters are divided into the parameter groups *constants*, *factors* and *resulting variables* (Table 3.2). Constants are parameters which were kept constant for all experiments. Factors are parameters which were varied between the different experiments. Resulting variables are parameters which were measured depending on factors.

Table 3.2: *Overview of experimental parameters.*

parameter group	parameter	notation	unit	value(s)	
constants	adhesive friction coefficient of shear box itself (without material to be tested)	f_{box}	-	determined	
	maximum shear distance of upper shear frame	$d_{AL\_col\_max}$	mm	120	
	initial volume of active layer (at beginning of experiment)	$V_{AL}(0h)$	l	73.4	
	initial volume of permafrost block (at beginning of experiment)	$V_{PF}(0h)$	l	10.6	
	ambient air temperature for cooling of permafrost block	$T_{air\_PF\_cool}$	°C	-10.0	
	set ambient air temperature during experiment	T_{air_set}	°C	1.0	
	initial temperature of active layer (at beginning of experiment)	$T_{AL}(0h)$	°C	1.0	
	initial surface temperature of permafrost layer (at beginning of experiment)	$T_{PF\_s}(0h)$	°C	-0.8	
factors	grain size of active layer	d_{AL}	mm	0-2 (sand)	0-22 (gravel)
	grain size of permafrost layer	d_{PF}	mm	0-0.5 (silty sand)	0-2 (sand)
	initial volumetric water content of active layer	$\theta_{AL}(0h)$	%	0	15
	degree of volumetric ice saturation of permafrost layer	S_{i_PF}	%	0	100
resulting variables	vertical distance of permafrost surface profile to reference level	y_{PF_s}	mm	measured	
	collective downslope displacement of upper shear frame as function of inclination angle	$d_{AL\_col}(\alpha)$	mm	measured	
	internal downslope displacement of active layer as function of depth (depth interval 10mm)	$d_{AL\_int}(z)$	mm	measured	
	friction angle between acitve layer and permafrost (inclinination angle at maximum shear distance)	Φ	°	measured	
	actual ambient air temperature during experiment as function of time	$T_{air\_act}(t)$	°C	measured	
	ground temperature of active layer (AL) and permafrost (PF) at depth z below AL/PF surface with z[mm] = 80, 160, 240, 320 for AL and 1, 15 for PF as function of time	$T_{AL/PF}(z,t)$	°C	measured	
	volumetric water content of active layer (AL) and permafrost (PF) at depth z below AL/PF surface with z[mm] = 0, 80, 160, 240, 320 for AL and 0-10, 10-33 for PF	$\theta_{AL/PF}(z)$	%	measured	

Constants

In order to calculate the error of the measured angles at which collective downslope displacement occurred and of the measured friction angle due to the friction of the shear box itself, its static friction coefficient had to be determined as a first constant. Therefore the empty shear box with the upper shear frame in its starting position was inclined by pulling up the end of the base plate with a hook using a manual winch until the upper shear frame started to slide downslope. Then the inclination angle was measured. To obtain a representative value this experiment was carried out 22 times. The static friction coefficient f_{box} could be determined using the average of the measured inclination angles φ; for φ the downslope force F_{D_box} equals the friction force F_{R_box} of the upper shear frame

$$F_{D\_box} = F_{R\_box} \tag{3.1}$$

$$m_{box} \cdot g \cdot \sin\varphi = f_{box} \cdot m_{box} \cdot g \cdot \cos\varphi$$

where m_{box} is the mass of the upper shear frame. Canceling and dividing by $\cos\varphi$ leads to

$$\tan\varphi = f_{box} \tag{3.2}$$

The maximum shear distance, i.e. the distance between the guiding elements of the upper shear frame and the constructive limitations (see experimental setup), could be adjusted by the starting position of the upper shear frame. As it was chosen to be 120 mm for all experiments, it is about a third of the total height of the shear box (upper and lower shear frame together). The volume of the permafrost block and the active layer could be changed during the experiment by settlement or dilation and abrasion. These volumes are therefore given as initial volumes at the beginning of the experiment in (Table 3.2). The temperature of the permafrost block and the active layer also varied during the experiment. The initial values are therefore given in table Table 3.2. To simulate summer conditions of maximum thaw depth at the potential shear plane (highest risk of active layer sliding failure), the ground temperatures were chosen to be close to the melting point (slightly positive for the active layer and slightly negative for the permafrost block). They were not chosen exactly at the melting point, because phase changes would have made it impossible to control the phase of the water in the active layer (liquid) and the permafrost (solid). In contrast to the ground temperatures the ambient air temperatures were kept constant - for cooling the permafrost block in the cold chamber at -10°C and during the experiment in the climate chamber at 1°C.

Factors

For each factor a high and a low value was chosen (Table 3.2). These two values are expected to span a wide, realistic range of field conditions. Therefore the maximum grain size of the coarse grained granular material (high value) for the active layer and the permafrost was chosen one order of magnitude higher than that of the fine grained granular material (high value). As the finer grains in the active layer tend to be washed out, but to be accumulated close to the permafrost surface, the maximum grain size of both values for the permafrost were chosen one order of magnitude smaller than the equivalent one of the active layer. Only dry granular material was used for the minimum possible value for the initial volumetric water content of the active layer as well as for the degree of volumetric ice saturation of the permafrost layer. The higher value for the initial volumetric water content of the active layer had to be limited to 15%, because this is roughly the field capacity of the gravel used in the experiments. A degree of volumetric ice saturation of 100% means that the whole pore space is filled with ice. Experiments with this value therefore represent conditions of saturated permafrost.

Permafrost surface profile

Among the resulting variables the permafrost surface profile was the only one which had to be measured without the active layer on top directly before each shearing experiment. The permafrost surface was scanned along the centerline of its longitudinal axis using a laser scanner constructed at SLF which was equipped with a micro laser sensor (NAIS, LM10) and driven by a step motor (Figure 3.4). The scanned section was 400 mm long and located in the middle of the 800 mm long permafrost surface. The horizontal resolution Δx of the laser scanner is 30 µm and the vertical resolution Δy 3.5 µm.

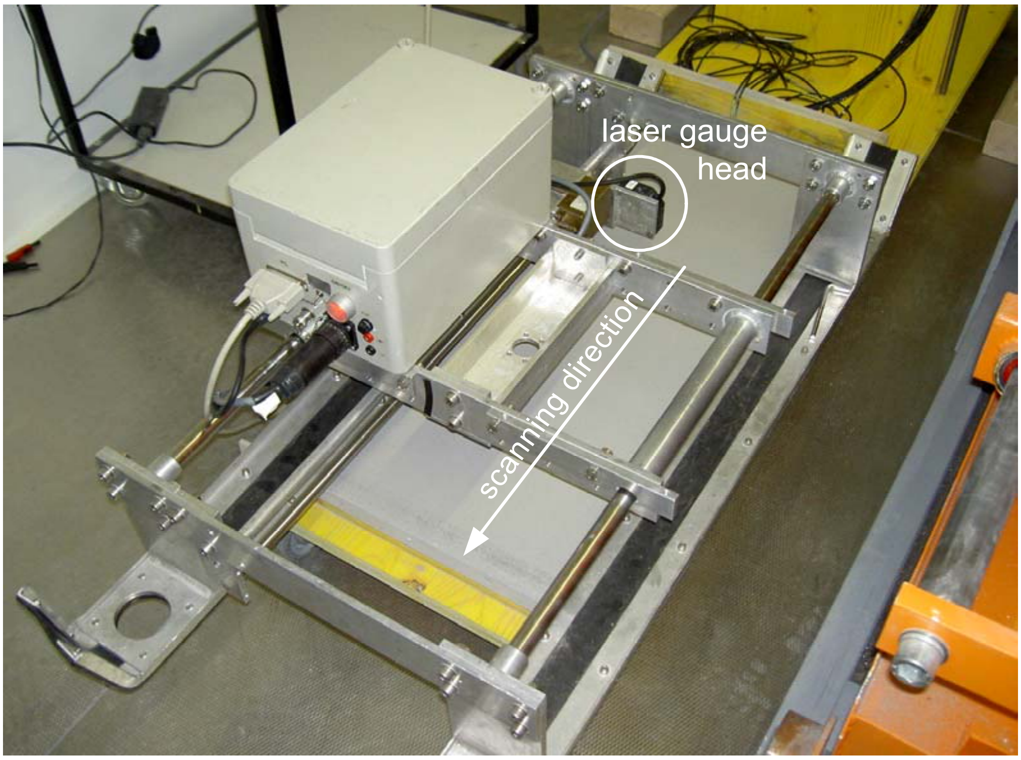

Figure 3.4: *Laser scanner to scan the surface profile of the permafrost block.*

In the following the processing of the scanned profile (raw data) of the permafrost surface is described. An example of the raw data obtained with the scanner is shown in Figure 3.5, where the y-axis represents the measured vertical distance y_{PF_s} between the laser gauge head and the actually scanned point of the permafrost surface and the x-axis the horizontal scanning distance.

In this scanning profile irregularities with different causes and at different scales are superimposed and have to be distinguished. There are irregularities which are due to the real surface itself, but also some which are caused by the measuring equipment. The latter ones had to be eliminated in order to extract the relevant information on the surface itself. The resulting profile was processed in a two-step filter in order to separate irregularities at different scales. One example of the processing of the measured profile is shown here.

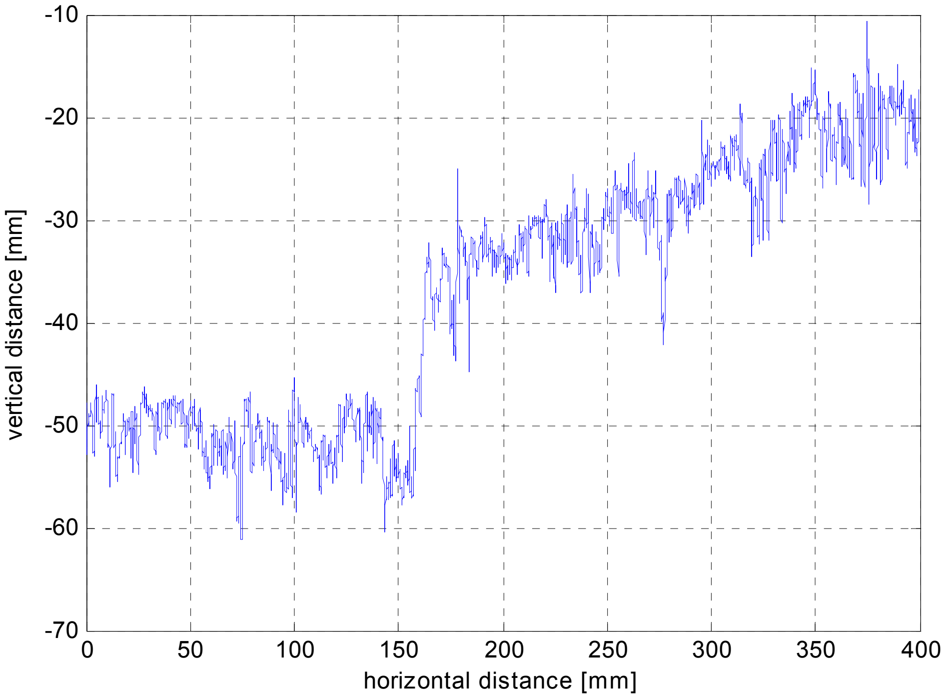

Figure 3.5: *Example of a measured profile (raw data) of the permafrost surface (replicate 1 of the systematic experiment no. 5 in the* 2^{4-1}*-experimental plan, using the laser scanner equipped with a micro laser sensor NAIS, LM10). The decrease of* y_{PF_s} *between about 150 mm and 170 mm horizontal distance as well as the declining trend thereafter is due to the measurement setup of the scanner but not to the real surface profile. This phenomenon occurred during each experiment.*

As the permafrost surface is scanned relative to the axis along which the laser head is moved, y_{PF_s} depends on the position of this reference level relative to the surface to be scanned (Rometsch & Letzner 1993). If the reference level is moved vertically during the scanning process or is not exactly parallel to the surface to be scanned, the measured curve for the profile shows irregularities, although they do not exist in the real surface profile.

As the seating of the laser scanner on the brass rails of the lower shear frame is quite small (Figure 3.4), the horizontal movement of the heavy step motor along the scanning direction could have led to small imbalances and therefore to vertical movements of the laser gauge head relative to the surface to be scanned. This is the first kind of irregularity caused by the measuring equipment. In the measured profile this kind of irregularity can be detected easily, because its wavelength is several orders of magnitude higher than those of the irregularities of the real surface profile. The abrupt increase of y_{PF_s} between about 150 mm and 170 mm horizontal distance in Figure 3.5 therefore can be ascribed to the measuring equipment. In the other experiments the irregularities caused by the measuring equipment also appeared in the same part of the scanned profile. To eliminate these types of irregularities for the further analysis, the equivalent section had to be cut out of the measured profile (Figure 3.6). In order to have the same total horizontal distance of the remaining profile for all single experiments the length of the cut out section had to be directed to the longest irregularity of all experiments. According to this criterion the longest possible horizontal distance of the remaining profile turned out to be about 280 mm. To attain a total analyzable horizontal profile distance l_t of 250 mm for the calculation of the surface parameters one wavelength of the rough filter (8 mm, see below) had to be added for each profile section. Thereby the sections should be as long as possible to attain highest representativity. As two sections were chosen, the total horizontal scanning distance had to be 266 mm (Figure 3.6).

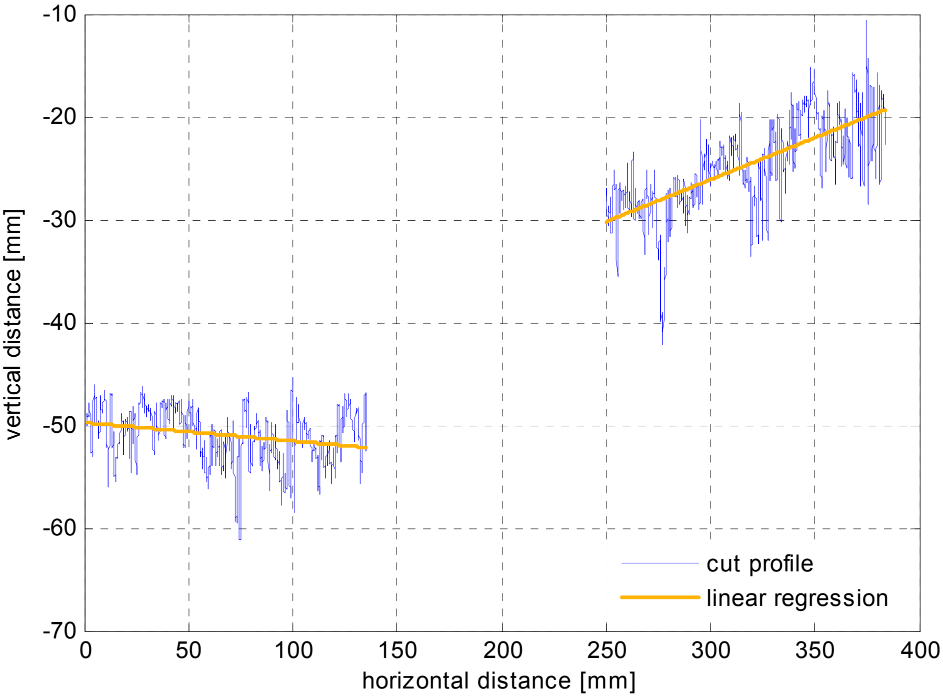

Figure 3.6: *Removal of sections with irregularities caused by vertical movements of the measuring equipment for the same example as shown in Figure 3.5. The straight lines are linear regressions of the remaining profile sections along which the profile is aligned in a next step.*

The second kind of irregularity caused by the measuring equipment arises when the reference level is not exactly parallel to the surface to be scanned. Its mechanical parallel alignment is very costly. It is much easier and more exact to do the parallel alignment numerically (Rometsch & Letzner 1993). According to these authors, the deviation of the measured from the real surface profile (due to the sloping position of the reference level relative to the scanned surface) is equal to the slope of the linear regression for the measured profile or profile section (Figure 3.6). To eliminate this kind of irregularity for the further analysis the equivalent profile section with an ideal profile consisting of a horizontal straight line had to be aligned along the linear regression line. The aligned profile (Figure 3.7) is

$$y_{PF\_a}(x) = y_{PF\_s}(x) - y_{lr}(x) \tag{3.3}$$

where $y_{lr}(x)$ is the linear regression line of the measured profile section and x the actual horizontal scanning distance.

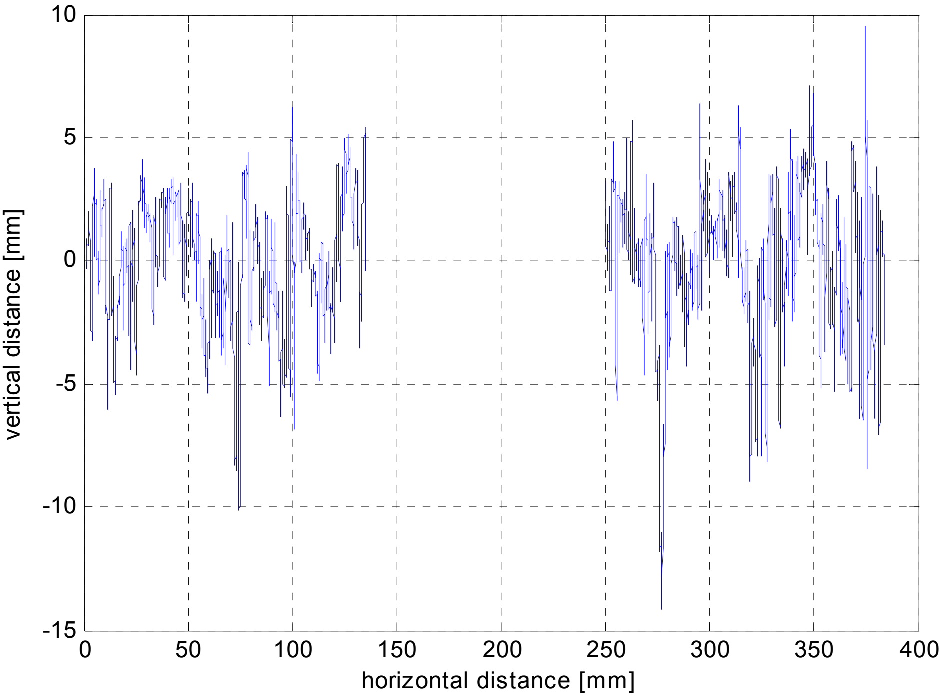

Figure 3.7: *Alignment of the profile sections along the equivalent linear regression lines for the same example as shown in Figure 3.5 and Figure 3.6. The aligned profile represents the real surface profile (at the scale of the scanning resolution) excluding the systematic errors induced by the measuring equipment.*

By aligning the measured profile sections along the linear regression lines the systematic errors caused by the measuring equipment is excluded. Therefore the aligned profile represents the real surface profile (at the scale of the scanning resolution).

Although the aligned profile is now unaffected by irregularities due to the measuring equipment, it is still a superposition of irregularities at different scales. In the metallurgy, where this technique is frequently used, the aligned profile is usually separated into irregularities at two scales. Thereby large scale irregularities are referred to as waviness and small scale ones as roughness (Rometsch & Letzner 1993). The separation of the waviness from the roughness is done by the application of a filter which is defined by a cut-off wavelength λ_c. The waviness profile $y_{PF\_wavy}(x)$ is filtered out of the aligned profile $y_{PF\_a}(x)$ by calculating the running mean using the cut-off wavelength as window size, i.e.

$$y_{PF\_wavy}(x) = \frac{1}{\lambda_c} \cdot \int_0^{\lambda_c} y_{PF\_a}(x)\, dx \tag{3.4}$$

The roughness profile is the difference between the aligned and the waviness profile, i.e.

$$y_{PF\_rough}(x) = y_{PF\_a}(x) - y_{PF\_wavy}(x) \tag{3.5}$$

In the present study this filtering method was used twice to process the aligned profile of the permafrost surface (Figure 3.8).

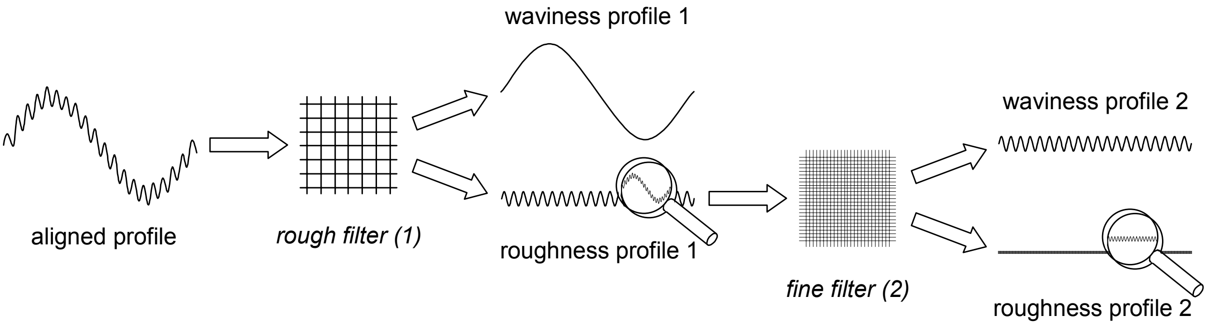

Figure 3.8: *Processing of the aligned profile. The cut-off wavelengths of the filters are* λ_{c1} = *8 mm for the rough filter (1) and* λ_{c2} = *0.8 mm for the fine filter (2).*

First the aligned profile was roughly filtered (1) using a cut-off wavelength of 8 mm in order to distinguish between the waviness of the whole permafrost surface and its roughness due to the granular material it consists of (Figure 3.9).

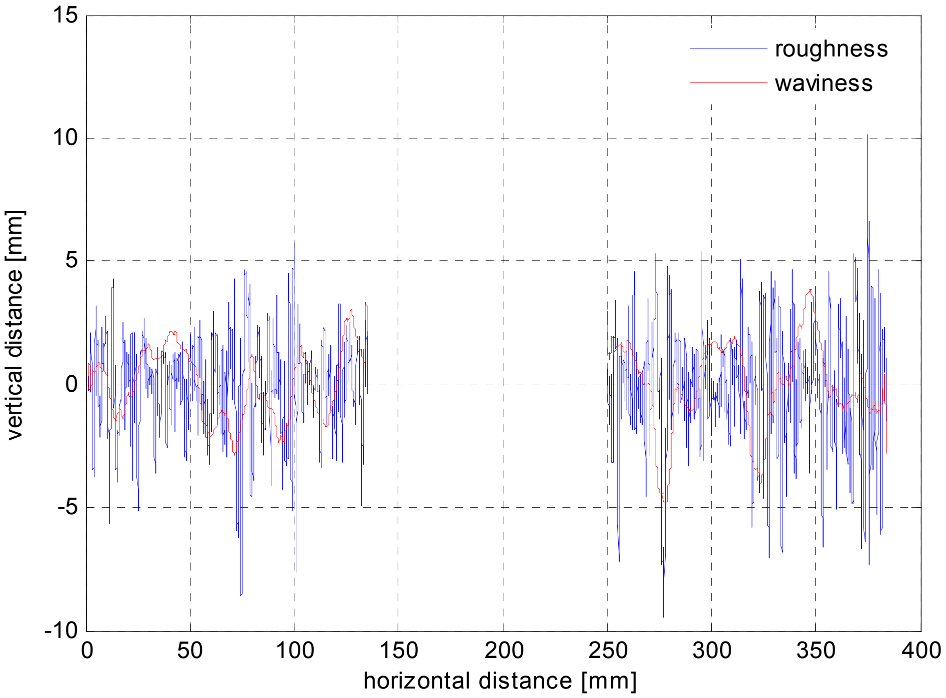

Figure 3.9: *Waviness and roughness extracted from the aligned profile (Figure 3.7) by rough filtering (1) using a wavelength of* λ_{c1} = *8 mm.*

Then the roughness profile 1 was finely filtered (2) using a wavelength of 0.8 mm (Figure 3.10). Thus, the two profiles extracted by filter 2 give the waviness and roughness of the permafrost surface at a scale one order of magnitude smaller than the profiles extracted by filter 1. The scale of the roughness profile 2 is in the range of the asperities of a sand grain's surface.

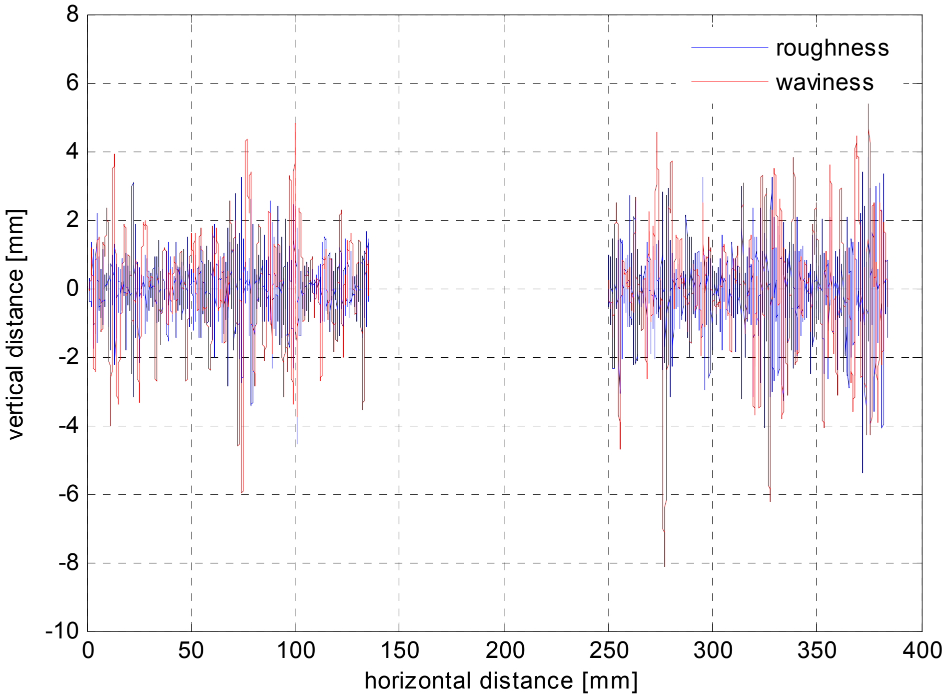

Figure 3.10: *Waviness and roughness extracted from the roughness profile 1 (Figure 3.9) by fine filtering (2) using a wavelength of* $\lambda_{c2} = 0.8$ *mm.*

As the permafrost surface was scanned by a laser scanner, the filters used to process the surface profile are phase correct according to the standard ISO 11562 (ISO 1996).

The aligned profile and the roughly and finely filtered waviness and roughness profiles form the base for the deduction of all surface parameters used for this study which are compiled in Table 3.3 and described below.

The parameters R_a, W_a, $R_{z(DIN)}$ and W_z have to be determined on the basis of a measuring length l_m five times the wavelength of the used filter by definition. In mechanical engineering this reference length is laid down by the standard ISO 4287 (ISO 1997) for all standardized surface parameters. To determine the surface parameters named above the mean of three single values was built, for which the three equivalent measuring lengths were distributed equally over the total analyzable horizontal profile distance l_t. All other surface parameters were determined on the basis of l_m equal to l_t to get values which are representative for the whole permafrost surface.

Table 3.3: *Surface parameters deduced from the aligned and filtered profiles, used for the quantitative description of the permafrost surface.*

surface parameter	**notation**	**unit**	**standard**
average roughness	R_a	mm	ISO 4287
average waviness	W_a	mm	-
average total roughness	$R_{z(DIN)}$	mm	ISO 4287
average total waviness	W_z	mm	-
root-mean-square roughness	R_q	mm	ISO 4287
root-mean-square waviness	W_q	mm	-
average peak roughness	R_{pm}	mm	ISO 4287
total waviness height	W_t	mm	VDI/VDE 2631 Sheet 6
average absolute slope	Δ_a	-	ISO 4287
angle of average absolute slope	ζ_a	°	-
root-mean-square average slope	Δ_q	-	ISO 4287
angle of root-mean-square average slope	ζ_q	°	-
average wavelength	λ_a	mm	ISO 4287
root-mean-square wavelength	λ_q	mm	ISO 4287
actual profile length	L_0	mm	ISO 4287
profile length ratio	l_r	-	ISO 4287
arithmetic mean (first moment) of amplitude distribution	m_1	mm	-
variance (second moment) of amplitude distribution	m_2	mm^2	-
skewness (third moment) of amplitude distribution	m_3	-	-
kurtosis (fourth moment) of amplitude distribution	m_4	-	-
macro bearing ratio	t_{pa}	%	ISO 4287
micro bearing ratio	t_{pi}	%	ISO 4287
maximum slope of bearing ratio curve	a_{max}	-	-
factor between maximum slopes of two bearing ratio curves	k	-	-

The average roughness R_a is the mean deviation of a roughness profile from its equivalent waviness profile. According to Rometsch & Letzner (1993) it is defined as

$$R_a = \frac{1}{l_m} \cdot \int_0^{l_m} \left| y_{PF\_rough}(x) \right| dx \tag{3.6}$$

It is easy to interpret but neither allows to differentiate between peaks and grooves nor between different profile forms. Analogously to R_a the average waviness W_a was defined for a waviness profile using y_{PF_wavy} instead of y_{PF_rough} in equation (3.6). Therefore it gives the mean deviation of a waviness profile from the center line of the aligned profile (i.e. from the linear regression line along which the measured profile was aligned).

To determine the average total roughness $R_{z(DIN)}$ of a roughness profile the measuring length l_m has to be divided into five equal sections each as long as the cut-off wavelength of the used filter. Out of each section the maximum difference z_i of y_{PF_rough} between a peak and the following valley is taken and the arithmetic mean of these five values is built. Thereby a peak has to be above, a valley below the center line. According to Rometsch & Letzner (1993) $R_{z(DIN)}$ therefore is

$$R_{z(DIN)} = \frac{1}{5} \cdot \sum_{i=1}^{5} z_i \tag{3.7}$$

This responds more sensitively to variations in the surface profile than R_a. Analogously to $R_{z(DIN)}$ the average total waviness W_z was defined for a waviness profile.

The root-mean-square roughness R_q is the mean square deviation of a roughness profile from its equivalent waviness profile. According to Rometsch & Letzner (1993) it is defined as

$$R_q = \sqrt{\frac{1}{l_m} \cdot \int_0^{l_m} {y_{PF\_rough}}^2(x)\, dx} \tag{3.8}$$

As y_{PF_rough} is squared for the calculation of R_q, it responds more sensitively to variations in the surface profile than R_a. R_q equals the standard deviation of the profile's amplitude distribution. This parameter is therefore important for the statistical analysis of the surface profile, i.e. for the calculation of the second, third and fourth momentum of the amplitude distribution (see below). Analogously to R_q the root-mean-square waviness W_q was defined for a waviness profile using y_{PF_wavy} instead of y_{PF_rough} in equation (3.8).

For the determination of the average peak roughness R_{pm} of a roughness profile five wavelengths following each other are used analogously to the determination of $R_{z(DIN)}$. However, instead of the maximum difference z_i between a peak and the following groove the value of the highest peak p_i of y_{PF_rough}, i.e. its distance to the center line, is taken out of each wavelength to determine R_{pm}. According to Rometsch & Letzner (1993) R_{pm} is the arithmetic mean of the five peak values p_i. Therefore the equation for R_{pm} is

$$R_{pm} = \frac{1}{5} \cdot \sum_{i=1}^{5} p_i \tag{3.9}$$

The ratio $R_{pm}/R_{z(DIN)}$ allows to distinguish different profile shapes. Values for $R_{pm}/R_{z(DIN)}$ lower than 0.5 indicate rounded profile shapes, those higher than 0.5 sharp ones.

The total waviness height W_t is the only standardized parameter for a waviness profile. According to Rometsch & Letzner (1993) it is defined as the difference between the highest crest $y_{PF\_wavy\_max}$ and the lowest valley $y_{PF\_wavy\_min}$ of a waviness profile, thus

$$W_t = y_{PF\_wavy\_\max} - y_{PF\_wavy\_\min} \tag{3.10}$$

This parameter is suitable to control production processes, in this case the production of the permafrost block. To have similar conditions for the whole shear test series W_t of the waviness profile 1 should not vary significantly between the experiments.

The average absolute slope Δ_a and the root-mean-square average slope Δ_q of the profile is standardized for a roughness profile only. However, in this study it was also applied to waviness profiles. If Δ_a or Δ_q originates from a roughness or a waviness profile is indicated by the indices 'rough' or 'wavy'. According to Rometsch & Letzner (1993) the average absolute slope is defined as

$$\Delta_a = \frac{1}{n} \cdot \sum_{i=1}^{n} \left| \frac{y_{PF}(x_{i+1}) - y_{PF}(x_i)}{\Delta x} \right| \tag{3.11}$$

and the root-mean-square average slope as

$$\Delta_q = \sqrt{\frac{1}{n} \cdot \sum_{i=1}^{n} \left(\frac{y_{PF}(x_{i+1}) - y_{PF}(x_i)}{\Delta x} \right)^2} \tag{3.12}$$

where $y_{PF}(x)$ is the ordinate of the roughness or waviness profile, n the number of ordinates and Δx the difference between x_{i+1} and x_i which equals the horizontal resolution of the laser scanner. Δ_q responds more sensible to extreme values, because the slope of each interval is squared before calculating the mean. The higher the values for Δ_a and Δ_q, the sharper the peaks are.

As an angle is easier to be imagined than a relation of lengths, the equivalent angles for Δ_a and Δ_q were calculated additionally. The angle of the average absolute slope is

$$\varsigma_a = \arctan \Delta_a \tag{3.13}$$

and that of the root-mean-square average slope

$$\varsigma_q = \arctan \Delta_q \tag{3.14}$$

The average wavelength λ_a of the profile gives the mean distance between two local peaks or valleys in the profile. It indicates the scale of the considered surface irregularities. The equivalent root-mean-square wavelength is called λ_q. According to Rometsch & Letzner (1993) these parameters are defined as

$$\lambda_a = 2\pi \cdot \frac{R_a}{\Delta_a} \tag{3.15}$$

and

$$\lambda_q = 2\pi \cdot \frac{R_q}{\Delta_q} \tag{3.16}$$

The actual profile length L_0 gives the length of the profile after it had been stretched to become horizontal. It is calculated as

$$L_0 = \sum_{i=1}^{n} \sqrt{\left(y_{PF}(x_{i+1}) - y_{PF}(x_i)\right)^2 + \Delta x^2} \tag{3.17}$$

The ratio between L_0 and l_m is called profile length ratio l_r. The higher l_r, the more the surface is fissured.

The following statistical surface parameters are based on the amplitude distribution of the profile, where the amplitude is the profile ordinate $y_{PF}(x)$. The amplitude distribution was calculated for the aligned profile and the roughness profiles 1 and 2 using 100 profile ordinate classes (Figure 3.11).

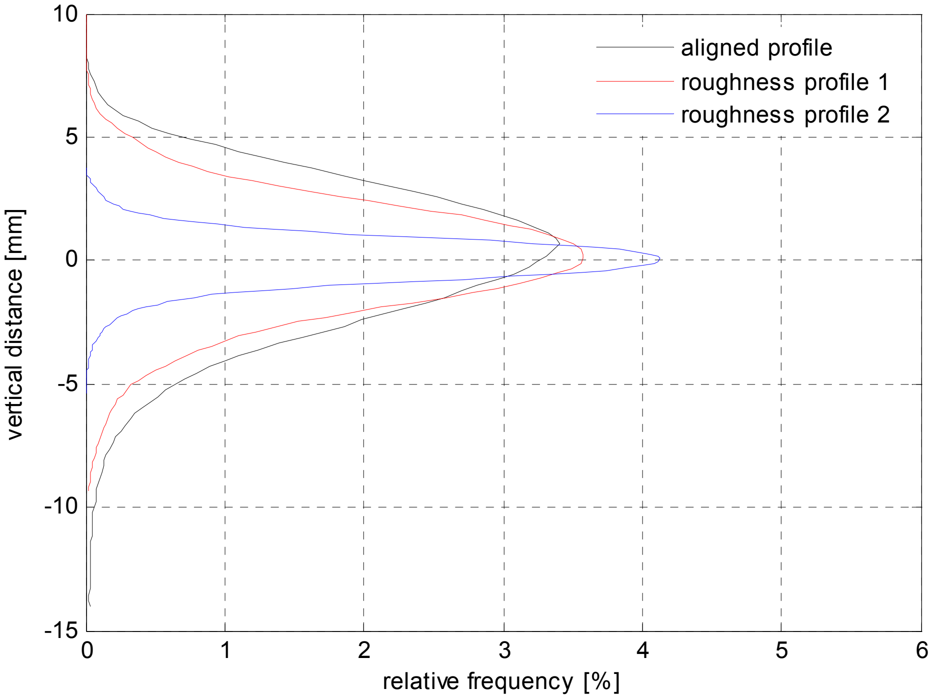

Figure 3.11: *Amplitude distribution of the aligned profile and the roughness profiles 1 (λ_{c1} = 8 mm) and 2 (λ_{c2} = 0.8 mm) for the same example as shown in Figure 3.7, Figure 3.9 and Figure 3.10.*

The properties of the amplitude distribution are mathematically defined by moments. They were calculated according to Rometsch & Letzner (1993). The first momentum m_1 is the arithmetic mean of the profile. It is defined as

$$m_1 = \frac{1}{n} \cdot \sum_{i=1}^{n} y_{PF\_i} \tag{3.18}$$

where n is the number of profile ordinate classes. As m_1 of an aligned and a filtered profile equals zero by definition the absolute value of y_{PF} instead of y_{PF} itself was used. Therefore

$$\lim_{n \to \frac{l_m}{\Delta x}} |m_1| = R_a \tag{3.19}$$

The second momentum m_2 of the amplitude distribution is the variance of the amplitude. It is defined as

$$m_2 = \frac{1}{n} \cdot \sum_{i=1}^{n} \left(y_{PF\_i}\right)^2 \tag{3.20}$$

and therefore

$$\lim_{n \to \frac{l_m}{\Delta x}} m_2 = R_q^{\ 2} \tag{3.21}$$

The third momentum m_3 is the skewness which describes the symmetry of the amplitude distribution curve relative to the center line of the profile. It is defined as

$$m_3 = \frac{1}{R_q^{\ 3}} \cdot \frac{1}{n} \cdot \sum_{i=1}^{n} \left(y_{PF\_i}\right)^3 \tag{3.22}$$

Negative skewness values mean that the material is concentrated near the upper edge of the surface profile.

The fourth momentum m_4 is the kurtosis which describes the sharpness of the amplitude distribution curve. It is defined as

$$m_4 = \frac{1}{R_q^{\ 4}} \cdot \frac{1}{n} \cdot \sum_{i=1}^{n} \left(y_{PF\_i}\right)^4 \tag{3.23}$$

The sharper the amplitude distribution curve, the wider and sharper the peaks and valleys of the profile.

To quantify the profile shape the macro bearing ratio t_{pa} (for the aligned profile) and the micro bearing ratio t_{pi} (for the roughness profile) are important. For their determination a horizontal intersection line is laid through the profile at a profile depth y according to Rometsch & Letzner (1993). The stretches where the intersection line cuts the profile are added and give the intersection length l_{isa} for the aligned profile and l_{isi} for the roughness profile. The ratio between l_{isa} or l_{isi} and the measuring length l_m is the macro material content t_{pa} or the micro material content t_{pi}. The determination of t_{pa} and t_{pi} as a function of the depth y of the intersection line leads to the bearing ratio curve or Abbott-curve of the aligned profile

$$t_{pa}(y) = \frac{l_{isa}(y)}{l_m} \tag{3.24}$$

and the roughness profile

$$t_{pi}(y) = \frac{l_{isi}(y)}{l_m} \tag{3.25}$$

The bearing ratio curve is the cumulated sum of the amplitude distribution curve. It was calculated for the aligned profile and the roughness profiles 1 and 2 (Figure 3.12).

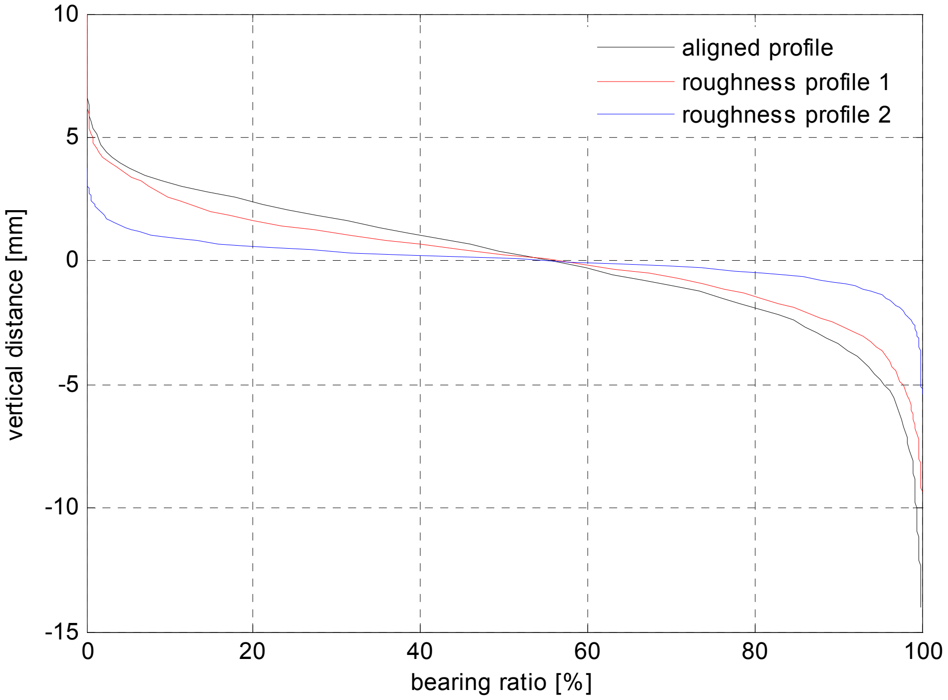

Figure 3.12: *Bearing ratio curves or Abbott-curves of the aligned profile and the roughness profiles 1 (λ_{c1} = 8 mm) and 2 (λ_{c2} = 0.8 mm). They are the cumulative sum curves of the amplitude distribution functions shown in Figure 3.11.*

The maximum change of the bearing ratio with depth, i.e. the maximum slope a_{max} of the bearing ratio curve depending on the vertical distance of the profile, was determined using an interval I of 1% of the total profile depth (a_{max_1} for small variations) and 40% (a_{max_40} for a running mean). The maximum slope is

$$a_{\max\_I} = \max\left(\frac{t_{pa}(y_{i+I}) - t_{pa}(y_i)}{y_{i+I} - y_i}\right) \tag{3.26}$$

with i running from 1 to 100. a_{max_I} was determined for the aligned profile and the roughness profile 1 and 2. In order to compare the bearing ratio curves of the different profiles for both intervals the factor k between the maximum slope of the aligned and the roughness profile 1 ($k_{a\_r1\_I}$), the aligned and the roughness profile 2 ($k_{a\_r2\_I}$) and between the roughness profile 1 and 2 ($k_{r1\_r2\_I}$) was calculated.

Collective downslope displacement

The collective downslope displacement of the upper shear frame, i.e. the active layer as a whole, as a function of the inclination angle was measured in two different ways for the two experiment series (see below). In addition to the data itself, this procedure allowed the two methods to be compared. In the first experiment series the active layer downslope displacement and the equivalent inclination angle were measured manually after each visible surge of the upper shear frame. In the second experiment series the downslope displacement and the equivalent angle were recorded continuously with a video camera. To avoid a parallax error the video camera was mounted on a cantilever fixed at the base plate and oriented perpendicular to the goniometer and the reference scale (Figure 3.13). When the downslope displacement equaled the maximum shear displacement, the experiment was terminated.

In addition to the downslope force F_{D_AL} and the friction force F_{R_AL} of the active layer the upper shear frame induces a downslope force F_{D_box} and a friction force F_{R_box}. These interfering forces modify the inclination angle α_0 at which the active layer would have undergone the collective downslope displacement $d_{AL\_col}(\alpha_0)$ without the influence of the upper shear frame. However, only the modified inclination angle α_m is measurable. The modification of α_0 depends on the distribution of the weight of the active layer and the upper shear frame over the friction area and therefore on the internal forces between the active layer and the upper shear frame. As these internal forces and therefore the weight distribution over the friction area is unknown, a plausible special case of the weight distribution had to be assumed. Using this special case the inclination angle α_0 for a collective downslope displacement which is only due to the active layer without the influence of the upper shear frame could be calculated. Before α_0 had been determined for two *extreme* cases to give the possible range of α_0.

In the first extreme case the total weight (active layer and upper shear frame) bears on the contact area between the active layer and the permafrost A_{AL}. α_0 could be determined by building the balance between the downslope force and the friction force

$$F_D = F_R \tag{3.27}$$

$$(m_{AL} + m_{box}) \cdot g \cdot \sin\alpha_0 = f_{AL} \cdot (m_{AL} + m_{box}) \cdot g \cdot \cos\alpha_0 \qquad |: \cos\alpha_0$$

$$\tan\alpha_0 = f_{AL}$$

$$\tan\alpha_0 = \tan\alpha_m$$

$$\alpha_0 = \alpha_m$$

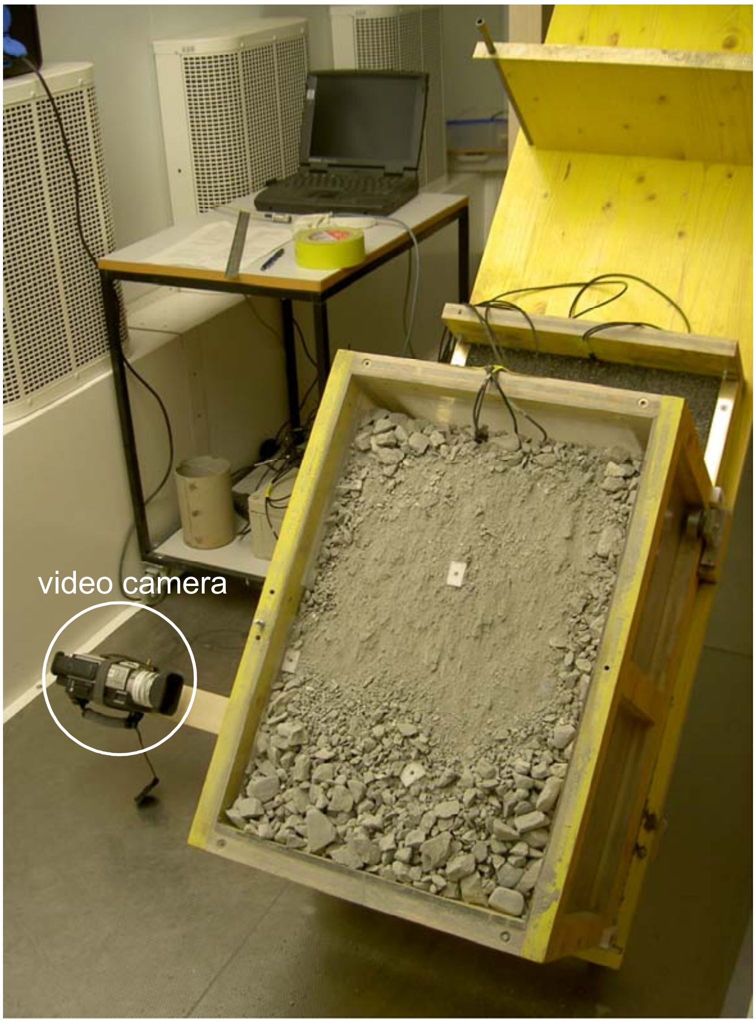

Figure 3.13: *Video camera mounted on a cantilever fixed at the base plate of the shear box to measure the downslope displacement of the upper shear frame as a function of the angle of inclination continuously.*

In the second extreme case the total weight bears on the contact area between the brass rails and the upper shear frame A_{box}. As the static friction coefficient of the upper shear frame f_{box} is independent on the weight, α_0 equals the friction angle of the upper shear frame φ.

Whereas these two extremes are unlikely to occur, a regular weight distribution over A_{AL} and A_{box} is a plausible assumption. The balance of forces in the moment of downslope displacement for this special case is

$$(m_{AL} + m_{box}) \cdot g \cdot \sin\alpha_m = (m_{AL} + m_{box}) \cdot g \cdot \cos\alpha_m \cdot \left(f_{AL} \cdot \frac{A_{AL}}{A_{AL} + A_{box}} + f_{box} \cdot \frac{A_{box}}{A_{AL} + A_{box}} \right)$$

After canceling, dividing by $\cos\alpha_m$ and substituting $A_{AL} + A_{box}$ by A_{tot} the equation becomes

$$\tan\alpha_m = f_{AL} \cdot \frac{A_{AL}}{A_{tot}} + f_{box} \cdot \frac{A_{box}}{A_{tot}} \qquad (3.28)$$

Without the modifying influence of the upper shear frame the balance of forces for an inclination angle α_0 would be

$$m_{AL} \cdot g \cdot \sin\alpha_0 = f_{AL} \cdot m_{AL} \cdot g \cdot \cos\alpha_0$$

After canceling and dividing by cosα_0 the equation becomes

$$\tan\alpha_0 = f_{AL} \tag{3.29}$$

Now α_0 can be determined depending on α_m by inserting (3.29) in (3.28)

$$\tan\alpha_m = \tan\alpha_0 \cdot \frac{A_{AL}}{A_{tot}} + f_{box} \cdot \frac{A_{box}}{A_{tot}}$$

Replacing f_{box} by tanφ and solving the equation by α_0 results in

$$\alpha_0 = \arctan\left(\tan\alpha_m \cdot \frac{A_{tot}}{A_{AL}} - \tan\varphi \cdot \frac{A_{box}}{A_{AL}} \right) \tag{3.30}$$

Internal downslope displacement

The internal downslope displacement of the active layer as a function of the depth is equivalent to the vertical deformation profile of the active layer within the upper shear frame. It was measured with a column of displacement markers positioned within the active layer behind the transparent side wall and 340 mm distant from the back wall of the upper shear frame (Figure 3.3). This method is based on the visualization of solifluction by a column of tiles within the tested soil in laboratory experiments effected by Harris & Davies (1996) and Harris et al. (1996). The single displacement markers have a length of 30 mm, a width of 20 mm and a height of 10 mm, which therefore determines the vertical resolution of the deformation profile with active layer depth. To keep the friction between the deformation markers themselves and with the acrylic glass wall low, they were made of Teflon. A straight alignment of the column was obtained by drilling a hole in the centre of each displacement marker, allowing them to be spiked along a rigid metal rod. This rod with the displacement markers spiked on it was placed perpendicular to the permafrost surface and fixed to the upper shear frame with a mount. After filling the upper shear frame with the active layer material, the rod could be pulled out carefully without moving the displacement markers. At the end of the experiment the displacement of each marker relative to the upper shear frame could be read off by means of a deformation scale attached to the side wall of the upper shear frame (Figure 3.3).

Friction angle between active layer and permafrost

The friction angle between the active layer and the permafrost is the key resulting variable in this study. It is the inclination angle (after correction, see below) at the maximum shear distance and was measured with a manual goniometer. The resolution of its scale was 1 degree; however, the angle could be read off to approximately 0.1 degrees by estimating the position of the goniometer needle between two scale dashes indicating degree units. Due to the modifying effect of the upper shear frame on the inclination angle the friction angle had to be corrected in the same way as all other inclination angles for which a collective downslope displacement occurred. So this correction was done by using equation (3.30).

Air and ground temperature

Before and during the experiment the temperature was measured in the active layer and the permafrost at six depths below the surface of the active layer and additionally in the air to control the set value (Table 3.2). Thermistors were used (Campbell Scientific, thermistor 107) with a resolution of 0.1°C. Their steel capsules have a diameter of 5 mm and a length of 70 mm. They were initially calibrated in a snow-water mixture at 0°C. Temperatures were recorded with a data logger (Campbell Scientific CR10X) at 10 second intervals. All thermistors were embedded horizontally in the middle of the long axis of the permafrost or the active layer and oriented in a vertical plane through the centerline of the device. The two thermistors in the permafrost were fixed with a mount screwed on the bottom of the lower shear frame in its middle (Figure 3.3) to avoid their displacement during the fabrication of the permafrost layer. As the water in the middle of the permafrost block freezes last during its fabrication, one thermistor was placed at about half of the height of the permafrost in order to control when the block was completely frozen. To control the temperature just below the permafrost surface, but to avoid an influence on its frictional conditions, another thermistor was placed with its upper edge 1 mm below this plane. Four thermistors were embedded in the active layer during filling of the upper shear frame at regular distances of 80 mm with the lowest on top of the permafrost surface.

Volumetric water content

After each experiment samples of at least 300 g were taken from the granular material in order to determine its volumetric water content. In the active layer five samples were taken at regular distances of 80 mm with the lowest just above the permafrost surface. In the experiments with dry permafrost ($S_{i\_PF} = 0\%$) samples were taken from each visibly distinguishable layer, i.e. wetted or dry. The depth of the equivalent interface between these layers - if existing - turned out to be 330 mm below the active layer surface. After the probe extraction they were weighed (wet soil mass), dried in the oven at 105°C until the minimum possible water content at this temperature was reached and weighed again (dry soil mass). Then the gravimetric water content could be calculated as

$$\theta_g = \frac{m_{s\_wet} - m_{s\_dry}}{m_{s\_dry}} \tag{3.31}$$

where m_{s_wet} is the wet soil mass and m_{s_dry} the dry soil mass of the probe. With the apparent soil density ρ_s and the density of water ρ_w the volumetric water content could then be calculated as

$$\theta_v = \theta_g \cdot \frac{\rho_s}{\rho_w} \tag{3.32}$$

Experimental design

In order to statistically determine the influence of factors on resulting variables in an efficient manner (each experiment required moving about 900 kg of material and was therefore highly time-consuming), an experimental design had to be elaborated. Investigating four factors at two values (steps) each results in a total number of $2^4 = 16$ possible factor-step combinations.

Complete factorial 2^4-experimental design

A systematic order of these factor step combinations, using -1 for the low step and 1 for the high step of a factor, leads to a complete factorial 2^4-experimental design according to Kleppmann (2003) (Table 3.4).

For each factor there are eight pairs of factor-step combinations which only differ in the considered factor. For each of these pairs the difference of the equivalent mean values (of n repetitions) for the resulting variable can be calculated. The mean of these differences is a measure for the influence of the considered factor on the resulting variable and is called the effect. It is calculated as the sum of each mean value for the resulting variable multiplied by the equivalent factor-step divided by eight (for 16 factor step combinations; in general division by half of the number of factor-step combinations). The mean of single variances s^2 is calculated analogue to the effects but without multiplication by a factor-step.

Table 3.4: *Complete factorial 2^4-experimental design according to Kleppmann (2003). It consists of 16 factor-step combinations derived from four factors and two steps for each factor. Each factor-step combination has a systematic experiment number (syst. exp. no.). For four factors six twofold interactions between factors, four threefold and one fourfold are possible. γ_i is the mean, s_i^2 the variance of n single measuring values of the i^{th} factor step combination (row). s^2 is the mean of the single variances. '-1' denotes the low step (value) of a factor, '1' the high one.*

syst. no.	**factors**				**interactions**											**resulting variable**	
i	A	B	C	D	AB	AC	AD	BC	BD	CD	ABC	ABD	ACD	BCD	ABCD	γ_i	s_i^2
1	-1	-1	-1	-1	1	1	1	1	1	1	-1	-1	-1	-1	1	γ_1	s_1^2
2	1	-1	-1	-1	-1	-1	-1	1	1	1	1	1	1	-1	-1	γ_2	s_2^2
3	-1	1	-1	-1	-1	1	1	-1	-1	1	1	1	-1	1	-1	γ_3	s_3^2
4	1	1	-1	-1	1	-1	-1	-1	-1	1	-1	-1	1	1	1	γ_4	s_4^2
5	-1	-1	1	-1	1	-1	1	-1	1	-1	1	-1	1	1	-1	γ_5	s_5^2
6	1	-1	1	-1	-1	1	-1	-1	1	-1	-1	1	-1	1	1	γ_6	s_6^2
7	-1	1	1	-1	-1	-1	1	1	-1	-1	-1	1	1	-1	1	γ_7	s_7^2
8	1	1	1	-1	1	1	-1	1	-1	-1	1	-1	-1	-1	-1	γ_8	s_8^2
9	-1	-1	-1	1	1	1	-1	1	-1	-1	-1	1	1	1	-1	γ_9	s_9^2
10	1	-1	-1	1	-1	-1	1	1	-1	-1	1	-1	-1	1	1	γ_{10}	s_{10}^2
11	-1	1	-1	1	-1	1	-1	-1	1	-1	1	-1	1	-1	1	γ_{11}	s_{11}^2
12	1	1	-1	1	1	-1	1	-1	1	-1	-1	1	-1	-1	-1	γ_{12}	s_{12}^2
13	-1	-1	1	1	1	-1	-1	-1	-1	1	1	1	-1	-1	1	γ_{13}	s_{13}^2
14	1	-1	1	1	-1	1	1	-1	-1	1	-1	-1	1	-1	-1	γ_{14}	s_{14}^2
15	-1	1	1	1	-1	-1	-1	1	1	1	-1	-1	-1	1	-1	γ_{15}	s_{15}^2
16	1	1	1	1	1	1	1	1	1	1	1	1	1	1	1	γ_{16}	s_{16}^2
Σ	$\Sigma A_i\gamma_i$	$\Sigma B_i\gamma_i$	$\Sigma C_i\gamma_i$	$\Sigma D_i\gamma_i$	$\Sigma AB_i\gamma_i$	$\Sigma AC_i\gamma_i$	$\Sigma AD_i\gamma_i$	$\Sigma BC_i\gamma_i$	$\Sigma BD_i\gamma_i$	$\Sigma CD_i\gamma_i$	$\Sigma ABC_i\gamma_i$	$\Sigma ABD_i\gamma_i$	$\Sigma ACD_i\gamma_i$	$\Sigma BCD_i\gamma_i$	$\Sigma ABCD_i\gamma_i$		Σs_i^2
effect	$\Sigma_A/8$	$\Sigma_B/8$	$\Sigma_C/8$	$\Sigma_D/8$	$\Sigma_{AB}/8$	$\Sigma_{AC}/8$	$\Sigma_{AD}/8$	$\Sigma_{BC}/8$	$\Sigma_{BD}/8$	$\Sigma_{CD}/8$	$\Sigma_{ABC}/8$	$\Sigma_{ABD}/8$	$\Sigma_{ACD}/8$	$\Sigma_{BCD}/8$	$\Sigma_{ABCD}/8$	s^2 =	$\Sigma s_i^2/8$

An interaction between two or more factors implies that the effect of a factor is influenced by the other factors. If each interaction (column) for each systematic number (row) is assigned to the product of the equivalent factor steps, the effect of each interaction on the resulting variable can be calculated analogue to the effect of a factor (Kleppmann 2003).

In order to evaluate the significance of the effects, they have to be compared with the (positive) confidence interval

$$\delta = t \cdot s_d \tag{3.33}$$

at different confidence levels, where t is the critical value of the student-distribution and s_d the standard deviation of the effects. The t-values can be taken from statistic tables or software depending on the degree of freedom and the confidence level. The degree of freedom is

$$f = m \cdot (n-1) \tag{3.34}$$

where m is the number of factor step combinations and n the sample size. The standard deviation of the effects is

$$s_d = \sqrt{\frac{4}{m \cdot n} \cdot s^2} \tag{3.35}$$

where s^2 is the mean of the single variances. If the absolute value of the effect is at least as high as the confidence interval, then the effect will be significant at the considered confidence level.

To be able to calculate the variances the sample size has to be a least two. The total number of single tests in the whole series, i.e. the experiment size is

$$N = m \cdot n \tag{3.36}$$

The experiment size of a complete factorial 2^4-experimental design would therefore be 32. In order to reduce the experiment size a fractional factorial or screening experiment design was used instead of a complete factorial one and is described below.

Fractional factorial experiment design

The principle of a fractional factorial experiment design is to substitute a manifold (at least threefold) interaction by a further factor. Thereby the number of factor-step combinations remains constant, while the number of factors is increased. If the effect of the threefold interaction ABC in a complete factorial 2^3-experimental design (Table 3.5, left) is not significant and therefore negligible, a further factor D can be analyzed instead.

With the substitutions ABC → D and -ABC → D the two possible fractional factorial 2^{4-1}-experimental designs (or briefly 2^{4-1}-design) are built (Table 3.5, middle). Each of them consists of eight factor-step combinations selected from the complete factorial 2^4-experimental design (or 2^4-design; Table 3.5, right). The selection is made in such a manner that the four dimensional experimental space is covered as homogenously as possible. In the shear test series of this study factor A is the grain size of the active layer d_{AL}, B the initial volumetric water content of the active layer θ_{AL_0}, C the grain size of the permafrost layer d_{PF} and D the degree of volumetric ice saturation of the permafrost layer S_{i_PF}. In order to include the factor-step combination of dry sand in the active layer and ice free sand in the permafrost as a reference case to be compared with other studies, the 2^{4-1}-design resulting from the substitution -ABC → D was chosen.

Table 3.5: *Conversion of a complete factorial 2^3-experimental design (left) into the two possible fractional factorial 2^{4-1}-experimental designs (centre). Each of them consists of eight factor-step combinations from the complete factorial 2^4-experimental design (right) marked in the equivalent shading. (According to Kleppmann 2003).*

2^3-experimental design							
syst. no.	factors/effects						
i_2^3	A	B	C	AB	AC	BC	ABC
1	-1	-1	-1	1	1	1	-1
2	1	-1	-1	-1	-1	1	1
3	-1	1	-1	-1	1	-1	1
4	1	1	-1	1	-1	-1	-1
5	-1	-1	1	1	-1	-1	1
6	1	-1	1	-1	1	-1	-1
7	-1	1	1	-1	-1	1	-1
8	1	1	1	1	1	1	1

substitution
ABC → D

2^{4-1}-experimental design				
substitution ABC → D				
syst. no.	factors/effects			
i_2^{4-1}	A	B	C	D
1	-1	-1	-1	-1
2	1	-1	-1	1
3	-1	1	-1	1
4	1	1	-1	-1
5	-1	-1	1	1
6	1	-1	1	-1
7	-1	1	1	-1
8	1	1	1	1

substitution
-ABC → D

2^{4-1}-experimental design				
substitution -ABC → D				
syst. no.	factors/effects			
i_2^{4-1}	A	B	C	D
1	-1	-1	-1	1
2	1	-1	-1	-1
3	-1	1	-1	-1
4	1	1	-1	1
5	-1	-1	1	-1
6	1	-1	1	1
7	-1	1	1	1
8	1	1	1	-1

2^4-experimental design						
syst. no.			factors/effects			
i_2^4	i_2^{4-1}		A	B	C	D
	ABC → D	-ABC → D				
1	1	-	-1	-1	-1	-1
2	-	2	1	-1	-1	-1
3	-	3	-1	1	-1	-1
4	4	-	1	1	-1	-1
5	-	5	-1	-1	1	-1
6	6	-	1	-1	1	-1
7	7	-	-1	1	1	-1
8	-	8	1	1	1	-1
9	-	1	-1	-1	-1	1
10	2	-	1	-1	-1	1
11	3	-	-1	1	-1	1
12	-	4	1	1	-1	1
13	5	-	-1	-1	1	1
14	-	6	1	-1	1	1
15	-	7	-1	1	1	1
16	8	-	1	1	1	1

The effects of the four factors and the eleven interactions in the 2^{4-1}-design are calculated with the means of the resulting variable analogous to the 2^4-design. Therefore the products of the factor steps have to be built for the interaction columns (Table 3.6).

There are two columns each containing the negative values of the other one, e.g. A and BCD (for the substitution ABC → D there were each two columns with identical values). For the analysis of the effects this means that a distinction between them is not possible. The effect of a factor calculated in the way shown above turns out to be the difference of the effects of a factor and a threefold interaction, e.g. A - BCD (for the substitution ABC → D it would be the sum instead of the difference). This phenomenon is called mixing of effects. The reason for this loss of information towards the 2^4-design is the bisection of the number of factor step combinations.

***Table 3.6:** 2^{4-1}-design (substitution -ABC → D) with factor and interaction columns. The fact that there are two columns each containing the negative values of the other one means that their effects cannot be distinguished: they are mixed. (According to Kleppmann 2003).*

syst. no.	**factors**				**interactions**										
i_2$^{4-1}$	A	B	C	D	AB	AC	AD	BC	BD	CD	ABC	ABD	ACD	BCD	ABCD
1	-1	-1	-1	1	1	1	-1	1	-1	-1	-1	1	1	1	-1
2	1	-1	-1	-1	-1	-1	-1	1	1	1	1	1	1	-1	-1
3	-1	1	-1	-1	-1	1	1	-1	-1	1	1	1	-1	1	-1
4	1	1	-1	1	1	-1	1	-1	1	-1	-1	1	-1	-1	-1
5	-1	-1	1	-1	1	-1	1	-1	1	-1	1	-1	1	1	-1
6	1	-1	1	1	-1	1	1	-1	-1	1	-1	-1	1	-1	-1
7	-1	1	1	1	-1	-1	-1	1	1	1	-1	-1	-1	1	-1
8	1	1	1	-1	1	1	-1	1	-1	-1	1	-1	-1	-1	-1

Whether the mixing of effects is relevant for the calculated effects of factors or not, depends on the structure of mixing which can be expressed by the resolution of a fractional factorial experimental design (Kleppmann 2003). The resolution is denoted in roman numbers and defined as

$$r = n_{fme\_1} + n_{fme\_2} \tag{3.37}$$

where n_{fme_1} is the number of interacting factors of an arbitrary effect and n_{fme_2} the number of interacting factors of the corresponding mixed effect. Thereby the number of a single factor effect is counted as I. In a 2^{4-1}-design the effects of the four single factors are mixed with the effects of the four threefold interactions and the effects of three twofold interactions are mixed with the effects of the three other twofold interactions. The resolution of a 2^{4-1}-design therefore is IV. As threefold interactions are rarely relevant for the resulting variable, their mixing with single factors is much less critical than the mixing among effects of twofold interactions, as is the case for the resolution III, e.g. in a 2^{3-1}-design (Kleppmann 2003).

The ideal sequence of the experiments would have been in blocks - each including all the eight factor step combinations determined in the 2^{4-1}-design - with a random order of the systematic experiment number within each block to exclude trends. So each factor step combination (i.e. systematic experiment) had to be realized once in the first block, then each experiment had to be repeated (second replicate) in the second block. In fact the experiments were performed blockwise (Table 3.7), but in order to reduce the technical effort involved, the experiments with a dry active layer were effected first, followed by those with a wet active layer. As the conditions in the climate chamber were controlled continuously and could be kept quite stable, the contamination of the experimental results by a trend could be neglected.

In the 2^{4-1}-design used the number of factor step combinations m is eight and the sample size n was chosen to be 2. According to equation (3.29) the degree of freedom f therefore is eight. For this degree of freedom the t-values taken from a statistic table (Kleppmann 2003) are 2.306 at the 95%-confidence level, 3.355 at the 99%-confidence level and 5.041 at the 99.9%-confidence level.

Table 3.7: *Sequence of single experiments for the systematic 4-factorial shear test series.*

chronological no. of experiment	systematic no. of experiment	block no. (no. of realization)
1	5	1
2	1	1
3	2	1
4	6	1
5	8	1
6	3	1
7	4	1
8	7	1
9	2	2
10	5	2
11	6	2
12	1	2
13	3	2
14	8	2
15	7	2
16	4	2

Complete 2^2-experimental design

To analyze the effects of the two permafrost factors (its grain size and degree of ice saturation) on the surface parameters a complete 2^2-experimental design was used (Table 3.8).

Table 3.8: *Complete 2^2-experimental design to analyze the effects of the two permafrost factors grain size d_{PF} and degree of ice saturation S_{i_PF} on the surface parameters of the permafrost block.*

syst. no. 2^4 plan	syst. no. 2^{4-1} plan	syst. no. 2^2 plan	factors		int. act.	resulting variable					
			d_{PF}	S_{i_PF}							
a, b	a, b	i	C	D	CD	y_a1_i	y_a2_i	y_b1_i	y_b2_i	γ_i	s_i^2
2, 3	2, 3	1	-1	-1	1	y_a1_1	y_a2_1	y_b1_1	y_b2_1	γ_1	s_1^2
9, 12	1, 4	2	-1	1	-1	y_a1_2	y_a2_2	y_b1_2	y_b2_2	γ_2	s_2^2
5, 8	5, 8	3	1	-1	-1	y_a1_3	y_a2_3	y_b1_3	y_b2_3	γ_3	s_3^2
14, 15	6, 7	4	1	1	1	y_a1_4	y_a2_4	y_b1_4	y_b2_4	γ_4	s_4^2
Σ			$\Sigma C_i\gamma_i$	$\Sigma D_i\gamma_i$	$\Sigma CD_i\gamma_i$						Σs_i^2
effect			$\Sigma_C/2$	$\Sigma_D/2$	$\Sigma_{CD}/2$					$s^2 =$	$\Sigma s_i^2/4$

As the number of factor step combinations m in the 2^2-design is four and the sample size n as well due to the given experiment size N of 16, the degree of freedom f is twelve. The equivalent t-values are 2.179 at the 95%-confidence level, 3.055 at the 99%-confidence level and 4.318 at the 99.9%-confidence level (Kleppmann 2003).

Experiment preparation and procedure

To guarantee comparable conditions for all experiments, a defined procedure for each single experiment was followed. Each step of this procedure is described below.

As the granular materials provided for an experiment included a small amount of water already before the experiment because of being exposed to the humidity of the air, it had to be dried first in an oven at 105°C in portions of 42 litres (Figure 3.14). The material was dried until the lowest possible water content at this temperature was reached. Then the dried material was stored in a dry, ventilated cold chamber at a temperature of -17°C until it reached a given temperature.

Figure 3.14: *Drying of granular material filled in tins and boxes in an oven at 105°C.*

The next step was the preparation of the artificial permafrost layer. In case of an ice saturated permafrost block the material first had to be saturated with water. The dry granular material was poured into a bucket filled with water. This suspension was mixed and left for several hours until all the air in the pore spaces had been replaced by water. Afterwards the excess water on top of the saturated granular material was siphoned off. Before the lower shear box was filled with the dry or wet granular material provided for the permafrost block, the two lowest thermistors (Table 3.2) had been installed in the lower shear frame by means of a thermistor mount (Figure 3.3). The lower thermistor was inserted through a horizontal hole in the thermistor mount, the higher one was laid in a V-shaped slot on top and attached with adhesive tape (Figure 3.15). The thermistor cables were fixed to the bottom of the lower shear frame with adhesive tape and led out at its rear.

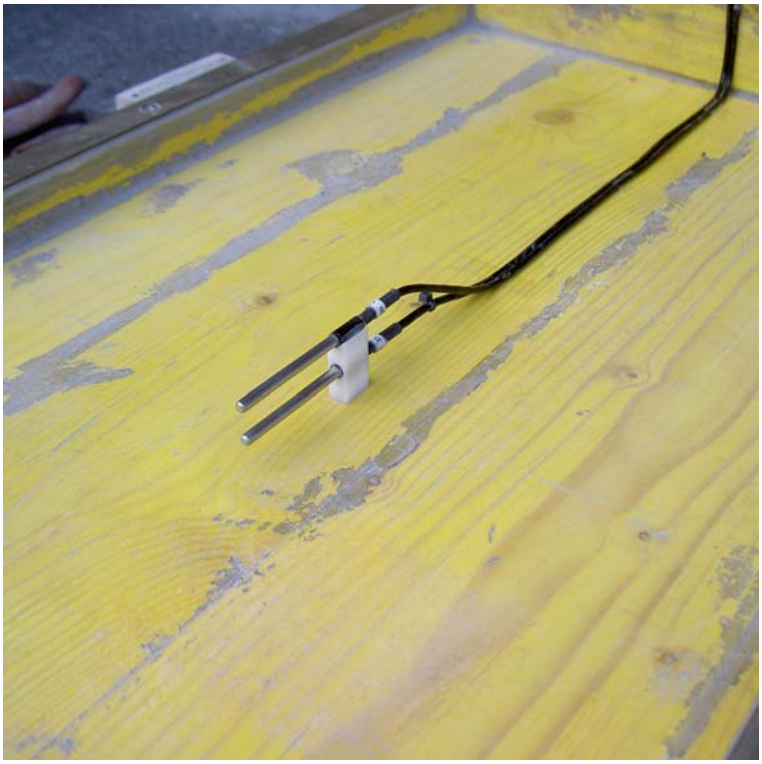

Figure 3.15: *Installation of the two lowest thermistors in the lower shear frame before filling it with the granular material provided for the permafrost block.*

Then the lower shear frame was filled with the granular material provided for the permafrost block. The bulk material was poured up a little higher than the lateral brass rails. The excess material (higher than the brass rails) was then removed by scraping it off with an alloy bar guided on the brass rails. A defined and repeatable surface could thus be obtained (Figure 3.16).

When wet material was used for the permafrost block its surface had to be dried off by heating ventilators until all superficial excess water had been evaporated. This measure was necessary to prevent the creation of an ice layer at the surface of the permafrost block. The permafrost block was then cooled (i.e. frozen in case of wet material) in a cold chamber at an ambient air temperature of -10°C until the centre of the permafrost block had reached a temperature lower than -4°C. Then the shear box was moved to the climate chamber with an ambient air temperature of 1°C in order to warm the permafrost block slowly until its initial surface temperature for the experiment of -0.8°C was attained. Before this, the surface profile of the permafrost block was scanned with the laser scanner described in the chapter 'Experimental parameters' and shown in Figure 3.4.

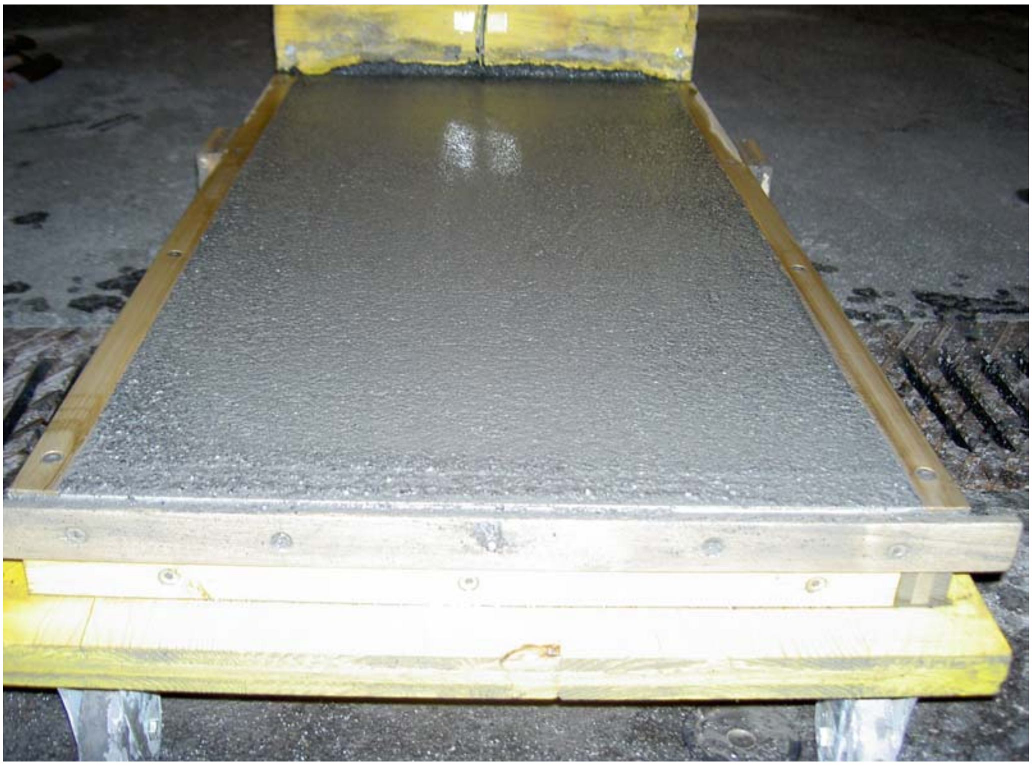

Figure 3.16: *Surface of the artificial permafrost layer (in this case wet sand) after scraping off the excess material with an alloy bar on the brass rails. The small inhomogeneities at the front are beyond the maximal shear distance and therefore do not affect the shearing process.*

In the meantime the artificial active layer was prepared. The dried material was filled in flat plastic tubs and set in the climate chamber with an ambient air temperature of 1°C. In case of a moist active layer the higher value for the volumetric water content (15%) had to be set. With the initial volume of the active layer V_{AL} and the apparent density of the dry solid materials for the active layer ρ_s, which was assumed to be constant for all experiments, the required dry mass of the active layer m_{AL_dry} could be calculated. The volume of the water to be added to the dry granular material for the active layer is

$$V_{AL\_w} = \theta_v \cdot V_{AL} \tag{3.38}$$

where θ_v is the volumetric water content. In combination with the density of water ρ_w then the required water mass m_{AL_w} of the active layer could be calculated. Before the water could be mixed with the dry granular material it was tempered to 1°C in the climate chamber. The mixing of the dry granular material and the water was done in three portions to keep the quantity of the material to be mixed at one time manageable. Therefore a third of m_{AL_dry} and m_{AL_w} was weighed and mixed manually in a flat tub until no dry grains were visible any more. After having prepared the three single portions of moist material they were filled in a big plastic box and mixed thoroughly. To prevent evaporation and therefore a change of the volumetric water content before the experiment, the plastic box containing the moist material was covered with a cap and pasted up airtight by adhesive tape.

Then the upper shear frame was placed on the brass rails of the lower shear frame in its starting position, ready to be filled and the ball bearings (Figure 3.3) were screwed on as protection against tilting. When the active layer material (1°C) was filled in the upper shear frame on top of the warming permafrost block, the surface temperature of the latter rose very rapidly due to heat conduction and in case of a moist active layer also convection. As the permafrost surface temperature should be not higher than -0.8°C at the beginning of the experiment, the upper shear frame had to be filled before the surface of the warming permafrost block attained this temperature. The chosen temperature difference at the permafrost surface between filling in the active layer material and attaining -0.8°C depended on the thermal diffusivity of the artificial active layer and permafrost and therefore on the factor-step combination.

Before the upper shear frame was filled with the active layer material the column of deformation markers spiked on the fixing rod (see chapter ‘Experimental parameters’ and Figure 3.3) had been placed at the side wall of the upper shear frame. Whilst the material was poured in, the upper four thermistors were embedded in the active layer material and the cables were led out of the upper shear frame in the rear.

The experiment was then started by inclining the shear box using a manual winch until the upper shear frame started to slide downslope visibly in a surge like manner. Thereafter the inclination angle was kept constant until the active layer came to a rest by itself. The experiment was continued by repeating the last two steps until the maximum shear distance was reached and therefore the friction angle was attained.

3.3.2 Results and analysis of systematic shear test series

In this section the measured data are presented and analyzed. First the determination of the static friction coefficient is shown, because this constant is needed to correct the friction angles. For each resulting variable the raw data are processed and new parameters are derived to be evaluated statistically afterwards.

Static friction coefficient of the shear box

The average measured inclination angle of sliding of the empty shear box is 17.6° with a standard deviation of 1.2°. Using equation (3.26) and replacing f_{AL} by f_{box} it can be calculated to be 0.32. For the application of f_{box} see ‘Collective downslope displacement’.

Permafrost surface profile

In this subsection only the results of statistically significant surface parameters and characteristics are presented. In a first part the influence of the scale at which a surface profile is observed, on the surface parameters is analyzed. In a second part the influence of the factors grain size d_{PF}, and degree of ice saturation S_{i_PF} of the permafrost block and of the interaction between them on the surface parameters is analyzed.

Influence of scale

For all 16 experiments the surface parameters depended on the observed scale regardless of the factors. To analyze the influence of the scale of the processed profiles they were selected and ordered in two different ways. For the wavelengths λ_a and λ_q, the angles of the average slope ζ_a and ζ_q of the profile and the profile length ratio l_r a stepwise inclusion of finer irregularities starting from a coarse scale was used. In this kind of scale grading the waviness profile 1 is observed, then the waviness profile 2 and at least the roughness profile 2. Regarding the amplitude distribution function and the bearing ratio curve, a stepwise exclusion of the waviness was performed. Therefore the coarsest scale is the aligned, unfiltered profile, going on to the roughness profile 1 and ending with the roughness profile 2.

The average and the root-mean-square wavelength over all experiments decline from one to the next profile scale by about one order of magnitude (Figure 3.17a). Therefore λ_a and λ_q are useful to characterize the observed profile scale. For the waviness profile 1 it characterizes the coarse irregularities of the whole permafrost surface, for the waviness profile 2 the irregularities due to the granular material and for the roughness profile 2 the irregularities due to the asperities of the sand grains.

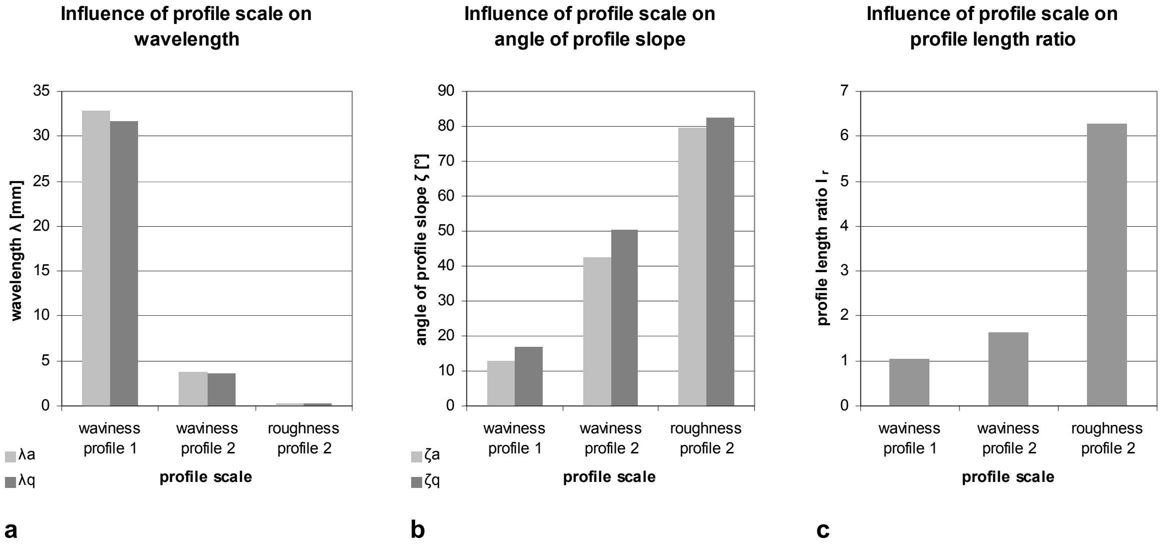

Figure 3.17: Influence of the profile scale on the average wavelength λ_a and the root-mean-square wavelength λ_q (a), the angles of the average slope ζ_a and ζ_q of the profile (b) and the profile length ratio l_r (c). Note that the steps of the profile scale are logarithmic, because the cut-off wavelength λ_{c1} is one order of magnitude higher than λ_{c2}.

The finer the profile scale, the higher the angles of the average slope ζ_a and ζ_q of the profile are (Figure 3.17b), i.e. the sharper the surface profile is. At the scale of the waviness profile 1 ζ_a and ζ_q are in the range of the dilatancy angle for similar materials at a relative density of about 0.9 determined by other researchers under conditions of plain strain (Cornforth 1964, Marachi et al. 1969, Stroud 1971, Cornforth 1973). (Dilatancy refers to the volume expansion which occurs during shearing caused by the grains of the upper layer being moved upwards by micro elevations of the lower layer.) This means that ζ_a and ζ_q at the given scale are well mapped by the dilatancy angle, if the relative density is close to the maximum density, because then the grains of the layer sheared off cannot evade but have to follow the relief of the fixed layer. Therefore dilatancy could be explained by the waviness at the scale of profile 1, while ζ_a and ζ_q at finer scales are far too high for dilatancy angles. The profile length ratio l_r increases towards finer scales (Figure 3.17b and c). This indicates that the surface becomes more fissured.

The absolute arithmetic mean and the variance of the amplitude distribution function decline towards finer scales (Table 3.9 and Figure 3.11). This is trivial, but typical, when the waviness is gradually excluded towards a finer scale. The skewness stays close to zero, i.e. on average over all experiments the amplitudes are distributed symmetrically to the center line at all investigated profile scales. The increase of the kurtosis - i.e. of the sharpness of the amplitude distribution function - towards finer scales indicates that the material is increasingly concentrated along the centre line. As the bearing ratio curve is the integral of the amplitude distribution function, the highest change of the material content with profile depth (a_{max}, for both intervals) also increases towards finer scales.

Table 3.9: *Influence of the profile scale on surface parameters of the amplitude distribution function and the bearing ratio curve.*

parameter	notation	unit	profile scale aligned profile	 roughness profile 1	 roughness profile 2
absolute arithmetic mean of amplitude distribution	$\lvert m_1 \rvert$	mm	1,506	0,765	0,303
variance of amplitude distribution	m_2	mm^2	4,770	1,514	0,237
skewness of amplitude distribution	m_3	-	-0,011	-0,027	-0,110
kurtosis of amplitude distribution	m_4	-	4,418	5,716	11,583
maximum slope of bearing ratio curve (interval 1)	a_{max_1}	-	32,133	66,429	154,844
maximum slope of bearing ratio curve (interval 40)	a_{max_40}	-	17,815	28,589	41,504

The analysis above shows that the interpretation of surface parameters is only possible by taking into account the profile scale at which they are observed.

Influence of factors

The coarsest scale at which the factors grain size d_{PF}, degree of ice saturation S_{i_PF} of the permafrost block or the interaction between them had a significant effect on the surface parameters is the roughness profile 1 (Table 3.10).

This means that a macroscopically similar surface of the whole permafrost block (at the scale of the aligned profile and the waviness profile 1) was attained in all single experiments. 80% of the significant effects of the two permafrost factors and their interaction on the surface parameters are apportioned to the grain size d_{PF}. However, there are also three parameters ($R_{pm}/R_{z(DIN)}$ and m_3 of roughness profile 1 and m_3 of roughness profile 2) which were significantly affected by the degree of ice saturation S_{i_PF} or the interaction between d_{PF} and S_{i_PF}.

At the scale of the roughness profile 1 the positive effects of the grain size d_{PF} on R_q, λ_a and λ_q indicate the rougher character of a sand surface in comparison with a silty sand surface. As m_3 is affected by the interaction of d_{PF} and S_{i_PF}, the effect of d_{PF} on it depends on the factor step of S_{i_PF}. m_3 is only negative in the case of sand without ice (high factor step of d_{PF} and low factor step of S_{i_PF}), i.e. the material is concentrated closer to the peaks than to the valleys of the surface profile. The reason therefore could be that the grains are pushed apart from each other due to the expansion of ice during freezing. Therefore the valleys become wider which leads to an increase of the skewness. This result is in accordance with the increasing effect of d_{PF} on $R_{pm}/R_{z(DIN)}$ because it implies that the peaks become sharper relative to the whole profile and the valleys become wider. This means that the permafrost block is slightly oversaturated if it contains ice. The effect of d_{PF} on a_{max_1} and a_{max_40} can be interpreted as an increasing concentration of material along the centre line with decreasing grain size.

Table 3.10: *Surface parameters on which the factors of the permafrost block (d_{PF} = grain size, S_{i_PF} = degree of ice saturation) or an interaction IA between them had a significant effect (fields shaded dark grey = 99.9% significance level, light grey = 99% significance level, white = 95% significance level or lower).*

profile scale	**parameter**	**notation**	**unit**	**effect**		
				d_{PF}	S_{i_PF}	IA
roughness profile 1	root-mean-square roughness	R_q	mm	0.897	0.231	0.019
	ratio of average peak to total roughness	$R_{pm}/R_{z(DIN)}$	-	-0.035	0.087	0.053
	average wavelength	λ_a	mm	0.436	0.018	0.026
	root-mean-square wavelength	λ_q	mm	0.400	-0.046	-0.015
	skewness of amplitude distribution	m_3	-	-0.509	0.702	0.698
	maximum slope of bearing ratio curve (interval 1)	a_{max_1}	-	-43.271	-24.610	12.605
	maximum slope of bearing ratio curve (interval 40)	a_{max_40}	-	-21.071	-5.516	6.231
waviness profile 2	total waviness height	W_t	mm	6.583	0.566	-0.283
	angle of average absolute slope	ζ_a	°	23.935	6.774	-3.069
	angle of root-mean-square average slope	ζ_q	°	24.888	5.467	-4.288
	profile length ratio	l_r	-	0.787	0.187	0.033
roughness profile 2	average roughness	R_a	mm	0.195	0.070	-0.029
	root-mean-square roughness	R_q	mm	0.298	0.087	-0.055
	average wavelength	λ_a	mm	0.151	-0.013	-0.009
	root-mean-square wavelength	λ_q	mm	0.152	-0.033	-0.021
	absolute arithmetic mean of amplitude distribution	$\lvert m_1 \rvert$	mm	0.195	0.070	-0.029
	skewness of amplitude distribution	m_3	-	-0.443	0.797	0.197
	maximum slope of bearing ratio curve (interval 1)	a_{max_1}	-	-84.415	-35.392	16.016
comparison of bearing ratio curves	factor between maximum slope of aligned and roughness profile 1 (interval 1)	$k_{a\_r1\_1}$	-	-0.747	-0.097	0.093
	factor between maximum slope of roughness profiles 1 and 2 (interval 40)	$k_{r1\_r2\_40}$	-	0.525	-0.067	0.014

As sand grains are in the range of the scale of waviness profile 2, W_t, ζ_a and ζ_q increase with d_{PF} at this scale. The increase of l_r with d_{PF} implies that the profile becomes more fissured. Therefore this result is consistent with the previous ones.

The increasing effect of d_{PF} on R_a (i.e. $|m_1|$) and R_q at the scale of roughness profile 2 shows that the roughness due to the asperities of single sand grains is higher than the roughness due to the granularity of a silty sand surface. This coincides with the increasing effect of d_{PF} on λ_a and λ_q. As the average wavelength represents twice the equivalent diameter of silt grains or of the asperities of single sand grains, the latter ones are still coarser than silt grains. The positive effect of S_{i_PF} on the skewness m_3 indicates wider valleys for the slightly ice oversaturated permafrost block than for ice free conditions. This can be explained in the same way as at the scale of the roughness profile 1 by the grains being pushed apart from each other due to the expanding ice in the voids. However, at the scale of the roughness profile 2 silt grains are crucial for this process. The negative effect of d_{PF} on a_{max_1} means that the material is more strongly concentrated along the centre line (at this scale) for a silty sand than a sand surface. This can be understood by the asperities of single sand grains being coarser than silt grains.

A comparison of the aligned and the roughness profile 1 shows that the factor $k_{a\_r1\_1}$ between the maximum slopes of the bearing ratio curves is higher for silty sand than for sand. Regarding the maximum slope of the bearing ratio curve there is no significant difference between a silty sand and a sand surface at the scale of the aligned profile. However, as silty sand is more strongly concentrated along the centre line (higher values of a_{max_1} and a_{max_40} for silty sand) than sand at the scale of roughness profile 1, $k_{a\_r1\_1}$ also has to be higher for silty sand. Comparing roughness profiles 1 and 2 the surface structure which is focused on changes from the compound of mineral grains to the asperities of single mineral grains in case of a sand surface. However, there is no such categorical change for silty sand, because the grain size of a fraction of 99% is still smaller than the cut-off wavelength λ_{c2} of the second (fine) filter. Therefore the factor $k_{r1\_r2\_40}$ between the maximum slopes of the bearing ratio curves of roughness profile 1 and 2 is higher for a sand than a silty sand surface.

Collective downslope displacement

First the results of the methods 1 and 2 (used in replicate 1 and 2) are compared. Secondly the general course of the curve for the relation between the inclination angle α_0 and the collective downslope displacement d_{AL_col} and thirdly the influence of the factors on the collective downslope displacement is analyzed.

Comparison of methods

The results of methods 1 (manual) and 2 (video camera) are shown in Figure 3.18. Until about the first third of the maximum shear distance the curve of method 1 deviates considerably from the curve of method 2 which can be seen as a reference. The maximum absolute difference of about 10° is reached at a displacement of 3 mm.

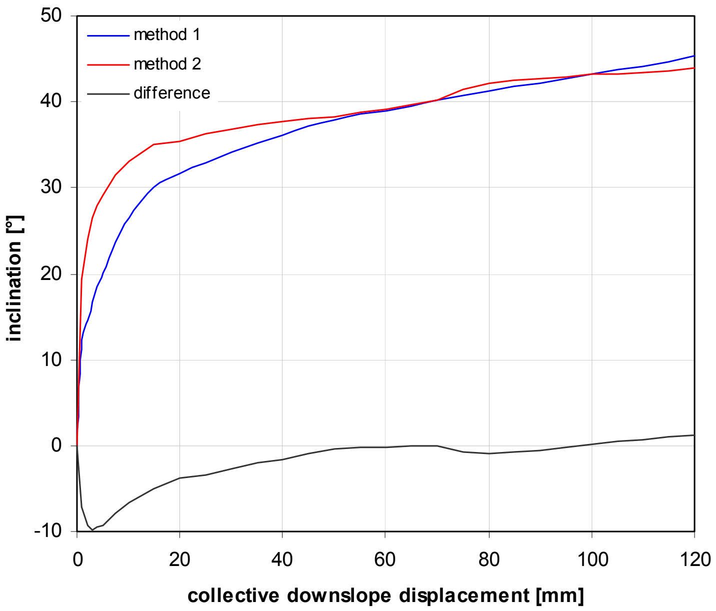

Figure 3.18: *Comparison of the results of method 1 and 2. The curves of method 1 and 2 each are the mean curves of all eight single experiments for which the same method was applied to determine the collective downslope displacement. In order to build these mean curves the same values for the collective downslope displacement had to be chosen for all single experiments. The chosen values at which no measurement exists were interpolated linearly.*

The reason for these high deviations are the small displacements over a wide range of inclination angles in the first section of the curves; as the frequency of measurement steps is much lower for the manual method (1) than with a video camera (method 2). As the general course of the curve is bent to the right, but the missing measurement points are interpolated linearly, the latter must be too low. After the absolute deviation has reached its maximum it declines uniformly to reach 0 at about half of the maximum shear distance. Over about the last two thirds of the maximum shear distance the difference between the two methods is only marginal (mostly less than 1°).

A stepwise displacement can only be captured using a video camera (method 2) as can be seen in the example of the systematic experiment no. 7 (Figure 3.19). The resolution necessary to display these steps is too low for manual measurements (method 1).

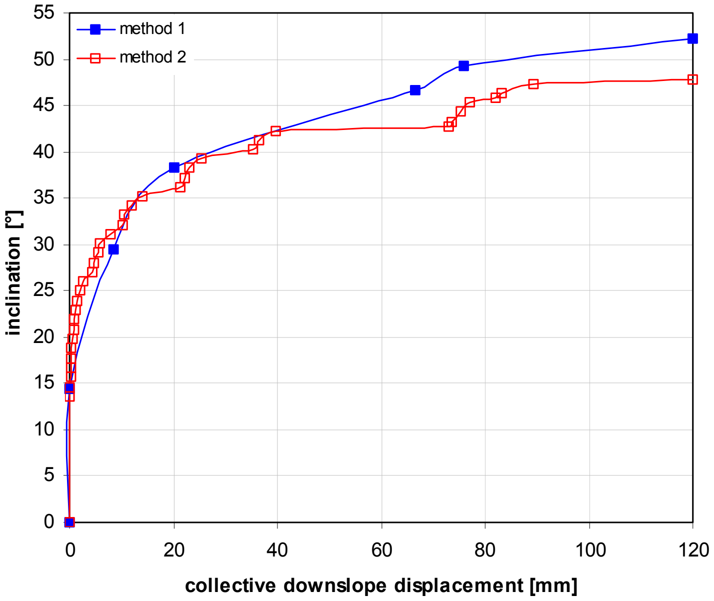

***Figure 3.19**: Comparison of the resolution of methods 1 and 2 determining the collective downslope displacement by means of the systematic experiment 7 as an example. The squares within the curves indicate the measuring points.*

General course of curve

To analyze the general course of the relation between the inclination angle α_0 and the collective downslope displacement d_{AL_col}, the average curve of all eight systematic experiments was calculated (Figure 3.20).

In Figure 3.20 d_{AL_col} remains stable at 0 mm until α_0 is about 15°. Thereafter the curve is steep, that is high changes of α_0 are needed to affect a definite value of d_{AL_col}. With d_{AL_col} increasing, the curve then flattens out continuously regarding its main course. However, there are some steps in the curve where its slope increases with d_{AL_col} increasing. Even the two most distinct steps at 20 mm and 35° and at 70 mm and 40° are not abrupt.

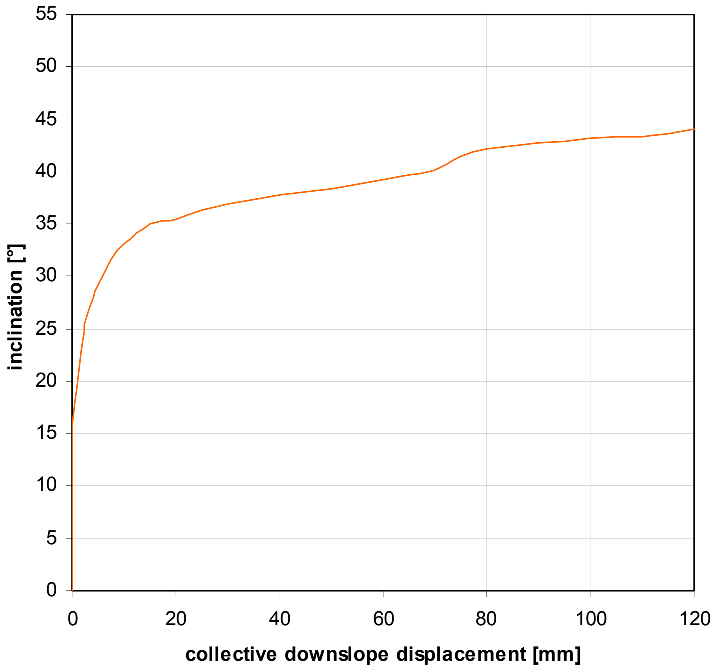

***Figure 3.20**: General course of the curve for the relation between the inclination angle and the collective downslope displacement (average of all experiments). As the resolution is higher for method 2 than for method 1, only the data of method 2 were used for the calculation of the average curve.*

This is due to averaging over eight experiments; as the steps neither exist in all experiments nor at the same place they are smoothed by averaging. However, in the curves of method 2 representing the single experiments the steps - if present - are much more distinct, e.g. for systematic experiment no. 7 (red curve, Figure 3.19). As long as the curve is steep stress is built up at the shear plane (at the interface between the permafrost and the active layer) by the increasing downslope force, but the active layer still can resist and therefore only moves a little. When the stress becomes too high, a sudden relaxation occurs resulting in a high collective downslope displacement at a constant inclination angle (flat parts of the curve). By rearrangement and interlocking of the grains within the active layer it stabilizes itself and therefore prevents a further downslope displacement when the inclination angle is kept constant. The process then starts again when the inclination angle is further increased. This stepwise response is typical for granular materials (Gray 2001).

Influence of factors

The influence of the factors on the collective downslope displacement is now analyzed. Due to the fractional experimental design including eight different experiments for each factor, four experiments are apportioned to the low step of this factor and four to the high one. Therefore for both steps of each factor an average curve out of each four single curves for the relation between α_0 and d_{AL_col} could be established (Figure 3.21). As the resolution of the data of method 1 was not sufficient for these average curves only data from method 2 could be used. The difference of these two curves displays the effect of the considered factor on the relation between α_0 and d_{AL_col}. As no standard deviation can be determined due to only one replicate of each experiment, the statistical significance of this effect cannot be proven. However, at least for the maximum shear distance or the friction angle, the significance of the effect is provable (see section ‘Friction angle between active layer and permafrost’).

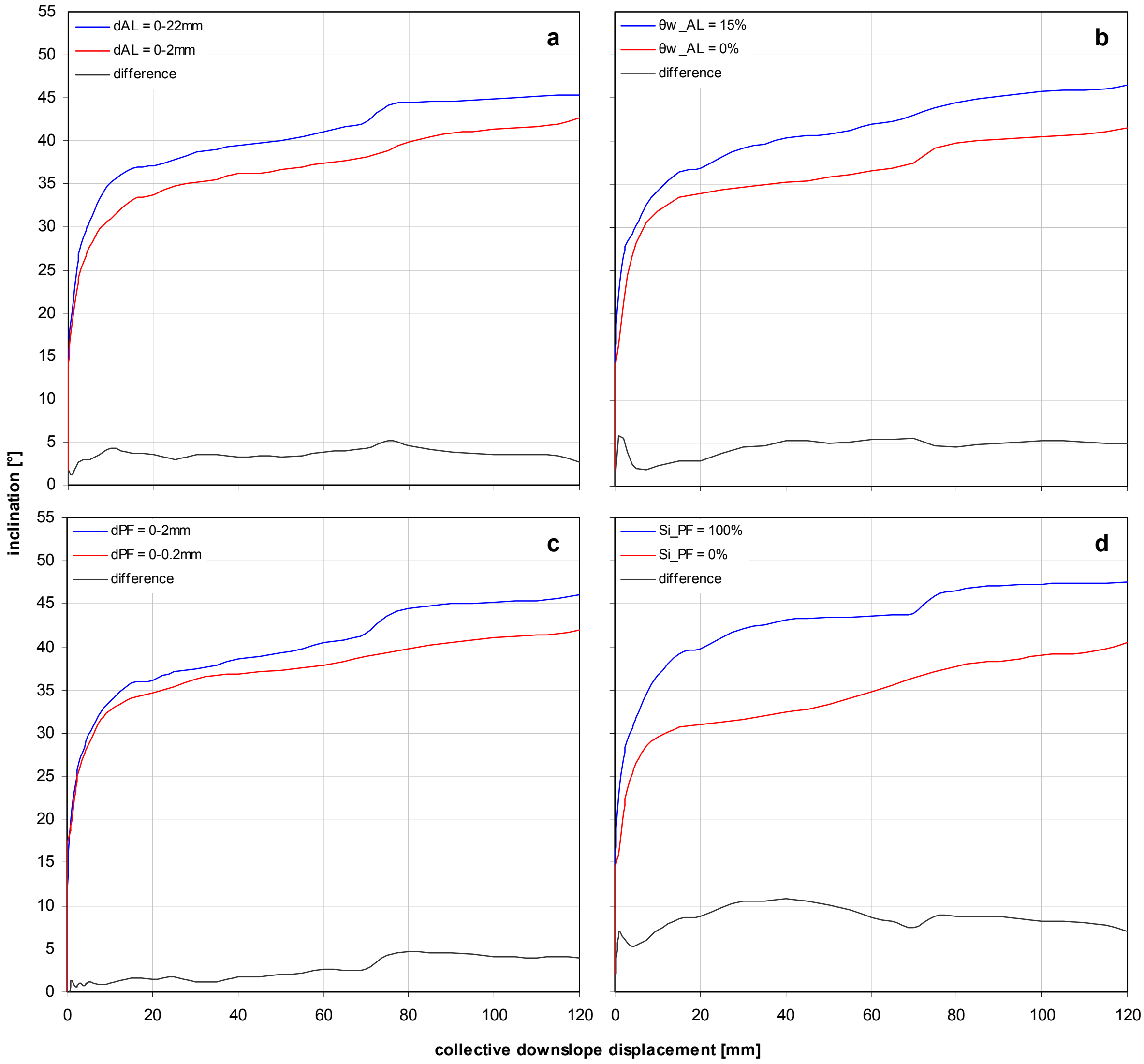

Figure 3.21: *Influence of a) the grain size of the active layer* d_{AL}*, b) the volumetric water content of the active layer* θ_{w_AL}*, c) the grain size of the permafrost* d_{PF} *and d) the degree of ice saturation of the permafrost* S_{i_PF} *on the relation between the inclination angle and the collective downslope displacement.*

For each factor the difference of the two compared curves never becomes negative over the whole shear distance of 120 mm. This means that the direction (sign) of all factors' effects on the friction angle between the active layer and the permafrost is independent of the chosen maximum shear distance (at least from 0 to 120 mm).

The effect of the degree of ice saturation of the permafrost S_{i_PF} is the highest of all factors over the whole shear distance (Figure 3.21). The effect of the volumetric water content of the active layer θ_{w_AL} is higher than the effect of the permafrost's grain size d_{PF} over the same displacement range, but higher than the effect of the active layer's grain size d_{AL} only over the last third of the shear distance (80-120 mm). Also the effect of d_{PF} is higher than the effect of d_{AL} only over this range. Thereby it is remarkable that the beginning of this range is limited by the discontinuity directly before which is described above. From these observations it can be concluded that the ranking order of the factor's effects is independent of the maximum shear distance for d_{AL_col} higher than 80 mm.

For d_{AL}, d_{PF} and S_{i_PF} the most distinct discontinuity in the generally flattening course of the curves compared in pairs (where d_{AL_col} is about 70 mm) is more pronounced in the curve representing the high factor step. However, for θ_{w_AL} the observed discontinuity is more pronounced in the curve representing the lower factor step (dry conditions). These results can be explained by the mechanism of interlocking of grains due to their rearrangement (see above). According to this the interlocking has to be increased for higher grain sizes (explanation for d_{AL} and d_{PF}). If the grains of the immobile permafrost block are embedded in an ice matrix and therefore cannot move, the interlocking at the interface between the active layer and the permafrost must be higher than without ice in the permafrost (explanation for S_{i_PF}). Due to the apparent cohesion and the lubricating effect of water within the pores of a granular material the interlocking is lowered by an increasing water content.

Internal downslope displacement

Relative values are used to ensure independence from the absolute dimensions of the active layer box and the chosen maximum shear distance for the internal downslope displacement depending on depth. The internal downslope displacement was divided by the maximum shear distance to obtain the relative internal downslope displacement q_{AL}. The depth at which a displacement had been measured was divided by the total depth of the active layer to get the relative depth ζ_{AL}. The curve of q_{AL} depending on ζ_{AL} is the (relative internal) deformation profile. First the general course of these deformation profiles is analyzed, then the influence of the factors on them.

General course of deformation profile

To determine the general course of these deformation profiles the average of all systematic experiments was built for both replicates separately (Figure 3.22).

The average deformation profile shows an exponential course. That is, the highest absolute changes of the displacement occur at the greatest depth (shear plane between active layer and permafrost) declining upwards. The lowest (most negative) value of q_{AL} (at $\zeta_{AL} = 100\%$) is called q_{AL_min}. A value of -100% for q_{AL_min} would mean that no shear displacement (relative to the immobile permafrost block) occurred at the interface between active layer and permafrost which is the case for a continuum flow with no-slip boundary condition. So the difference between the minimum possible value for q_{AL_min} (-100%) and its actual value denotes the basal shear displacement, which turns out to be about 60% of the maximum shear distance on average. A value of 0% for q_{AL_min} would mean that the basal shear displacement equals the maximum shear distance which is the case for a rigid body. However, the tested material of the active layer is in between these two extreme cases which is due to its granular nature.

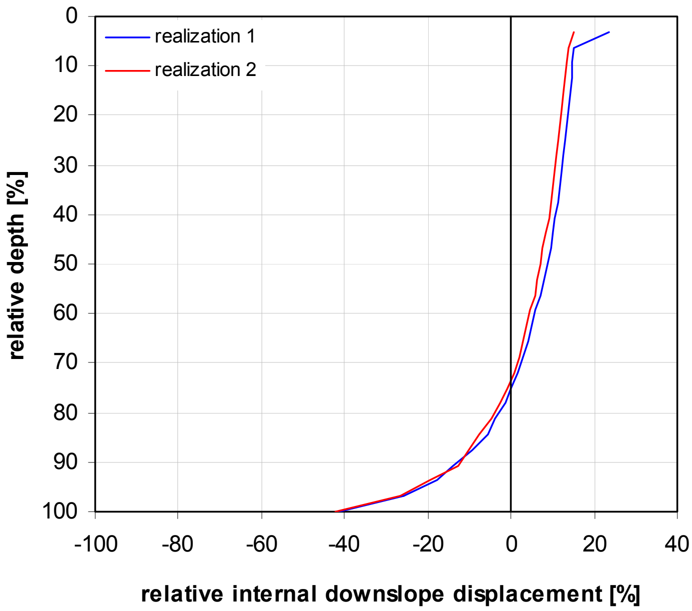

***Figure 3.22**: General course of the average relative internal deformation profile. Positive values on the x-axis denote a downslope displacement relative to the upper shear frame in the direction of the collective downslope displacement.*

The deformation of a soil column which was originally perpendicular to the shear plane is due to shearing between the layers within the granular material. Regarding the shearing process relative to the upper shear frame sliding downslope this means that the material of the active layer is drawn back by the resistance of the basal shear plane while it is compressed by its own downslope force above a relative depth of about 75% (positive values for q_{AL}). The total deformation within the active layer over its whole depth is more than half of the maximum shear distance. The strong displacement in the uppermost layer (above ζ_{AL} = 6%) can be apportioned to rolling of the grains at the surface of the active layer. Rolling occurred only in some experiments. However, as the displacement in these cases was high, they strongly affected the average of all systematic experiments. Besides the rolling effect the deformation profile of a sheared off active layer is similar to a glacier's.

Comparing the average deformation profiles of replicate 1 and 2 the deviations between them are only small. The standard deviation between the two replicates averaged first over all systematic experiments and then over all depths is 1.4. However, if the profiles are averaged first over all depths and then over all systematic experiments, the standard deviation will be 2.9.

Influence of factors

The influence of the factors on the deformation profile was analyzed by determining statistically their effect on selected parameters characterizing the profiles. These parameters are q_{AL_min}, Δq_{AL_roll} (relative displacement at surface of active layer due to rolling of grains), $d_{AL\_grad\backslash roll}$ (gradient of total deformation excluding the influence of rolling in the uppermost layer) and $d_{AL\_grad\_shear}$ (gradient of shear deformation).

On q_{AL_min} only the volumetric water content of the active layer θ_{w_AL} has a significant effect (Figure 3.23).

In contrast to dry conditions a volumetric water content of 15% increases the backward displacement of the active layer at its interface with the permafrost relative to the upper shear frame by more than 20% of the maximum shear distance. Therefore the lubricating effect of the water is not the dominant one as might have been expected. The retaining influence of the higher water content is rather caused by the attraction between the active layer and the permafrost due to the apparent cohesion of water. However, as the embedding of the permafrost grains in an ice matrix was expected to have the greatest retaining effect on the active layer's base, it is remarkable that the effect of S_{i_PF} on q_{AL_min} is not significant and much smaller than the one of θ_{w_AL}.

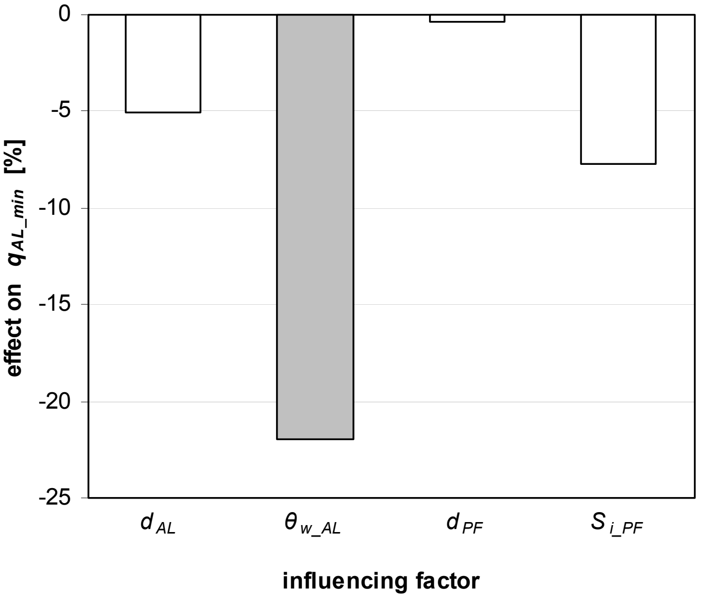

Figure 3.23: *Effect of the four influencing factors on the relative internal downslope displacement at the permafrost surface q_{AL_min}. Grey shading indicates significance at the 99%-level.*

Δq_{AL_roll} was calculated as difference between the maximum of q_{AL} which was measured (q_{AL_max}) and the maximum of q_{AL} as it would have been without rolling at the surface of the active layer ($q_{AL\_max\backslash roll}$). Therefore $q_{AL\_max\backslash roll}$ was determined by extrapolating the deformation profile linearly to the surface of the active layer using the third and fifth highest value for q_{AL}. As the occurrence and distance of rolling is strongly influenced by chance, the average variance over all experiments is very high in comparison with the factors' effects on Δq_{AL_roll}. Therefore none of the effects are significant.

The gradient of total deformation excluding the influence of rolling in the uppermost layer was calculated as

$$d_{AL\_grad\backslash \mathrm{roll}} = \left(d_{AL\_\mathrm{int\_max}\backslash \mathrm{roll}} - d_{AL\_\mathrm{int\_min}}\right) / z_{AL\_\mathrm{max}} \qquad (3.39)$$

where $d_{AL\_int\_min}$ is the minimum, $d_{AL\_int\_max\backslash roll}$ the maximum internal downslope displacement excluding the influence of rolling and z_{AL_max} the thickness of the active layer. Therefore

$d_{AL\_int\_max\backslash roll}$ had been determined analogously to $q_{AL\_max\backslash roll}$. As for q_{AL_min} only θ_{w_AL} has a significant effect on $d_{AL\_grad\backslash roll}$ (Figure 3.24).

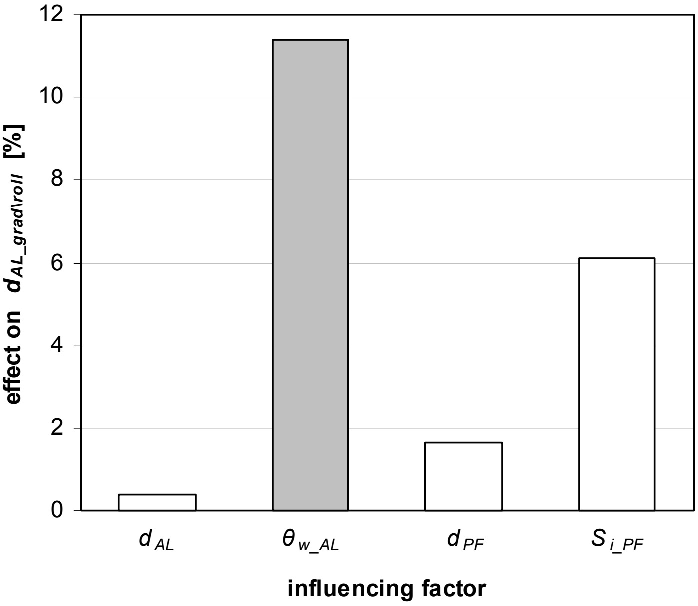

***Figure 3.24**: Effect of the four influencing factors on the gradient of total deformation excluding the influence of rolling in the uppermost layer $d_{AL\_grad\backslash roll}$. Grey shading indicates significance at the 99%-level.*

The positive effect of θ_{w_AL} on $d_{AL\_grad\backslash roll}$ can be explained in the same way as the result for q_{AL_min}. The combination of both results shows that a higher absolute shear deformation at the base of the active layer indicates a higher deformation over the whole profile. This means that higher absolute values for q_{AL_min} are not compensated by a lower compression in the upper three quarters of the active layer.

To determine the gradient of shear deformation a shear band was defined as that part of the active layer for which the relative internal downslope displacement is negative, i.e. where the active layer material has been drawn back relative to the upper shear frame. The gradient of shear deformation was calculated as

$$d_{AL\_grad\_shear} = \Delta d_{shear} / \Delta z_{shear} \tag{3.40}$$

where Δd_{shear} is the shear deformation (difference between 0 and q_{AL_min}) and Δz_{shear} the thickness of the shear band. High values for $d_{AL\_grad\_shear}$ indicate intensive shearing between the active layer and the permafrost. The resulting variable is affected significantly by θ_{w_AL} and S_{i_PF} (Figure 3.25).

The positive effect of θ_{w_AL} on $d_{AL\_grad\_shear}$ can be explained by apparent cohesion due to the water within the pores of the granular material. The positive effect of S_{i_PF} on $d_{AL\_grad\_shear}$ can be explained by the ice in the pore space of the permafrost's granular material preventing the grains from translocating and rotating (Figure 3.28) and therefore increasing the shearing at the base of the active layer.

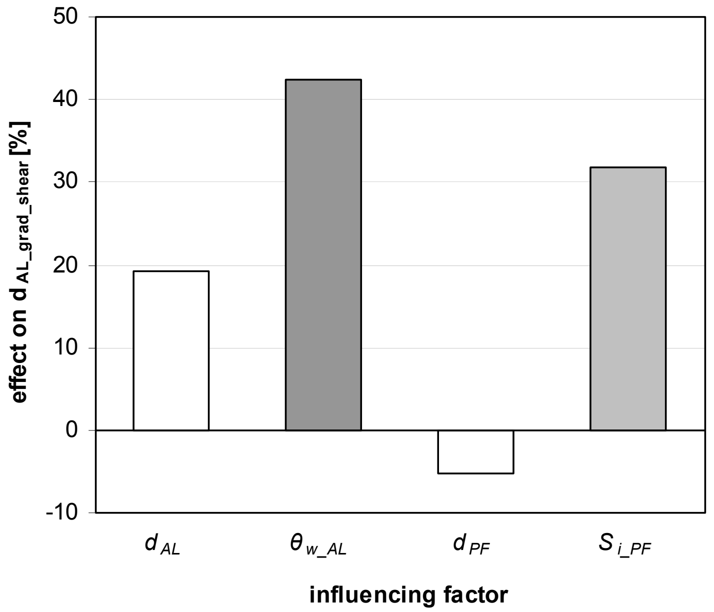

***Figure 3.25**: Effect of the four influencing factors on the gradient of shear deformation in the active layer $d_{AL\_grad\_shear}$. Dark grey shading indicates significance at the 99.9%-level, light grey shading at the 99%-level.*

Friction angle between active layer and permafrost

All investigated factors showed a significant positive effect on the friction angle between the active layer and the permafrost *Φ* (Figure 3.26 and Figure 3.27).

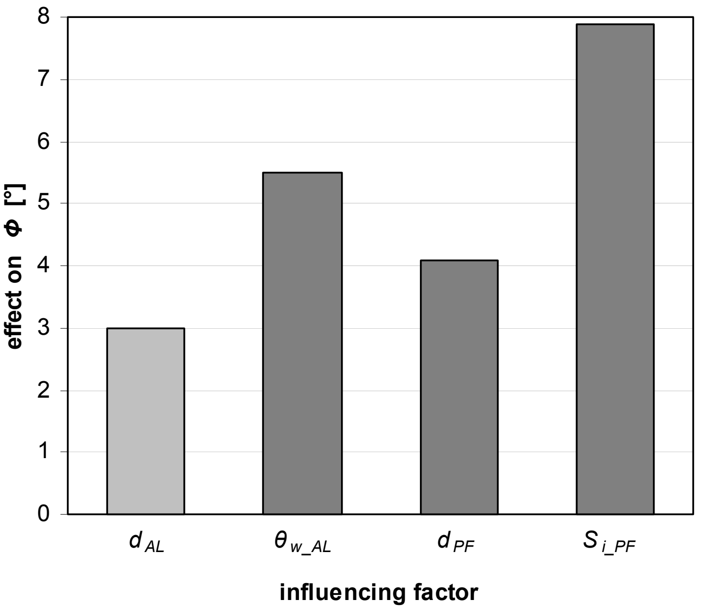

***Figure 3.26**: Effect of the four influencing factors on the friction angle between the active layer and the permafrost Φ. Dark grey shading indicates significance at the 99.9%-level, light grey shading at the 99%-level.*

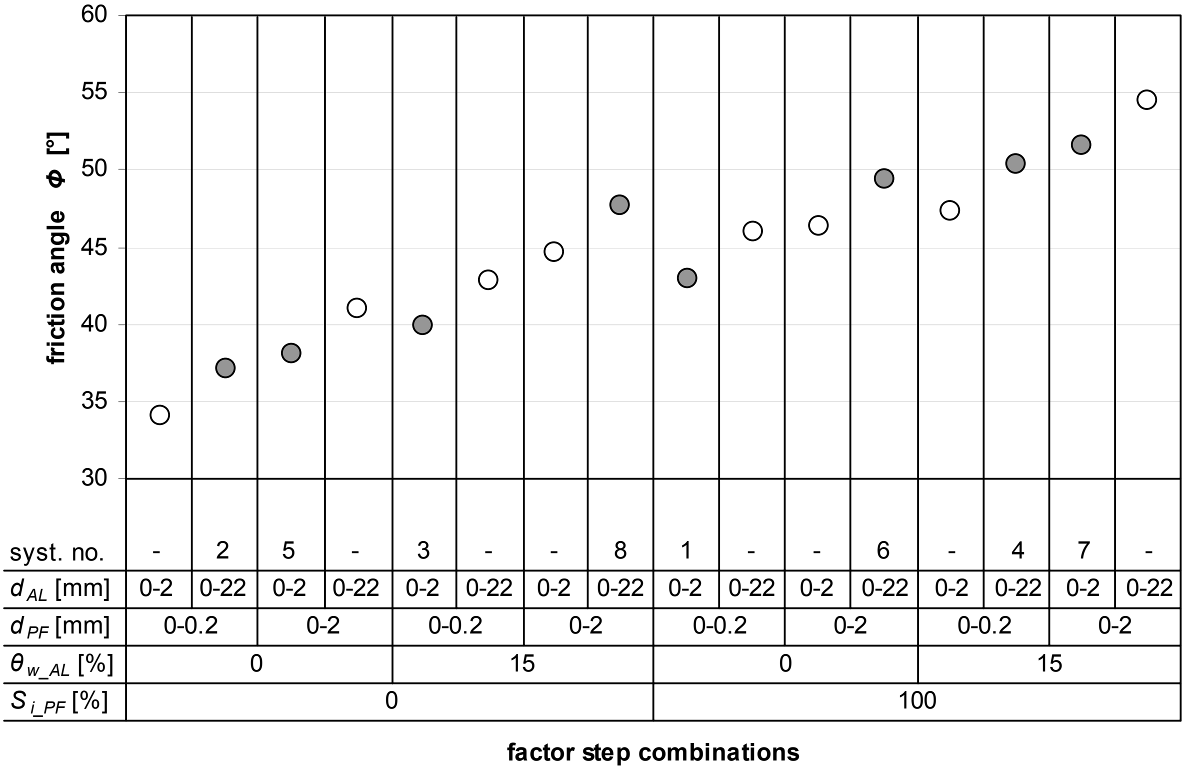

***Figure 3.27**: Friction angle Φ between the permafrost and the active layer depending on the factor step combinations of a complete factorial 2^4-experimental design. For the realized combinations (grey dots) the systematic experiment number of the fractional 2^{4-1}-experimental design is given. The friction angle for the remaining combinations (white dots) were calculated using the determined effects of the factors. The factor step combinations were sorted by the importance of the factors' effects.*

The effects of the water, and of the ice content on Φ were higher than those of grain size, and the effects of the permafrost-factors were greater than the equivalents for the active layer. The systematic experiment no. 5 serves as a reference for the internal friction angle of dry homogenous sand (mean: 38.1°). This reference shows that realistic values for the internal friction angle are measured with the inclinable shear box compared to other shear test studies (Shibuya et al. 1997, Springman et al. 2003).

Influence of grain size

The positive effect of increasing grain sizes (d_{AL} and d_{PF}) on Φ is in good accordance with the results of other studies (e.g. Shibuya et al. 1997)) and the general formula for Φ depending on the grain size distribution (Lang et al. 2003). However, this study additionally showed that the grain size of the permafrost (d_{PF}) is more important (effect about 1° higher) than that of the active layer (d_{AL}). Theoretically three reasons for this are conceivable: the grain size of the (1) immobile or (2) lower or (3) finer grained layer is more important than that of the opposite. As for the friction between two bodies it does not matter which one is moved relative to the other one, reason (1) can be ruled out. An explanation for reason (2) could be that the grains of the active layer can more easily move upwards perpendicularly to the shear plane than those of the permafrost can move in the opposite direction (as the active layer is limited at the surface only by air, while the permafrost layer is limited at its base by solid material). For reason (3) one could argue that finer material has a lower internal friction angle which would limit the friction angle of a 2-layer-shearing-system. However, the effect of d_{PF} is higher than that one of d_{AL}, but it is not limiting; otherwise d_{AL} would not influence Φ at all. The generally positive effect of the grain size on Φ can be explained by the roughness at the shear plane. For increasing grain sizes, the roughness also increases (see chapter 'Permafrost surface profile') which leads to a higher friction between the two layers shearing against each other.

Influence of volumetric water content

At first glance the strong positive effect of θ_{w_AL} on Φ seems to contradict other studies (e.g. Springman et al. 2003)), where the shear resistance decreases with the water content increasing. However, in these studies the level of the water content was chosen much higher than in the present study. Therefore it can be concluded that Φ is highest for an intermediate water content and not for very dry conditions or for high water contents. This conclusion is in accordance with the study of Krahn et al. (1989), who refer to an optimum moisture content for slope stability depending on grain size distribution. The stabilizing effect of an increasing water content before this maximum can be explained by the apparent cohesion; this is due to the suction of the water within the pore space between the grains of the two layers sheared off against each other (in this case the active layer and the permafrost). The reason for a decreasing shear strength after the maximum is the loss of suction with the water content increasing (Springman et al. 2003).

Influence of degree of ice saturation

The fact that Φ is nearly eight degrees higher for an ice saturated than an ice-free, dry permafrost layer can be understood when considering that the ice prevents the grains contained in the permafrost from moving (Figure 3.28). As the grains of the permafrost embedded in an ice matrix can neither translocate nor rotate and therefore cannot make way for the grains of the active layer at the shear plane being pulled downslope, the shear resistance of the permafrost surface is higher with than without pore ice.

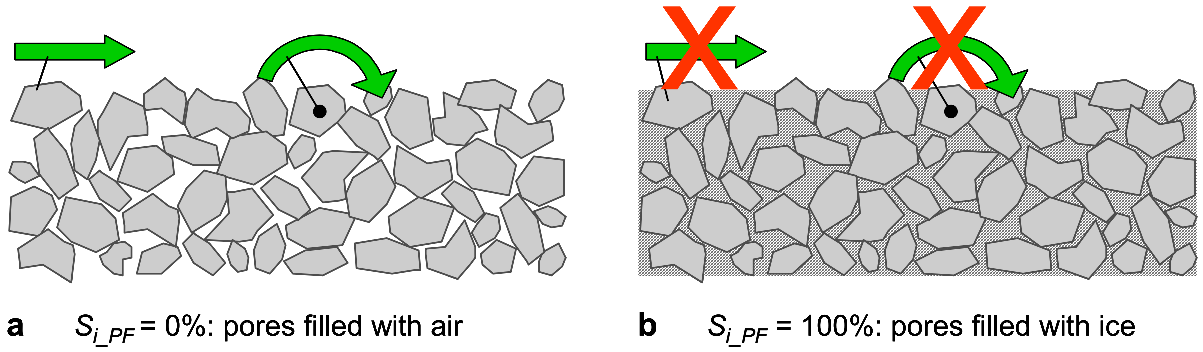

a S_{i_PF} = 0%: pores filled with air **b** S_{i_PF} = 100%: pores filled with ice

***Figure 3.28**: Suggested explanation for the increasing effect of the degree of ice saturation of the permafrost S_{i_PF} on the friction angle between the active layer and the permafrost Φ. Translocation and rotation of the grains is possible in case a), but impeded by the presence of pore ice in case b).*

Air and ground temperatures

First the general course of the air and ground temperatures is analyzed, then the influence of the factors on them.

General course of air and ground temperatures

To display the general course of the air temperature and ground temperatures in the active layer and the permafrost at different depths depending on time the averages of all experiments were established (Figure 3.29).

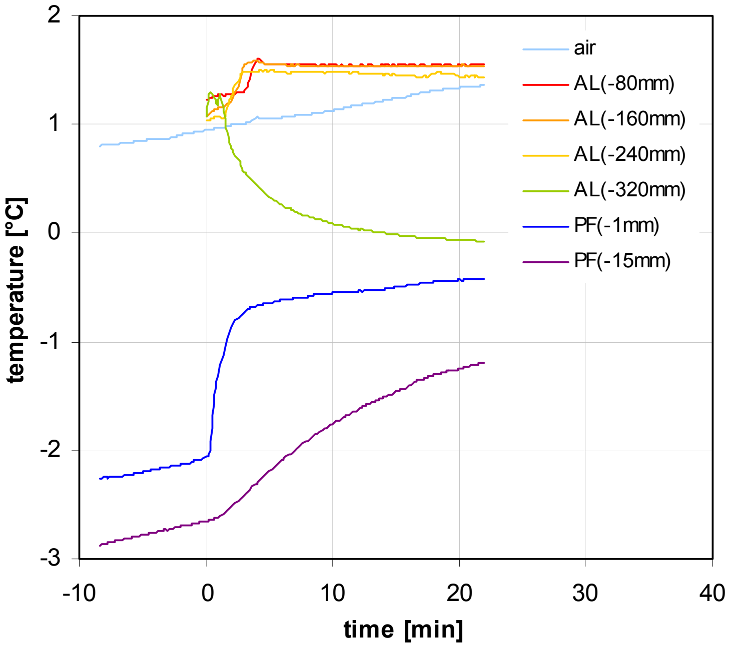

Figure 3.29*: General course of the air and ground temperatures in the active layer (AL) and the permafrost (PF) averaged over all experiments. Therefore the reference time for all experiments (0 minutes on the x-axis) was defined as the time at which the active layer material started to be filled into the upper shear box on top of the permafrost. The depth below the surface of the equivalent layer in which the temperatures were measured is given in brackets.*

The air temperature increased slightly during the experiments due to a human body working in the climate chamber and to repeated opening of the door. However, the air temperature was relevant only to temper the material for the active layer and to slowly warm up the permafrost before the experiment.

As the upper shear frame was successively filled from its base (-320 mm) upwards, the three upper thermistors only measured the ground temperature at the given depth after they had been embedded in the active layer material. The filling of the upper shear frame took about five minutes. The ground temperature remained nearly stable down to a depth of about –160 mm at the initial temperature during the whole experiment. The cooling effect of the permafrost block only influenced about the lowest quarter of the active layer (-240 mm), which is indicated by the slow temperature decrease at this depth.

The temperature at the base of the active layer (-320 mm) on top of the permafrost block decreased rapidly after the experiment had been started and flattened out gradually. This is due to conductive heat transfer from the active layer material to the permafrost block. For the same reason the temperature at the permafrost surface (-1 mm) immediately increased when the active layer material came into contact with it. After about four minutes the temperature curve flattened conspicuously. The temperatures at the base of the active layer and at the surface of the permafrost gradually approached each other.

At a depth of –15 mm below the permafrost surface the thermal response to the heat supply from the active layer material was delayed by at least a minute and much weaker compared to that of the permafrost surface temperature. The delay can be explained by the time dependence of heat conduction and the weaker response by heat absorption above.

Theoretically the depth-time dependent temperature below the permafrost surface after the deposition of the active layer material on the permafrost block can be described by

$$T(z,t) = T_0 + \Delta T \cdot erfc\left(\frac{z}{2\sqrt{\kappa t}}\right) \tag{3.41}$$

whereas $$erfc(\eta) = 1 - \frac{2}{\sqrt{\pi}} \int_0^{\eta} e^{-\eta^2} d\eta$$

is the complementary error-function with the substitution

$$\eta = \frac{z}{2\sqrt{\kappa t}}$$

where z is the depth below the permafrost surface, t is time after deposition of the active layer material, T_0 is the initial temperature of the permafrost block and ΔT the temperature difference with the active layer, κ the thermal diffusivity of the permafrost block and *erfc* the complementary error-function. However, this equation only would be valid under the assumption that the spatial extension of the two layers are infinite and the temperature of the active layer constant which is definitely not the case, as shown by the measurements.

Influence of factors

The factors θ_{w_AL} and S_{i_PF} showed a significant effect on the course of the temperature at the interface between the active layer and the permafrost block (Figure 3.30 and Figure 3.31).

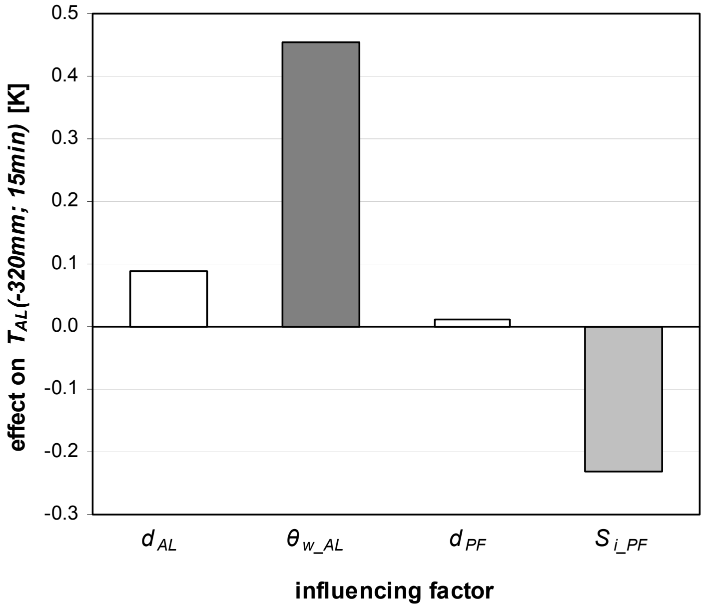

***Figure 3.30**: Effect of the four influencing factors on the temperature at the base of the active layer (i.e. –320 mm below its surface) 15 minutes after beginning the experiment. Dark grey shading indicates significance at the 99.9%-level, light grey shading at the 99%-level.*

The positive effect of θ_{w_AL} and the negative effect of S_{i_PF} on the temperature at the active layer base T_{AL}*(-320 mm)* 15 minutes after beginning the experiment and on the temperature step caused by depositing the active layer material at the permafrost surface ΔT_{PF}*(-1 mm)* is due to differences in the volumetric heat capacity; it is more than three orders of magnitudes higher for water and ice than for air. At a given rate of heat transfer from the active layer to the permafrost this implies a slower decrease of T_{AL}*(-320 mm)* for a moist active layer compared to a dry one but a faster decrease for an ice saturated permafrost body than an ice free one. As much more heat is transferred to the permafrost from a moist active layer, ΔT_{PF}*(-1 mm)* therefore has to be higher. However, as the effective heat capacity of an ice saturated permafrost body is higher than that of an ice free one, ΔT_{PF}*(-1 mm)* has to be higher for the former than the latter case.

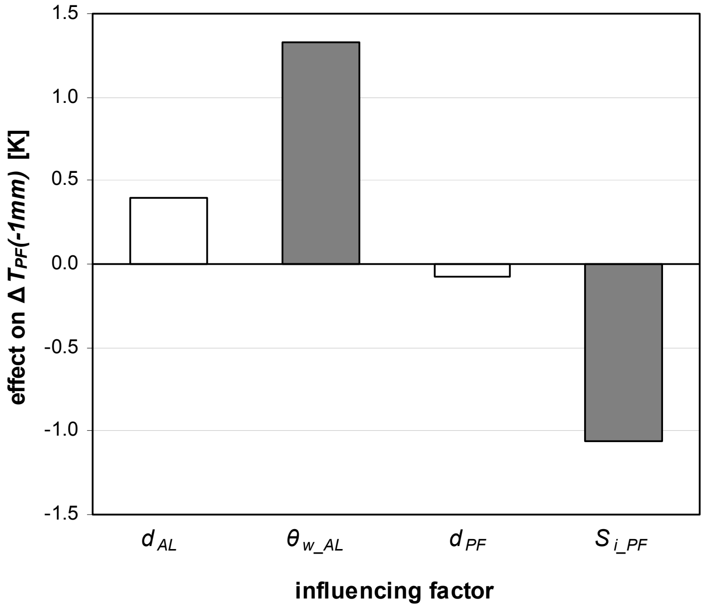

***Figure 3.31**: Effect of the four influencing factors on the temperature step at the permafrost surface (or rather 1 mm below) due to depositing the active layer material on it. Grey shading indicates significance at the 99.9%-level.*

Volumetric water content

When the active layer is initially dry, the volumetric water content θ_{w_AL} is trivial as it remains at zero during the whole experiment and therefore only an analysis of the three other factors' effects for a moist active layer (θ_{w_AL} = 15%) makes sense. According to the 2^{4-1} experimental design four different factor step combinations for a moist active layer were investigated. To quantify the effects of three influencing factors with two steps each a 2^{3-1} experimental design is necessary. However, the four investigated factor step combinations for a moist active layer (systematic experiments 3, 4, 7, 8) are not the same as would be needed for a 2^{3-1} experimental design. Therefore the statistical significance of the effects of the three factors d_{AL}, d_{PF} and S_{i_PF} cannot be determined. However, a qualitative analysis of the distribution of the post experiment volumetric water content with depth $\theta_{AL}(z)$ for the four different factor step combinations is very meaningful concerning the factors' influence (Figure 3.32 and Figure 3.33).

The influence of the three factors can be analyzed by comparing two pairs of each two systematic experiments coinciding in the observed factor.

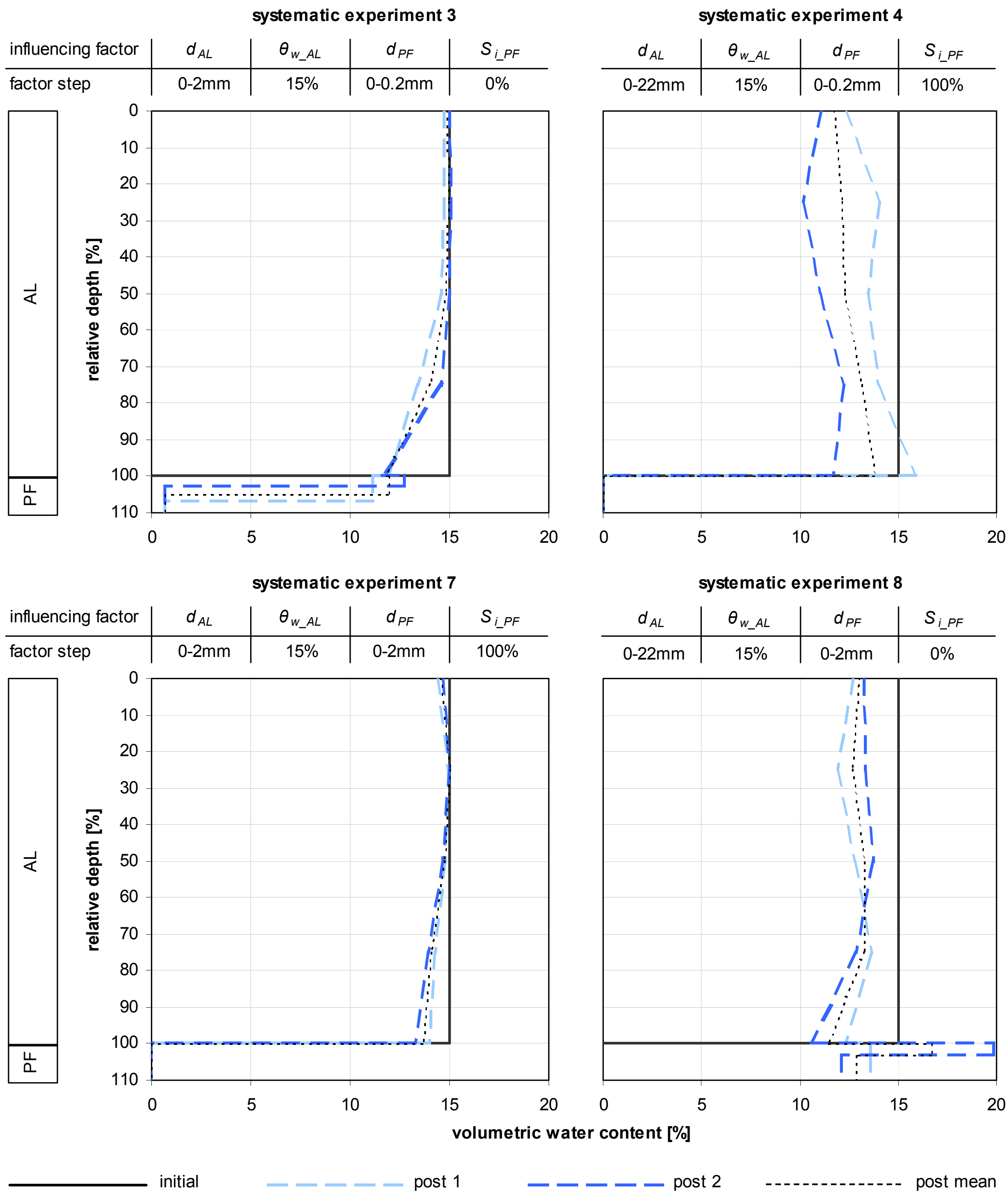

Figure 3.32: *Distribution of the volumetric water content with depth for the four systematic experiments comprising a moist active layer before (initial) and after (post) the experiment for the two replicates separately (post 1 and post 2) and for their mean (post mean). AL = active layer, PF = permafrost block.*

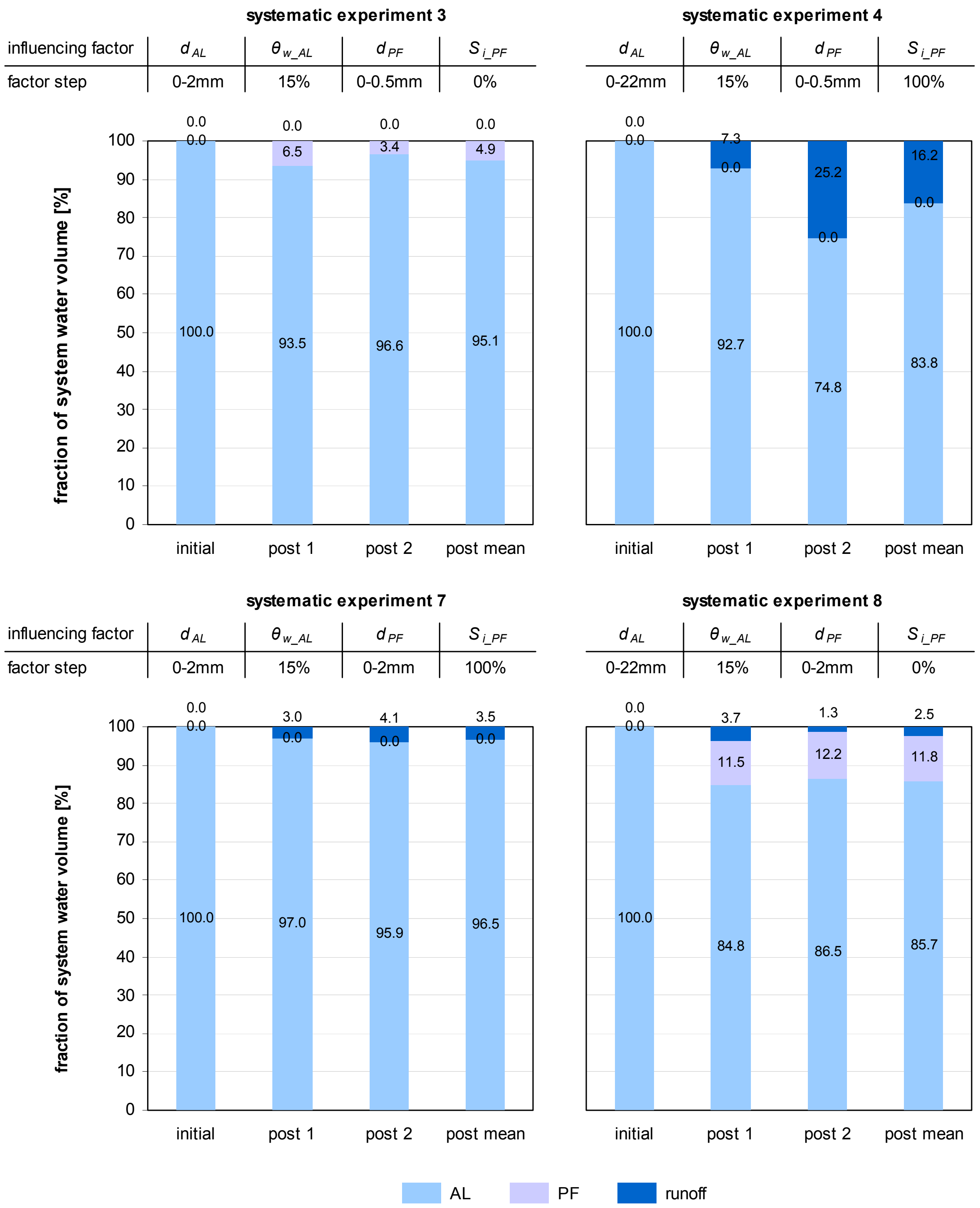

Figure 3.33: *Redistribution of the initial water volume (11 litres, equivalent to 100%) over the components* active layer *(AL),* permafrost block *(PF) and* runoff on the permafrost block *(runoff) before (initial) and after (post) the experiment for the two replicates separately (post 1 and post 2) and for their mean (post mean) comprising the four systematic experiments with* $\theta_{w\_AL} = 15\%$*. As the duration of the experiments was short and the air temperature low, the influence of evaporation could be neglected. AL = active layer, PF = permafrost block.*

Influence of grain size

A comparison of the systematic experiments 3 and 7 with 4 and 8 shows that an increasing grain size of the active layer d_{AL} lowers $\theta_{AL}(z)$. This is due to the higher field capacity of fine material than that of coarse grained material, which regulates the water loss of the active layer. The consequence of a higher water loss of the active layer depends on S_{i_PF}. For an ice saturated permafrost block the water runoff on the permafrost surface is increased (about four times from experiment 7 to 4). For an ice free permafrost block the water infiltration into the permafrost block below is increased (more than two times from experiment 3 to 8). In experiment 8 the amount of water released by the active layer was even too large to be completely infiltrated into the permafrost block. The remaining water therefore drained off the permafrost surface as runoff.

The influence of the grain size of the permafrost block d_{PF} is analyzed by comparing the systematic experiments 3 and 4 with 7 and 8. d_{PF} only has an influence on the water distribution if the pores of the permafrost block are not completely filled with ice, as it would otherwise be impermeable. As this is the case for the experiments 4 and 7, only experiments 3 and 8 can be compared to analyze the influence of d_{PF} on the water distribution. In both experiments an infiltration front could be recognized. However, when the permafrost material consisted of silty sand (experiment 3) it was more evident than when the material was sand (experiment 8). With sand more water infiltrated the permafrost than for silty sand which can be explained by the higher hydraulic conductivity of sand than of silty sand at the high prevailing water contents. However, the higher post experiment water content of the permafrost block in experiment 8 has already been explained by d_{AL} (see above). Therefore both factors d_{AL} and d_{PF} have an influence on these results, but due to the mixed effects their respective proportions cannot be quantified.

Influence of ice and water content

Comparing the experiments 3 and 8 with 4 and 7 reveals the influence of S_{i_PF} on the water distribution. Ice saturation of the permafrost (experiments 4 and 7) completely prevents water infiltration, i.e. its surface is impermeable. Therefore the whole amount of water released by the active layer was drained on the permafrost surface as runoff. However, runoff on the permafrost surface also occurs for ice free or partly saturated permafrost if the ratio at which the active layer releases water exceeds the infiltration ratio of the permafrost (experiment 8).

In experiment 7 θ_{AL} remained constant at a relative depth of about 30%, but decreased slightly towards the surface. As the decreasing influence on θ_{AL} declined with depth, the reason for this is probably evaporation. However, according to the $\theta_{AL}(z)$-curves this was only 60 ml or 0.58% of V_w and can therefore be neglected.

3.3.3 Discussion of systematic shear test series

Shear plane

In addition to shear tests within homogenous materials the present study showed that for the infinite slope model to be applied in laboratory experiments it is necessary to take into consideration the different characteristics of both layers - the mobile and the immobile. In this study the mobile layer was represented by the active layer and the immobile layer by the permafrost. Due to this two-layer-system the stability problem investigated here is governed by the frictional behavior at the interface of the layers, i.e. the shear plane. The friction at the interface between two solid bodies is physically determined by surface irregularities. In this study laser-generated surface measurement methods were applied allowing these irregularities of the permafrost surface acting as shear plane to be quantified. Thus, the grain size and the ice content could be linked to the surface characteristics of the shear plane and to its frictional behavior by means of the friction angle. The results showed that surface irregularities contribute to interface friction at different scales (waviness, roughness due to grains, asperities on grains). Therefore the method used here is a promising approach to investigate stability problems governed by interface friction.

Pore water pressure

Regarding the effect of the volumetric water content of the active layer on the friction angle it is important to take into account its short term variation in time. The suction for a water content up to a value for which Φ is at its maximum is therefore called the *apparent* cohesion. This apparent cohesion has at least a short term stabilizing effect on the slope. However, if the ground is already partly saturated, its capacity to absorb additional water (e.g. from rainfall) will be lower than in dry conditions. For a given time and infiltration rate the height of the water saturated zone above the ponding layer (in this case whether the surface of the actual permafrost or a finer grained layer ('past permafrost') is higher. Consequently, the pore water pressure and finally the uplift force will increase, reducing the friction between the ponding layer and the water conducting layer above and thus also the slope stability.

Dependence of friction on scale of shear plane profile

The friction coefficient between two bodies sheared off against each other is due to their surface irregularity. However, there are surface irregularities at many different scales and at each scale the irregularity contributes to the friction. In this respect, the additional friction, i.e. the shear strength due to dilatancy, merely contributes to the total friction (or shear strength) at one particular scale. Systematic shear tests are suggested for the future to quantify the relationship between surface irregularity and dilatancy. Furthermore, the irregularity of a surface can be compared with the porous structure of a soil; it also strongly depends on the scale, and at each scale the porous structure contributes to the hydraulic conductivity (Vogel et al. 2005). To derive the friction from the surface irregularity it is therefore essential to specify the scale by the cut-off wavelength the surface profile was filtered with, the measurement length and the resolution of the laser scanner. In this study the surface profile was only measured for the upper surface of the permafrost block. The laser scanner which was used, requires a free surface. As the underside of the active layer would have been altered if turned upside down, its surface profile could not be measured with the method used. However, as the analysis of the grain size effects on the friction angle showed, the grain size of the permafrost is more important than that of the active layer. It is remarkable that the irregularity of roughness profile 1 and 2 is not only influenced by the grain size, but also by the ice content. This is probably due to the grains being pushed apart from each other by the expansion of water during freezing. It has to be mentioned that the artificial permafrost surface is an extreme case insofar as it was made completely planar (macroscopically) by manual smoothing. In the field the permafrost surface in a scree slope is mostly more irregular and potentially interspersed with stones and rocks. However, as only a small element of a real slope was fictively selected for the laboratory simulation, this should be the weakest one which is responsible for a potential slope failure (i.e. a conservative scenario). To take into account the maximum shear strength of the interface between the permafrost and the active layer of a whole slope, the shear plane of the laboratory device has to have a minimum area, above which the surface irregularity remains constant. Analogously to the representative elementary volume (REV) this area could be called representative elementary area (REA). However, the determination of the detailed surface irregularities at the interface between the active layer and the permafrost in the field would be nearly impossible and the REA would be probably too large for the laboratory. It is therefore reasonable to anticipate the weakest slope element (with a size of the shear box) determined by the smallest grain sizes for a slope stability analysis.

Combined thermal and mechanical effect of water

The analysis of the ground temperatures showed that for θ_{w_AL} = 15%, $T_{AL}(-320\ mm)$ remained positive and for S_{i_PF} = 100%, $T_{PF}(-1\ mm)$ remained negative at least until failure occurred. Consequently, the influence of adfreeze between the active layer and the permafrost on Φ can be excluded, which is due to the initial permafrost surface temperature having been chosen close to 0°C. However, if the heat absorption capacity of the permafrost prior to thawing is higher (due to lower temperatures and a higher ice content), adfreeze will take place if the active layer base is moistened (by infiltration of snowmelt water, rainwater or downslope seepage on the permafrost surface). This is probable when insulation by the snow cover starts late in autumn (or winter). Slope stability will be increased as a consequence. Additionally, the experiments showed the warming effect of liquid water in frozen ground. When the heat absorption capacity of the permafrost is low (which occurs when insulation by the snow cover starts early in the autumn or in summer, when the thaw depth is greatest), the relatively warm water can melt and even erode the permafrost due to its additional shearing force caused by its current due to the hydraulic gradient. This combined thermal and mechanical effect of water can destabilize the slope.

Relevance of soil hydraulic properties on slope stability

The analysis of the water contents after the experiments confirmed that ice saturated permafrost acts as an impermeable layer. Snowmelt or rainwater infiltrated into the ground ponds on the permafrost surface and runs downslope on it. A saturated zone on the permafrost can thus be formed. Whether this is the case or not and the consequences it will have regarding slope stability, depends on the field capacity and the hydraulic conductivity of the active layer. Before the field capacity of the active layer is reached, the water will be totally absorbed by the active layer, which is probable for short, moderate infiltration periods; in this case no saturated zone will be formed. However, as soon as the volumetric water content in the active layer exceeds its field capacity, no more water can be absorbed and a saturated zone will form. Then the hydraulic gradient (corresponding approximately to the slope inclination) and the hydraulic conductivity are crucial for the drainage rate of the water on the permafrost and therefore for the height of the saturated zone. The higher the hydraulic gradient and the hydraulic conductivity (depending on water content) are, the lower the height of the saturated zone, the pore water pressure and the uplift force, and therefore the higher the remaining shear strength is.

Definition of failure

As the relation between the inclination angle and the collective downslope displacement showed, the final failure of the active layer (at Φ) does not occur abruptly as for a rigid body; it is rather indicated by many small pre-failures (due to rearranging and interlocking of the grains) resulting in a stepwise shearing or apparently continuous creeping. This raises the question of whether the definition of the final failure or Φ by the upper shear frame achieving the maximum shear distance of 120 mm is justified and reasonable, because it could be argued that the failure defined as the final one may just be another pre-failure. Indeed, although the threshold for the maximum shear distance is necessary for practical reasons, it is arbitrary, but not random. The trend of the curve for the relation between the inclination angle and the collective downslope displacement flattens out continuously, aspiring to a gradient of zero. Alternatively, the increasing rate of the displacement approaches infinity when the shear distance approaches infinity. Therefore the threshold for the maximum shear distance should be chosen where the increasing rate of the displacement is unacceptably high. The defined maximum shear distance is about three times the yearly surface displacement of the slope measured in the field (see chapter 2.3.4), to give an indication. However, this study focused on determining the effects of the influencing factors on Φ rather than absolute values for Φ. Therefore the comparability of the experiments was most important, which was satisfied by determining Φ in the same way each time.

Prediction of failure

The explanation for the positive effect of θ_{w_AL} on Φ by apparent cohesion is supported by the strong effect of θ_{w_AL} on q_{AL_min} and $d_{AL\_grad\_shear}$ demonstrating the suction between the active layer and the permafrost. The results of the deformation profiles also show that the granular material responds more plastically if containing water. This means that a failure of an active layer containing water is preceeded by important deformation, so if the slope deformation is carefully monitored, the danger can be recognized better than in the case of brittle failure.

Transferability of results

As the grain sizes chosen for the active layer and the permafrost in the experiments are typical for alpine scree slopes in permafrost terrain (compare e.g. Springman & Teysseire 2001, Arenson et al. 2002, Springman et al. 2003), a wide range of realistic field cases are already covered. However, with a broader data base gained by experiments using an inclinable shear box, a model could be developed which allows the determination of Φ (between active layer and permafrost) depending on d_{AL}, d_{PF}, θ_{w_AL} and S_{i_PF}. In addition, the internal friction angles of the homogenous and dry active layer and permafrost material should be measured using a plane shear box or a triaxial shear apparatus (e.g. Arenson et al. 2004). This would allow Φ to be determined based on these parameters.

3.3.4 Summary of systematic shear test series

A series of systematic shear tests were performed in the climate chamber using an inclinable shear box at the scale 1:5 compared to the thickness of the active layer at the field study site (chapter 2). The lower shear frame contained the artificial permafrost block, the upper shear frame the artificial active layer. In these experiments the influence of (1) the grain size of an artificial active layer and (2) of the permafrost block, (3) the volumetric water content of the active layer and (4) the degree of ice saturation of the permafrost on the friction angle between the two layers were investigated and analyzed statistically. All four factors had a significant positive effect on the friction angle. The degree of ice saturation proved to be the most important influencing factor. When the grains at the permafrost surface were imbedded in an ice matrix, the friction angle was eight degrees higher than for a dry permafrost block without ice. This result implies a probable long term decrease of the active layer slope stability in alpine permafrost terrain under conditions of global warming. When the active layer deepens into finer grained material which was previously fixed in the ice matrix of the permafrost, the shear strength and therefore the slope stability will be reduced. This will increase the probability of active layer slope failures in steep scree slopes situated in permafrost terrain.

3.4 Physical simulation of thaw-induced failure of the active layer

For the systematic shear test series the thermal and hydrological conditions during a single experiment were kept constant and the angle was changed until failure occurred. For the simulation of a thaw-induced failure of the active layer, the inclination angle of the simulated slope was kept constant and the thermal and hydrological conditions were changed until failure occurred.

3.4.1 Methods for simulation of thaw-induced active layer failure

Experimental setup

The experiments were conducted in the SLF climate chamber with the air temperature varying between -3°C and 20°C. The permafrost block was produced at an air temperature of -5°C (lowest possible temperature of climate chamber). To simulate solar radiation, neon light was used providing a maximum radiation flux of 43 W/m^2.

For the physical simulation of a thaw-induced active layer failure a scale 1:2-shear box was used (Figure 3.34). As the volume and therefore the load of the filled 1:2-shear box is one order of magnitude greater than that of the 1:5-shear box, the device is mainly made of steel. Two L-shaped, braced steel girders connected by crossbeams form the fixed array for the slope adjustment. The lower shear frame is inclinable via a cable winch and contains the artificial permafrost block, which is 1.15 m long, 1.00 m wide and 0.19 m deep. The upper shear frame containing the artificial active layer is on guiding rails mounted onto the lower shear frame and held by ball bearing sleeves at the four edges of the upper shear frame. This allows the upper shear frame to slide downslope with hardly any friction induced by the measuring device itself. The side walls of the upper shear frame consist of 8 mm thick acrylic glass panels which allow observation of the processes within the artificial active layer. At the rear and front the active layer is framed by vertical water resistant wooden panels; its longitudinal section is therefore a parallelogram. As the vertical panels are parallel to the direction of infiltration, they avoid unnatural conditions with an excessively wet wedge in the active layer at the front of the upper shear frame and a nearly dry wedge at the rear side. The lowermost 10 cm of the front panel framing the active layer consists of a perforated steel sheet coated with a textile filter. This allows the water in the active layer to drain freely on the permafrost surface while the solid material is retained.

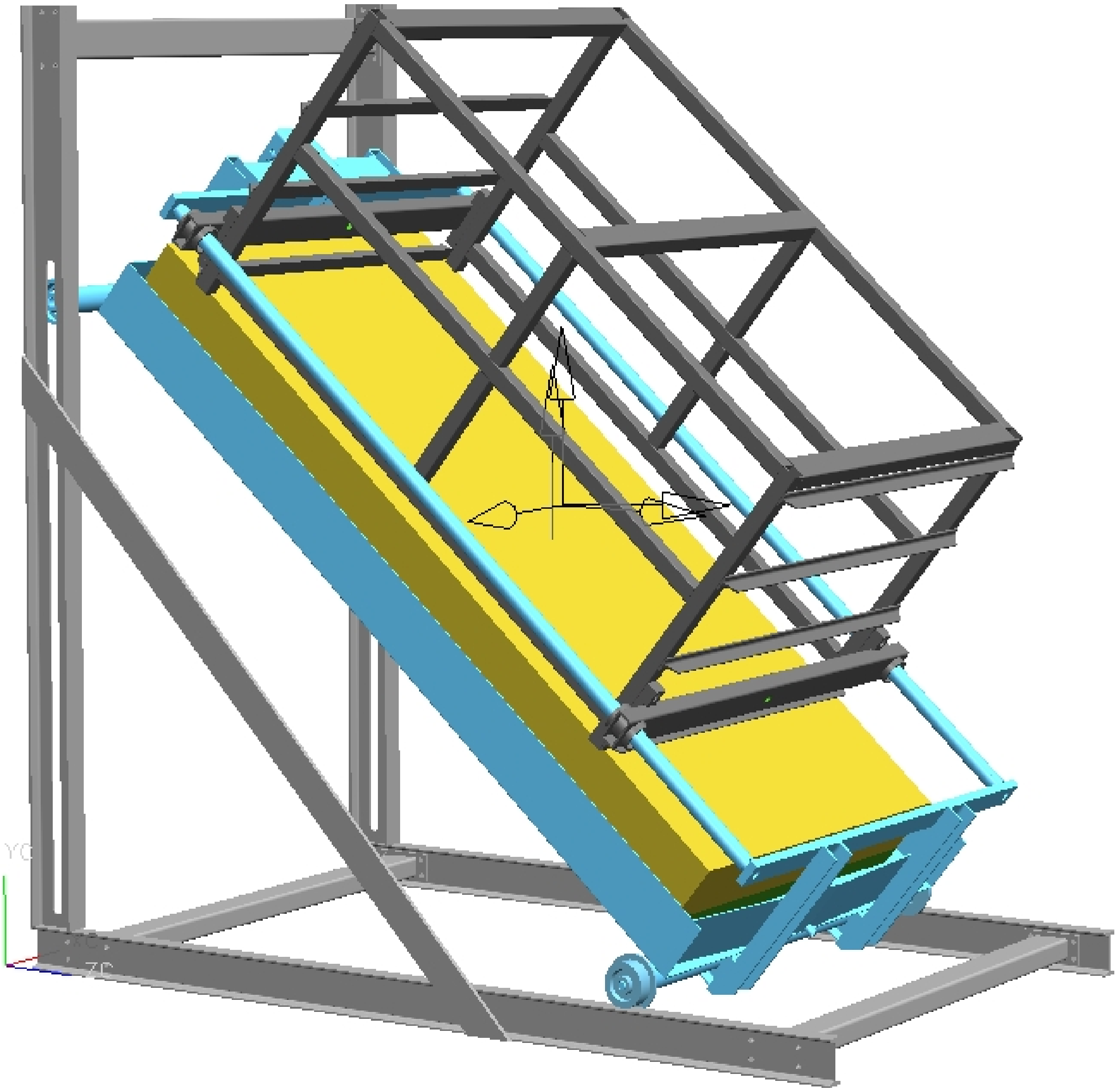

***Figure 3.34**: Scale 1:2-shear box used for the physical simulation of a thaw-induced active layer. The scale refers to the depth of the active layer at the field study site (see chapter **2.2.3**). Note that this shows only the steel construction of the shear box to which wooden panels were mounted limiting the permafrost block and the active layer as shown in Figure 3.35.*

The active layer is 0.75 m thick (normal to shear plane), 0.75 m long (downslope direction) and 1.00 m wide (Figure 3.35). The inclined infiltration area (active layer surface) therefore is 0.75 m^2, the horizontal infiltration area 0.60 m^2. To compensate the downslope force (minus the friction) of the upper shear frame itself when inclined, it was connected with a counterbalance (box filled with the equivalent mass of gravel) via a steel cable over a roller.

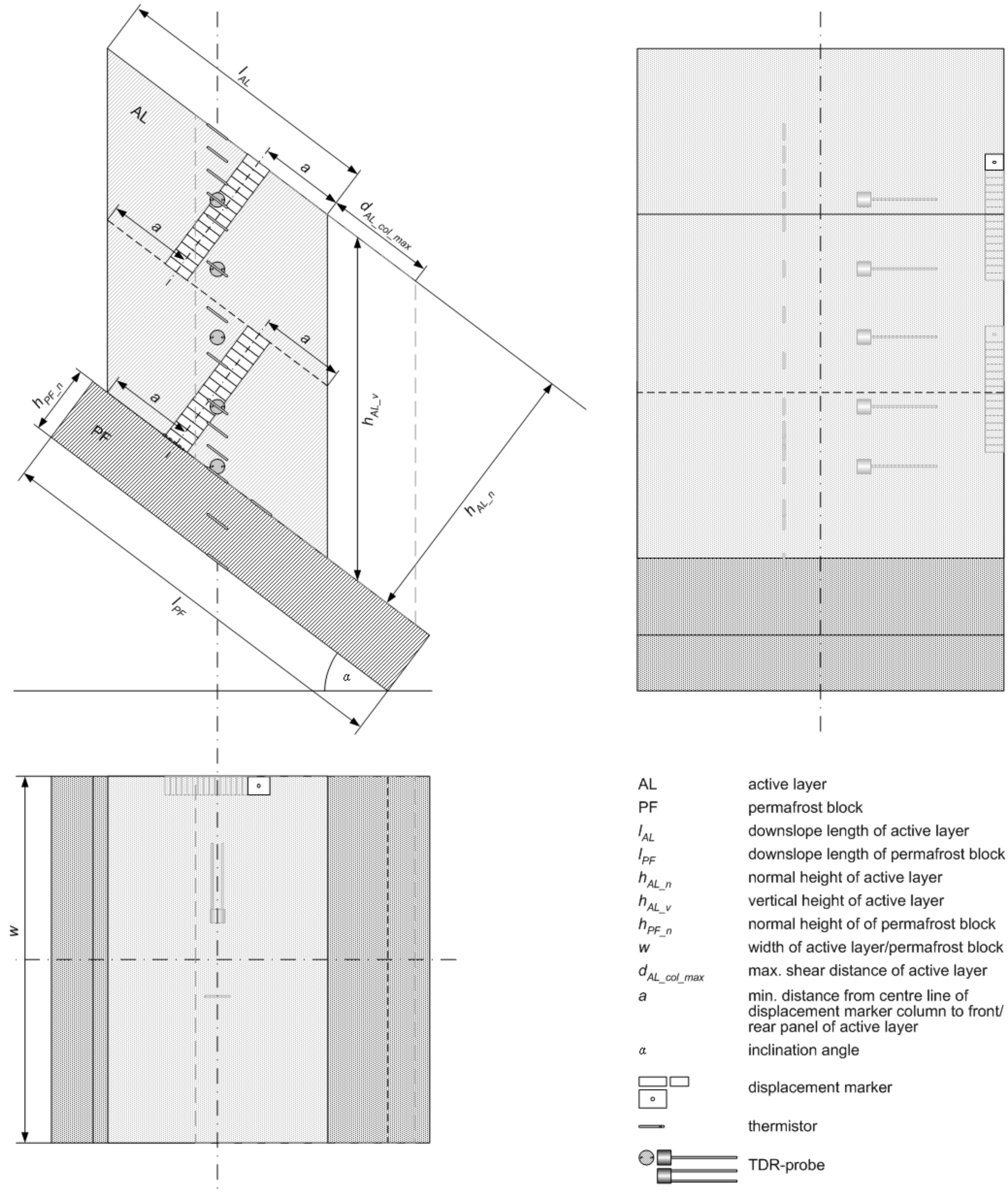

***Figure 3.35**: Geometry of simulated active layer and permafrost and position of embedded probes.*

Experimental parameters

The experimental parameters are divided into the parameter groups *constants, initial conditions, factors and resulting variables* (Table 3.11). Constants are parameters which were kept constant during the whole experiment. Initial conditions are parameters which were set at the beginning of the experiment, but could vary during its course. In contrast to the systematic shear test series where the initial conditions were kept constant from one experiment to the next, the initial conditions for this simulation could not be included in the constants as there is only one experiment. Factors are parameters which were regulated during the experiment. Resulting variables are parameters which were measured during the experiment. Correlations between factors and resulting variables could be analyzed by means of a time series.

Table 3.11*: Overview of experimental parameters. For the temporal course of the factors see Figure 3.36.*

parameter group	parameter	notation	unit	value(s)			
constants	inclination angle of shear box	α	°	37.0			
	grain size near surface of active layer (0-15cm depth)	$d_{AL}(0\text{-}15cm)$	mm	16-22 (grit)			
	grain size in lower part of active layer (15-75cm depth)	$d_{AL}(15\text{-}75cm)$	mm	0-22 (gravel)			
	grain size of permafrost layer	d_{PF}	mm	0-2 (sand)			
	maximum shear distance of upper shear frame	$d_{AL\_col\_max}$	mm	300			
	temperature of infiltration water	T_w	°C	0.0			
initial conditions	volume of active layer	$V_{AL}(0h)$	l	562.5			
	volume of permafrost layer	$V_{PF}(0h)$	l	218.5			
	actual dry apparent density near surface of active layer (0-15cm depth)	$\rho_{AL}(0\text{-}15cm,0h)$	kg/m^3	1370			
	actual dry apparent density in lower part of active layer (15-75cm depth)	$\rho_{AL}(15\text{-}75cm,0h)$	kg/m^3	1704			
	actual dry apparent density of permafrost layer	$\rho_{PF}(0h)$	kg/m^3	1767			
	relative dry apparent density near surface of active layer (0-15cm depth)	$I_{D\_AL}(0\text{-}15cm,0h)$	-	0.17			
	relative dry apparent density in lower part of active layer (15-75cm depth)	$I_{D\_AL}(15\text{-}75cm,0h)$	-	0.01			
	relative dry apparent density of permafrost layer	$I_{D\_PF}(0h)$	-	0.38			
	ground temperature of active layer and permafrost	$T_{AL/PF}(0h)$	°	-3.0			
	volumetric water content near surface of active layer (0-15cm depth)	$\theta_{AL}(0\text{-}15cm,0h)$	%	0.1			
	volumetric water content in lower part of active layer (15-75cm depth)	$\theta_{AL}(15\text{-}75cm,0h)$	%	0.9			
	degree of volumetric ice saturation of permafrost layer	$S_{i\_PF}(0h)$	%	100			
factors	infiltration rate as function of time	$I(t)$	mm/h	0	10	20	40
	set ambient air temperature as function of time	$T_{air\_set}(t)$	°C	-3	0	10	20
	radiation flux as function of time	$J(t)$	W/m^2	0	13	43	
resulting variables	vertical distance of permafrost surface profile to reference level as function of horizontal distance	$y_{PF\_s}(x)$	mm	measured			
	collective downslope displacement of upper shear frame as function of time	$d_{AL\_col}(t)$	mm	measured			
	internal downslope displacement of active layer as function of depth (depth interval 25mm) and time	$d_{AL\_int}(z,t)$	mm	measured			
	perpendicular displacement of active layer near surface (0-15cm) as function of time	$d_{AL\_per}(t)$	mm	measured			
	actual ambient air temperature during experiment as function of time	$T_{air\_act}(t)$	°C	measured			
	ground temperature of active layer (AL) and permafrost (PF) at depth z below AL/PF surface with z[cm] = 0, 15, 30, 45, 60, 75 for AL and 10, 19 for PF as function of time	$T_{AL/PF}(z,t)$	°C	measured			
	volumetric water content of active layer at depth z below active layer surface with z[cm] = 0, 15, 30, 45, 60, 75 as function of time	$\theta_{AL/PF}(z,t)$	%	measured			
	height of water saturated zone above permafrost surface	h_w	*mm*	measured			
	water discharge at front of permafrost surface as function of time	$Q(t)$	*l/s*	measured			
	evaporation rate over free water surface at water and air temperature T with T[°C] = -3, 0, 10, 20 as function of time	$W(T,t)$	mm/h	measured			

Constants

In order to simulate a thaw-induced failure of the active layer under conditions similar to those at the field study site, the same inclination angle as in the field (37°, see chapter 2.1) was chosen and kept constant in the laboratory experiment. Also the grain size distribution with depth in the field was simulated in the laboratory: coarse material (grit) practically devoid of fine particles in the uppermost part of the active layer near the surface, which drains well and therefore prevents surface runoff, coarse material with the pores filled with fine particles (gravel) in the lower eighty percent of the active layer and fine material (sand with a relevant silt fraction) in the permafrost. In fact the scree at the field study site also contains grain sizes higher than 63 mm (cobbles, stones and blocks), especially near the ground surface. However, the effect of such coarse single grains would have been too high in relation to the size of the shear box, i.e. the granular material would no longer have been homogenous macroscopically, the degree of chance therefore unacceptably high and the results not repeatable. As the slope stability is generally increased with an increasing grain size, the results of such laboratory experiments reveal minimum values of the relevant parameters for a thaw-induced failure of the active layer. Thus, the simulation is on the conservative side for the assessment of slope stability at the field study site. The maximum shear distance of the upper shear frame was chosen in the same relation to the height of the active layer as for the 1:5-shear box and is about one third of the total height of the shear box (upper and lower shear frame together). In order to keep the temperature of the water used for the simulation of the infiltration during snowmelt constant at 0°C (as is the case in the field), a snow-water mixture was used and stirred regularly.

Initial conditions

The volumes, the actual and relative dry apparent densities of the permafrost block and the active layer could change during the experiment by settlement, dilation and abrasion. The initial values at the beginning of the experiment are therefore given for these volumes in Table 3.11. The actual dry apparent densities were determined by weighing the dry material for the distinct layers with a given volume separately. Using the volumes and densities the level of the effective normal stress could be calculated to be about 15 kN/m^2. The initial ground temperatures of the active layer and the permafrost were chosen within the ground temperature range measured at the field study site directly before snow meltwater infiltration. The initial volumetric water contents (before freezing) of the active layer were measured gravimetrically by means of samples of at least 1000 g taken whilst filling the active layer material into the upper shear frame, at depths of 0, 15, 30, 45, 60 and 75 cm below the active layer surface. The active layer was practically dry at the beginning of the experiment, as the granular materials were stored in a dry ventilated room several months before the experiment. As ice saturated conditions near the permafrost surface are widespread in Alpine permafrost regions (Vonder Mühll et al. 2000), the permafrost block in the laboratory simulation was also saturated with ice.

Factors

In a first step, the infiltration of snow meltwater into the frozen ground was simulated at an ambient air temperature of 0°C (Figure 3.36) in order to observe at which infiltration rate the active layer would fail. The infiltration was started at a rate of 10 mm/h, which is equivalent to an extraordinary heavy rainfall (Springman et al. 2003), but still lower than the maximum value measured at the field study site during the snowmelt period (about 13 mm/h; see chapter 2.3.2). During the extreme rainfall events at the end of August 2005 in the European Alps short-term peak values (hourly sum) of 16 mm/h were measured in the region of Gasen/Haslau (Styria, Austria, Lang et al. 2006, by unpublished data from the Hydrographic Service of Styria, www.wasserwirtschaft.steiermark.at). In two further steps the infiltration rate was doubled each time to simulate the successive increase of meltwater infiltration after the begin of snowmelt, as observed in the field (see chapter 2.3.2). At night the ambient air temperature was set at –3°C during the infiltration period in order to simulate night frost. The water was pumped through a micro drip system (Gardena) comprising of 30 drip elements which were evenly distributed over the inclined infiltration area of the active layer surface. The pressure regulated drip elements supply exactly 2 l/h each, i.e. 30 x 2 l/h = 60 l/h over an area of 0.6 m^2, so 100 l/(m^2h) = 100 mm/h. To attain the required infiltration rate the water pump was temporally regulated, using time intervals of five minutes; a rate of 10 mm/h for example could be attained by the pump supplying water for 30 seconds within the time interval. The infiltration is therefore inhomogeneous over time. However, this effect is strongly dampened due to the hydraulic conduction and storage properties of the soil, and is thus negligible. In addition, the long term infiltration rate would have been much more inaccurate, if non pressure regulated drip elements were used and the water supply was controlled by a throttle valve. The infiltration rate was set to the next higher value as soon as the water discharge remained constant. The influence of radiation could not be completely eliminated, due to the illumination of the climate chamber during the infiltration periods (Figure 3.36).

To simulate rapid thawing of the active layer after the end of snowmelt in late spring, when the warming atmosphere and the increasing solar radiation directly influence the ground surface temperature, the air temperature in the climate chamber was increased in two steps and the artificial radiation was set at the maximum possible value (Table 3.11 and Figure 3.36). During the simulation of active layer thawing under snow free conditions the lowering of the air temperature during the night was omitted in order to accelerate the thawing process which therefore became a time-lapse simulation.

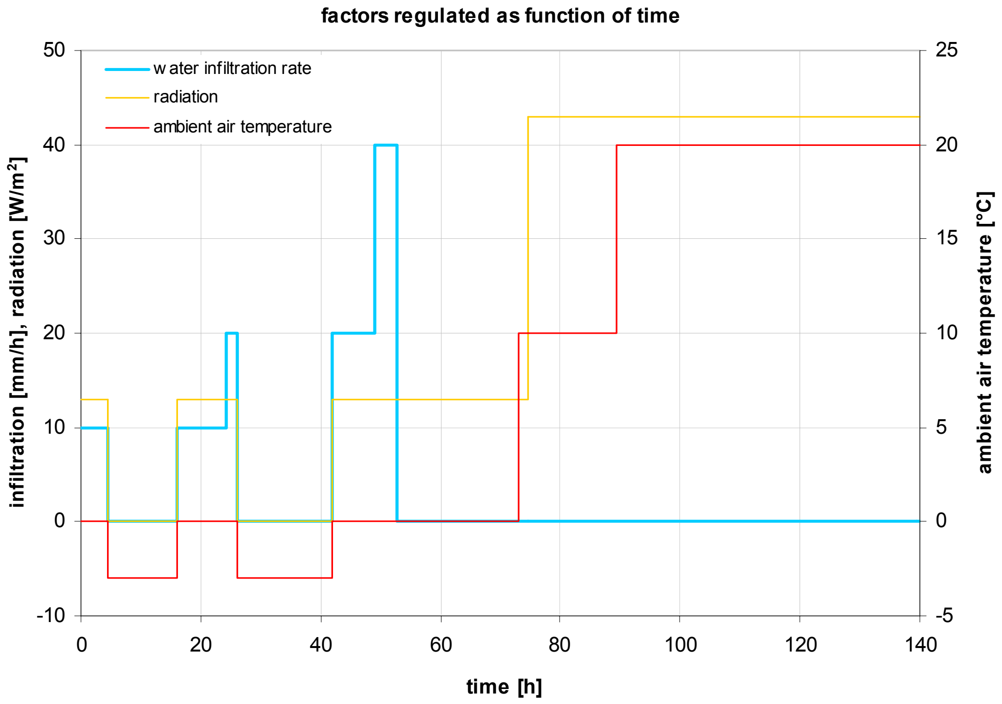

Figure 3.36: Temporal course of the regulated factors during the physical simulation of a thaw-induced failure of the active layer.

Permafrost surface profile

The permafrost surface profile was measured and analyzed in the same manner as described for the systematic shear test series (page 61). However, in order to capture the variability of the profile over the width of the permafrost surface, five sections were scanned in this case. The sections were 400 mm long and started at a distance of 200 mm from the rear end of the permafrost block. The central section was situated along the longitudinal center line of the permafrost surface, the others were oriented parallel at a distance of 37.5 mm and 500 mm to the left and right.

Collective downslope displacement

An ultrasonic sensor (Baumer electric, UNAM 3019 197/S14) was mounted in front of the lower shear frame to measure the distance to the front of the upper shear frame with a frequency of 10 s^{-1} in order to capture the moment of failure. Data were recorded automatically in a laptop. To reduce data processing, minute means were calculated besides the moment of failure. The actual collective downslope displacement was calculated as being the difference between the initially and actually measured distance.

Internal downslope displacement

The internal downslope displacement depending on depth (i.e. the deformation profile of the active layer) was measured using the method of displacement markers (see page 75) and the dimensions of the single displacement markers were enlarged by a factor of 2.5 in this case (75 mm long, 50 mm wide, 25 mm high). As the vertical longitudinal section of the active layer is not a rectangle but a parallelogram, a column of displacement markers normal to the shear plane would result in very short distances from the uppermost and lowermost displacement marker to the front and rear vertical borders of the parallelogram respectively. In these positions the markers would not reveal a representative deformation profile of the active layer, because their displacement would be hindered strongly by the borders. Two columns were therefore embedded in the active layer, for the upper and lower halves of the active layer depth (normal to shear plane). Each column was positioned so that the distance from the uppermost marker to the front border of the parallelogram was equal to the distance of the lowermost marker to the rear border. This distance (referring to the middle of longitudinal axis of the markers) is

$$a = \frac{1}{2}\left(l_{AL} - \frac{1}{2}\tan\alpha \cdot h_{AL\_n} \right) \tag{3.42}$$

where l_{AL} is the downslope length of the active layer, h_{AL_n} the height of the active layer normal to the shear plane and α the inclination angle (Figure 3.35). Thus, a is 23.4 cm.

The deformation profile was measured for each set factor combination, i.e. at the initial state (shear box horizontal), after inclining the shear box, after infiltrating at a rate of 10, 20, 40 mm/h and after thawing at an ambient air temperature of 10°C and 20°C. The influence of each factor combination on the internal downslope displacement therefore could be determined.

Dilatancy

In order to quantify the effect of dilatancy (see page 85) at failure, a part of the near surface grit layer visible through the transparent side wall and a ruler for scaling were recorded with a video camera during the whole experiment. In the video sequence showing the main failure, the time dependent vertical displacement of ten randomly chosen grit grains were measured using the image processing software *image J*. The vertical displacement was then converted into displacement perpendicular to the shear plane and related to the collective downslope displacement for the equivalent period of time. The dilatancy angle could finally be determined as steepest gradient in the gained curve relating the perpendicular to the downslope displacement.

Air and ground temperature

For the temperature measurements the same calibrated thermistors and data logger (Campbell Scientific CR10X) were used as in the systematic shear test series (page 76). Temperatures were recorded at 10 second intervals. Due to the limited storage capacity of the data logger the temperatures could not be recorded continuously. The position of the thermistors within the active layer and the permafrost is shown in Figure 3.35. The air temperature was measured to control the set value.

Water discharge

The water discharge was determined manually. The water draining from the permafrost surface was collected via a drain leading into a plastic container in front. The discharged water volume ΔV_{dis} depending on time t and collected within a time interval Δt was determined by weighing it using a balance with a resolution of 10 g (equivalent to a volume of 10ml) and dividing this mass by the density of water. The water discharge rate was calculated as

$$q(t) = \frac{\Delta V_{dis}(t)}{\Delta t \cdot A_{AL\_hz}} \tag{3.43}$$

where A_{AL_hz} is the horizontal area of the active layer surface or base. During infiltration and at least two hours thereafter the measuring interval was ten minutes; otherwise it was suited to the discharge present. The sediment delivery ratio was negligible.

Volumetric water content

The volumetric water content of the active layer was determined at five different depth using the technique of time domain reflectometry (TDR). The TDR-probes were embedded in the active layer as shown in Figure 3.35. They measure the relative permittivity ε_{rc} of the surrounding material composed (index c) by different phases. ε_{rc}-values were recorded with a data logger (Campbell Scientific CR10X) at 2 minute intervals. The strong dependence of ε_{rc} on the volumetric water content θ_v allows to calculate θ_v using the algorithm of Roth et al. (1990) for which no calibration of the probes is required. Accordingly,

$$\theta_v = \frac{\left(\frac{\varepsilon_{rc}}{\varepsilon_{rw}(20°C)}\right)^{\alpha} - (1-e)\cdot\left(\frac{\varepsilon_{rs}}{\varepsilon_{rw}(20°C)}\right)^{\alpha} - e\cdot\left(\frac{\varepsilon_{ra}}{\varepsilon_{rw}(20°C)}\right)^{\alpha}}{\left(\frac{\varepsilon_{rw}(T)}{\varepsilon_{rw}(20°C)}\right)^{\alpha} - \left(\frac{\varepsilon_{ra}}{\varepsilon_{rw}(20°C)}\right)^{\alpha}} \tag{3.44}$$

where ε_r is the relative permittivity of air (index a), mineral soil (index s) and water (index w) depending on the temperature T, α the geometry parameter and e the porosity of the granular material. According to the Weast & Astle (1982) $\varepsilon_{rw}(T)$ is given by

$$\varepsilon_{rw}(T) = 78.54\cdot\left[1 - 4.579\cdot10^{-3}\cdot(T-25) + 1.19\cdot10^{-5}\cdot(T-25)^2 - 2.8\cdot10^{-8}\cdot(T-25)^3\right] \tag{3.45}$$

The temperature at the depth of the TDR-probes was measured (see above) or interpolated in case of spatial or temporal data gaps. The other parameters remained constant during the experiment or varied marginally in terms of their influence on the volumetric water content. According to Roth et al. (1990) $\alpha = 0.46$ (generally valid for soils), $\varepsilon_{ra} = 1.0$ and $\varepsilon_{rs} = 3.9$ for mineral soils. The porosity e was calculated as

$$e(z) = 1 - \frac{\rho_{AL}(z)}{\rho_r} \tag{3.46}$$

where z is the depth below the active layer surface, ρ_{AL} the actual dry apparent density of the active layer (see Table 3.11) and ρ_r the real density of the solid material (see Table 3.1).

Saturated zone

The height of the water saturated zone above the permafrost surface is equivalent to the hydrostatic pressure if no excess pore water pressures are assumed. It was measured with a mini-piezometer.

A thin horizontal tube was mounted at the side wall of the upper shear frame perpendicular to the downslope direction directly above the permafrost surface. It connects the saturated zone inside the upper shear frame with a vertical piezometer-tube outside. The gap between the horizontal tube and the notch in the side wall of the upper shear frame was sealed with grease to avoid water leakage. The end of the tube located in the saturated zone of the active layer was covered with a permeable filter. The other end was fixed to the vertical tube via a sealed connection. According to the physical law of communicating tubes, the height of the water saturated zone above the permafrost surface equals the height of the water level in the vertical tube. It was measured by means of an ultrasonic probe situated on top of the vertical tube. The measured values were recorded at 2 minute intervals.

Evaporation

The volume of the evaporated water V_{evap} was estimated depending on the ambient air temperature T_{air} gravimetrically (resolution of balance: 0.1 g) over a free water surface with an area A_w of 1525 cm^2 for the time t of three and a half hours. According to Kraus (2001) the evaporation over ground is about the half as over a free water surface. The evaporation rate W_g over the surface of the active layer was therefore determined as

$$W_g\,(T_{air}) = \frac{V_{evap}}{2\,t\,A_w} \tag{3.47}$$

Experiment preparation and procedure

Permafrost block

The gaps in the lower shear frame were sealed with silicon and the lowermost thermistor at the base of the permafrost block was fixed onto the base plate of the lower shear frame. Saturated sand was filled into the lower shear frame and poured up a little higher than the side boards. The material was then compacted using a concrete vibrator. Excess material was scraped off with a wooden board guided by the side boards. To install the second thermistor a vertical slot was cut into the compacted sand and closed again. The level of the sand surface was measured with a spirit balance. During freezing of the saturated sand at –5°C a few millimeters of frost heave occurred due to the volumetric expansion at phase change. The permafrost surface was therefore thawed using a gas burner, the excess material removed and the surface leveled again. Finally the permafrost block was frozen again at –5°C. This procedure was repeated until no excess material remained, i.e. the upper shear frame could slide freely over the permafrost surface, and the surface was level. Thereafter the temperature of the permafrost block was adjusted to –3°C (Table 3.11).

Active layer

First the gaps in the upper shear frame itself were sealed with silicon, then the gap between the upper and lower shear frame was sealed with grease to prevent leakage of water and fine solid material and to enable the sliding displacement of the upper shear frame. To prevent an early movement of the upper shear frame during the filling of the active layer material, it was temporarily fixed in its initial position relative to the lower shear frame. The granular material provided for the active layer was stored in a dry ventilated room several months before the experiment. Then the nearly dry material was pre-cooled outside at negative temperatures in order to prevent thawing of the permafrost block when pouring the active layer material on it. This was done when the lower column of displacement markers had been positioned normal to the shear plane by spiking them on steel rod which was temporarily fixed to the upper shear frame. The active layer material was filled into the horizontal shear box in layers. After half of the filling height had been reached, the second column of displacement markers for the upper half of the active layer was installed in the same manner. The thermistors and TDR-probes were also embedded in the active layer at the positions shown in Figure 3.35 and Table 3.11.

Inclination

Before inclining the shear box the counterbalance box was coupled onto the upper shear frame via a steel cable over a roller in order to compensate its downslope force. The shear box was then carefully inclined via a cable winch until the constant slope angle of the experiment was reached (see Table 3.11).

Insulation

After the end of the simulated infiltration of snow meltwater the whole shear box besides the active layer surface and the free surface at the front of the permafrost block was tightly covered with 20 cm thick polystyrene insulation panels (thermal conductivity: 0.039 W/mK) to allow simulation of the thawing of the active layer from above by air temperature and radiation. A small window of about 0.1 m^2 was left open to film the near surface grit layer for the determination of vertical displacements (see page 117). As the free permafrost surface in front of the active layer decreased during the shearing process it was insulated with flexible bubble bags.

3.4.2 Results of simulation of thaw-induced active layer failure

Permafrost surface profile

In this experiment the surface parameters are used to characterize the single permafrost surface profile which acts as failure plane (Figure 3.37 and Figure 3.38).

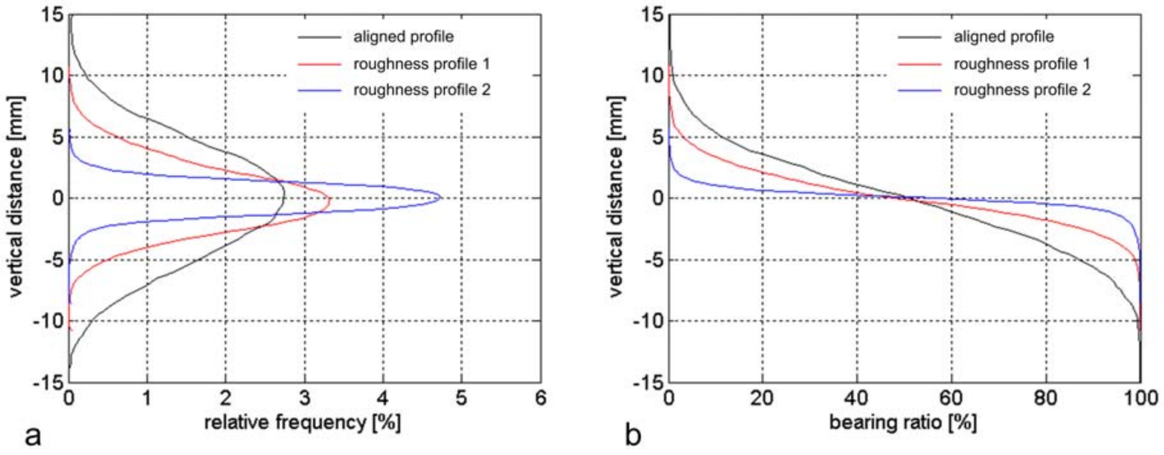

Figure 3.37: *Amplitude distribution functions (a) and bearing ratio curves (b) of the scanned surface profile with median values for the variance and skewness of the amplitude distribution and the maximum slope of the bearing ratio curve at the scale of roughness profile 1.*

As Figure 3.38 and Figure 3.37 show, the parameters to describe the surface of the permafrost block strongly depend on the observed profile scale. A comparison of the R_q values of the aligned and the filtered profiles indicates that the roughness would be far overestimated without filtering out the waviness. Analog conclusions can be made regarding the amplitude distribution functions and the bearing ratio curves. The irregularities caused by the manual smoothing of the permafrost surface are reflected by the aligned profile, thus they are not relevant for the roughness of the failure plane. The median value 0.5 for the ratio $R_{pm}/R_{z(DIN)}$ means that the profile valleys and peaks have the same shape.

The deviations of λ and ζ for waviness profile 1 from the equivalent results of the systematic shear tests (see Figure 3.17) have to be ascribed to statistical spread, because the values for silty sand (which contribute to these results) do not differ significantly from those for sand

(Table 3.10). The other differences (concerning λ and ζ) between the experiments with the 1:2- and 1:5-shear box can be explained by the effect of the grain size and the degree of ice saturation. In addition, the analyzed surface profiles of the experiments with the 1:2-shear box show that the values of ζ not only increase with the scale becoming finer, but also the range of values clearly decreases.

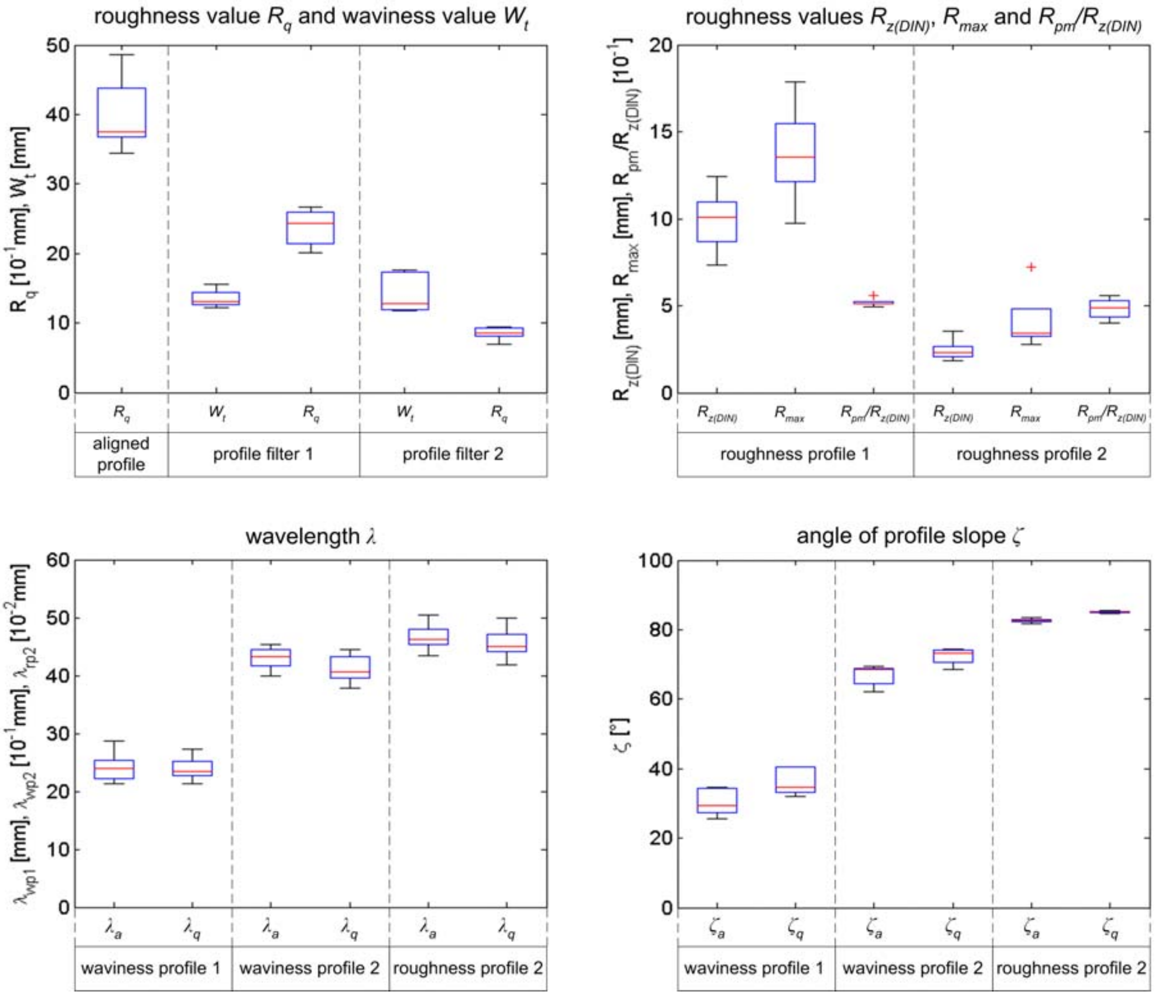

***Figure 3.38**: Box & whisker plots for the parameters characterizing the surface of the permafrost block. The blue box indicates the lower and upper quartile value, the red line is the median. The black whiskers show the extent of the data. Outliers are indicated by a red +. The indices wp1, wp2 and rp2 refer to waviness profile 1 and 2 and roughness profile 2. Note the modified scale of the y-axis for wp2 and rp2. Number of replicates n = 5.*

Collective downslope displacement

Time scale of hours

The collective downslope displacement over the complete displacement range of 300 mm depending on time is described by a sigmoid curve (black line in Figure 3.39).

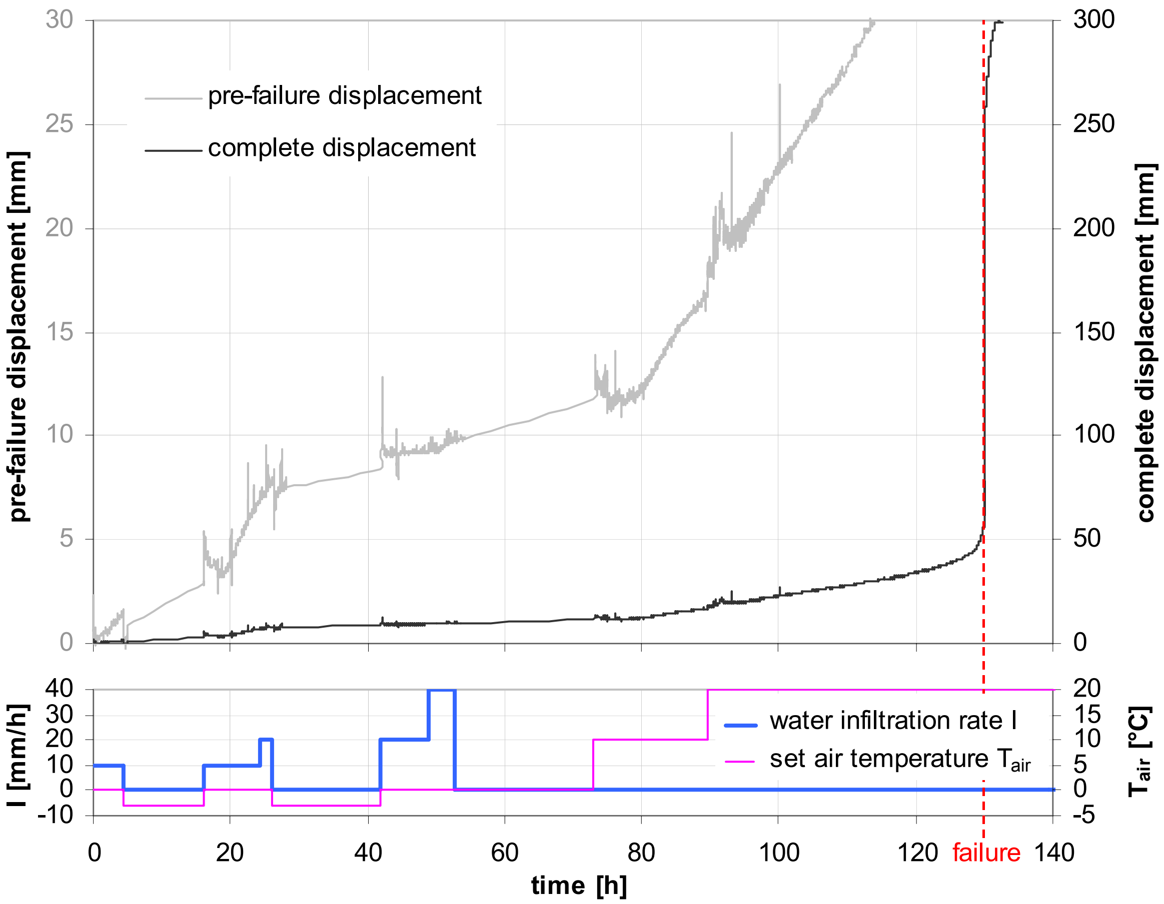

Figure 3.39*: Collective downslope displacement of upper shear frame depending on time (time scale of hours). In the periods from 5h to 16h, 28h to 42h and 54h to 73h the displacement were linearly interpolated because no data were available. The plot at the base displays the treatments (temporal course of the regulated infiltration rate and air temperature).*

The first flat part of the curve (until about 120h) far exceeded the infiltration period (until 53h) and covers more than 90% of the total experiment time but only 12% of the total shear distance. As this part appears more or less linear compared to the complete curve it can be referred to as pre-failure primary creep. Thereafter the curve shows a distinct exponential increase, i.e. an accelerated displacement indicating secondary creep. 130h after the begin of the experiment, 87h after the end of infiltration and 57h after the begin of thawing by increasing the air temperature the steepness of the curve increased sharply: two thirds of the total displacement occurred in only a thousandth (7 minutes) of the total experiment time. Thus, this part of the curve denotes the tertiary creep phase or the failure of the active layer as a whole. Incidentally, failure was preceded by loud cracking and creaking noises. However, the displacement was strongly retarded over the last sixth of the total shear distance which can be interpreted as self-stabilizing.

By enhancing the displacement scale by one order of magnitude the pre-failure creeping proved to be not linear (grey line in Figure 3.39) and allows the influence of the factors on the displacement to be analyzed. The distinct increase of the curve at 19h coincides with the first appearance of a water discharge indicating field capacity of the active layer (see section

Water discharge). Further water being infiltrated could not be retained by the active layer and therefore led to an enhanced creeping rate. However, the increase of the infiltration rate at 42h and 49h, did not cause any further responses in the displacement rate. This may be due to ice formation in the meantime, hindering the downslope displacement due to its cohesion (see section *Ice content of active layer depending on depth* in the discussion). After the infiltration had been stopped at 26.17h, the displacement curve was markedly flatter. This indicates the major influence of the first infiltration period on creeping after field capacity has been reached (compare 2.3.4). As the displacement rate did not vary significantly between the first of these periods at an air temperature of –3°C and the second one at 0°C, the temperature – if not positive – seemed to have little or no influence on creep rate. However, as in the theories of primary creep (Vyalov 1962) as well as secondary creep (Hult 1966) of frozen soil the deformation depends on temperature, this result seems to be an exception. Nevertheless, above 0°C the ground temperature showed a clear effect (at least in the short term) on creep rate, when the air temperature was changed from 10°C to 20°C. This is probably due to the loss of cohesion caused by melting of the ice.

Time scale of seconds

Focusing on the failure at a time scale of seconds shows that the failure can be divided into two sigmoid displacement steps (Figure 3.40).

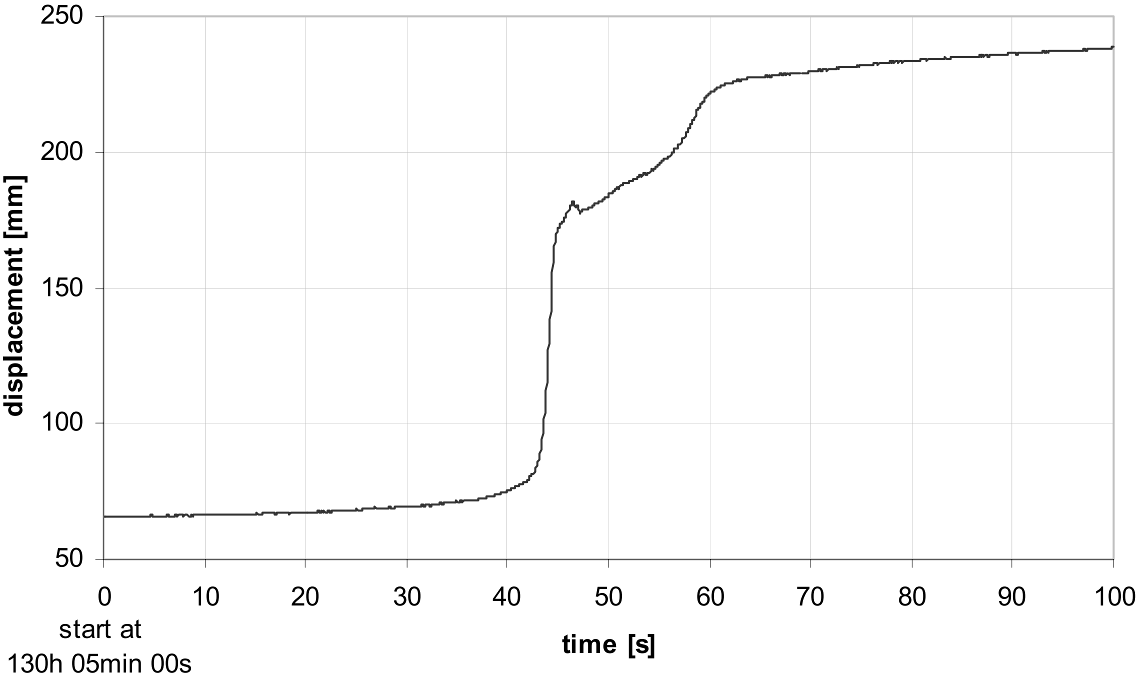

Figure 3.40: *Collective downslope displacement of upper shear frame depending on time in the short term (time scale of seconds) during failure. Note that the time axis is in seconds and starts at 130h 05min 00s referring to the long term time scale (Figure 3.39).*

The first step comprised a displacement of about one third of the total shear distance, the second one about one sixth. The gradient of the first step was much steeper than that of the second one which is reflected in the maximum displacement rate of the first step (110 mm/s at 44.2s) being one order of magnitude higher than that of the second step (11.6 mm/s at 58.6s). Between the first and second step the collective downslope displacement decreased by about 5 mm which indicates an elastic behavior.

Internal downslope displacement

After the shear box had been inclined the internal downslope displacement at all depths was set to zero in order to obtain the influence on the deformation of the active layer which was solely caused by the hydrological and thermal treatment in a slope position (Figure 3.41).

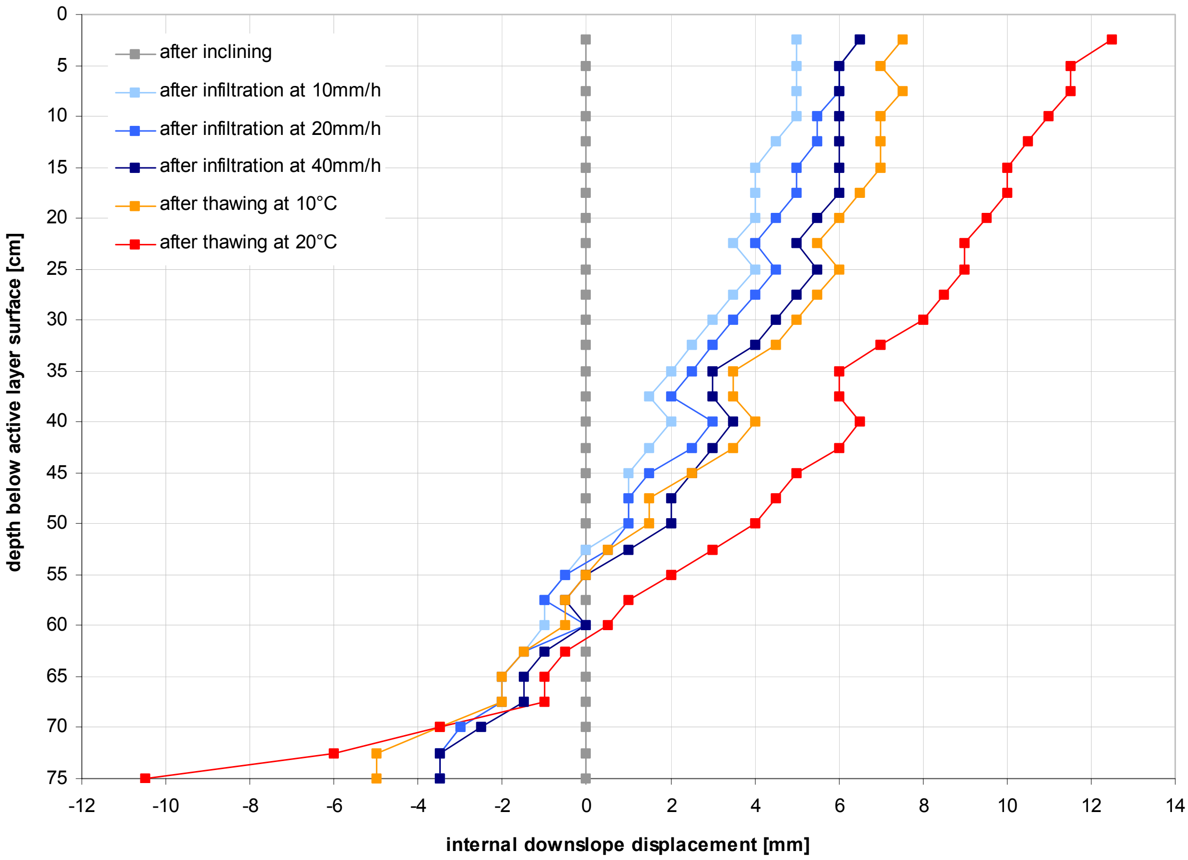

***Figure 3.41**: Deformation profiles of the active layer on top of the permafrost block (with its surface at 75 cm depth) after each setting of factors. Note that the time intervals between the steps are not equal.*

With regard to the internal downslope displacement dAL_int the active layer could be divided into an upper zone with dAL_int > 0 and a lower zone with dAL_int ≤ 0 at each time step. This indicates that the deformation of the active layer material was dominated by compression in the upper zone which is therefore referred to as the compression zone and by shearing in the lower zone which is therefore referred to as the shear zone. The border between these two zones deepened in the course of the experiment from at least 53 cm below the active layer surface after infiltrating at 10 mm/h down to 61 cm at the end of the experiment. Thus the shear zone decreased from about 1/3 to 1/5 of the active layer thickness during the experiment. Between 53 cm and 61 cm depth the two distinguished deformation modes (compression and shearing) were dominant during different periods of the experiment (first shearing, then compression except for a layer at 60 cm depth). The maximum absolute shear deformation (10.5 mm) at the base of the active layer was only 3.5% of the total shear distance. This result clearly indicates a plug-like downslope sliding movement of the active layer on the surface of the permafrost block acting as failure plane. However, the deformation within a depth interval of 2.5 cm (resolution of internal downslope displacement) was highest at or close to the active layer base and showed a decreasing trend upwards. This is in good accordance with the equivalent results of the systematic shear test series (see page 93). At some depths the internal downslope displacement was higher than above (e.g. at 25 cm and 40 cm depth). This phenomenon can be explained by the effect of single grains with a big diameter relative to the resolution of the internal downslope displacement.

It is important to note that the time intervals between the different settings of factors were not equal. In order to obtain the influence of these factor settings on the deformation independent on the time of the intervals, the rate of the internal downslope displacement was calculated as

$$\dot{d}_{AL\_\mathrm{int}} = \frac{d_{AL\_\mathrm{int}}(t)}{t} \tag{3.48}$$

where t is the time and $d_{AL\_\mathrm{int}}(t)$ is the internal downslope displacement. Only the effective time during which the factors were set to the values to be investigated was taken into consideration, i.e. the pauses (4.5h to 16.17h, 26.17h to 41.83h and 52.67h to 73.00h; see Figure 3.36) were excluded, because a change of the deformation profile during these periods did not have to be expected. The highest absolute deformation rates (shearing and compression) occurred during the first infiltration step of 10 mm/h (Figure 3.42).

Within the compression zone of the deformation profile, the deformation rates for an infiltration rate of 10 mm/h were only exceeded below about 28 cm depth when infiltrating at 40 mm/h. During the second and third infiltration steps (20 mm/h and 40 mm/h), compression, but no shearing took place. Adfreeze of the active layer base to the permafrost block is suggested to explain this phenomenon. After the second infiltration step (20 mm/h) no further compression occurred in the uppermost 7.5 cm. It is possible that the maximum compression of the hardly compressible grit (see Table 3.1) due to infiltration was already reached. However, at most depths of the active layer a further compression was effected by infiltrating at 40 mm/h. Concerning the influence of infiltration on the deformation of the active layer the first wetting of the dry material was most important, and the actual infiltration rate was of secondary significance. This is in good accordance with the field results (chapter 2.3.4). With positive air temperatures, shearing below 45 cm depth occurred again indicating ice melt at the active layer base. The mean absolute deformation rate during positive air temperatures was about three times lower than the mean rate during infiltration. However, the absolute shearing rate at the active layer base during thawing at an air temperature of 20°C was quite high which has to be attributed to the failure of the active layer within this period. The mean absolute deformation rate was about double for an air temperature of 20°C than 10°C. This indicates the positive effect of air temperature on the deformation rate above 0°C.

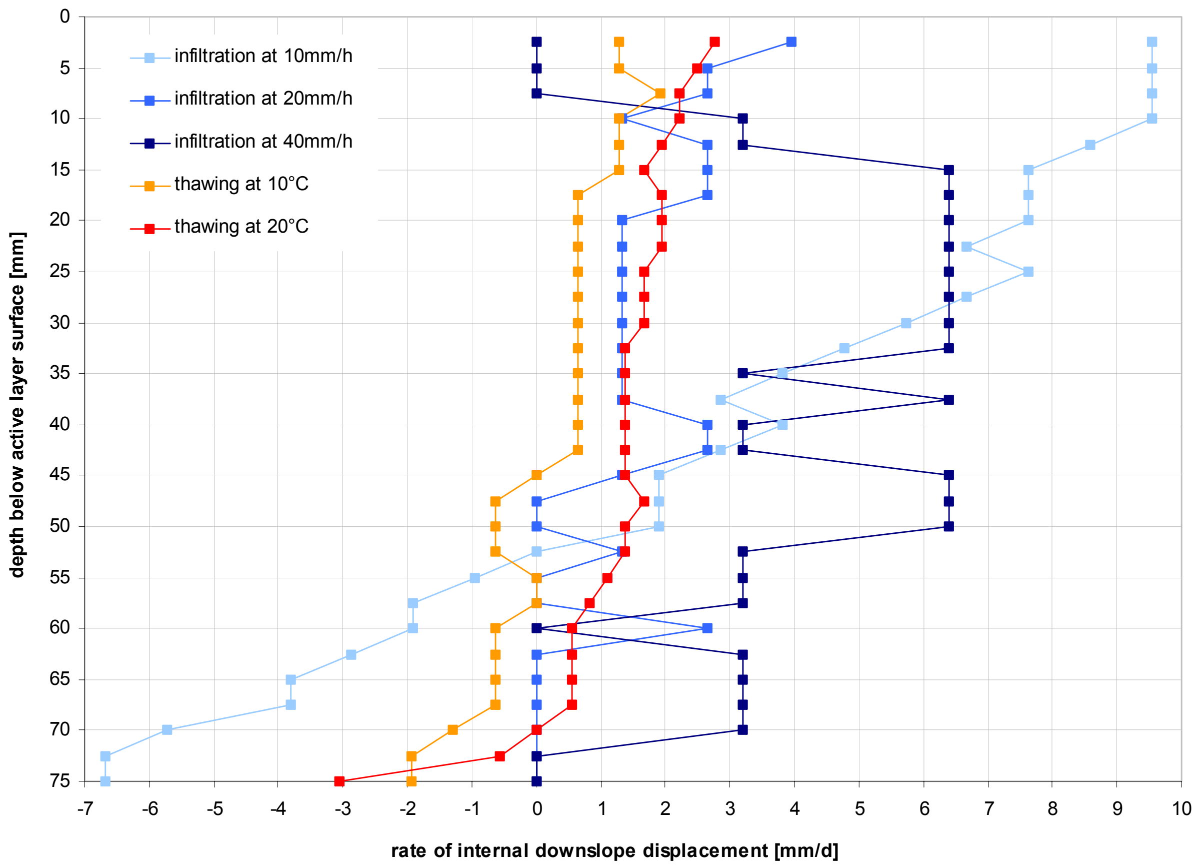

Figure 3.42: *Deformation rates within the active layer depending on depth for each setting of factors.*

Perpendicular displacement

The video sequence selected to analyze dilatancy at the main failure started 130h 04min 17s after the begin of the experiment and lasted 150s. As the short term fluctuations of the measured curves could be ascribed to the measurement method, polynomial curve fits were calculated to smooth the curves (Figure 3.43).

The perpendicular displacement at failure was very small (<1 mm for the mean dilation), even though the value for the grain which experienced the maximum dilation was four times higher. Accordingly, the angle of dilation Ψ was only 0.9° on average, with a maximum of 2.1°. This can be explained by the low relative density (see Table 3.11) at the given stress level; due to the large pores within the granular material the grains at the base of the active layer are able to overcome the asperities of the permafrost surface without (or only little) affecting the positions of the other grains. According to Bolton (1986) dilation at a given stress level decreases linearly with decreasing relative density I_D and becomes zero at and below the initial relative density. However, the phenomenon of dilation was at least observed with the method used.

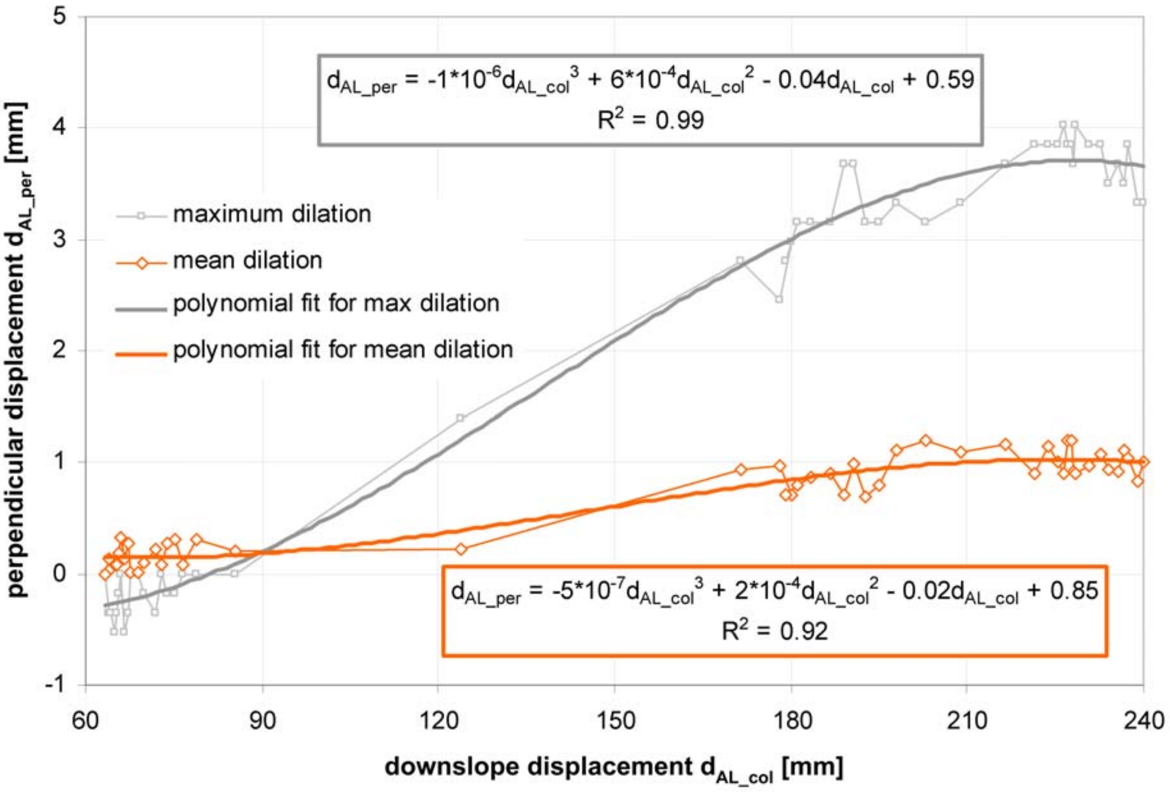

Figure 3.43: *Dilation at failure. The equations and the confidence level for the curve fits are framed with the same kind of line used for the equivalent curve fit. Number of replicates n = 10.*

Air and ground temperatures

First the temperatures measured during the entire duration of the experiment will be shown and analyzed. Then selected parts of the temperature measurement series will be highlighted at a shorter time scale (several hours) to give insights into special hydrological and thermal phenomenon and processes caused by the set factors.

The long term response of the ground temperatures to the air temperature sequence was strongly dampened and delayed with depth (e.g. warming from 0-3.50h, cooling after 26.17h, warming after 73.00h and 89.50h in Figure 3.44). This kind of thermal response is typical for heat conduction, as the temperatures did not change suddenly, but gradually (see e.g. Hinkel & Outcalt 1994, Kane et al. 2001). However, as soon as water was infiltrated into the frozen ground, heat transfer by convection and latent heat flux (release during freezing, absorption during thawing) has to be considered as well. Thus, the time lag between the setting of the air temperature from 0°C to 10°C and the increase of ground temperature above 0°C not only depended on depth below the heated surface, but also on the ice content. As long as ice coexisted with liquid water at a given depth during thawing, the ground temperature constantly remained at 0°C, demonstrating the zero curtain effect (Outcalt et al. 1990). The ground temperatures near the surface of the active layer (0-15 cm) already slightly exceeded 0°C before the air temperature was set from 0°C to 10°C despite the fact that infiltrated water with a temperature of 0°C was used. This could have been due to two reasons: (1) the active layer surface was heated additionally by the absorption of radiation, (2) the water for the infiltration was heated in the tube on its way from the reservoir to the drip system due to pumping it upwards and to the black tube absorbing radiation. After the air temperature had been set to positive values the ground temperatures near the active layer surface still exceeded the given air temperature (after 79.60h and 94.00h at 0 cm and after 125.00h at 5 cm). This phenomenon can be explained by absorption of radiation at the active layer surface, especially because the radiation was set to the highest value during this period.

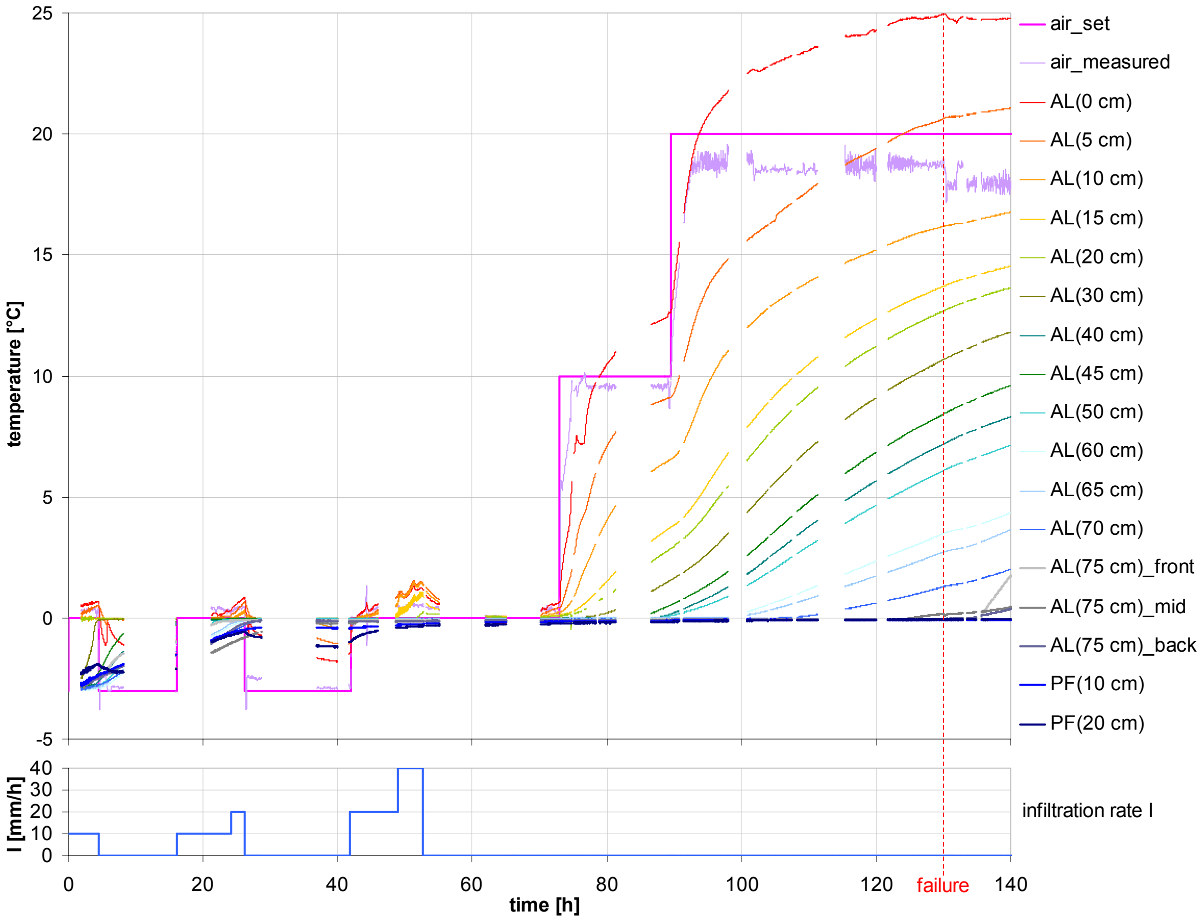

Figure 3.44: *Set and measured air temperatures and ground temperatures at a long term time scale. The depth below the surface of the active layer (AL) or the permafrost (PF) is given in brackets, the additional indications ‘front’, ‘mid’ and ‘back’ refer to the thermistor position relative to the downslope direction (Figure 3.35). Due to interruptions and the limited storage capacity of the measuring equipment the temperatures could not be recorded continuously. The plot at the base displays the temporal course of the regulated infiltration rate.*

The first selected part of the temperature measurements which is focused on in detail covers the period from 2h to 8h after the experiment begin and includes a change of the set air temperature (Figure 3.45).

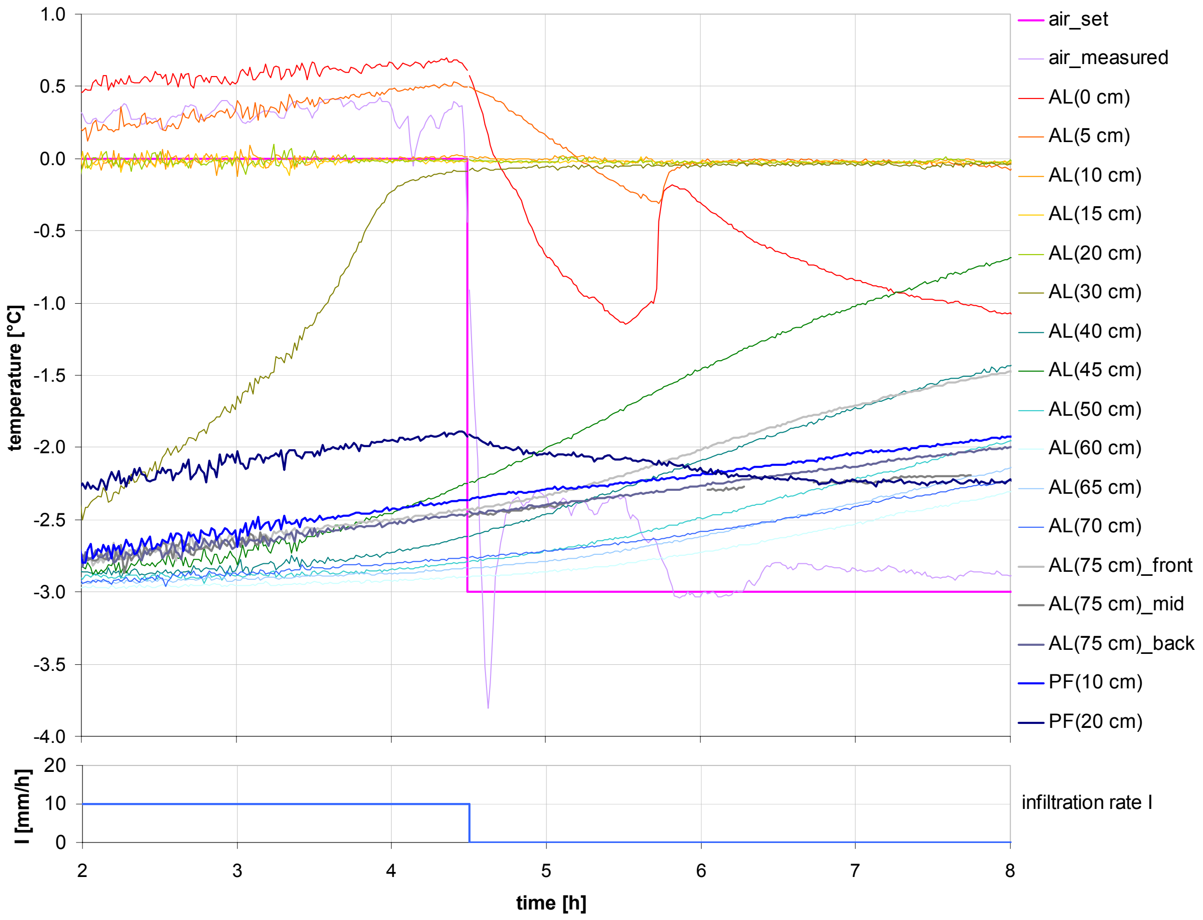

***Figure 3.45**: Air and ground temperatures before and after the air temperature was set from 0°C to –3°C (at 4.5h) simulating the transition from day to night conditions during the infiltration period (see Figure 3.36). For the notations see Figure 3.44. The plot at the base displays the temporal course of the regulated infiltration rate.*

Only two hours after the experiment had been started the ground to a depth of at least to 20 cm warmed up from –3°C to 0°C or even higher (0-5 cm) due to heating by the ambient air and infiltration of meltwater. The temperatures around 0°C indicate the coexistence of liquid water and ice. The short term fluctuations until about 3.75h were due to the infiltration pulses of the water being slightly warmer than 0°C (see above). Thereafter the ice content was high enough to dampen these fluctuations. The temperatures within the active layer below 20 cm converged towards 0°C (at a rate decreasing with depth), even after the air temperature had been lowered and the infiltration stopped at 4.50h. This is due to the propagation time of heat being transferred through the ground by conduction. At least before the set air temperature was changed the temperature was lowest at 60 cm depth and increased with depth. As the underside of the lower shear frame containing the permafrost block was only insulated 53h after the beginning of the experiment, heat was also conducted from the base of the permafrost block upwards. This was also shown by the immediate response of the temperature at the base of the permafrost block to the change of the set air temperature at 4.5h. However, the temperature propagation from the base of the permafrost block upwards was much slower than from the active layer surface downwards due to the lower thermal diffusivity of the permafrost (caused by the higher ice content) in comparison with the active layer. The zero curtain persisting between 10 cm and 20 cm after the air temperature had been set to –3°C and the infiltration stopped indicate that unfrozen water was still present. The ground temperatures (0-5 cm) clearly decreased after resetting the air temperature and infiltration, and the effect was dampened with depth. As no zero curtain occurred at these depths, the available water had to be super-cooled (due to rapid flow). At 5.70h – when the measured air temperature decreased – the temperature in the uppermost 5 cm of the active layer suddenly increased by 0.2°C at 5 cm and 0.8°C at 0 cm. As the temperature did not increase gradually, but suddenly, the involved heat transfer process is most probably non-conductive. Convection can be ruled out, because no water was infiltrated at this time. Thus, the temperature increase can only be ascribed to the release of latent heat due to freezing of the super-cooled water (compare Kane et al. 2001). The amount of released heat is

$$Q = \rho \cdot V \cdot c \cdot \Delta T \tag{3.49}$$

where ρ is the density, V the affected volume, c the heat capacity and ΔT the temperature difference within the observed period of time for the warmed body. If the initial dry apparent density of grit $\rho_{AL}(0\text{-}15\ cm,\ 0h)$ (see Table 3.11) is approximately used for ρ, and 0.8 $J/g^{-1}K^{-1}$ for c of grit, Q turns out to be 20550 J within the uppermost 5 cm of the active layer for ΔT being 0.5 K in average. Dividing Q by the latent heat of fusion for ice (334 J/g) leads to the mass of ice built during the observed freezing process to be about 62 g. After the instantaneous temperature increase (at 5.80h) the temperature at 5 cm depth gradually converged to the melting point reaching it at about 6h, whereas the temperature at the active layer surface directly decreased after a local peak of –0.2°C. This shows that unfrozen water remained at a depth of 5 cm and below, but all available water froze at the active layer surface. All the available water at 5 cm depth was only frozen at about 7.8h.

Focusing on the period of the highest infiltration rate illustrates the influence of the infiltrated meltwater on the ground temperatures (Figure 3.46). During infiltration (before 52.67h) the uppermost 15 cm of the active layer experienced regular short term temperature fluctuations, and these also occurred at 20 cm depth after the temperature had exceeded 0°C at 51.63h. These fluctuations appeared at a frequency of exactly five minutes and increased with depth (until 15 cm depth). As this frequency was the same as that of the infiltration pulses and the regular short term fluctuations stopped when the infiltration was stopped, they can be attributed to infiltration. The positive temperatures in the uppermost 20 cm of the active layer, which showed an increasing trend during infiltration but an exponential decrease thereafter, can be explained by the infiltrated water being slightly warmer than 0°C (see above).

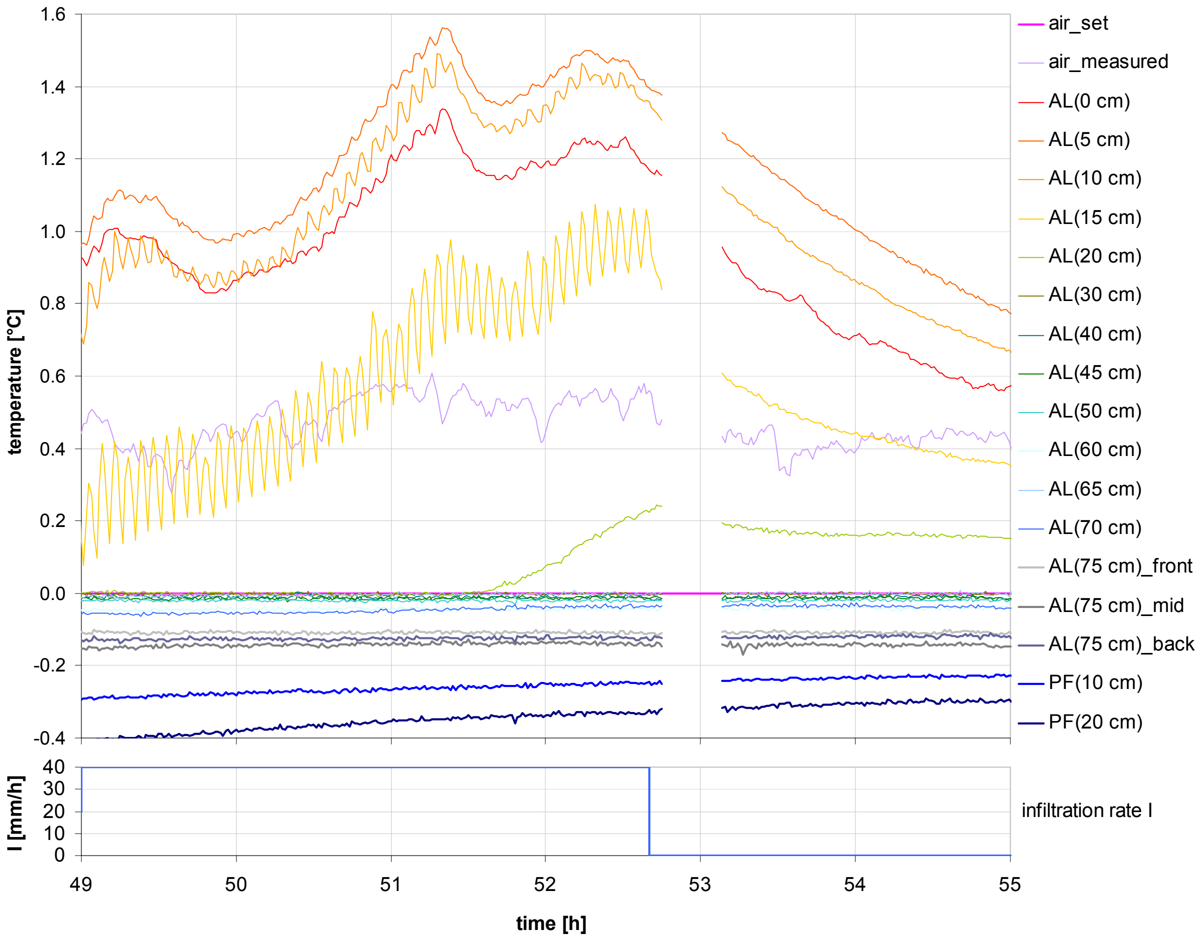

Figure 3.46: *Air and ground temperatures during infiltration at 40 mm/h and two hours and 20 minutes thereafter. For the notations see Figure 3.44. The plot at the base displays the temporal course of the regulated infiltration rate.*

The period of time covering the successive deviation of the temperature at the active layer base from the zero curtain includes the failure of the active layer (at 130.07h; Figure 3.47). This deviation occurred first in the middle of the active layer base and about 11h and 10h later at the front and back respectively. Therefore the 0°C-isotherm penetrating downwards was not parallel to the shear plane but slightly curved. As the front and back walls of the upper shear frame were insulated, the heat could penetrate downwards faster in the middle than in the front and back positions. The temperature at 75 cm depth in the middle position experienced an instantaneous decrease at 130.07h which was exactly coincident with the failure of the active layer. As the base of the active layer was warmest and at positive temperatures in the middle, the downslope displacement of the middle thermistor due to failure means a translocation to a cooler region and therefore a temperature decrease. According to this explanation, the thermistor at the front position should also have shown a temperature decrease at failure, and the thermistor at the back position - having been shifted to a warmer region - a temperature increase. However, this was not the case. This phenomenon can be understood by considering that the zero curtain guaranteed constant temperatures throughout the entire region where it prevailed. It is noticeabel that the temperature increase at the active layer base is much faster in the front than in the mid and back position after the onset of the deviation from the zero curtain. This can be ascribed to the insulation at the front wall of the upper shear frame having been pushed up by material scraped off from the permafrost surface during failure. Thus, at the front of the upper shear frame - in contrast to the middle and back - the heat could penetrate to the active layer base not only from the active layer surface but also from the front.

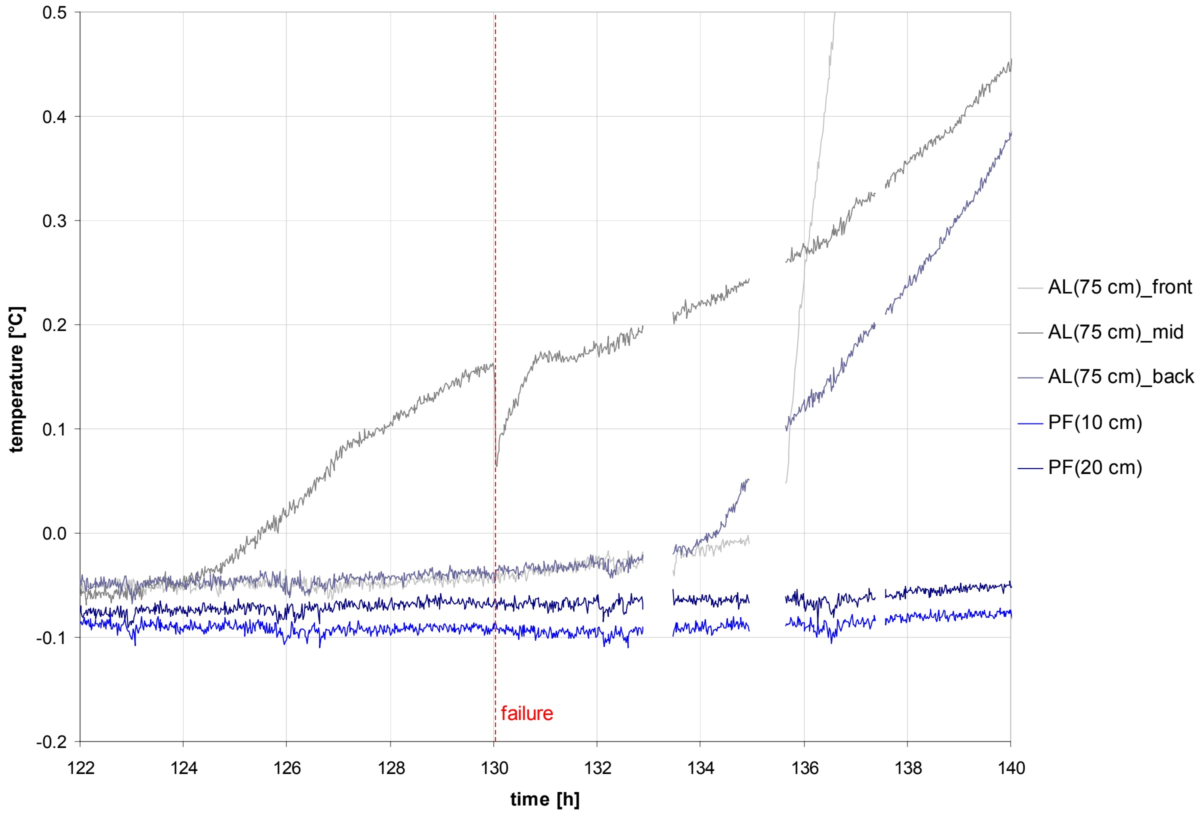

Figure 3.47*: Air and ground temperatures in the permafrost block and at the active layer base when its temperatures successively exceeded the melting point. For the notations see Figure 3.44.*

Water discharge

The first water discharge from the surface of the impermeable permafrost occurred at 18.50h, i.e. after infiltrating six hours and fifty minutes at a rate of 10 mm/h (Figure 3.48). If it is argued that the field capacity must have been reached at this point of time, the active layer would have a mean field capacity of 8%. However, this value is unrealistically low for two reasons: (1) a considerable part of the water must have become frozen due to temperatures at or below 0°C dominating at this time leading to lower densities within the water- or ice-filled pore space and therefore to a lower content of water or water equivalent of ice; (2) a part of the pore space was not accessible to water, as ice was blocking narrow pore capillaries. For these two reasons the water equivalent content having been reached when the first water discharge occurred is better referred to as the *apparent field capacity below 0°C*. After this point had been reached the discharge rate converged to the set infiltration rate, i.e. after setting a new infiltration rate the discharge rate first increased steeply and then continuously flattened out until the infiltration rate was changed again (after 18.5h, 24.17h, 41.83h, 49.00h). After stopping the infiltration the discharge rate suddenly responded and decreased steeply (after 26.17h, 52.67h). However, it did not completely come to a standstill, but its curve flattened out converging to the set infiltration rate of 0 mm/h. This dampened respond of the discharge to the infiltration rate reflects the active layer acting as a hydrological buffer.

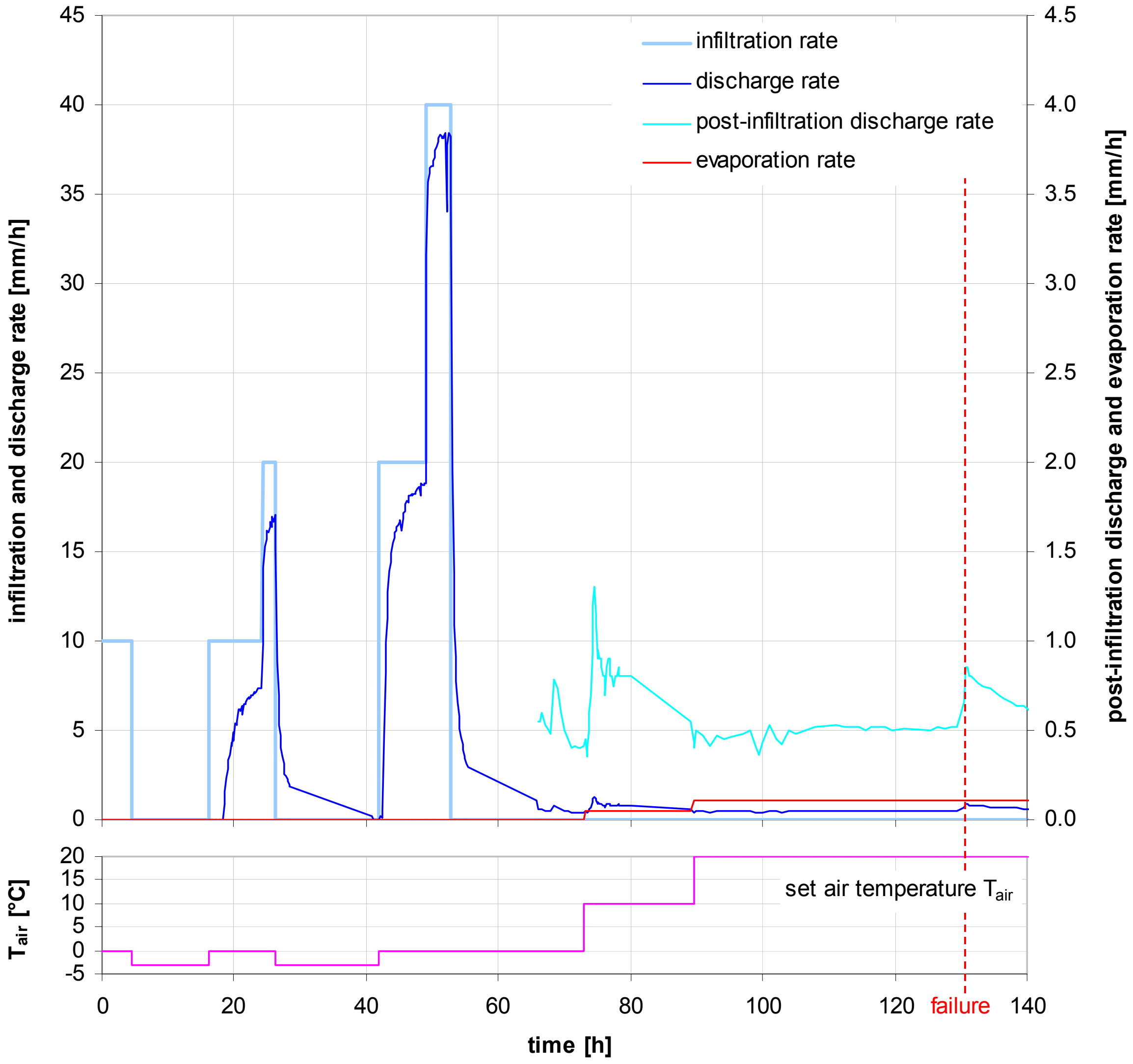

__Figure 3.48__: Water fluxes in the entire active layer as a function of time. In order to elucidate the small variations of the evaporation and discharge rate during thawing at positive air temperatures these fluxes are shown at a scale ten times smaller. The linear sections from 28.50h to 40.83h, 55.33h to 65.3h and 80.00h to 89.00h are due to the low resolution (no measurements were taken during these periods of time). An exponential rather than a linear decline is more likely to have occurred. The plot at the base displays the temporal course of the set air temperature.

In addition, after the infiltration period and the subsequent decline in discharge variations still occurred, but at a smaller scale. As no more water was infiltrated these variations must be due to the melting of ice. This can be confirmed by the increase of the discharge rate at 73.67h only 40 minutes after changing the set air temperature from 0°C to 10°C, which intensified the melting process. However, the short increase until the peak was followed by a slow, but long decrease reflecting the hydrological dampening effect of the active layer gradually releasing the water gained by the melting of ice. Another fast increase of the discharge rate followed by a long flattening tail occurred at 129.5h after a long stable phase. As the temperatures at 75 cm depth were close to 0°C at this time (Figure 3.47) this instantaneous increase can be ascribed to the thaw front penetrating into the ice saturated permafrost block indicating that the active layer was completely thawed exactly at this moment. This gives strong evidence that the failure of the active layer - only half an hour later - was caused by the loss of cohesion due to ice.

Summing the water volumes that were infiltrated (V_{inf}), discharged (V_{dis}) and evaporated (V_{evap}) within the time t since the experiment began allows the volumetric content of the water equivalent (water or ice) in the active layer to be determined at each time (Figure 3.49) as

$$\theta_{AL\_we}(t) = \frac{V_w(0h) + V_{\inf}(t) - V_{dis}(t) - V_{evap}(t)}{V_{AL}(0h)} \tag{3.50}$$

where $V_w(0h)$ is the initial water volume within the entire active layer and $V_{AL}(0h)$ the initial volume of the active layer which is assumed to be approximately constant.

The mean water equivalent content had two peaks (26.17h and 52.67h) at the end of each infiltration phase after the first discharge had occurred. This means that the active layer could have accumulated about twice the apparent field capacity (see above) at 52.67h which was possible for two reasons: (1) a part of the newly infiltrated water froze in the ground below 0°C and was therefore fixed as ice; (2) the infiltration rate exceeded the hydraulic conductivity of the active layer which consequently could not expel the excess water as fast as it was infiltrated. The second reason is confirmed by considering the strong decline of the mean water equivalent content after infiltration had stopped. However, the course of the curve shows the hydraulic dampening effect of the active layer once more, this time by means of its water equivalent content.

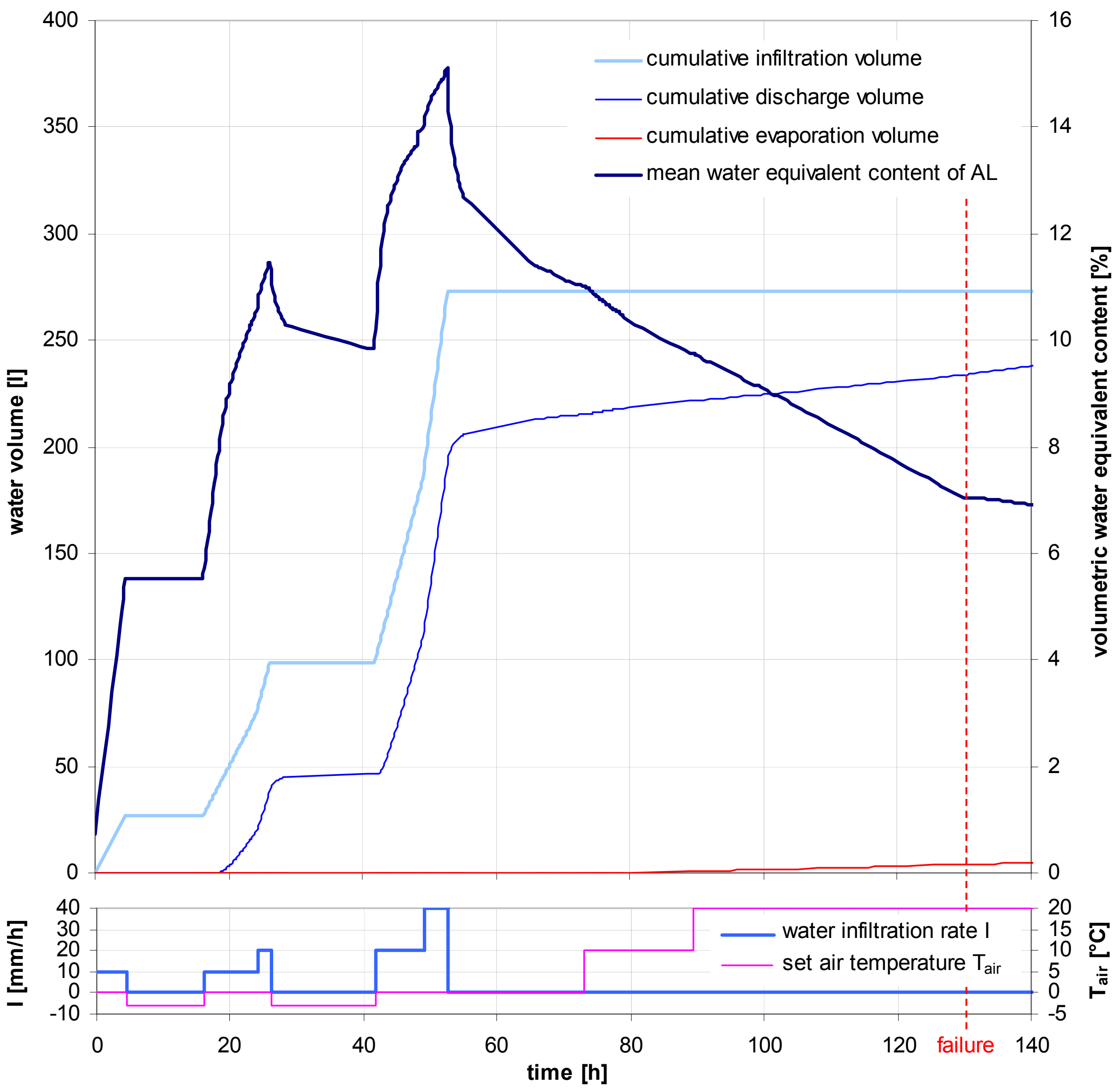

Figure 3.49: *Cumulative volumes of the water fluxes (left y-axis) and calculated mean water equivalent content of the active layer (AL, right y-axis). For the linear sections of the discharge volume and the water equivalent content from 28.50h to 40.83h, 55.33h to 65.3h and 80.00h to 89.00h see the note given in the caption of Figure 3.48. The plot at the base displays the treatments (temporal course of the regulated infiltration rate and air temperature).*

Volumetric water content

Using the TDR-measurements the volumetric water content of the total active layer could be calculated depending on time anticipating a value of zero at the surface and interpolating between the surface and the measuring depths. At 129.5h - when the active layer was completely thawed - the water content of the total active layer measured by TDR should have been the same as the equivalent value θ_{AL_we}(129.5h) determined by means of the discharge measurements (see Figure 3.49). However, this was not the case; θ_{AL_we}(129.5h) proved to be 0.712 times the value measured by TDR. This deviation could have been caused by reasons pertaining to both methods, the determination of the water content by means of the discharge measurements (1-2) and the TDR-measurements (3-5): (1) The evaporation from the active layer surface was not directly measured and thus its effect on the determination of θ_{AL_we} by means of the discharge measurements could have been underestimated. (2) The infiltration rates which were also used for the determination of θ_{AL_we} could have deviated slightly from the set values due to inaccuracy of the dripping elements. (3) The model of Roth et al. (1990) used to calculate the water content is only conceived for the three phases air, solid soil material and water, but not for ice, which was present in the experiment. However, as the relative permittivity ε_r of ice (3.15) is very small compared to the value of liquid water (88.15 at 0°C), the deviation is marginal. (4) The algorithm calculating the relative permittivity ε_r by means of the shape of the electromagnetic signal propagating along the TDR-rods depending on time is only an approximation. (5) Water could have flowed preferentially along the electric cables of the TDR-probes leading to abnormally high values for the water content. The last two uncertainties due to the TDR-system are likely to have had the highest influence on the deviation. As the TDR-measurements reflect correct relative values between different depths and time steps rather than correct absolute values, they were multiplied by the correction factor 0.712 (Figure 3.50) derived from the comparison with θ_{AL_we}(129.5h) determined by the discharge measurements (see above).

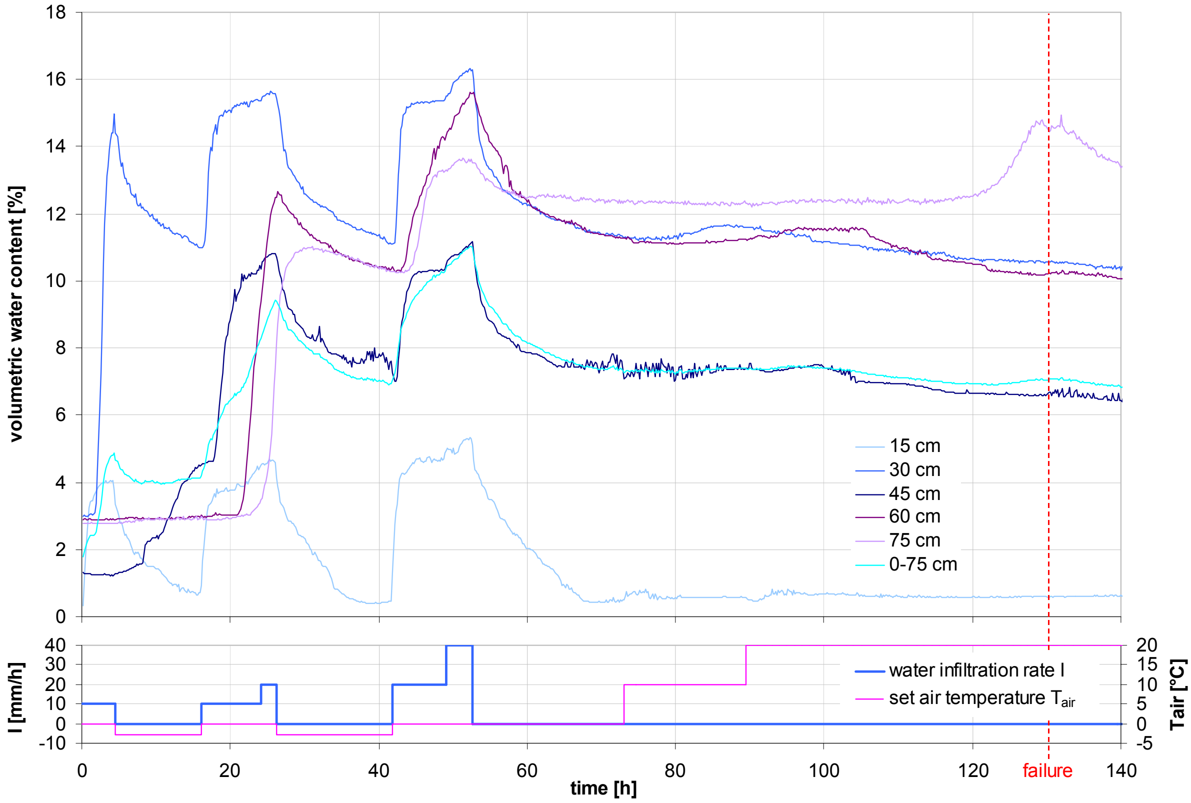

__Figure 3.50__: Volumetric water content of the active layer depending on depth. The original values measured by means of a TDR-system were corrected by comparing the value at 129.5h - when the active layer was completely thawed - with the value at the same time determined by means of the discharge measurements (see Figure 3.48). The plot at the base displays the treatments (temporal course of the regulated infiltration rate and air temperature).

During the total period of simulated meltwater infiltration (0-53h) the water contents reflected the temporal infiltration pattern (compare Figure 3.36 and Figure 3.50). This result is remarkable, especially the decrease each time after the infiltration had been stopped, because after the ground had reached field capacity the water content was expected to remain constant or to decrease only slightly due to freezing and evaporation. Thus, the water content during (or at least at the end of) each infiltration phase exceeded the field capacity of the active layer, which is only possible when the infiltration rate exceeds the hydraulic conductivity of the active layer. According to this explanation the water contents should also have reflected the relative quantities of the infiltration rate. However, they did not, especially the ratio between the maximum water contents at the end of the second and third infiltration phase (26.17h and 52.67h) strongly deviated from the ratio between the infiltration rates at the same points of time. This phenomenon can be understood by considering that the unsaturated hydraulic conductivity increases with the infiltration rate which is due to the increase of the conducting cross section of the pore space.

At the beginning of the first infiltration phase, the water content at 15 cm depth responded very rapidly which indicates a high permeability within the uppermost grit layer. The further wetting front advance within the gravel was much slower and took about two hours from 15 cm to 30 cm depth (i.e. 75 mm/h) and six and a quarter hours from 30 cm to 45 cm (i.e. 24 mm/h). Generally the time lag between the beginning of an infiltration phase and the equivalent response of the water content increased with depth. However, this effect became weaker after the active layer had first been moistened (see time lags for second and third infiltration phase). Additionally, the influence of the infiltration on the water content was dampened with depth. For example, the first infiltration phase caused clearly discernible peaks of the water content down to 30 cm depth, a clear increase at 45 cm depth, but no discernible response at 60 cm and 75 cm depth. At the beginning and end of the second and third infiltration phases the responses to the increasing and decreasing rates of the water content decreased with depth. In addition, the peaks of the water content due to infiltration were increasingly dampened with depth (compare curves at 30 cm and 75 cm depth) indicating again the hydraulic dampening effect of the active layer. The water content at 15 cm depth was nearly always the lowest reflecting the low field capacity and the high hydraulic conductivity of the coarsely porous grit in comparison with gravel. During the infiltration period the water content was highest at 30 cm depth. As the hydraulic dampening of the grit layer just above was very poor (see above), it caused a high water flux to the gravel layer below leading to high water contents.

In the period of thawing induced by positive air temperatures (73h to 140h) increases of the water contents must have been due to the melting of ice as no more water was infiltrated. Consequently, these increases indicate the time of melting at the equivalent depth and their magnitude reflects the ice content of this particular layer. In fact, only about twelve minutes after the temperature had been changed from 0°C to 10°C the water content in the uppermost layer (at 15 cm depth) increased slightly, reaching a local maximum at about 76h. At 30 cm depth a local maximum was reached at about 88.1h, at 45 cm at about 99.5h (even though very weakly pronounced), at 60 cm at about 105.3h and at 75 cm at about 129.5h (the maximum at the same depth at 132.0h was due to the ice melting of the permafrost block, as the active layer had been thawed completely at 129.5h). This sequence of local water content maxima with depth is in accordance with the thawing front having penetrated downwards due to warming from the active layer surface. The water content increase was highest at 75 cm, that is the ice content within the active layer was highest at its base. It is noticeable that the water content due to the melting of ice at 75 cm was even higher (15%) than during infiltration. With the total maximum degree of water saturation of 45% at 30 cm depth at 52.55h the active layer was far below water saturation at all depths during the entire experiment.

Water saturated zone

The height of the water saturated zone was measured to be zero throughout the experiment. This could have been caused by icing of the filter at the end of the thin horizontal tube of the mini-piezometer reaching in the active layer. A first plausibility check for this result is the analysis of the degree of water equivalent saturation of the pore space for the active layer as a whole which is

$$S_{we\_AL} = \frac{\theta_{AL\_we}}{E_{AL}} \tag{3.51}$$

where θ_{AL_we} is the content of the water equivalent (water or ice) within the active layer as a whole and e_{AL} the mean porosity of the active layer which is the sum of the single porosities for the grit (e_{grit}) and gravel (e_{gravel}) layer each weighted by their volumetric portion. The single porosity e of a homogenous granular material is calculated as

$$e \;=\; \frac{V_p}{V} \;=\; \frac{V - V_s}{V} \;=\; 1 - \frac{V_s}{V} \;=\; 1 - \frac{\rho_a}{\rho_r} \tag{3.52}$$

where V is the total volume of the granular material, V_p the pore volume, V_s the volume of the solid grains, ρ_a the apparent density of the granular material and ρ_r the real density of the solid grains. If the dry apparent density of the uppermost 15 cm (grit) and the lower 60 cm (gravel) of the active layer (see Table 3.11) is used for ρ_a and for ρ_r the value given in Table 3.1 E_{grit} will turn out to be 0.493, e_{gravel} 0.369 and e_{AL} 0.394. Using equation 3.51 the maximum value for S_{we_AL} at 52.67h can be calculated to be 38.4%. Even if all the water was frozen, the degree of ice saturation of the active layer would be 41.8% (considering a volume expansion at phase change of 9%). As this value is still far below saturation of the pore space (100%), the measurement value is plausible after this first check. However, the mean value for the degree of water equivalent saturation may not be representative for the degree of water saturation of the pore space - additionally restricted by ice - at the active layer base, because the water could have been distributed irregularly within the active layer. Further evidence for the measured height of the water saturated zone is given by the measurement of the volumetric water content. As the maximum degree of water saturation at 75 cm was determined to be 45% (see chapter Volumetric water content), the height of the water saturated zone above the permafrost surface having been negligibly low is therefore confirmed. However, as the permafrost surface acted as an impermeable layer and thus generated a water discharge, at least a thin saturation film (below the resolution of the measurement equipment) must have occurred.

Evaporation

When the air temperature was set to 20°C and the radiation to 43 W/m^2 the evaporation rate was only 0.1 mm/h which is 1% of the lowest infiltration rate (Figure 3.48) and therefore almost negligible. However, evaporation caused the volumetric water equivalent content to be only about 7% at the end of the experiment (140h) and therefore even lower than the apparent field capacity (see above).

3.4.3 Discussion of simulation of thaw-induced active layer failure

Pre-failure creep

The pre-failure creep was mainly driven by the infiltration rather than the air temperature, as was shown by the rates of internal downslope displacement (Figure 3.42). During the infiltration period the first wetting proved to be more important for the creeping rate than the infiltration rate. Therefore the melting of ice bonds between the mineral grains and the lubrication effect due to the infiltrated water are suggested to be the causes of pre-failure creep of granular frozen ground.

Mean ice content of active layer

The mean ice content of the active layer (Figure 3.51) was calculated by subtracting the corrected mean water content for 0-75 cm depth (see Figure 3.50) from the mean water equivalent content (see Figure 3.49). During about the first half of the experiment, the ice content showed an increasing trend, and during the second half a decreasing trend. This can be explained by the two conditions necessary for the formation or long-term existence of ice: (1) temperatures not higher than 0°C, (2) the availability of water. During the first half of the experiment the temperatures were 0°C or below and the water availability was guaranteed by infiltration or unfrozen pore water (see Figure 3.36), so ice could form. During the second half of the experiment the temperature was mainly positive (change of air temperature at 73h) and no water was infiltrated, so the available ice in the ground gradually melted. When the infiltration was interrupted or stopped during the first half of the experiment, the water for the formation of ice must have originated from the unfrozen water available in the pore spaces. Therefore, the increasing rates of the ice content were lower for these phases than the highest rates during the infiltration phases. At the beginning of each infiltration phase the curve of the ice content sharply steepened. As the active layer had been cooled before each infiltration phase, its capacity to absorb heat and therefore to form ice during infiltration was increased. However, this strong increase did not prevail during the whole infiltration phases. At 22.17h (4h after the begin of the second infiltration phase) the ice content reached a local maximum and strongly decreased thereafter, although the factors (infiltration rate and set air temperature) were kept constant. The active layer must have been warmed to such an extent by the infiltrated water (slightly warmer than 0°C, see above) and by the latent heat released by earlier freezing of water, that the infiltrated water could no longer freeze (only considering the net water and ice balance), and instead partly melted the ice in the active layer. After a short strong increase at 41.83h (initiation of third infiltration phase) the ice content remained roughly constant for an infiltration rate at 20 mm/h and newly increased when the infiltration rate was increased at 49h. However, the ice content - in contrast to the second infiltration phase - only decreased markedly after the end of the infiltration (52.67h). Thus, the capacity of the active layer to absorb heat was higher for the third than the second infiltration phase, although more warm water (relative to the active layer) has been infiltrated.

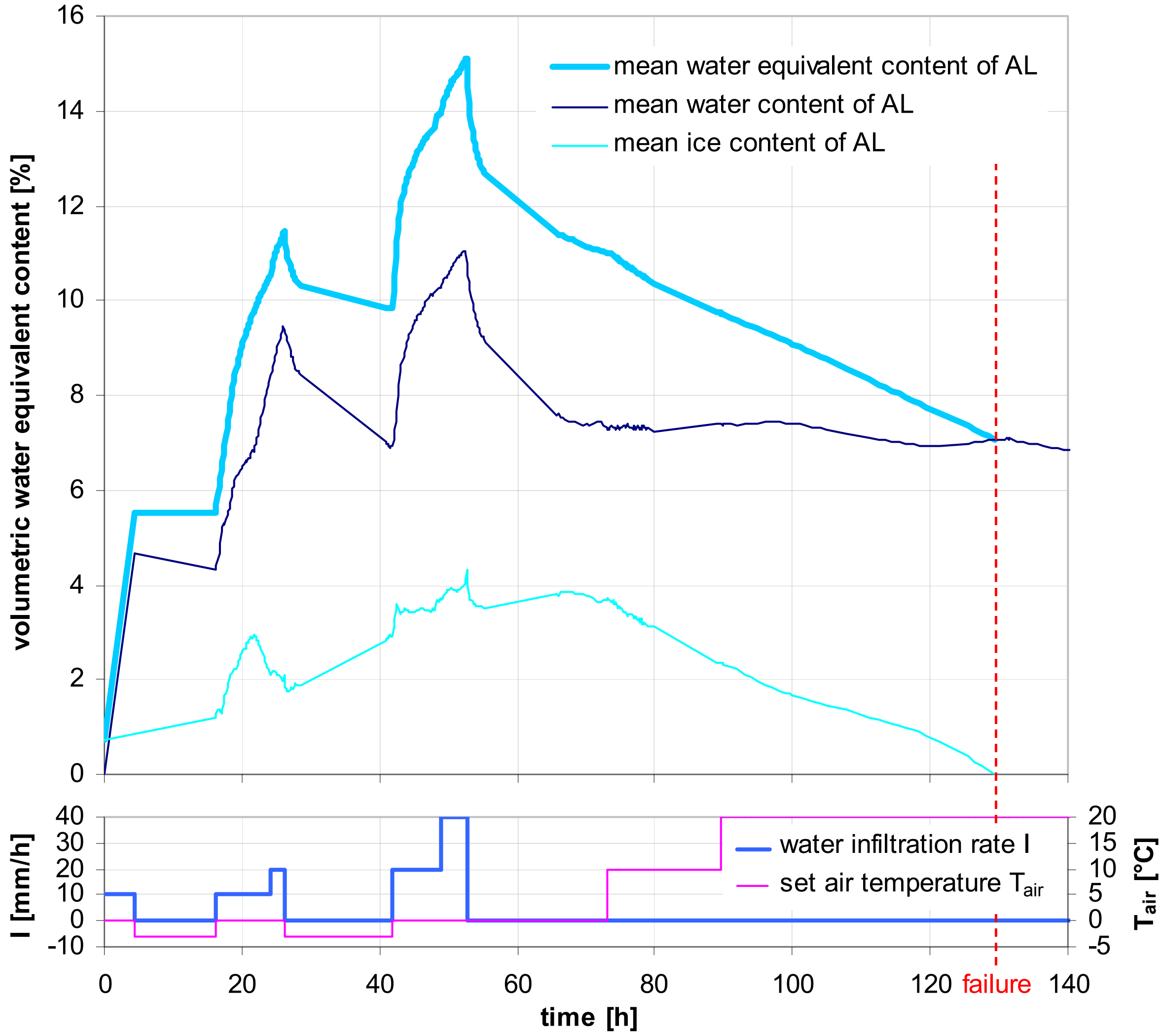

Figure 3.51: *Mean liquid and solid volumetric water contents of the active layer (AL). For the linear sections from 28.50h to 40.83h, 55.33h to 65.3h and 80.00h to 89.00h see the note given in the caption of Figure 3.48. Note that the ice content is given as water equivalent content. The plot at the base displays the treatments (temporal course of the regulated infiltration rate and air temperature).*

However, the combined water and ice (water equivalent) content at the initiation of the third infiltration phase was nearly two times higher than at the initiation of the second infiltration phase. This led to a higher capacity of the active layer to absorb heat, because the specific heat capacities of water and ice are far higher than that of air. The maximum ice content of the total experiment was 4.3% for the water equivalent and 4.7% taking into account a volumetric expansion of 9% at freezing; it occurred at the end of the third infiltration phase. As the porosity of the active layer was 0.394, this means a degree of volumetric ice saturation not higher than 12%, indicating ice-unsaturated conditions throughout the experiment. However, this conclusion is based on averaging over the entire active layer. As the ice was likely irregularly distributed within the active layer, local ice saturated conditions cannot be ruled out (see below).

Thaw depth of active layer

The thaw depth - where the temperature is exactly 0°C - of the active layer depending on time was calculated by means of the temperature profile for each time step interpolating between the negative and positive measured temperatures closest to 0°C (*calculated thaw depth* in Figure 3.52).

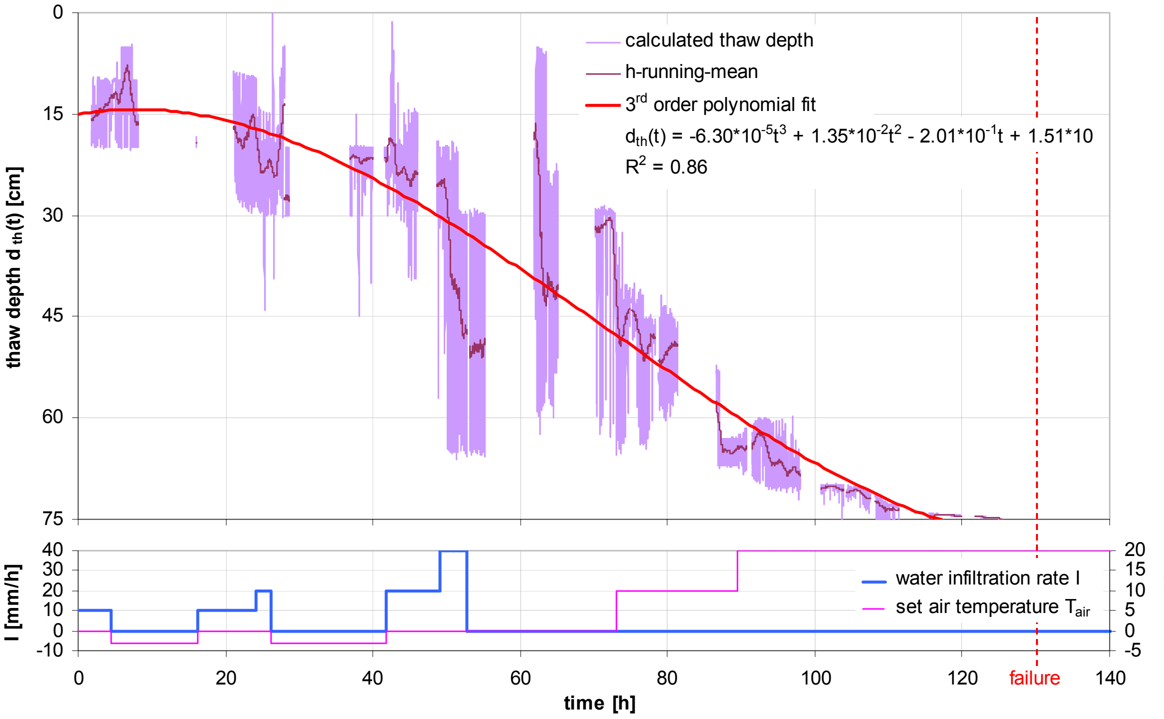

***Figure 3.52**: Thaw depth of the active layer as a function of time over the total experiment. The plot at the base displays the treatments (temporal course of the regulated infiltration rate and air temperature).*

This calculation method results in a broad scattering of the thaw depth, because the temperatures were close to 0°C throughout the active layer and freeze-thaw-processes occurred locally and temporally irregularly. To eliminate these short term fluctuations of the thaw depth an hourly running-mean was established (Figure 3.52). However, even this smoothed curve proved to be very noisy. To get a rough long term course of the thaw depth depending on time, the raw data (calculated thaw depth) were therefore fitted using a third order polynomial function (Figure 3.52). From this curve, thaw depths deepened rapidly in the uppermost 15 cm, but only gradually below. This response can be explained by the different thermal properties of grit in the uppermost 15 cm and gravel below. In the grit the heat transfer was much more efficient due to its larger pores favouring convection of air and water (compare the rapid increase of the water content in the grit layer; Figure 3.50). In contrast to the polynomial curve fit the hourly running-mean shows a marked increase of the thaw depth from about 49h to 52.67h. As this period of time exactly covers the last infiltration phase at a rate of 40 mm/h, the pronounced lowering of the thawing front can be ascribed to the infiltrated water. The subsequent decrease of the thaw depth is not reflected in the polynomial curve fit. In addition, the time, when the active layer was completely thawed (75 cm thaw depth), given by the curve fit is 11.5h earlier than the hydrologically determined point of time at 129.5h. For the time after the infiltration period the raw data were therefore fitted separately by a fifth order polynomial function (Figure 3.53).

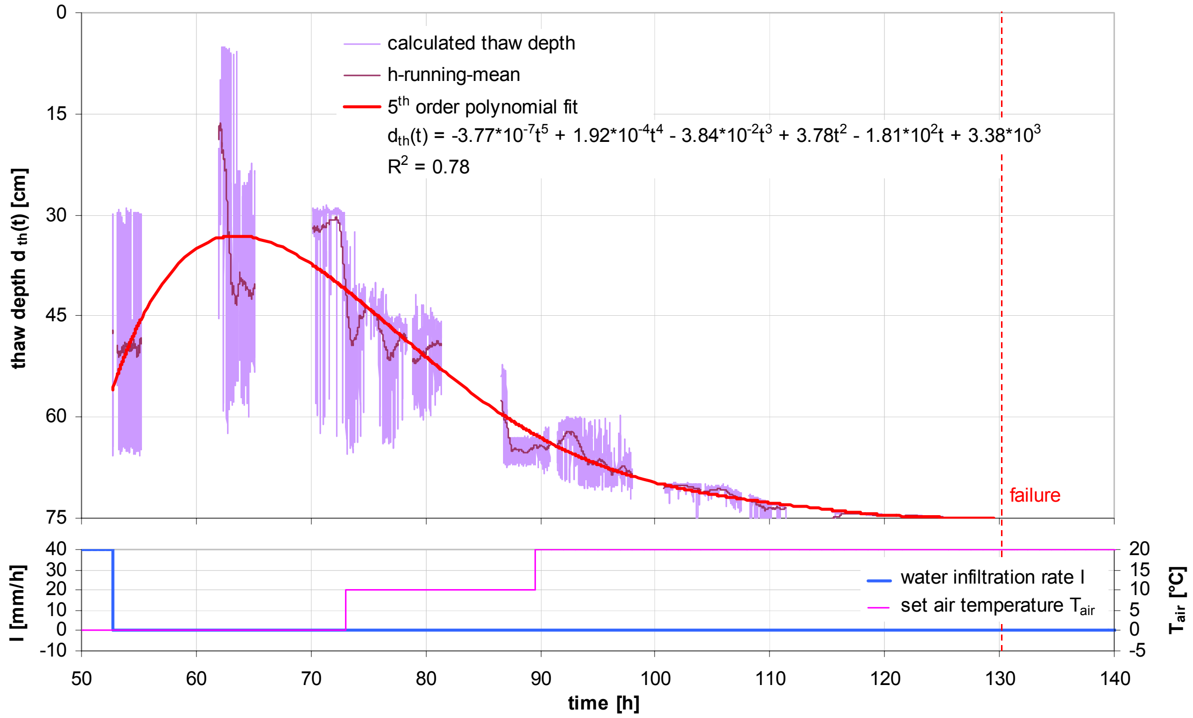

***Figure 3.53**: Thaw depth of the active layer as a function of time after the infiltration period (52.67h). As the polynomial fitting curve reached a maximum for the thaw depth at 124.40h, the last section of the thaw depth from this value to 129.5h (hydrologically determined point of time at which the active layer was completely thawed) was therefore fitted linearly. The plot at the base displays the treatments (temporal course of the regulated infiltration rate and air temperature).*

This curve fit reflects the decreasing of the thaw depth after the infiltration period up to a minimum of about 33 cm. This was only possible because the cooling of the upper part of the active layer (above 0°C) by the lower part and the permafrost block (below 0°C) was not compensated by the warming effect of the infiltrated water slightly above 0°C. This rise in the thaw depth roughly correlated with a temporary increase of the ice content, even though the latter one started and ended a bit delayed (Figure 3.51). The local minimum of the thaw depth was reached at about 64h, so the cooling capacity of the permafrost and the active layer part below 0°C was exhausted even before the air temperature was set to positive values (at 73h). Thereafter the thawing front deepened continuously until the active layer was completely thawed (75 cm thaw depth). The deepening rate of the thawing front reached a maximum at about 78h and steadily decreased thereafter, although the temperature gradient increased (compare Figure 3.44). The retarded deepening of the thawing front is thus likely to be caused by an increase of the ice content from 35 cm depth towards the active layer base, which will be discussed in the next section.

Ice content of active layer depending on depth

Although the smoothed thaw depth reached a minimum at 64h and continuously increased thereafter (polynomial fit in Figure 3.53), the maximum ice content after the infiltration period (and the following decline) was only reached at 68h (Figure 3.51). At this time the thaw depth is projected to have been 35 cm. Using this information the ice content of the active layer between 35 cm and 75 cm depth could be determined at depth intervals of 5 cm. For this, the time interval was determined during which the thaw depth deepened from the upper to the lower boundary of the observed depth interval by means of the fifth order polynomial curve fit for the thaw depth (Figure 3.53). The loss of the volumetric water equivalent of ice in the entire active layer melted off within this time interval was ascribed to the equivalent depth interval. Relating this volumetric water equivalent to the volume of the considered depth interval reveals its ice content after the infiltration period (and the following decline of the mean ice content of the active layer). However, as the mean ice content (as water equivalent) of the active layer reached the global maximum (over the total experiment) of 4.33% at 52.67h, there are still 0.48% ice left compared with the mean ice content at 68h (reference time for calculation of ice content in depth intervals, see above). The equivalent ice volume difference of 2.7 litres could not be distributed to the depth intervals by the method shown above. However, as the thaw depth during the decline of the mean ice content of the active layer after its maximum at 52.67h was far below 35 cm (Figure 3.53), the ice volume difference could only originate from the depth interval 35-75 cm. Due to the potential redistribution of the ice within this depth interval during the following increase of the mean ice content from 55.33h to 68.00h (Figure 3.51) the spatial distribution of the ice volume difference within this depth interval was not possible. Anticipating an equal distribution would result in an additional ice content (water equivalent) of 0.9% for the depth interval 35-75 cm which reveals the approximate ice content of the active layer depending on depth (Figure 3.54).

This ice distribution clearly shows that ice originating from infiltrated water was concentrated at the base of the active layer indicating that the permafrost block below acted as a freezing plate. When the volumetric water equivalent content of ice in the lowermost 5 cm of the active layer was about 25.3% at the end of the infiltration period, the volumetric water content was about 13.5% at the same depth. This means that the pore space of the gravel with a porosity of about 36.9% must have been completely saturated with about two thirds ice and one third water. According to these water and ice contents the degree of combined water and ice saturation is about 105%. However, as excess pore water pressures (exceeding the hydrostatic pressure) are very unlikely (no sealing of the pore space with ice from above), this apparent oversaturation must be ascribed to inaccuracy of the data.

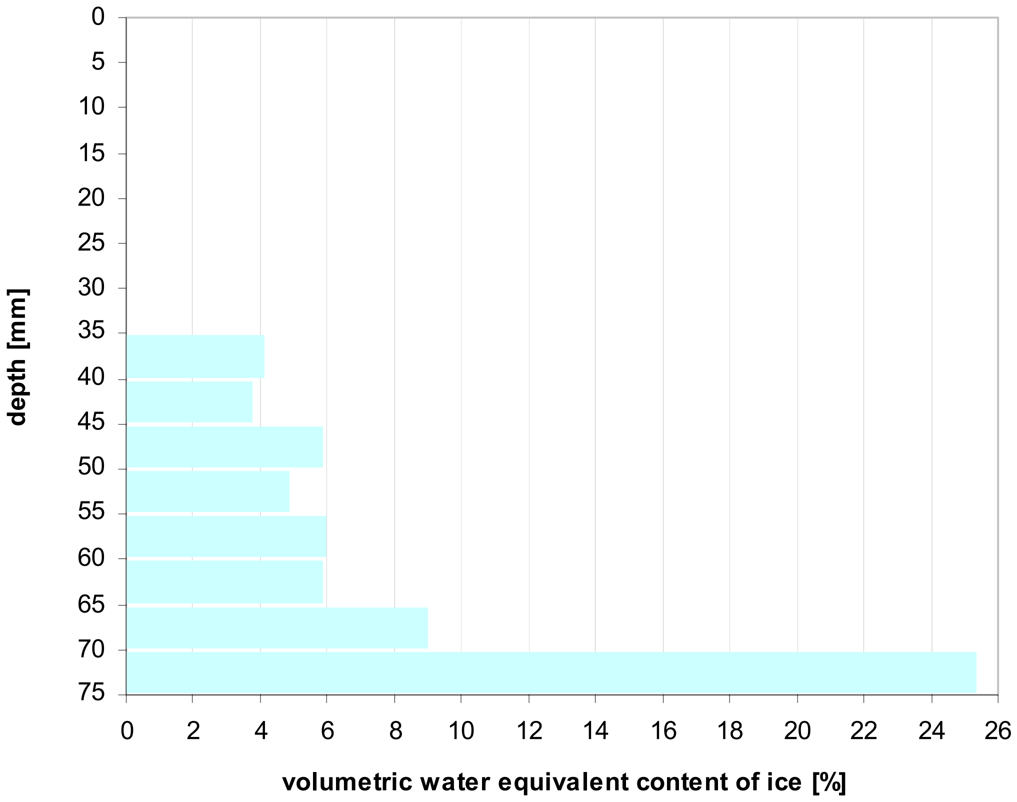

***Figure 3.54**: Volumetric water equivalent content of ice in the active layer depending on depth at the point of time when the mean ice content of the active layer reached its maximum (52.67h; see Figure 3.51). Note that ice could have existed within the depth interval 0-35 cm before this time (during the infiltration period), but it could not be quantified.*

Conditions at failure

Thermal conditions

For the thermal conditions at failure the temperatures at the active layer base - measured at distances of 15 cm in a back, middle and front position (see Figure 3.44 and Figure 3.35) - proved to be very instructive. As the active layer experienced a downslope displacement of about 200 mm during the main failure at 130h, the thermistor at the active layer base in the rear position must have moved past the position of the thermistor in the middle at the same depth before failure by about 50 mm (Figure 3.55). Additionally, a hollow of the 0°C-isotherm must have been formed in the permafrost block underneath the thermistor at the active layer base in the middle position (compare Figure 3.47) before failure. Unlike the temperature of the thermistor in the middle position, which suddenly dropped markedly at failure, because the thermistor was moved out of the hollow of the 0°C-isotherm, the temperature of the thermistor in the reat position remained at the zero curtain. Therefore the latter thermistor must have moved further than the front boundary of the hollow of the 0°C-isotherm. Anticipating a symmetrical shape of this hollow the length, at which the permafrost surface was already unfrozen, was not more than 10 cm at failure, i.e. 13.3% of the contact length (or rather contact area) between the active layer and the permafrost block.

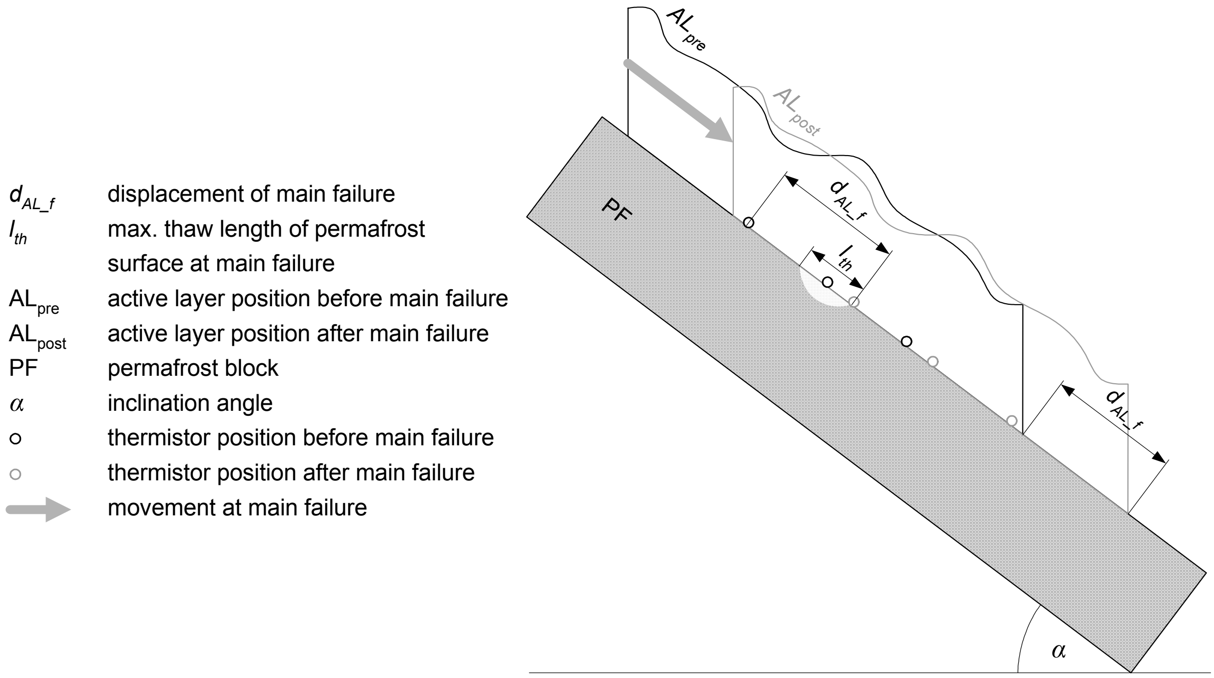

Figure 3.55*: Illustration of the thermistor positions at the base of the active layer directly before and after the main failure. Note that only the lowermost ~20 cm of the active layer are shown.*

Hydrological conditions

Concerning the hydrological conditions it was expected that the failure would occur during strong infiltration which was hypothesized to cause a water saturated zone on the permafrost surface leading to uplift of the active layer, to a reduction of the normal force and therefore reduced friction between the active layer and the permafrost and finally to failure. During infiltration at a rate of 10 mm/h creep rates of the active layer increased, enabling the reduction of stresses and during infiltration at a rate of 20 mm/h and 40 mm/h no relative displacement between the active layer and the permafrost occurred (see Figure 3.42). Therefore the infiltration of meltwater into the ground only slightly below 0°C proved to have a stabilizing rather than a destabilizing effect. This can be explained by the formation of ice during infiltration (see Figure 3.51), especially at the base of the active layer (see Figure 3.54). However, when the cooling capacity of the permafrost and the part of the active layer below 0°C is exhausted, the ice content is reduced (see curve of mean ice content of AL after 22.17h in Figure 3.51) and therefore its stabilizing effect during infiltration also diminishes. If infiltration continued until the active layer is completely thawed, which would depend on the height of the water equivalent of the snow cover, the destabilizing processes illustrated above would take place. Whether failure occurs at a given stress level and surface roughness of the permafrost depends on the height of the saturated zone, which is determined by the hydraulic conductivity of the ground, as well as by the rate and time of infiltration.

In the experiment, the failure occurred only 36 minutes after the active layer was determined to have thawed completely. This point of time was fixed by the thawing front reaching the permafrost (indicated by an instantaneous increase of the discharge at 129.5h, see Figure 3.48), but the thaw front was not completely parallel to the permafrost surface, so the real point in time for the active layer having become completely thawed was even closer to failure. The ice content at the active layer base directly before failure was calculated to be 25%, and the water content was 7%, so the pore space was occupied by about 75% ice, 20% water and 5% air. As the water discharge at failure was only 0.6 mm/h and thus far below the hydraulic conductivity of the gravel, water saturated conditions at the base of the active layer and therefore also a reduction of the friction due to an uplift of the active layer could be ruled out as reason for failure.

Failure mechanism

A synthesis of the observed thermal and hydrological conditions during the experiment leads to a proposed failure mechanism. At the begin of the experiment as well as at failure the active layer was free of ice. So the loss of ice within the active layer cannot be the reason for the failure. However, in contrast to the initial conditions when the particles at the surface of the finer grained permafrost block were tightly embedded within an ice matrix, this cohesion was lost when the thawing front started to penetrate into the permafrost block and to melt the ice. The fact that failure did not occur immediately when the active layer was completely thawed, but about half an hour later when the ice at the surface of the permafrost started to melt, supports the proposed failure mechanism. The stability was therefore limited by the angle of internal friction of the water saturated material in the finest grained layer, which was not higher than 37°. This is a realistic value, as the angle of repose (by which the angle of internal friction can be approximated) is about 40° for the dry sand used (see Table 3.1) and because a reduction due to the uplift and the lubricating effect under water saturated conditions has to be considered. The proposed failure mechanism is in accordance with the systematic shear test series and thus can be illustrated by Figure 3.28. It could be tested by the same experiment, but with a dry and ice free permafrost block. Although the mass of the active layer was increased by the water at failure in contrast to the initial conditions, this could not be the reason for failure, because the coefficient of friction between two surfaces is independent of the mass of the moving body. As the failure occurred only after the thaw front had started to enter the permafrost block, which became water saturated during thawing, the apparent cohesion due to water suction within the active layer and between the latter and the permafrost surface was not relevant for the failure.

Shear strength

To determine the shear strength between the active layer and the permafrost block first the balance of forces at failure has to be analyzed which is formulated in equation 3.27 and leads to

$$\tan\alpha = f_{AL} \tag{3.53}$$

where α is the inclination angle which equals the friction angle Φ between the active layer and the permafrost block at failure and f_{AL} the static friction coefficient. Then the shear strength can be calculated as

$$\tau_f = \frac{F_R}{A_{AL}} \tag{3.54}$$

$$\tau_f = \frac{f_{AL} \cdot m_{AL} \cdot g \cdot \cos\alpha}{A_{AL}}$$

$$\tau_f = \frac{\tan\alpha \cdot \left[\rho_{AL}(0-15cm) \cdot \frac{1}{5} V_{AL} + \rho_{AL}(15-75cm) \cdot \frac{4}{5} V_{AL} + \rho_w \cdot \theta_{AL} \cdot V_{AL} \right] \cdot g \cdot \cos\alpha}{A_{AL}}$$

$$\tau_f = \frac{\sin\alpha \cdot A_{AL} \cdot h_{AL\_n} \cdot \left[\rho_{AL}(0-15cm) \cdot \frac{1}{5} + \rho_{AL}(15-75cm) \cdot \frac{4}{5} + \rho_w \cdot \theta_{AL} \right] \cdot g}{A_{AL}}$$

$$\tau_f = \sin\alpha \cdot h_{AL\_n} \cdot g \cdot \left[\rho_{AL}(0-15cm) \cdot \frac{1}{5} + \rho_{AL}(15-75cm) \cdot \frac{4}{5} + \rho_w \cdot \theta_{AL} \right]$$

where F_R is friction, A_{AL} the contact area between the active layer and the permafrost block, V_{AL} the volume, h_{AL_n} the normal height and m_{AL} the mass of the active layer (including grit from 0-15 cm depth, gravel from 15-75 cm depth and water), $\rho_{AL}(z)$ the dry apparent density of the active layer depending on depth z, ρ_w the density of water, θ_w the volumetric water content of the active layer at failure and g the gravitational constant. For the parameter values given in Figure 3.35 and Table 3.11 and a water content of 7.1% at failure the shear strength between the active layer and the permafrost turns out to be 7.6 kN/m^2.

3.4.4 Summary of simulation of thaw-induced active layer failure

A thaw-induced failure of the active layer was simulated in the climate chamber using an inclinable shear box at a scale of 1:2 compared to the thickness of the active layer at the field study site and for the same slope inclination as in the field (chapter 2.1). The lower shear frame contained the artificial permafrost block, the upper shear frame the artificial active layer. First meltwater (0°C) was infiltrated into the dry and ice free frozen active layer at stepwise increasing infiltration rates, in order to investigate at which infiltration rate the active layer would fail due to its friction on the permafrost being reduced by the water ponding on the permafrost surface. However, even at an infiltration rate of 40 mm/h the active layer did not fail. Instead, ice formed in the active layer (especially at its base) leading to a further stabilization rather than a destabilization. After this simulated snowmelt period, the thawing of the active layer by direct radiation and with air temperatures above 0°C was simulated. When the thaw depth reached the active layer base, all the ice in the active layer was melted. However, the active layer only failed half an hour later, when the thawing front had started to penetrate into the permafrost surface. As the active layer was initially stable without ice, the failure is inferred to be due to the melting of ice in the fine grained permafrost in which the sand and silt grains had been embedded before. After the loss of cohesion due to ice, the shear strength of the sand strongly decreased resulting in failure.

3.5 Comparison of systematic shear tests and failure simulation

The main differences between the systematic shear test series and the physical simulation of active layer failure are methodological ones: for the systematic shear test series the conditions during individual experiments were kept constant and the slope angle was changed; for the physical simulation of active layer failure, the angle of inclination was kept constant and the conditions during the experiment were changed. In addition, the scale of the shear boxes used for the two experimental approaches differs by a factor of 2.5. The fact that both approaches led to the same main result regarding the failure mechanism confirmed the latter and the independence of scale.

4 Integral discussion of field and laboratory investigations

For the simulation of the thaw-induced active layer failure in the laboratory, the boundary conditions concerning slope inclination and grain size distribution were chosen to be very similar to those at the field study site, while the hydrothermal conditions were changed until failure occurred. Direct implications of this simulation for the special case of the field study site can therefore be made and will be discussed first. In the systematic shear test series the hydrothermal and granulometric conditions were set, while the slope inclination was increased until failure occurred. From these laboratory investigations general, but less clear implications can be derived for the stability of steep debris slopes in alpine permafrost.

4.1 Implications of the laboratory simulation for the field study site

Important processes during meltwater infiltration and thawing could be observed in the field as well as in the laboratory simulation: (1) response of the ground temperatures and (2) creep due to the change of hydrological parameters, (3) ice formation due to infiltrated meltwater and (4) its concentration at the active layer base. This showed that the conditions of the field study site could be simulated realistically in the climate chamber before failure. However, to capture the influence of the various factors prevailing in the field and interacting in a complex manner, the field investigations were essential.

In contrast, the downslope discharge on the impermeable permafrost layer, the accurate ice content of the entire active layer and thus its total water balance could only be determined under controlled laboratory conditions. In addition, these allowed the different parameters to be measured at the same place and therefore spatially to be exactly correlated in contrast to the field. Furthermore, the simulation of slope failure was only possible in the laboratory.

Despite the similarities to the field shown above, it has to be mentioned that the laboratory situation represents an extreme case, especially regarding the geotechnical conditions at the interface between the active layer and the permafrost. In the field the permafrost surface is not likely to be as planar as in the laboratory. Furthermore it is likely that there are not only sand and silt grains at the permafrost surface, but also some coarser grains increasing the roughness and therefore the shear strength. Finally, small weak locations at the active layer base within the slope having a factor of safety below one (and therefore would fail alone as simulated in the laboratory) can partly be supported by more stable areas downslope in the field. Therefore a failure of the active layer at the field study site is not likely for an inclination of 37°, but for higher slope angles. However, for a conservative slope stability assessment the worst case has to be considered which implies the weakest slope element.

Due to the good thermal insulation and the high albedo of snow it is very unlikely that the active layer temperatures in the field could exceed 0°C before the snow cover has completely disappeared in spring. According to the laboratory experiment where the active layer was stabilized rather than destabilized during the infiltration of meltwater in the ground at negative temperatures due to the formation of ice, the probability of the active layer failing during snowmelt in the field is very low (under ice unsaturated conditions), but will increase thereafter. It is evaluated to be highest in later summer, if the thaw depth exceeds average values and the uppermost permafrost layer contains ice, which is typical under alpine permafrost conditions. If the thaw front penetrates downwards (reinforced by the infiltration of warm rainwater) into finer grained sediments whose angle of internal friction is below the slope inclination, the slope will fail caused by the loss of strength due to the melt of ice in the fine sediments, i.e. the fine grains are no longer embedded in an ice matrix. This type of failure was simulated in the laboratory experiment and can be referred to as *failure due to ice melt in fine sediments*. This type is not only conceivable for the thaw front penetrating downwards from the active layer, but also upwards from the permafrost base or in both directions from a growing talik caused by ground temperature increases or flowing ground water. The potentially failing mass in the latter cases would be much greater than for an active layer failure.

Another type of failure may occur when warm rainwater is infiltrated at a high rate into an active layer above 0°C: as the cooling capacity of the permafrost is too low at this time, the infiltrated water will not freeze but pond on top of the permafrost surface, run downslope and create a saturated zone whose height increases with decreasing hydraulic conductivity. Buoyancy forces on the active layer will result, reducing the normal stress and therefore the friction between the active layer and the permafrost. If the shear strength between the unfrozen and frozen layer is so significantly reduced by this process, that it falls below the actual shear stress, the slope will fail. This type of failure, which can be referred to as *failure due to reduction of friction by saturated zone* has already been well investigated and described within the infinite slope model (e.g. Al-Khafaji & Andersland 1992), however, only for a ponding surface in general, not for an impermeable permafrost surface in particular. Therefore further investigations will be necessary to verify and understand the mechanism of this type of failure for scree slopes in permafrost terrain.

A combination of both proposed failure mechanisms increases the probability of failure. However, an intra-permafrost failure (due to a talik) or sub-permafrost one (see above) can only be triggered by a combination of the illustrated mechanisms when there is an aquiclude (e.g. permafrost surface below the talik or a stratum with a very low hydraulic conductivity within the talik or below the permafrost base), high pore water pressures in the aquifer (due to high hydrostatic pressures caused by infiltration rates exceeding the hydraulic conductivity of the aquifer or to entrapment of water between two aquicludes). The water could originate from snow or ice melt, rainfall, groundwater flux or an underground spring.

4.2 Implications of the shear test series for the field in general

In contrast to the field investigations and the physical simulation of a thaw-induced active layer failure in a single laboratory experiment, the systematic shear test series allowed the effect of each individual influencing factor on the friction angle between the active layer and the underlying permafrost to be separately determined. Considering the effects of grain size and ice saturation of the permafrost together, leads to the relevance of the experiments for real debris slopes in steep permafrost terrain under warming conditions in general: if the active layer deepens into finer grained material which was permanently frozen before and contained ice, the friction angle of the slope will be lowered. This can be deduced from the laboratory experiments by comparing the friction angle for a coarse active layer above a fine grainer permafrost containing ice with the friction angle for the same active layer and permafrost, but without ice. As the fine material in the active layer is washed out to depth under field conditions, but is fixed at the permafrost surface, it is realistic to assume that the uppermost layer of the permafrost is finer grained than the active layer, as was observed at the field study site (2.1).

The new potential shear plane could either remain at the interface between the finer and coarser material or could shift to the new permafrost surface. Which case occurs depends on the degree of water saturation of the finer grained lower part of the new active layer, its hydraulic conductivity (depending on the degree of water saturation) and the water percolation rate through the coarser part of the active layer. If the finer grained lower part of the new active layer is already water saturated or if its water conductivity is lower than the rate of water percolation through the coarser material above, the potential shear plane will likely remain at the interface between the coarser and finer material. Otherwise the potential shear plane will likely be shifted to the new (water impermeable) permafrost surface. If the new potential shear plane remains at the interface between the finer and coarser material, the decrease of the friction angle from the state before and after the active layer deepening is equal to the effect of the degree of ice saturation. However, if the new potential shear plane coincides with the new permafrost surface, the decrease of the friction angle is equal to the effect of the grain size of the active layer.

Besides the grain size and the presence of ice in the permafrost, the friction angle also depends on the water content of the unfrozen material. Water saturated conditions cause a reduction of the effective shear strength and can be considered in the slope stability analysis (see 4.1). For low water contents up to a threshold depending on grain size distribution the friction angle will be increased due to apparent cohesion caused by suction (for example Krahn et al. 1989). Beyond this threshold the friction angle will be decreased due to liquefaction (for example Springman et al. 2003). As the stabilizing effect of apparent cohesion is only temporary, and can disappear for example due to evaporation or saturation, it should not be considered in a conservative slope stability analysis.

The above discussion results in the following implications for a slope stability analysis in the field for debris slopes in alpine permafrost terrain, if the infinite slope model is applicable:

1. The active layer depth h_{AL} (normal to surface) should be estimated under further climate change by means of sophisticated models for the climate and the ground thermal conditions under consideration of measurements if available.
2. The effective angle of internal friction Φ' of the finest grained material within the future active layer should be determined (either by measuring in the laboratory or assessing by means of grain size distribution and shape of grains (Lang et al. 2003)), as it is crucial for slope stability.
3. The greatest possible height of the water saturated zone h_{sz} above the aquiclude (unfissured bedrock or impermeable permafrost layer) should be assessed from (1) the most extreme rainfall expected (according to climate models or long-term meteorological records), (2) the hydraulic conductivity of the finest grained material and (3) Darcy's law leading to

$$h_{sz} = \frac{l \cdot \left[I - \left(q_{\Delta ws} + q_{\Delta is}\right)\right]}{k_f \cdot \tan\alpha \cdot e} \tag{4.1}$$

where l is the upslope length to the end of the catchment, I is the infiltration (i.e. rainfall) rate, $q_{\Delta ws}$ and $q_{\Delta is}$ are the rates of the water and ice storage change in the active layer (which can be neglected in a first estimation), k_f is the hydraulic conductivity, e is the porosity and α is the slope inclination.

4. The stabilizing effect of the apparent cohesion due to water should be neglected to be on the safe side.
5. The factor of safety FS should be calculated using the effective resisting strength (numerator) and the driving stresses (denominator); in the effective resisting strength the reduction of the normal stress due to the water saturated zone is considered; the driving stresses comprise the stress due to the downslope force of the active layer including water (first summand) and the stress due to the force of the water streaming downslope (second summand); this results in

$$FS \quad = \quad \frac{\cos\alpha \cdot \left[\rho_{AL} \cdot h_{AL} - \rho_w \cdot h_{sz} \cdot (1-e)\right] \cdot \tan\phi'}{\sin\alpha \cdot h_{AL} \cdot \left(\rho_{AL} + \theta_v \cdot \rho_w\right) \quad + \quad \tan\alpha \cdot h_{sz} \cdot \rho_w} \tag{4.2}$$

where ρ_{AL} is the apparent density of the active layer, ρ_w the density of water, θ_v the mean volumetric water content of the entire active layer. If FS decreases below unity the slope will fail.

5 Conclusions

In the present study field and laboratory experiments were performed in order to improve understanding of the interrelations between hydrological and thermal processes of the active layer above alpine permafrost in steep debris slopes and their influence on slope stability. The following can be concluded:

1. The measuring equipment and design applied in this study proved to be suitable to reliably monitor hydrological, thermal and geotechnical processes occurring in the active layer above alpine permafrost in steep scree slopes for at least three years.
2. Temporal changes of hydrological parameters are closely correlated to ground thermal and geotechnical conditions; hydrological processes, especially during snowmelt, represent major controls of the thermal regime as well as of the downslope displacement of the active layer above alpine permafrost in steep debris slopes.
3. The laboratory experiments revealed that hydrothermal processes in the active layer consisting of coarse scree strongly affect slope stability; although the infiltration rates are highest during snowmelt, the risk of an active layer failure is not highest then, but in summer when warm rainwater effectively erodes the permafrost due to the combined thermal and mechanical effect of water flowing downslope on the impermeable permafrost.
4. Concerning the failure mechanism, the shear strength proved to decrease strongly when grains at the permafrost surface are no longer embedded in an ice matrix; in the context of global warming this implies that further active layer deepening into finer grained materials which were previously fixed in the ice matrix of the permafrost will reduce slope stability.
5. The application of an infinite slope stability analysis to assess the probability of active layer failures on steep scree slopes in alpine permafrost regions requires the consideration of special implications which were provided in this study.

6 Outlook

Concerning the field investigations, further monitoring of the hydrothermal and geotechnical processes will be conducted. Solutions for year-round measurements of infiltration, discharge on the impermeable permafrost layer, and the ice content would help to improve the accuracy of the water balance at the field study site. Measuring the electrical water conductivity in a buried bath which continuously guarantees saturated conditions would allow an assessment of the contact time of the discharging water with the ground and thus its origin.

The results obtained for the hydrothermal processes in the active layer above alpine permafrost can be used for a further sophistication of the soil part of the 1-dimensional numerical mass and energy balance model *SNOWPACK* (Lehning et al. 1999, Luetschg et al. 2004, Luetschg 2005). In a further step this would allow the spatial simulation of hydrothermal processes in the active layer to be improved by means of the 3-dimensional model *hydro@alpine_3D* (Lehning et al. 2006).

As the friction angle between the permafrost and the active layer is increased by the apparent cohesion of water due to suction, but is decreased for very high water contents due to liquefaction, there must be an optimum water content concerning slope stability. This could be determined by means of a further series of shear tests with stepwise increasing water contents using the small inclinable shear box presented in this study.

The physical simulation of a rainfall-induced active layer failure using the big inclinable shear box in the climate chamber under field conditions as regards slope inclination and soil texture is suggested for the future. This would allow an assessment of the hydrothermal conditions for slope instabilities at the field study site and similar periglacial debris slopes. In addition, an *in situ* active layer failure could be triggered by artificial infiltration in a controlled field experiment.

Using the conditions for active layer failure found in the laboratory experiments, a high resolution digital elevation model, information on the active layer depth and the ground texture, the factor of safety of debris slopes in alpine periglacial environments could be estimated spatially. This would help to focus on potential risk zones and situations (e.g. intense rainfall events) to be efficiently verified in the field.

References

Al-Khafaji AW, Andersland OB. 1992. *Geotechnical Engineering and Soil Testing*. Fort Worth [etc.]: Saunders College Publishing. 695 pp.

Andersland O, Ladanyi B. 2004. *Frozen ground engineering*. Hoboken, NJ: Wiley. 363 pp.

Arenson L, Hoelzle M, Springman S. 2002. Borehole deformation measurements and internal structure of some rock glaciers in Switzerland. *Permafrost and Periglacial Processes* 13: 117-135

Arenson L, Springman S. 2005a. Mathematical descriptions for the behaviour of ice-rich frozen soils at temperatures close to 0°C. *Canadian Geotechnical Journal* 42: 431-442

Arenson L, Springman S. 2005b. Triaxial constant stress and constant strain rate tests on ice-rich permafrost samples. *Canadian Geotechnical Journal* 42: 412-430

Arenson LU, Johansen MM, Springman SM. 2004. Effects of volumetric ice content and strain rate on shear strength under triaxial conditions for frozen soil samples. *Permafrost and Periglacial Processes* 15: 261-271

Arenson LU, Palmer AC. 2005. Rock glaciers, fault gouge and asphalt hard particles in a nonlinear creeping matrix. *Cold Regions Science and Technology* 43: 117-127

ASTM. 2000a. *Standard test methods for maximum index density and unit weight of soils using a vibratory table. Report D 4253 - 00*, American Society for Testing and Materials, West Conshohocken, PA

ASTM. 2000b. *Standard test methods for minimum index density and unit weight of soils and calculation of relative density. Report D 4254 - 00*, American Society for Testing and Materials, West Conshohocken, PA

Babu GLS, Rao RS, Peter J. 2005. Evaluation of shear strength functions based on soil water characteristic curves. *Journal of Testing and Evaluation* 33: 461-465

Bajewsky I, Gardner JS. 1989. Discharge and sediment-load characteristics of the Hilda rock-glacier stream, Canadian Rocky Mountains, Alberta. *Physical Geography* 10: 295-306

Baker R, Frydman S, Talesnick M. 1993. Slope Stability Analysis for Undrained Loading Conditions. *International Journal for Numerical and Analytical Methods in Geomechanics* 17: 15-43

Baker THW. 1979. Strain Rate Effect on the Compressive Strength of Frozen Sand. *Engineering Geology* 13: 223-231

Barsch D. 1988. Rock glaciers. In *Advances in periglacial geomorphology*, Clark MJ (ed.), pp. 69-90. Chichester: John Wiley and Sons Ltd

Barsch D. 1993. Periglacial Geomorphology in the 21st-Century. *Geomorphology* 7: 141-163

Bayard D, Stähli M, Parriaux A, Flühler H. 2005. The influence of seasonally frozen soil on the snowmelt runoff at two Alpine sites in southern Switzerland. *Journal of Hydrology* 309: 66-84

Beltrami H. 1996. Active layer distortion of annual air soil thermal orbits. *Permafrost and Periglacial Processes* 7: 101-110

Bernhard L, Sutter F, Haeberli W, Keller F. 1998. *Processes of snow/permafrost-interactions at a high-mountain siet, Murtèl/Corvatsch, eastern Swiss Alps*. Proceedings of the 7th International Conference on Permafrost, Yelloknife, Canada, 23-27 June 1998. Collection Nordicana, Centre d'études nordiques, Université Laval; 57: 35-41

Bishop AW. 1955. The use of the slip circle in the stability analysis of slopes. *Geotechnique* 5: 7-17

Bittelli M, Flury M, Roth K. 2004. Use of dielectric spectroscopy to estimate ice content in frozen porous media. *Water Resources Research* 40: W04212

Blijenberg HM. 1995. In-situ strength tests of coarse, cohesionless debris on scree slopes. *Engineering Geology* 39: 137-146

Boike J, Overduin PP. 1999. Seasonal changes in hydrology, energy balance and chemistry in the active layers of arctic tundra soils in Taymyr Peninsula. In *Land-ocean systems in the Siberian Arctic: Dynamics and History*, Kassens H (ed.), pp. 299-306. Berlin: Springer

Boike J, Overduin PP, Hagedorn B, Gintz D, Salzwedel U. 1996. Active layer hydrology. In *The Expedition Taymyr 1995; The Expedition Kolyma 1995 of the ISSP Pushchino Group: Russian-German Cooperation*, Bolshiyanov DY, Hubberten HW (eds), pp. 95-96. Bremerhaven: Alfred Wegener Institut for Polar and Marine Research

Boike J, Roth K, Overduin PP. 1998. Thermal and hydrologic dynamics of the active layer at a continuous permafrost site (Taymyr Peninsula, Siberia). *Water Resources Research* 34: 355-363

Bolton MD. 1986. The Strength and Dilatancy of Sands. *Geotechnique* 36: 65-78

Bovis MJ. 1993. Hillslope geomorphology and geotechnique. *Progress in Physical Geography* 17: 173-189

Brenning A. 2005. Geomorphological, hydrological and climatic significance of rock glaciers in the Andes of Central Chile (33-35 degrees S). *Permafrost and Periglacial Processes* 16: 231-240

Brown RJE, Kupsch WO. 1974. *Permafrost terminology*. Ottawa: National Research Council of Canada. 62 pp.

Burn CR. 1990. *Snowmelt infiltration into frozen soil at sites in the discontinuous permafrost zone near Mayo, Yukon Territory*. Proceedings of the Northern Hydrology Symposium, Saskatoon, Canada, 10-12 July 1990, Prowse TD, Ommanney CSL (eds). National Hydrology Research Institute, Environment Canada; 445-459

Burn CR. 2000. The thermal regime of a retrogressive thaw slump near Mayo, Yukon Territory. *Canadian Journal of Earth Sciences* 37: 967-981

Burn CR, Smith CAS. 1988. Observations of the thermal offset in near-surface mean annual ground temperatures at several sites near Mayo, Yukon-Territory, Canada. *Arctic* 41: 99-104

Carey SK, Quinton WL. 2005. Evaluating runoff generation during summer using hydrometric, stable isotope and hydrochemical methods in a discontinuous permafrost alpine catchment. *Hydrological Processes* 19: 95-114

Christiansen HH. 2004. Meteorological control on interannual spatial and temporal variations in snow cover and ground thawing in two northeast greenlandic circumpolar-active-layer-monitoring (CALM) sites. *Permafrost and Periglacial Processes* 15: 155-169

Cornforth DH. 1964. Some experiments on the influence of strain conditions on the strength of sand. *Geotechnique* 14: 143-167

Cornforth DH. 1973. *Prediction of drained strength of sand from relative density and its role in geotechnical projects involving cohesionless soils. Report 523*, American Society for Testing and Materials, Philadelphia

Croce PV, Pane V, Znidarcic D, Ko HY, Olsen HW, Schiffman RL. 1985. Evaluation of consolidation theories by centrifuge modelling. In *Applications of Centrifuge Modelling to Geotechnical Design*, Craig WH (ed.), pp. 381-401. Rotterdam: Balkema

Davies MCR, Hamza O, Harris C. 2001. The effect of rise in mean annual temperature on the stability of rock slopes containing ice-filled discontinuities. *Permafrost and Periglacial Processes* 12: 137-144

Davies MCR, Hamza O, Lumsden BW, Harris C. 2000. Laboratory measurement of the shear strength of ice-filled rock joints. *Annals of Glaciology* 31: 463-467

Delaloye R, Reynard E, Lambiel C, Marescot L, Monnet R. 2003. *Thermal anomaly in a cold scree slope (Creux du Van, Switzerland)*. Proceedings of the 8th International Conference on Permafrost, Zurich, Switzerland, 21-25 July 2003, Phillips M, Springman SM, Arenson LU (eds). Lisse, The Netherlands: Balkema Publishers; 175-180

Egginton PA, French HM. 1985. Solifluction and related processes, Eastern Banks-Island, NWT. *Canadian Journal of Earth Sciences* 22: 1671-1678

Ehlers W. 2001. *Theoretical and numerical methods in continuum mechanics of porous materials*. Proceedings of the IUTAM Symposium, Stuttgart, 5-10 September 1999, Ehlers W (ed.). Kluwer Academic Publishers: Dordrecht, The Netherlands. 422 pp.

Ehlers W, Bluhm J, eds. 2002. *Porous media: theory, experiments, and numerical applications*. Berlin: Springer. 458 pp.

Faybishenko B. 2004. Nonlinear dynamics in flow through unsaturated fractured porous media: Status and perspectives. *Reviews of Geophysics* 42: RG2003

Flerchinger GN, Seyfried MS, Hardegree SP. 2006. Using soil freezing characteristics to model multi-season soil water dynamics. *Vadose Zone Journal* 5: 1143-1153

Fredlund DG, Morgenstern NR, Widger RA. 1978. Shear-strength of unsaturated soils. *Canadian Geotechnical Journal* 15: 313-321

French HM. 1976. *The periglacial environment*. London: Longman. 309 pp.

French HM. 1996. *The periglacial environment*. Harlow, Longman. 341 pp.

Friedman SP, Jones SB. 2001. Measurement and approximate critical path analysis of the pore-scale-induced anisotropy factor of an unsaturated porous medium. *Water Resources Research* 37: 2929-2942

Gan KJ, Fredlund DG. 1988. Multistage direct shear testing of unsaturated soils. *Geotechnical Testing Journal* 11: 132-138

Gardaz JM. 1998. *Permafrost prospecting, periglacial and rock glacier hydrology in mountain areas. Case studies in the Valais Alps*. Doctoral thesis. University of Fribourg. 184 pp.

Glen JW. 1952. Experiments on the deformation of ice. *Journal of Glaciology* 2: 111-114

Glen JW. 1955. The creep of polycristalline ice. In *Proceedings of the Royal Society*, ed. R Society, pp. 519-538. London: Royal Society

Glen JW. 1974. *The physics of ice*, U.S. Army Cold Regions Research and Engineering Laboratory, Hanover, New Hampshire. 79 pp.

Gorbunov AR, Marchenko SS, Seversky EV. 2004. The thermal environment of blocky materials in the mountains of central Asia. *Permafrost and Periglacial Processes* 15: 95-98

Goughnour RR, Andersland O. 1968. Mechanical properties of a sand-ice system. *Journal of the soil mechanics and foundations division, American Society of Civil Engineers* 94: 923-950

Gray DH, Megahan WF. 1981. *Forest vegetation removal and slope stability in the Idaho Batholith*. Ogden: U.S. Department of Agriculture. 23 pp.

Gray J. 2001. Granular flow in partially filled slowly rotating drums. *Journal of Fluid Mechanics* 441: 1-29

Gruber S, Hoelzle M, Haeberli W. 2004a. Permafrost thaw and destabilization of Alpine rock walls in the hot summer of 2003. *Geophysical Research Letters* 31: L13504

Gruber S, Hoelzle M, Haeberli W. 2004b. Rock-wall temperatures in the Alps: Modelling their topographic distribution and regional differences. *Permafrost and Periglacial Processes* 15: 299-307

Haeberli W. 1985. *Creep of mountain permafrost: internal structure and flow of alpine rock glaciers*. Zurich: Mitteilungen der Versuchsanstalt für Wasserbau, Hydrologie und Glaziologie der Eidgenössischen Technischen Hochschule Zürich 77. 142 pp.

Haeberli W. 1990a. Permafrost. In *Internationale Fachtagung über Schnee, Eis und Wasser der Alpen in einer wärmeren Atmosphäre: 11. Mai 1990 in Zürich*, Vischer D (ed.), pp. 71-88. Zurich: Versuchsanstalt für Wasserbau, Hydrologie und Glaziologie der Eidgenössischen Technischen Hochschule Zürich

Haeberli W. 1990b. *Pilot analyses of permafrost cores from the active rock glacier Murtel I, Piz Corvatsch, Eastern Swiss Alps: a workshop report*. Zurich: Mitteilungen der Versuchsanstalt für Wasserbau, Hydrologie und Glaziologie an der Eidgenössischen Technischen Hochschule Zürich 9. 38 pp.

Haeberli W. 1992. Construction, environmental problems and natural hazards in periglacial mountain belts. *Permafrost and Periglacial Processes* 3: 111 - 124

Haeberli W, Beniston M. 1998. Climate change and its impacts on glaciers and permafrost in the Alps. *Ambio* 27: 258-265

Haeberli W, Hallet B, Arenson L, Elconin R, Humlun O, et al. 2006. Permafrost creep and rock glacier dynamics. *Permafrost and Periglacial Processes* 17: 189-214

Haeberli W, Hoelzle M, Keller F, Schmid W, Vonder Muhll D, Wagner S. 1993. *Monitoring the long-term evolution of mountain permafrost in the Swiss Alps*. Proceedings of the 6th International Conference on Permafrost, Beijing, China, 5-9 July 1993. Wushan Guangzhou, China: South China University of Technology Press; 214-219

Haeberli W, Huggel C, Kääb A, Zgraggen-Oswald S, Polkvoj A, et al. 2004. The Kolka-Karmadon rock/ice slide of 20 September 2002: an extraordinary event of historical dimensions in North Ossetia, Russian Caucasus. *Journal of Glaciology* 50: 533-546

Haeberli W, Kääb A, Hoelzle M, Bösch H, Funk M, et al. 1999. *Eisschwund und Naturkatastrophen im Hochgebirge*. Zurich: vdf, Hochschulverlag an der ETH. 190 pp.

Haefeli R. 1967. Kriechen und progressiver Bruch in Schnee, Boden, Fels und Eis. *Schweizerische Bauzeitung* 85: 1-9

Hammond C, Hall D, Miller S, Swetik P. 1992. *Level I Stability analysis (LISA) documentation for version 2.0*. Ogden: Intermountain Research Station. 190 pp.

Hanson S, Hoelzle M. 2004. The thermal regime of the active layer at the Murtèl rock glacier based on data from 2002. *Permafrost and Periglacial Processes* 15: 273-282

Harris C. 1993. The role of climate and soil properties in periglacial solifluction: evidence from laboratory experiments. In *Solifluction and Climatic Variation in the Holocene*, ed. B Frenzel, pp. 295-308. Stuttgart: Gustav Fischer

Harris C, Davies MCR. 1996. *Processes of Thaw-Induced Mass Movement in Non-cohesive Soils: Results of an Instrumented Slope Simulation Experiment*. Chichester: John Wiley & Sons Ltd. 1153-1171 pp.

Harris C, Davies MCR. 1998. *Pressures recorded during laboratory freezing and thawing of a natural silt-rich soil*. Proceedings of the 7th International Conference on Permafrost, Yelloknife, Canada, 23-27 June 1998. Collection Nordicana, Centre d'études nordiques, Université Laval; 57: 433-439

Harris C, Davies MCR, Coutard JP. 1995. Laboratory simulation of periglacial solifluction: significance of porewater pressures, moisture contents and undrained shear strengths during soil thawing. *Permafrost and Periglacial Processes* 6: 293-311

Harris C, Davies MCR, Coutard JP. 1996. An experimental design for laboratory simulation of periglacial solifluction processes. *Earth Surface Processes and Landforms* 21: 67-75

Harris C, Rea B, Davies M. 2001. Scaled physical modelling of mass movement processes on thawing slopes. *Permafrost and Periglacial Processes* 12: 125-135

Harris C, Vonder Mühll D, Isaksen K, Haeberli W, Sollid JL, et al. 2003. Warming permafrost in European mountains. *Global and Planetary Change* 39: 215-225

Harris SA, Pedersen DE. 1998. Thermal regimes beneath coarse blocky materials. *Permafrost and Periglacial Processes* 9: 107-120

Hauck C. 2001. *Geophysical methods for detecting permafrost in high mountains*. Zurich: Mitteilungen der Versuchsanstalt für Wasserbau, Hydrologie und Glaziologie der Eidgenössischen Technischen Hochschule Zürich 171. 204 pp.

Hayashi M, Quinton WL. 2004. A constant-head well permeameter method for measuring field-saturated hydraulic conductivity above an impermeable layer. *Canadian Journal of Soil Science* 84: 255-264

Haynes FD, Karalius JA. 1977. *Effect of temperture on the strength of frozen silt*. Hanover, New Hampshire: Reports of the U.S. Army Cold Regions Research and Engineering Laboratory 77-3. 27 pp.

Herminghaus S. 2005. Dynamics of wet granular matter. *Advances in Physics* 54: 221-261

Hillel D. 1980. *Fundamentals of soil physics*. New York: Academic Press. 413 pp.

Hinkel KM, Outcalt SI. 1994. Identification of heat-transfer processes during soil cooling, freezing, and thaw in central Alaska. *Permafrost and Periglacial Processes* 5: 217-235

Hinkel KM, Outcalt SI, Nelson FE. 1990. Temperature variation and apparent thermal diffusivity in the refreezing active layer, Toolik Lake, Alaska. *Permafrost and Periglacial Processes* 1: 265-274

Hinkel KM, Outcalt SI, Taylor AE. 1997. Seasonal patterns of coupled flow in the active layer at three sites in northwest North America. *Canadian Journal of Earth Sciences* 34: 667-678

Hinkel KM, Paetzold F, Nelson FE, Bockheim JG. 2001. Patterns of soil temperature and moisture in the active layer and upper permafrost at Barrow, Alaska: 1993-1999. *Global and Planetary Change* 29: 293-309

Hoelzle M. 1994. *Permafrost und Gletscher im Oberengadin. Grundlagen und Anwendungsbeispiele für automatisierte Schätzverfahren*. Zurich: Mitteilungen der Versuchsanstalt für Wasserbau, Hydrologie und Glaziologie der Eidgenössischen Technischen Hochschule Zürich 132. 121 pp.

Hult JAH. 1966. *Creep in engineering structures*. Waltham, Massachusetts: Blaisdell. 115 pp.

Humlum O. 1997. Active layer thermal regime at three rock glaciers in Greenland. *Permafrost and Periglacial Processes* 8: 383-408

Indraratna B, Welideniya HS, Brown ET. 2005. A shear strength model for idealised infilled joints under constant normal stiffness. *Geotechnique* 55: 215-226

Ishikawa M, Sharkuu N, Zhang YS, Kadota T, Ohata TT. 2005. Ground thermal and moisture conditions at the southern boundary of discontinuous permafrost, Mongolia. *Permafrost and Periglacial Processes* 16: 209-216

Ishikawa M, Zhang YS, Kadota T, Ohata T. 2006. Hydrothermal regimes of the dry active layer. *Water Resources Research* 42: W04401

ISO. 1996. *ISO 11562. Geometrical Product Specifications (GPS) - Surface texture: Profile method - Metrological characteristics of phase correct filters*. Berlin: Beuth

ISO. 1997. *ISO 4287. Geometrical Product Specification (GPS) - Surface texture: Profile method - Terms, definitions and surface texture parameters*. Berlin: Beuth

Iverson RM, Major JJ. 1986. Groundwater seepage vectors and the potential for hillslope failure and debris flow mobilization. *Water Resources Research* 22: 1543-1548

Jaesche P, Veit H, Huwe B. 2003. Snow cover and soil moisture controls on solifluction in an area of seasonal frost, eastern Alps. *Permafrost and Periglacial Processes* 14: 399-410

Johnson PG. 1981. The structure of a talus-derived rock glacier deduced from its hydrology. *Canadian Journal of Earth Sciences* 18: 1422-1430

Kane DL, Hinkel KM, Goering DJ, Hinzman LD, Outcalt SI. 2001. Non-conductive heat transfer associated with frozen soils. *Global and Planetary Change* 29: 275-292

Kane DL, Hinzman LD, Zarling JP. 1991. Thermal response of the active layer to climatic warming in a permafrost environment. *Cold Regions Science and Technology* 19: 111-122

Kaplar CW. 1971. *Some strength properties of frozen soil and effect of loading rate*. Hanover, New Hampshire: Reports of the U.S. Army Cold Regions Research and Engineering Laboratory 159. 25 pp.

Keller F. 1994. *Interaktionen zwischen Schnee und Permafrost. Eine Grundlagenstudie im Oberengadin*. Zurich: Mitteilungen der Versuchsanstalt für Wasserbau, Hydrologie und Glaziologie der Eidgenössischen Technischen Hochschule Zürich 127. 145 pp.

Keller F, Frauenfelder R, Gardner JS, Hoelzle M, Kneisel C, et al. 1998. *Permafrost map of Switzerland*. Proceedings of the 7th International Conference on Permafrost, Yellowknife, Canada, 23-27 June 1998. Collection Nordicana, Centre d'études nordiques, Université Laval; 57: 557-562

Kienholz H. 1995. Gefahrenbeurteilung und -bewertung - auf dem Weg zu einem Gesamtkonzept. *Schweizerische Zeitschrift für Forstwesen* 146: 701-725

Kim TH, Sture S. 2004. Effect of moisture on attraction force in beach sand. *Marine Georesources & Geotechnology* 22: 33-47

Kishida H, Uesugi M. 1987. Tests of the interface between sand and steel in the simple shear apparatus. *Geotechnique* 37: 45-52

Kleppmann W. 2003. *Taschenbuch Versuchsplanung*. Munich: Carl Hanser. 301 pp.

Krahn J, Fredlund DG, Klassen MJ. 1989. Effect of soil suction on slope stability at Notch Hill. *Canadian Geotechnical Journal* 26: 269-278

Kraus H. 2001. *Die Atmosphäre der Erde: eine Einführung in die Meteorologie*. Berlin: Springer. 470 pp.

Lachenbruch AH, Marshall BV. 1986. Changing climate - geothermal evidence from permafrost in the Alaskan Arctic. *Science* 234: 689-696

Lambe TW, Whitman RV. 1969. *Soil mechanics*. New York: Wiley. 553 pp.

Lang E, Andrecs P, Hagen K, Stary U. 2006. Die Auslöser des Katastrophenereignisses 2005. In *Naturgefahren, Erdbewegungen und Erosion*, ed. NuL Bundesforschungs- und Ausbildungszentrum für Wald, Institut für Naturgefahren und Waldgrenzregionen. Vienna: waldwissen.net: Informationen für die Forstpraxis

Lang HJ, Huder J, Amann P. 2003. *Bodenmechanik und Grundbau : das Verhalten von Böden und Fels und die wichtigsten grundbaulichen Konzepte*. Berlin: Springer. 317 pp.

Lehning M, Bartelt P, Brown B, Russi T, Stöckli U, Zimmerli M. 1999. SNOWPACK model calculations for avalanche warning based upon a new network of weather and snow stations. *Cold Regions Science and Technology* 30: 145-157

Lehning M, Volksch I, Gustafsson D, Nguyen TA, Stähli M, Zappa M. 2006. ALPINE3D: a detailed model of mountain surface processes and its application to snow hydrology. *Hydrological Processes* 20: 2111-2128

Lewkowicz AG. 1988. Slope processes. In *Advances in periglacial geomorphology*, Clark MJ (ed.), pp. 325-368. Chichester: John Wiley and Sons Ltd

Lewkowicz AG, Clarke S. 1998. *Late-summer solifluction and active layer depth, Fosheim Peninsula, Ellesmere Island, Canada*. Proceedings of the 7th International Conference on Permafrost, Yelloknife, Canada, 23-27 June 1998. Collection Nordicana, Centre d'études nordiques, Université Laval; 57: 641-666

Lewkowicz AG, Harris C. 2005a. Frequency and magnitude of active-layer detachment failures in discontinuous and continuous permafrost, northern Canada. *Permafrost and Periglacial Processes* 16: 115-130

Lewkowicz AG, Harris C. 2005b. Morphology and geotechnique of active-layer detachment failures in discontinuous and continuous permafrost, northern Canada. *Geomorphology* 69: 275-297

Luetschg M. 2005. *A Model and Field Analysis of the Interaction between Snow Cover and Alpine Permafrost*. Zurich: Schriftenreihe Physische Geographie, Geographisches Institut der Universität Zürich. 258 pp.

Luetschg M, Stoeckli V, Lehning M, Haeberli W, Ammann W. 2004. Temperatures in two boreholes at Fluela Pass, Eastern Swiss Alps: the effect of snow redistribution on permafrost distribution patterns in high mountain areas. *Permafrost and Periglacial Processes* 15: 283-297

Makowski E. 1986. *Modellierung der künstlichen Bodenvereisung im grundwasserdurchströmten Untergrund mit der Methode der finiten Elemente*. Bochum: Ruhr-Universität. 292 pp.

Marachi ND, Chan CK, Seed HB, Duncan JM. 1969. *Strength and deformation characteristics of rockfill materials*. Berkley: Reports of the University of California TE-69-5

Matsuoka N. 2001. Solifluction rates, processes and landforms: a global review. *Earth-Science Reviews* 55: 107-134

Matsuoka N. 2005. Temporal and spatial variations in periglacial soil movements on alpine crest slopes. *Earth Surface Processes and Landforms* 30: 41-58

McRoberts EC, Morgenstern NR. 1973. *A study of landslides in the vicinity of the Mackenzie River, mile 205 to 660*: Canada Environmental-social Committe; Northern pipelines, Task Force on Northern Oil Development

McRoberts EC, Morgenstern NR. 1974. The stability of thawing slopes. *Canadian Geotechnical Journal* 11: 447-469

McRoberts EC, Nixon JF. 1977. *Extensions to thawing slope stability theory*. Proceedings of the 2nd International Symposium on Cold Regions Engineering, Fairbanks, Alaska, 12-14 August 1976, Burdick JL, Johnson P (eds). Cold Regions Engineers Professional Association; 262-276

Menzel L. 1995. *Bodenfeuchtemessung mittels Time Domain Reflectometry (TDR): Funktion und Anwendung. Report 55*, Geographisches Institut ETH Zürich, Zurich

Miller RD. 1980. Freezing phenomena in soils. In *Applications of Soil Physics*, ed. D Hillel, pp. 254-99. New York: Academic Press

Mittaz C, Hoelzle M, Haeberli W. 2000. First results and interpretation of energy-flux measurements over Alpine permafrost. *Annals of Glaciology* 31: 275-280

Morgenstern NR, Nixon JF. 1971. One-dimensional consolidation of thawing soils. *Canadian Geotechnical Journal* 8: 558-565

Morgenstern NR, Price VE. 1965. The analysis of the stability of general slip surfaces. *Geotechnique* 15: 79-93

Morgenstern NR, Roggensack WD, Weaver JS. 1980. The behavior of friction piles in ice and ice-rich soils. *Canadian Geotechnical Journal* 17: 405-415

Morgenstern NR, Sangrey DA. 1978. Methods of stability analysis. In *Landslides: analysis and control*, ed. RL Schuster, RJ Krizek pp. 155-171. Washington: Transportation research Board - National Academy of science

Muller SW. 1945. *Permafrost and permanently frozen ground and related engineering problems. Report 62*, United States Engineers Office, Ann Arbor, Michigan

Nase ST, Vargas WL, Abatan AA, McCarthy JJ. 2001. Discrete characterization tools for cohesive granular material. *Powder Technology* 116: 214-223

Nickling WG, Bennett L. 1984. The shear-strength characteristics of frozen coarse granular debris. *Journal of Glaciology* 30: 348-357

Niu FJ, Cheng GD, Ni WK, Jin DW. 2005. Engineering-related slope failure in permafrost regions of the Qinghai-Tibet Plateau. *Cold Regions Science and Technology* 42: 215-225

Nowak S, Samadani A, Kudrolli A. 2005. Maximum angle of stability of a wet granular pile. *Nature Physics* 1: 50-52

Onda Y, Matsukura Y. 1997. Mechanism for the instability of slopes composed of granular materials. *Earth Surface Processes and Landforms* 22: 401-411

O'Sullivan C, Bray JD, Riemer M. 2004. Examination of the response of regularly packed specimens of spherical particles using physical tests and discrete element simulations. *Journal of Engineering Mechanics-Asce* 130: 1140-1150

Outcalt SI, Nelson FE, Hinkel KM. 1990. The zero-curtain effect: heat and mass-transfer across an isothermal region in freezing soil. *Water Resources Research* 26: 1509-1516

Péwé TL. 1991. Permafrost. In *The heritage of engineering geology: the first hundred years.*, ed. GA Kiersch, pp. 277-298. Boulder, Colorado: Geological Society of America

Phillips M. 2000. *Influences of snow supporting structures on the thermal regime of the ground in alpine permafrost terrain*. Davos: Eidgenössisches Institut für Schnee- und Lawinenforschung. 146 pp.

Phillips M. 2006. Avalanche defence strategies and monitoring of two sites in mountain permafrost terrain, Pontresina, Eastern Swiss Alps. *Natural Hazards* 39: 353-379

Phillips M, Ladner F, Muller M, Sambeth U, Sorg J, Teysseire P. 2007. Monitoring and reconstruction of a chairlift midway station in creeping permafrost terrain, Grachen, Swiss Alps. *Cold Regions Science and Technology* 47: 32-42

Phillips M, Margreth S, Ammann WJ. 2003. *Creep of snow-supporting structures in alpine permafrost*. Proceedings of the 8th International Conference on Permafrost, Zurich, Switzerland, 21-25 July 2003, Phillips M, Springman SM, Arenson LU (eds). Lisse, The Netherlands: Balkema Publishers; 891-896

Phillips M, Schweizer J. 2007. Effect of mountain permafrost on snowpack stability. *Cold Regions Science and Technology* 47: 43-49

Phukan A. 1985. *Frozen ground engineering*. Englewood Cliffs - N.J.: Prentice-Hall. 336 pp.

Pierrat P, Caram HS. 1997. Tensile strength of wet granular materials. *Powder Technology* 91: 83-93

Rebetez M, Lugon R, Baeriswyl PA. 1997. Climatic change and debris flows in high mountain regions: The case study of the Ritigraben torrent (Swiss Alps). *Climatic Change* 36: 371-389

Rist A, Phillips M. 2005. First results of investigations on hydrothermal processes within the active layer above alpine permafrost in steep terrain. *Norwegian Journal of Geography* 59: 177-183

Roggensack WD. 1977. *Geotechnical properties of fine-grained permafrost soils*. University of Alberta, Edmonton. 423 pp.

Romanovsky VE, Osterkamp TE. 2000. Effects of unfrozen water on heat and mass transport processes in the active layer and permafrost. *Permafrost and Periglacial Processes* 11: 219-239

Rometsch R, Letzner RD. 1993. *Rauheitsmessung - Theorie und Praxis*. Villingen-Schwenningen: Schnurr Druck. 107 pp.

Roth K, Schulin R, Fluhler H, Attinger W. 1990. Calibration of Time Domain Reflectometry for Water-Content Measurement Using a Composite Dielectric Approach. *Water Resources Research* 26: 2267-2273

Rowlinson JS, Widom B. 1982. *Molecular theory of capillarity*. Oxford: Clarendon Press. 327 pp.

Savidou C. 1988. Centrifuge modelling of heat transfer in soil. *Centrifuge* 88: 583-591

Sawada Y, Ishikawa M, Ono Y. 2003. Thermal regime of sporadic permafrost in a block slope on Mt. Nishi-Nupukaushinupuri, Hokkaido Island, Northern Japan. *Geomorphology* 52: 121-130

Schrott L. 1999. *Typische und atypische Permafrostvorkommen - Klimatische Bedingungen, geomorphologische Indikatoren und Prospektionsmethoden. Report 37*, Naturhistorischer Verein der Rheinlande und Westfalens e.V., Bonn

Shibuya S, Mitachi T, Tamate S. 1997. Interpretation of direct shear box testing of sands as quasi-simple shear. *Geotechnique* 47: 769-790

Shur Y, Hinkel KM, Nelson FE. 2005. The transient layer: Implications for geocryology and climate-change science. *Permafrost and Periglacial Processes* 16: 5-17

Sidle RC, Pearce AJ, O'Loughlin CL. 1985. *Hillslope stability and land use*. Washington, D. C.: American Geophysical Union. 140 pp.

Skempton AW, DeLory FA. 1957. *Stability of natural slopes in London clay*. Proceedings of the 4th International Conference on Soil Mechanics and Foundation Engineering; 378-381

Smith MW, Burn CR. 1987. Outward Flux of Vapor from Frozen Soils at Mayo, Yukon, Canada - Results and Interpretation. *Cold Regions Science and Technology* 13: 143-152

Speck CK. 1994. *Änderung des Grundwasserregimes unter dem Einfluss von Gletschern und Permafrost*. Zurich: Versuchsanstalt für Wasserbau, Hydrologie und Glaziologie an der Eidgenössischen Technischen Hochschule Zürich. 164 pp.

Springman S, Teysseire P. 2001. *Artificially induced rainfall instabilities on moraine slopes.* Proceedings of the International Conference on Landslides, Davos, Switzerland, 17-21 June 2001, Kühne M (ed.). Essen: Verlag Glückauf; 209-223

Springman SM, Jommi C, Teysseire P. 2003. Instabilities on moraine slopes induced by loss of suction: a case history. *Geotechnique* 53: 3-10

Stadler D, Forrer I, Aeby P, Studer B, Gähwiller P, Flühler H. 1998. *Visualizing and Quantifying Water Infiltration in Frozen Soils*. Zurich: Soil Physics, Institute of Terrestrial Ecology, Swiss Federal Institute of Technology Zurich. 62 pp.

Stadler D, Stähli M, Aeby P, Flühler H. 2000. Dye tracing and image analysis for quantifying water infiltration into frozen soils. *Soil Science Society of America Journal* 64: 505-516

Stähli M, Bayard D, Wydler H, Flühler H. 2004. Snowmelt infiltration into alpine soils visualized by dye tracer technique. *Arctic Antarctic and Alpine Research* 36: 128-135

Stoop P. 1989. *Über den Wärmehaushalt eines alpinen Permafrostgebietes*. Diploma thesis. Swiss Federal Institute of Technology Zurich, Zurich. 76 pp.

Stroud MA. 1971. *Sand at low stress levels in the S.S.A.* Doctoral thesis. Cambridge University, Cambridge

Sun ZZ, Ma W, Li DQ. 2005. In situ test on cooling effectiveness of air convection embankment with crushed rock slope protection in permafrost regions. *Journal of Cold Regions Engineering* 19: 38-51

Suzuki K, Kubota J, Ohata T, Vuglinsky V. 2006. Influence of snow ablation and frozen ground on spring runoff generation in the Mogot Experimental Watershed, southern mountainous taiga of eastern Siberia. *Nordic Hydrology* 37: 21-29

Taylor DW. 1948. *Fundamentals of soil mechanics*. New York: Wiley. 700 pp.

Tenthorey G. 1993. *Paysage géomorphologique du Haut-Val de Réchy (Valais, Suisse) et hydrologie liée aux glaciers rocheux*. Dissertation thesis. University of Fribourg, Fribourg, Switzerland. 307 pp.

Terzaghi K, Peck R. 1967. *Soil Mechanics in Engineering Practice*. New York: John Wiley and Sons. 729 pp.

Tharp TM. 1987. Conditions for crack-propagation by frost wedging. *Geological Society of America Bulletin* 99: 94-102

van Mechelen JLM. 2004. Strength of moist sand controlled by surface tension for tectonic analogue modelling. *Tectonophysics* 384: 275-284

Veneziano D, Essiam AK. 2003. Flow through porous media with multifractal hydraulic conductivity. *Water Resources Research* 39: 1166

Vogel HJ, Tolke J, Schulz VP, Krafczyk M, Roth K. 2005. Comparison of a Lattice-Boltzmann model, a full-morphology model, and a pore network model for determining capillary pressure-saturation relationships. *Vadose Zone Journal* 4: 380-388

Von Maubeuge KP, Eberle MA. 1998. *Can geosynthetic clay liners be used on slopes to achieve long-term stability?* Proceedings of the 3rd International Congress on Environmental Geotechnics, Lisbon, Portugal, 7-11 September 1998, Sêco e Pinto, P (ed.). Lisse, The Netherlands: Balkema Publishers; 375-380

Vonder Mühll D, Delaloye R, Haeberli W, Hoelzle M, Krummenacher B. 2001. *Permafrost Monitoring Switzerland PERMOS: 1. Jahresbericht 1999/2000*, University of Basel, Basel. 32 pp.

Vonder Mühll D, Haeberli W. 1990. Thermal characteristics of the permafrost within an active rock glacier (Murtèl Corvatsch, Grisons, Swiss Alps). *Journal of Glaciology* 36: 151-158

Vonder Mühll DS, Hauck C, Lehmann F. 2000. Verification of geophysical models in Alpine permafrost using borehole information. *Annals of Glaciology* 31: 300-306

Vyalov SS. 1962. *The strength and creep of frozen soils and calculations for ice-soil retaining structures*. Hanover, New Hampshire: U.S. Army Cold Regions Research and Engineering Laboratory. 321 pp.

Waldner PA. 2002. *Water and solute release from a subalpine snow cover*. Doctoral thesis. Swiss Federal Institute of Technology Zurich, Zurich, Switzerland. 147 pp.

Weast RC, Astle MJ, eds. 1982. *CRC handbook of chemistry and physics: a ready-reference book of chemical and physical data*. Boca Raton, Florida: CRC Press

Whalley WB, Martin HE. 1992. Rock Glaciers 2. Models and Mechanisms. *Progress in Physical Geography* 16: 127-186

Williams PJ, Smith MW. 1989. *The Frozen Earth: Fundamentals of Geocryology*. Cambridge: Cambridge University Press. 306 pp.

Yamazaki Y, Kubota J, Ohata T, Vuglinsky V, Mizuyama T. 2006. Seasonal changes in runoff characteristics on a permafrost watershed in the southern mountainous region of eastern Siberia. *Hydrological Processes* 20: 453-467

Yasufuku N. 2002. *Constitutive and centrifuge modelling: two extremes*. Proceedings of the Workshop on Constitutive and Centrifuge Modelling: Two Extremes, Monte Verita, Switzerland, 8-13 July 2001, Springman S (ed.). Lisse, The Netherlands: Balkema Publishers; 365-367

Zhang MY, Lai YM, Gao ZH, Yu WB. 2006. Influence of boundary conditions on the cooling effect of crushed-rock embankment in permafrost regions of Qinghai-Tibetan Plateau. *Cold Regions Science and Technology* 44: 225-239

Zimmermann M. 1990. Periglaziale Murgänge. In *Internationale Fachtagung über Schnee, Eis und Wasser der Alpen in einer wärmeren Atmosphäre: 11. Mai 1990 in Zürich*, ed. D Vischer, pp. 89-107. Zurich: Versuchsanstalt für Wasserbau, Hydrologie und Glaziologie der Eidgenössischen Technischen Hochschule Zürich

Zimmermann M, Mani P, Gamma P. 1997. *Murganggefahr und Klimaänderung - ein GIS-basierter Ansatz*. Zurich: vdf Hochschulverlag AG an der ETH Zürich. 161 pp.

Curriculum Vitae

Armin Rist

Born 31 January 1974 in Tübingen, Germany

Citizen of Mössingen, Germany

Education

1984 – 1993	High School: *Quenstedt-Gymnasium*, Mössingen, Germany. Focus on Mathematics and Science. Abitur in Mathematics and Physics.
1993 – 1994	Civil National Service: Retirement Home *Haus an der Steinlach*, Mössingen, Germany.
1995 – 1996	Enrolment in Mechanical Engineering: University of Stuttgart, Germany.
1997 – 2002	Enrolment in Environmental Sciences: Technical University of Munich, Science Centre Weihenstephan, Freising, Germany.
1999	Student Apprentice in Environmental Protection and Sustainable Development: Annapurna Conservation Area Project ACAP, Pokhara, Nepal.
2002	University Diploma in Environmental Sciences. Thesis: *Undercooled Scree Slopes Covered with Stunted Dwarf Trees in Switzerland - Abiotic Factors to Characterize the Phenomenon*. Swiss Federal Institute for Forest, Snow and Landscape Research WSL, Location Davos SLF, Switzerland and Technical University of Munich, Science Centre Weihenstephan, Freising, Germany.
2003	Graduated Trainee in Periglacial Mountain Research: Swiss Federal Institute for Forest, Snow and Landscape Research WSL, Location Davos SLF, Switzerland.
2003 – 2007	Dissertation in Physical Geography. Thesis: *Hydrothermal Processes within the Active Layer above Alpine Permafrost in Steep Scree Slopes and their Influence on Slope Stability*. Swiss Federal Institute for Forest, Snow and Landscape Research WSL, Location Davos SLF, Switzerland and Physical Geography Division, Department of Geography, University of Zurich, Switzerland. Advised by Dr. Marcia Phillips (WSL-SLF, Davos), Prof. Dr. Wilfried Haeberli (Dept. of Geography, University of Zurich) and Dr. Walter Ammann (WSL-SLF, Davos).